



TECHNISCHE
UNIVERSITÄT
WIEN
Vienna | Austria

DISSERTATION

Electron Vortex Beams: Production and Application

Ausgeführt zum Zwecke der Erlangung des akademischen Grades eines
Doktors der technischen Wissenschaften unter der Leitung
von

Ao. Univ. Prof. Dr. Peter Schattschneider

E138

Institut für Festkörperphysik

eingereicht an der Technischen Universität Wien
Fakultät für Physik

von

Dipl.-Ing. Thomas Schachinger

00526782

Radetzkystraße 10/2/13

A-1030 Wien

Wien, Juni 2019

Kurzfassung

Transmissionselektronenmikroskope (TEM) stellen ein leistungsfähiges Werkzeug sowohl für die Abbildung als auch für die Analytik auf der Größenskala von Nanometern und darunter dar. Durch den Einbau von computergenerierten holographischen Masken in das Kondensorsystem eines TEMs ist es möglich die Wellenfunktion des Elektrons in beliebiger Art und Weise zu manipulieren. Die erste Anwendung dieses Prinzips war die Herstellung von Elektronenvortexstrahlen (EVS). Diese tragen sowohl einen quantisierten Bahndrehimpuls als auch ein quantisiertes magnetisches Moment.

Binäre holographische Absorptions-Vortexmasken, die mittels einer Gallium-Ionenfeinstrahlanlage (FIB) geschnitten werden, stellen eine leistungsfähige und relativ einfache Methode zur Erzeugung von EVS dar.

Für jene zwei Anwendungen von EVS, die in dieser Arbeit untersucht wurden, werden u.a. große holographische Masken mit kleiner Gitterperiode und hoher Beugungseffizienz benötigt. Deshalb wurden in dieser Arbeit Optimierungen des Herstellungsprozesses der binären holographischen Absorptionsmasken durchgeführt. Insbesondere wurde untersucht, ob und inwiefern sich die Materialauswahl und die Beschichtungsparameter für die Herstellung elektronenabsorbierender Metallfilme, sowie die FIB Schneidstrategie, auf das Ergebnis des FIB Schneidvorgangs auswirken.

Während die Versuche bezüglich der FIB Schneidstrategie keine klaren Vorteile in der Maskenqualität zeigten, ergab die Verwendung eines neu entworfenen stabileren Probenhalters, sowie ein eigens für die Maskenherstellung entworfenes Driftkorrekturskript, deutliche Verbesserung der Maskenschneidresultate. Ebenso konnte mithilfe der Verwendung von Iridium und Osmium – jene Materialien mit der höchsten Dichte und sehr hohen Festigkeitswerten – der Bedarf stabilisierender Querstege im Vergleich zum typischerweise verwendeten Platin deutlich reduziert werden. Weiters ergab die Optimierung der Beschichtungsparameter eine massive Verringerung der Elektronentransparenz der Osmiumfilme im Vergleich zu nicht optimierten Schichten. Allerdings zeigten die hochreinen Osmiumschichten auch sehr große Druckspannungen, welche zu starker Deformation der Stege des Beugungsgitters führten. Indem der kritische Arbeitsgasdruck für die Beschichtung mittels Kathodenzerstäubung gefunden wurde, konnten diese Schichtspannungen auf ein Minimum reduziert werden. Diese Maßnahmen führten dazu, dass es nun möglich ist sehr große und zugleich feinstrukturierte holographische Vortexmasken zu erstellen.

Bedingt durch die intrinsische Chiralität von EVS werden sie als viel versprechende Alternative zur Messung des magnetischen Zirkulardichroismus (EMCD) gesehen. In magnetischen Materialien entstehen atomar kleine EVS während des inelastischen Streuprozesses. Mithilfe einer holographischen Vortexmaske, welche als Bahndrehimpulsfilter nach der Probe eingesetzt wurde, konnte die Bahndrehimpulsverteilung der

Elektronenwelle nach der Wechselwirkung mit der Probe analysiert werden. Somit stellt diese Methode eine Alternative zum klassischen EMCD dar, um Magnetismus auf der Nanometerskala zu messen, und dies, ohne eine aufwändige und teils langwierige Probenorientierung durchführen zu müssen. Bei Messungen an zwei verschiedenen Mikroskopen und verschiedenen Testproben konnten Hinweise auf ein schwaches EMCD Signal von 3 % bis 7 % detektiert werden, was eine gute Übereinstimmung mit Multi-Slice-Simulationen darstellt. Zusätzlich konnte eine Umkehrung des EMCD Signals zwischen den $L_{3,2}$ -Absorptionskanten, sowie bei Magnetfeldumkehr der Objektivlinse beobachtet werden. Dies stellt einen weiteren Hinweis auf ein tatsächlich vorhandenes EMCD Signal dar. Experimentell gleicht die Vortexfilter-EMCD-Methode der Scanning-TEM-Technik. Daher ist die räumliche Auflösung dieser alternativen EMCD-Methode im Wesentlichen gegeben durch den Strahldurchmesser auf der Probe. Dieser betrug 1 nm bzw. 0.8 nm, womit gezeigt werden konnte, dass Nanometer sowie Sub-Nanometer Auflösung möglich sind. Multi-Slice-Simulationen weisen darauf hin, dass mit dieser Methode, unter Verwendung eines High-End-TEMs, welches mit einem Korrektor für die chromatischen Aberrationen des Objektivs ausgestattet ist, auch atomare Auflösung möglich sein sollte. Diese neue EMCD-Technik könnte in Zukunft zur Untersuchung von Grenzflächenmagnetismus von z.B. Riesenmagnetowiderstand (GMR) Dünnschichtsystemen angewendet werden, sowie möglicherweise dazu beitragen neue magnetische Speichertechnologien zu entwickeln die auf der Detektion und Manipulation einzelner Atome beruhen.

Die zweite Anwendung von EVS beschäftigt sich mit der Untersuchung der Wechselwirkung des Elektronenbahndrehimpulses mit dem magnetischen Linsenfeld eines TEMs. Dabei zeigte sich, dass das Rotationsverhalten von EVS interessante Besonderheiten aufweist. So wurde die langsame Larmor-Rotation, die, um drei bis vier Größenordnungen schnellere, Gouy-Rotation, sowie die Rotation bzw. fehlende Rotation von freien Landau-Zuständen beobachtet. Diese drei verschiedenen Klassen von Rotationsfrequenzen konnten mit Hilfe eines quantenmechanischen Ansatzes erklärt werden. Zusätzlich wurde eine dimensionslose universelle Funktion gefunden, die die Rotationsfrequenzen der EVS, welche über vier Größenordnungen reichen und unter verschiedenen experimentellen Bedingungen aufgenommen wurden, sehr gut beschreibt.

Abstract

Transmission electron microscopes (TEMs) are a powerful tool for nanoscale imaging and material analytics. By placing computer-generated holographic masks in the condenser system of a TEM, it is possible to arbitrarily shape the electrons' wavefront. The archetypical case of engineered electron wavefronts are electron vortex beams (EVBs). They carry a quantized orbital angular momentum as well as a quantized magnetic moment.

Binary amplitude holographic vortex masks fabricated by focused ion beam (FIB) milling represent a powerful and straightforward method to produce electron vortices. For the two applications of EVBs studied in this work, i. a. large-scale, high diffraction efficiency holographic devices with low grating periodicities are needed. Therefore, optimizations to improve the production process of binary amplitude holographic vortex masks have been carried out. In particular, it has been investigated if and how the material choice and the deposition parameters of the metallic membranes used for the production of binary amplitude holograms as well as the FIB milling strategy affect the FIB milling result.

While tests in order to emend the FIB milling strategy did not show a significant advancement in the holograms' fidelity, the introduction of a newly designed high stability sample holder and a custom made drift correction script showed marked improvements in the FIB milling performance. Likewise, in comparison to the traditionally used Platinum, the employment of Iridium and Osmium – known to have the highest density of all elements and very high mechanical strength – reduced the need for a stabilization grating. Upon improvement of the sputter deposition parameters, Osmium thin films showed massively reduced electron transmission values, compared to non-optimized films. However, the high thin film purity came at the expense of high compressive inner stresses causing grating deterioration and -collapse. By finding the critical sputtering pressure of Osmium, these inner tensions could be strongly reduced. These measures facilitated the production of finely structured large-scale vortex masks.

Due to the intrinsic chirality of EVBs, they have become a promising candidate for electron energy-loss magnetic chiral dichroism (EMCD) measurements. In magnetic materials, atom-sized EVBs are naturally produced in the inelastic scattering events. By employing a holographic vortex mask as an orbital angular moment filtering element in a post-specimen geometry, the orbital angular momentum content of the outgoing vortex electron waves could be analysed. This represents an alternative approach to classical EMCD for the measurement of magnetism on the nanometre scale, without the need for a tedious crystal alignment. Measurements on two different TEMs and different test samples delivered evidence for the detection of a faint

EMCD signal of 3% to 7%, which is in good agreement with multi-slice simulations. Also, signal reversals for the $L_{3,2}$ -edges and for magnetisation switching have been observed, further hinting at the presence of a real EMCD signal. Because this alternative EMCD method resembles a scanning TEM technique, the resolution of the method is essentially determined by the size of the focused electron probe. The spot size in these proof-of-principle experiments was 1 nm and 0.8 nm, respectively. Thus, nanometre and even sub-nanometre resolution could be achieved. Accompanying multi-slice simulations suggested the possibility of reaching even atomic resolution when using chromatic aberration corrected state-of-the-art instrumentation. This new approach may be used to explore interface magnetism in, e.g., thin film stacks, showing the giant magneto-resistive (GMR) effect, and may pave the way to the development of atomic scale magnetic memory technology.

EVBs have also been used to study the interaction of the electrons' orbital angular momentum with the magnetic lens field of a TEM. It could be found that their rotational behaviour reveals peculiar rotational-dynamics, including slow Larmor-rotation, three to four orders faster Gouy-rotations and freely floating electron Landau-states. These three different rotation-regimes could be reconciled using a quantum approach. A dimensionless universal function was found that describes experimental data, covering the rotational-dynamics of electron vortices over four orders of magnitude for different experimental conditions.

Acknowledgements

At this point I really want to thank my supervisor Prof. Peter Schattschneider for his support throughout this thesis, and for the freedom he gave me to try things out on my own. A lot of thanks should also go to my colleague Dr. Stefan Löffler for numerous discussions on electron vortex beams, his critical mind and for always taking the time to help and troubleshoot in various kinds of problems, mostly related to scripting or coding. E.g. he implemented adaptations and improvements to the multi-slice code and assisted me in writing DM3 scripts for data analysis. I also want to acknowledge Prof. Johannes Bernardi and the whole USTEM-team for providing an engaging work environment and the TEM, SEM and FIB infrastructure. Especially my colleagues Prof. Michael Stöger-Pollach, who helped me with the EELS spectrometer in the first vortex EMCD experiments, Dipl. Ing. Andreas Steiger-Thirsfeld, who spent a lot of (evening) time milling test structures and vortex masks on the FIB instrument and Jakob Gruber, who helped me with practical issues in the lab and the workshop, should be mentioned.

A lot of thin film characterisation was done in Prof. Christoph Eisenmenger-Sittners' lab, so I want to thank him for providing the thin film characterisation tools and also for lending me the platinum sputtering target. Also, the valuable work of Arthur Weber, who prepared the sputtered iron samples and Stefan Sack, who implemented the possibility to simulate amorphous materials using the multi-slice code, is very much appreciated.

Many thanks are also addressed to the IFW Dresden team around Dr. Bernd Rellinghaus for providing the nano-crystalline iron and cobalt samples and beam time on their *Helios* FIB instrument. Especially Tina Sturm helped me a lot with her systematic stream file milling tests. Moreover, I appreciate the work of Dr. Federico Venturi who produced the phase masks for the Jülich experiments, Dr. Amir H. Tavabi for helping with the *Titan Holo* microscope alignment and Rafal E. Dunin-Borkowski for providing beam time at the *Titan Holo* at the ER-C in Jülich. I am also indebted to Michal Horak, M. Sc. for operating the *Helios* FIB at the CEITEC in Brno delivering valuable insights into FIB milling of different materials and providing the iron-rhodium sample and to Tomáš Řiháček, M.Sc. providing silicon-nitride membranes for FIB milling tests.

Of course, I also want to appreciate the financial support by the Austrian Academy of Science (ÖAW) in the form of a DOC scholarship, the Austrian Science Fund (FWF) (projects: I543-N20 and P29687-N36), the *Hochschuljubiläumstiftung der Stadt Wien* (project: H-294689/2016), the European Microscopy Society (EMS) for awarding me two scholarships for visiting congresses and the Austrian Society of Electron Microscopy (ASEM) for generous travel reimbursements, which enabled

me to take part at many delighting conferences throughout Europe. Not forgetting USTEM, who financed parts of the sputter coater Peltier bake-out and cooling system and Computer-Studio Wehsner GmbH, who sponsored the computer case for the system.

Also, many thanks to Mia Schachinger for taking the time to proofread the manuscript.

Finally, I want to express my gratitude towards my wife Marie-Luise, for taking care of our four wonderful children, especially in the last few months. Without her support 'behind the scene' this thesis would not have been possible.

Contents

1	Introduction	17
1.1	Motivation	17
1.2	Background	17
1.3	Outline	22
2	Fundamentals	23
2.1	Transmission Electron Microscopy	23
2.2	Electron-Energy-Loss Spectrometry	32
2.3	Energy-Loss Magnetic Chiral Dichroism	38
2.4	Electron Vortex Beams	43
2.4.1	Wavefront Engineering	44
2.4.2	General Introduction	45
2.4.3	Theory	46
2.4.4	Electron Vortex Production	52
2.5	Alternative Electron Vortex Production Methods	56
2.6	Vorticity Filtering in a TEM	59
2.7	Multi-Slice Simulation Technique	61
2.8	The Dual Beam Machine and Focused-Ion-Beam Milling	65
2.9	Thin Film Production	68
2.9.1	Magnetron Sputtering	68
2.9.2	Vacuum Technology	74
2.9.3	Thin Film Characterisation Techniques	78
3	Device Modifications and New Measurement Tools	87
3.1	Sputter Coater Vacuum System	87
3.1.1	Vacuum Logging	88
3.1.2	Modelling the pump-down behaviour	89
3.1.3	Vacuum System Improvements Measures	92
3.2	The Sputter Coater Vacuum Chamber and Sample Heating- and Cooling System	98
3.3	A Basic Thin-film Tensiometer to Estimate Thin Film Stresses	102
3.4	Focused Ion Beam Milling at a Reduced Working Distance	107
3.5	A Focused Ion Beam Sample Stage for TEM Grids and Membranes	109
3.6	Focused Ion Beam Milling Drift Correction Script for the Production of Holograms	110

4	Optimization Strategies for the Production of Binary Holographic (Amplitude) Vortex Masks	117
4.1	Vector Scan Approach for Focused-Ion-Beam Milling of Holographic Vortex Masks	117
4.2	Testing a Spatial Dwell Time Modulation as a Means to Improve the Grating Cross-Sections	125
4.3	Improving the Thin Film Production	131
4.3.1	Influence of the Mask Material on Focused Ion Beam Milling of Holographic Vortex Masks	135
4.3.2	Optimizing the Thin Film Density	140
4.3.3	Optimizing the Thin Film Inner Stresses and Grain Size	145
4.4	Binary Holographic Phase Mask Results	160
4.5	Prospects to Mount Holographic Vortex Masks in a Standard Objective Aperture Strip	163
5	Recent Applications and Progress	167
5.1	Electron Vortex Beam Filter - EMCD	167
5.1.1	Introduction	168
5.1.2	Experimental Setups	168
5.1.3	Principle and Theory of the Single Atom Scattering Approach	173
5.1.4	OAM Conservation in Amorphous Materials - Elastic Multi-Slice Simulations	178
5.1.5	Artefact Sources	181
5.1.6	Inelastic Multi-Slice Simulations	187
5.1.7	Experimental Results	193
5.1.8	Discussion	204
5.2	Production of Peculiar Rotational States in Magnetic Fields Using Electron Vortex Beams	206
5.2.1	Introduction	206
5.2.2	Theory of the Rotation Dynamics	207
5.2.3	Simulation	210
5.2.4	Experimental	211
6	Conclusions and Outlook	217

List of Figures

1.1	Vortices on different length-scales	18
1.2	Schematic principle of vortex generation, vortex mask and resulting vortices	20
2.1	Historical evolution of the TEM	25
2.2	Schematic representation of a non-aberration-corrected transmission electron microscope (TEM)	28
2.3	Different contributions and limiting factors to the achievable spot size in a typical non-aberration-corrected field-assisted thermionic emitters (FEG) TEM	30
2.4	Different interactions and signals that are induced when a swift incident electron hits the TEM sample	33
2.5	Historic evolution of TEM post-column filters	34
2.6	(Post-column) magnetic prism schematics	36
2.7	Typical electron energy loss spectrometry (EELS) spectrum plus graphical explanation of its physical origin	37
2.8	A schematic explanation of the electron energy-loss magnetic chiral dichroism (EMCD) effect	40
2.9	Schematic classical EMCD measurement setup in a TEM	43
2.10	Probability density of <i>Bessel</i> beams	48
2.11	Plane views and cross-sections of the probability density of diffracting <i>Laguerre-Gaussian</i> (DLG) modes	49
2.12	Probability density of DLG vortex modes ($m = \pm 1, \pm 2$) and non-vortex modes ($m = 0$)	50
2.13	Cross-section of a wavefunction, propagating through vacuum after passing a binary holographic vortex mask (HVM)	52
2.14	Representation of transmission functions of HVMs and their diffraction patterns (electron vortex beam (EVB)s)	54
2.15	Finite-elements simulation of a nanoscale magnetic needle	58
2.16	Vorticity filtering principle using a binary HVM	60
2.17	Multi-slice simulation principle	62
2.18	Multi-slice (MS) simulation results example	64
2.19	Inelastic scattering multi-slice principle and the inelastic scattering kernels	64
2.20	The dual beam instrument, image and schematics	65
2.21	Sputter yield dependencies for Ga-ions, ion-energy and incidence angle	66
2.22	Magnetron sputtering principle and sputter coater image	69

List of Figures

2.23	Sputter yields for different Ar-ion energies and different target materials	71
2.24	Structure-zone model of <i>Thornton</i>	72
2.25	Illustrating the influence of the base pressure before sputtering on the thin film morphology	73
2.26	Thin film stylus profilometer schematics and image	79
2.27	Optical transmission thickness measurement principle	82
2.28	Optical transmittance T curves over thin film thickness d for various materials	83
2.29	Four point probe measuring principle	84
2.30	Four point probe measuring station for thin film electrical conductivity measurements	85
3.1	T-piece added to the Q150T sputter coater for an electrical feed-through	89
3.2	Calculated vacuum pump-down curves for the Q150T	91
3.3	High vacuum side backing line evolution	93
3.4	Before and after polishing comparison of the turbo molecular pump (TMP) connection pipe of the sputter coater	95
3.5	Before and after replacing the ‘L’-gasket of the sputter coater with a O-ring sealing	96
3.6	Logarithmic plot of the pump-down curves of the Q150T after various vacuum improvement measures	97
3.7	First version of the sputter coater thermal management system	99
3.8	Schematic of the new thermal management system for the Q150T sputter coater	101
3.9	Images of the sputter coater vacuum chamber and sample heating and cooling system	103
3.11	Schematics of thin film stress effects on substrate bending	105
3.12	Image of the self-built reflection tensiometer with the schematics overlaid	106
3.13	Focused-ion-beam machine (FIB) working distance (WD) 30 mm and 10 mm comparison	108
3.14	Self-built FIB holder for $\varnothing 3$ mm TEM apertures and membranes	110
3.15	Geomagnetic field variation and simulated Ga-ion-beam deflection in weak magnetic fields	111
3.16	Panel of the FIB drift correction routine dialogues	113
4.1	Comparison of ion-beam movement strategies	118
4.2	Stream file example	119
4.3	Schematics of the search algorithm, used to detect the outer boundaries of a connected region and spiral vector path example	120
4.4	Influence of the milling direction	121
4.5	Comparison of HVM milling results using raster- and vector-scanning	122
4.6	Comparison of HVM milling results using raster- and vector-scanning with improved thin film quality and higher pixel density	123
4.7	Schematic cross-section of one grating bar	126

4.8	Principle of the beam position-dependent dwell time adaption	127
4.9	Plane-view overview of the edge-dwell-time (EDT) test structures for different EDT parameters	128
4.10	Comparison of different EDT parameters by showing FIB prepared cross-sections of a test structure	129
4.11	Direct comparison of the different EDT parameters, extracted from Figure 4.10	130
4.12	Typical examples of grating collapses	132
4.13	Influence of the HVM primary grating transmission and the presence of a second-order grating on the DE	133
4.14	Schematic drawing of the layer structure of holographic amplitude masks	134
4.15	FIB milling results using the Quanta 3D, comparing different sputtered materials	137
4.16	FIB milling results comparing different membrane materials for $\text{\O}14.45\ \mu\text{m}$ and $g = 192\ \text{nm}$ HVMS	139
4.17	Monte-Carlo-Simulation of the scattering strength of materials showing a different density	140
4.18	Measured thin film resistivity values of the sputtered Os/Cr/Ir thin films	142
4.19	EDX analysis results of some of the sputtered Os thin films	143
4.20	O-content in OsCr thin films reduction upon reduced base pressure	144
4.21	Atomic emission spectra for different gas species	146
4.22	Image series extracted from a video of the ignition of the Ar plasma	146
4.23	Effects of thin film inner stress	147
4.24	Schematic of the mechanical supporting bar model	148
4.25	Result of the thin film tension optimization process	150
4.26	Inner stress versus Ar pressure curve	151
4.27	Influence of thin film inner stresses on the FIB milling results of HVMS	153
4.28	FIB milling results under non-optimized and optimized conditions of large-scale HVMS with low grating periodicities	154
4.29	Collimated sputtering schematics and image	155
4.30	Results of the collimated sputtering approach, scanning ion microscope (SIM) and TEM EVB images	157
4.31	Testing the three-step milling procedure to reduce or even completely avoid the use of a supporting grating	159
4.32	Binary phase HVM TEM low magnification and far-field images	161
4.33	Schematics of the floating-off process to place a thin film on an aperture strip for the production of HVMS	164
4.34	Floated off carbon thin film, placed on an aperture strip	165
5.1	Proof of the vortex filter functionality in vacuum at the <i>Tecnai F20</i>	168
5.2	Vortex filter EMCD experimental setups using post-specimen vortex filtering holograms	170

List of Figures

5.3	Gaussian ray optics of a standard TEM diffraction setup, the diffraction plane (DP) vortex filter setup and the selected area aperture (SAA)-plane vortex filter setup	171
5.4	Scattering profiles for non-magnetic isotropic transitions in momentum space for the Co L ₃ -edge	174
5.5	Schematic illustration of the vortex filtering principle for the three different scattering channels $\mu = 0, \pm 1$	176
5.6	Radial intensity profiles of a $m = \pm 1$ filtered image of a single atomic ionization, for the fully spin-polarized case	177
5.7	OAM conservation: Elastic multi-slice simulation, compared to an experimental test on an amorphous Fe-based alloy	179
5.8	MS simulation of the orbital angular momentum (OAM) conservation in α -Si ₃ N ₄	180
5.9	Incoherent broadened vortex profiles using the single atom scattering approach	182
5.10	Artificial difference signals as a result of defocus differences, mask tilt and astigmatism	183
5.11	Influence of a blazed HVM on the electron intensity distribution	186
5.12	inelastic scattering multi-slice simulation (IMS) defocus- and thickness series, calculated for an energy-loss of 708 eV for crystalline bcc-Fe and an amorphous Fe-based alloy	188
5.13	MS simulation result of elastic electron scattering of an incident atomic scale wavefunction, propagating through an amorphous Fe alloy	189
5.14	Extended IMS thickness series of bcc-Fe	190
5.15	A more realistic approach to incoherent source size broadening	191
5.16	IMS including incoherent source size broadening (ISSB) over one unit-cell of Fe	194
5.17	Trial vortex filtering EMCD experiment on Co	195
5.18	SAA vortex filter EMCD experiment on FeRh	200
5.19	SAA vortex filter EMCD experiment on Fe	201
5.20	DP vortex filter EMCD experiment on Fe	203
5.21	Comparison between an numerical simulated EVB and the analytical <i>Laguerre-Gaussian</i> (LG) mode	209
5.22	Principal experimental setup, HVM image and knife edge image	212
5.23	Experimental image of cut EVBs and experimental data of a full z -shift series	213
5.24	Comparison of various experimental results with theory and numerical simulations by using the universal function	215

List of Tables

2.1	Theoretical diffraction efficiency (DE) of different kinds of phase and amplitude HVMs	56
2.2	Structure zone model summary	73
2.3	Influence of the background gas pressure on monolayer formation times	75
2.4	Gas desorption values for different materials	76
2.5	Gas permeation values for different materials	77
2.6	Extinction coefficient and attenuation values for some materials	81
4.1	Results of the scanning electron microscope (SEM) EDT image analysis	131
4.2	Amplitude HVM materials with some of their mechanical, electrical and thermal properties	136
4.3	Leakage rate of the process gas line due to gas permeation for different tubing options	145
4.4	Transmission values for amplitude HVMs milled into various materials/thicknesses	156
4.5	Estimated absolute DE in units of electron counts of different HVMs, based on count rate measurements	163
5.1	<i>Clebsch-Gordan</i> coefficients C^μ for the L_3 -edge	176
5.2	Effect of lowering the ISSB on the beam current and the expected EMCD signal	192
5.3	Rotational frequencies in units of Ω for the numerical calculation, the diffracting LG approximation and the experimental data	214

1 Introduction

1.1 Motivation

Vortices are everywhere! – The ubiquitous presence of vortices in nature and their inherent beauty, tried to exemplify in Figure 1.1, were definitely one of the key aspects why I dived into the research around EVB. Besides, there is still a latent feeling in me that such an omnipresent phenomenon may be of fundamental importance to the understanding of what holds the universe together at its innermost folds.

At the time when I entered science in 2012 the excitement after the theoretical prediction of electron vortices in 2007 by *Konstantin Bliokh* et al. [3] and their subsequent experimental discovery shown in the seminal papers of *Uchida* et al. [4] and *Verbeeck* et al. in 2010 [5] was still around. It was realized that one can actively shape the electron wavefront and impart quantized units of orbital angular momentum to the electron by using nano-structured materials. This opened up the door for a more general research area, namely wavefront engineering, and it evolved to what is now a vibrant research field, striving for new production methods and applications of this new electron waveform.

1.2 Background

The discovery, in 2006, that magnetic chiral dichroism can be observed in the TEM [6] provided an unexpected alternative to X-ray magnetic chiral dichroism (XMCD) [7] and magnetic neutron scattering [8], both of which can only be performed in large and costly synchrotron/neutron sources, as well as optical methods like the (surface) magneto-optic *Kerr* effect (SMOKE or MOKE) [9]. All of these methods are limited in spatial resolution to tens or even hundreds of nanometres whereas EMCD has seen tremendous progress since then [10–13], achieving nanometre resolution [14, 15], and indications of sub-lattice resolution [12, 16, 17]. It opened new ways for studying magnetism on the nanometre and atomic scale, an aspect crucial for ultra-high density storage media and spintronics. An important aspect of this so-called classical EMCD method is that the crystalline specimen itself acts as a *Bragg* beam splitter for the inelastically scattered electrons and, at the same time, works as a vorticity analyser by interferometric means. This clever trick is also one of its inherent drawbacks when coming to technologically interesting questions like interface- and surface magnetism and magnetic properties of defects. Also, amorphous and nano-crystalline materials are not readily accessible by classical EMCD, calling for a new EMCD method overcoming these drawbacks. Vorticity filtering utilizing computer generated holographic

1 Introduction

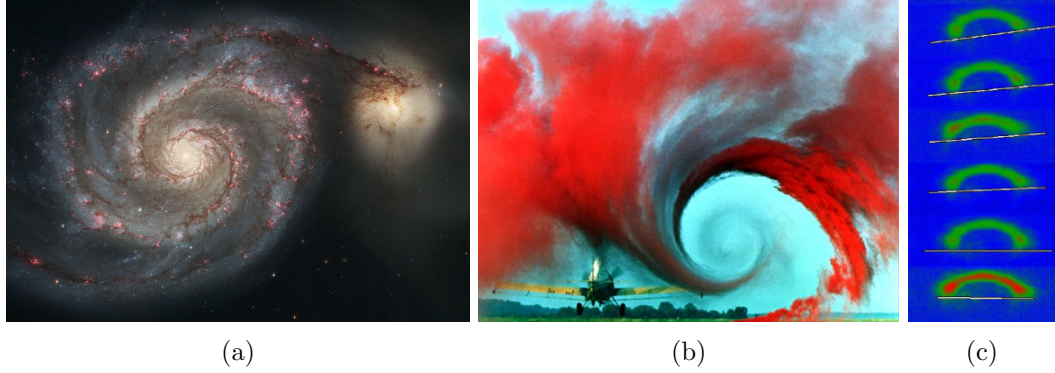


Figure 1.1: Vortices' presence on different length scales spanning roughly 10^{30} orders of magnitude. (a) The Whirlpool galaxy, a spiral galaxy [1]. (b) Wake vortex study: vortical motion in air induced by an airplane's wing tip [2]. (c) A three dimensional projection of a defocus series showing an electron vortex spinning through the magnetic lens field with 19 GHz, the diameter of the structure is ≈ 15 nm.

mask (HM) and an adapted experimental geometry is a promising candidate as will be elaborated in the following.

In 2010 with the prediction [3] and the independent discovery of EVB by *Uchida* and *Tonomura* [4] and *Verbeeck* et al. [5], who were using nano-structured HM, a whole new era began in the field of electron microscopy. The vivid field of singular optics [18], where phase vortices were originally described by *Nye* and *Berry* [19] and subsequently discovered by *Bazhenov* et al. and two years later by *Allen* and co-workers [20, 21] could now be expanded to (charged)¹ particle physics. On the one hand it was proven and realised for the first time that the electrons' wavefront can be shaped in a way that it carries quantized OAM in units of \hbar , as well as quantized magnetic moment in units of the *Bohr* magneton by placing HMs with dislocation gratings (a HVM) in the condenser system of a TEM [5], see Figure 1.2. On the other hand, these investigations opened up the field of electron wavefront engineering in general, meaning that nearly any desired electron wavefront or probe geometry can be generated by 'simply' milling its *Fourier* transform into a thin metallic film, which would resemble an absorption- or amplitude mask. Or by milling the structure into few nanometre thick amorphous SiO_2 - or non-stoichiometric silicon nitride (SiN_x)-membranes, representing a phase shifting- or phase-mask [23–25]. With that, symmetry- or problem-adapted probe geometries can be prepared and used to enhance otherwise hidden signals or characteristics of the specimen [26, 27]. Also, aberration correction without the need for complex and costly C_s -correctors (complex arrangements of multi-pole magnetic fields) becomes feasible [28].

Coming back to EVBs, due to their OAM, which can be arbitrarily high in contrast

¹Recently, the production of neutron vortices has also been shown, see [22].

to the spin angular momentum, some peculiar effects and applications can be observed and will also be described in part three of this thesis. For example, it was known from optics that photons can be used to trap particles [29] as well as to impart OAM onto test objects [21], which inspired researchers to transfer that finding to electron vortices by showing manipulation of Au nanoparticles [30]. Also, when decomposing the scattering amplitude into a basis of OAM eigenstates it is possible to use elastic EVB scattering to detect crystals' chirality [31]. Moreover, it will be shown how EVBs can be used to produce free-electron *Landau*-states (LS) – which are quantised electron states in magnetic fields – and at the same time reveal a set of peculiar fast azimuthal dynamics of the order of 19 GHz in the magnetic field of the TEM objective lens [32]. Using standard electron imaging theory, one would expect to see only a single and constant rotation rate (image rotation) in a homogenous magnetic field, i.e. the *Larmor*-frequency [33]. Imparting OAM to the electron beam changes that simple picture, such that a multitude of rotational frequencies can be observed [32, 34].

Owing to the intrinsic chirality of EVBs, they have become a promising candidate for atomic scale EMCD measurements in an incident vortex geometry. And with that, they could become a versatile tool for spintronic applications on the scale of single atoms. However, it soon became clear that atom-sized EVBs are needed to achieve this goal [35, 36]. Even though important improvements were made in terms of high brightness atomic scale vortex production [37–40], up to now no successful realisation of the incident vortex EMCD or vortex scanning-transmission electron microscope (STEM)-EMCD approach has been reported. It should be noted here that faint atomic resolution EMCD signals have been shown without the need for atom-sized EVBs, using intelligent shaping of the incident wavefront with a C_s -corrector [41–43]. As an alternative one can utilize a HVM as a vorticity filtering device after the specimen. This is because OAM can be transferred to the probing electron when it excites electronic transitions to spin-polarized final states of the atoms in the sample. This transfer of OAM manifests itself in a vortical structure of the inelastically scattered probe electron. Using a fork mask as chiral filter is already established in optics [44]. This alternative ansatz for EMCD opens up the possibility to measure magnetic properties of amorphous materials (or multiphase materials including both crystalline and amorphous magnetic phases), since the specimen no longer needs to act as a crystal beam splitter itself. Also crystalline specimens could benefit from using the vortex filter setup and its inherent breaking of the *Bragg* limitation when, for example, substrate reflections overlap with the two EMCD measurement positions which would diminish the EMCD signal strength. Additionally, this setups' relative simplicity, compared to the incident vortex EMCD method, and the possibility to boost the spatial resolution to the nanometre scale, or even beyond, are tempting.

Actually, right from the inception of EVBs in 2010 [5] when *Jo Verbeeck*, *He Tian* and *Peter Schattschneider* published their seminal paper on the production and application of EVBs, the first application of EVBs and their holographic reconstruction was the chiral filter for an EMCD measurement on bcc Fe.

The confusing aspect is that, up to now, no replications, nor applications to other material systems using the proposed setup incorporating a vorticity filtering holo-

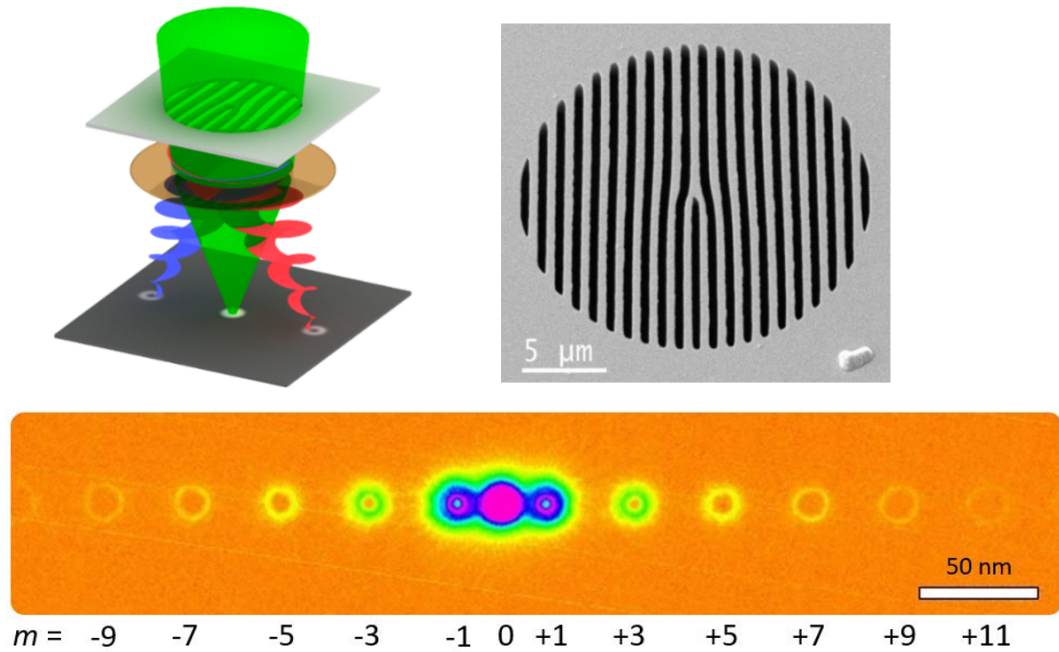


Figure 1.2: (a) Schematic principle of vortex generation. An incident plane electron wave hits a holographic fork mask. In the far-field the diffraction spots turned into ring like structures that now carry $OAM = m\hbar$, where m is the topological charge. m could be any positive or negative integer. (b) SEM image of a 20 μm holographic absorption or amplitude mask made of an Au/Pd alloy with a thickness of 1.5 μm and a grating periodicity of 1 μm . (c) TEM image of the resulting nanometre-sized ring like EVBs produced by the mask above.

graphic fork mask after the specimen and broad beam illumination have been published. In the light of the aforementioned advantages of this technique this is even more puzzling and calls for a critical re-examination and a more involved study of the underlying principle of this method. Since then, a multitude of other clever OAM filtering ideas came up, e.g. triangular shaped apertures, knife edges, astigmatic phase shifts [45, 46] and pinhole arrangements [47]. Recently, it has been shown that OAM sorters, based on optical OAM sorting schemes [48], can also be built for electrons in a TEM [49], and proposals to sort the EVBs' OAM incorporating only electromagnetic fields have been published [50–52]. But, on the one hand all of them show drawbacks, e.g. that the devices show strong OAM crosstalk, the analysis is fundamentally more complicated or that they are not practical for beams which are not OAM eigenstates or incoherent superpositions of different OAM states as is the case in EMCD. And on the other hand, neither of them has been successfully applied for vorticity filtering in EMCD measurements.

For both new EMCD methods (incident and vorticity filtering EMCD) there is a strong need for large-scale high-fidelity HVM in order to reach high convergence- or collection angles, respectively, and, thus, an increased signal-to-noise ratio (SNR). Also, their grating periodicity must be sufficiently small such that the $m = \pm 1$ order are well-separated from the central order. Moreover, pure symmetrically distributed OAM states are also a prerequisite for vorticity filtering EMCD experiments. In principle HVMs can be built such that the phase or amplitude or both of the incident electrons can be manipulated [53]. Traditionally, FIB machines with their few nanometre fine Ga-ion-beam have been used to cut HVMs in thin SiNx or metal membranes, as they are readily available in TEM laboratories. Recently, also the electron beam lithography technique has been used to fabricate large-scale and very fine structured holographic phase masks [54]. For the experiments shown in this thesis amplitude masks have been used due to their robustness and straightforward way of production. Also, in the light of low voltage TEM and SEM development [55, 56] and applications like the improvement of light element image contrast, reducing beam damage and/or the influence of *Cerenkov* radiation [57, 58] amplitude masks may be more practical compared to phase masks because inelastic scattering in the phase masks' material is unavoidable. However, when it comes to ever-increasing HVM sizes while at the same time the grating periodicities must be fine enough (≈ 600 nm and lower) for a decent separation of the EVBs, the question is, if the standard FIB production methods like raster- or serpentine scanning are sufficient. Advanced FIB milling strategies, employing a 'vector-scan' technique will be presented. Stream-files provide the possibility to fully control the position and dwell time of the ion-beam to generate spiral milling paths for every hole/void in the HVM structure. Additionally, the milling order and -direction after each pass is reversed and, inspired by [59], the influence of a position-dependent dwell time reduction in the proximity of the hole edges will be shown. For a certain amount of electron absorption the metal membrane has to have a few hundreds of nanometres up to a few micrometres of thickness, thus, increasing the negative effect of the beam shape on the optimal grating bar geometry. Using heavy elements like Au/Pd or Pt improves the situation but possibly due to

their relatively high ductility, single grating bars tend to bend, stick together and degrade while milling. It will be shown how this situation changes when alternative materials, like Ir and Os – having superior mechanical characteristics – are used.

1.3 Outline

The structure of this thesis is as follows: first a general introduction to transmission electron microscopy and the analytic technique electron-energy loss spectrometry will be given, followed by an introduction to the interferometric EELS technique energy-loss magnetic chiral dichroism. Then, an introduction to the theory of EVBs and an overview of various alternative EVB production methods as well as vorticity filtering devices will be given. Afterwards, the multi-slice simulation technique, which will be used to understand the experimental findings in chapter three, will be introduced. As a significant amount of effort went into the production and optimization of thin films and devices needed for deposition and characterisation for the production of HM, sections on focused-ion-beam milling and thin film production are included at the end of chapter two. In the third chapter device modifications and improvements necessary for the production of HVM will be described.

The fourth chapter is devoted to the production of holographic amplitude or absorptions vortex masks using focused-ion-beam machines. Different approaches, with the aim to increase the quality of the milled amplitude masks will be presented. Ranging from testing alternative scan strategies, like spiral vector-scanning, milling direction reversal and spacial dependent dwell time adaption to the question of whether the mask material, density and inner stresses of the HVMs influences the HVM milling results and to some extent also the EVB quality and distribution.

In the fifth chapter applications of EVBs in the form of an alternative EMCD technique – *vorticity filtering EMCD* – will be presented and described in detail, including the description of the experimental setup, a single scattering theory, multi-slice simulations, the discussion of artefact sources, the achievable SNR and experimental evidence of this new EMCD technique. At the end of chapter five, it will be shown that EVB show peculiar rotation-dynamics in the magnetic lens field of the TEM and how they can be used to produce free-electron *Landau*-states.

2 Fundamentals

In the course of this dissertation project a multitude of different measurement tools and devices have been used to grow, modify and characterise thin films as well as constitute to a new measurement method in transmission electron microscopy, so this chapter aims at giving a bit more than a general introduction to the methods and devices employed.

2.1 Transmission Electron Microscopy

Seeing is believing – among our six senses, our eyes with their roughly 130 millions of photoreceptor cells represent the most dominant information channel to our brain, creating to a large extents what could be called our ‘reality’ and defines the way how we perceive our every day environment as well as how we understand it. However, our vision ‘apparatus’ is limited to resolve structural features down to 50 μm , which is approximately the diameter of a humans hair, and so were explorations in the micro-cosmos. Before scientists started to explore the micro-cosmos, their focus laid on the other side of the length scale, the macro-cosmos. Optical devices, like the *Galilean* telescope, were used to study astronomy, no one thought of going into the other direction, into the micro-cosmos not until *Jan Swammerdams* started to use optical microscopes to discover red blood cells [60], *Robert Hooke* published his ‘*Micrographia*’ in 1665 showing detailed insights in the life of micro-organisms [61] and *Antoni van Leeuwenhoek* who was able to significantly improve the current resolution of the optical microscopes and thus fuelled the upcoming fascination for that young field of science.

Surprisingly, it lasted nearly two hundred years until *Carl Zeiß* together with *Ernst Abbe* and *Otto Schott* were able to produce optical microscopes that were more powerful than those rather simple single lens devices from *van Leeuwenhoek*. *Abbe* found a way to theoretically describe and predict the characteristics of optical lenses and also gave an expression for the maximum achievable resolution, which is known as the *Abbe* resolution limit for coherent illumination conditions,

$$d = \frac{\lambda}{n \sin \alpha} \quad (2.1)$$

where d stands for the line separation of an illuminated line grating or similar the minimal separation of two or more structural features that still can be visually distinguished, λ represents the wavelength of the illuminating light, n is the refractive index of the medium in between the objective lens and the specimen (e.g. immersion oil or air) and α which is the semi-acceptance angle of the objective [62]. *John*

2 Fundamentals

W. S. Rayleigh and *Hermann von Helmholtz* obtained a slightly different relation for self-luminous samples, which is called the *Rayleigh-criterion*, $0.61\lambda/NA$, with NA being the numerical aperture $n \sin \alpha$. This relation actually also holds true for electron-optical devices like the TEM due to the wave nature of the electron.

Since then developments in optical microscopy continued and in the last few decades some stunning new techniques came up, which all have in common that the diffraction limit, once defined by *Abbe* as a fundamental barrier, is circumvented using confocal microscopy techniques like the stimulated emission depletion approach (STED), photo-activated localization microscopy (PALM) and stochastic optical reconstruction microscopy (STORM), which earned the *Nobel Prize* in chemistry in 2014 [63, 64], structured illumination microscopy (SIM) [65, 66] and other microscopy techniques, utilizing near-field effects to overcome the diffraction limit like near-field scanning optical microscopy (NSOM) [67].

The progress towards ever-increasing resolution made in optical microscopy deeply reflects mankind's motivation to explore nature's building blocks in the micro- and nano-cosmos. It was the same kind of motivation that drove the pioneers of electron microscopy (EM), namely, *Hans Busch*, *Reinhold Rüdtenberg*, *Ernst Brüche* and *H. Johannson*¹, *Ernst Ruska*, *Max Knoll* and *Bodo van Borries* in the early 1930s to the invention of the transmission electron microscope [33, 68–71]. EM was therefore an early approach to improve the resolution power of microscopes beyond the optical diffraction limit. The inventors wanted to incorporate the lightest and smallest fundamental particle that had been discovered about three and a half decades ago by *J. J. Thompson*: the electron. Because from their point of view the electron had a classical electron radius of the order of a few femtometers. With the advent of the idea of matter waves of *Louis De Broglie* in 1925, *Ruska*, who was initially not aware of *De Broglie's* work, had to revisit his resolution limit expectations in 1932. Using Equation 2.1 and an aperture radius of 20 mrad he expected to reach a resolution of the order of 2.2 Å for 75 keV electrons [68]. The first commercially available electron microscopes, like the so-called 'Übermikroskop' from *Siemens and Halske*, see Figure 2.1 (a), did not come close to that limit but easily surpassed the optical resolution limit of roughly 200 nm. Many issues had to be overcome: the improvement of the vacuum system and electron sources, sample-contamination, -preparation and -damage/-heating issues, the understanding and reduction of the lens aberrations and the improvement of the microscope control and usability until, 40 years later, this limit could eventually be reached².

Figure 2.1 (b) shows an *Tecnai F20* instrument (located at the TU Wien, ThermoFisher/FEI), which represents the aforementioned stage of TEM evolution and is capable of routinely reaching a point resolution of 2.1 Å and thus of seeing single

¹*Rüdtenberg's* son suffered from leg paralysis which was diagnosed as poliomyelitis, an illness supposed to be caused by a virus too small to be resolvable under optical microscopes. From that on he wanted to invent a device capable to make those small virus particles visible. This started his work on a electrostatic TEM already in 1930, with a US patent granted already in 1931, two years before *E. Ruska* was granted a patent on his magnetic lens TEM version.

²Using higher accelerating voltages, not 75 keV.

2.1 Transmission Electron Microscopy

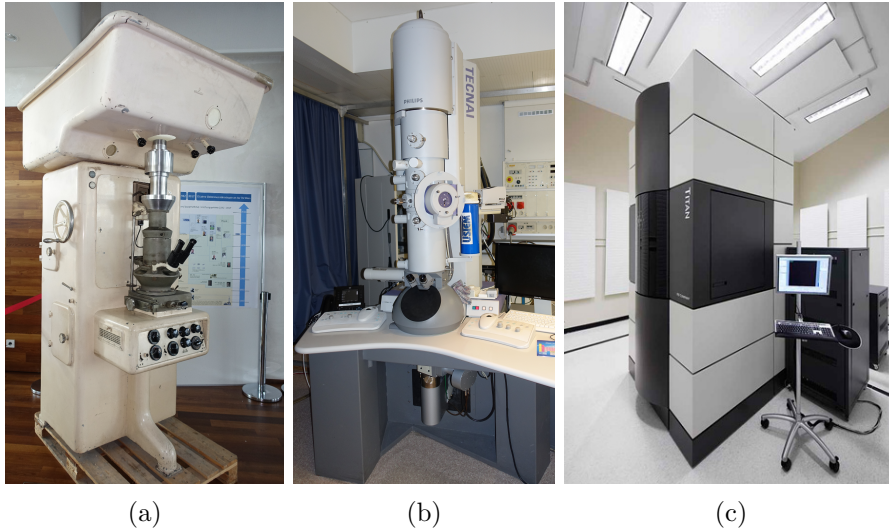


Figure 2.1: Historical evolution of the TEM ranging from the beginnings (a) one of the first commercially available TEMs, the *Übermikroskop 100*, Serial Number 26, built from *Siemens and Halske* in 1942 for the TU Wien to (b) a non-aberration-corrected *Tecnai F20* (FEI/ThermoFisher) field emission TEM at the moment in operation and actively used at the TU Wien to reach atomic resolution and (c) a state-of-the-art double corrected FEI *Titan* cubed high-base TEM (McMaster University in Hamilton, Canada) being able to discern atomic separations in the sub 100 pm regime.

2 Fundamentals

atomic columns. EM had become a heavily used and invaluable tool in material science and biology for structural investigations, and *Ernst Ruska* finally received the *Nobel Prize* in physics in 1986 for his "fundamental work in electron optics and for the design of the first electron microscope".

In 1936, *Otto Scherzer*, one of the early theoreticians dealing with electron lens aberrations, pointed out, that those lenses are subject to inherent and unavoidable chromatic- and spherical aberrations (C_c and C_s) only if the magnetic or electric lens fields are radial symmetric, static and there are no space charges on the optical axis, which is known as the *Scherzer Theorem*³. Unfortunately, all of this is true for standard round EM lenses and thus limits the achievable resolution to 50 to 100 times the electron's wavelength [74]. *Scherzer* himself proposed ways to overcome these limitations in 1947 but the successful implementation in the form of a C_s -corrector took another 48 years and was accomplished in 1995 by *Maximilian Haider* (a student of *Harald Rose* which in turn was a student of *Scherzer*) [75]. As of now, these complicated arrangements of magnetic multi-poles, built into TEMs like the one shown in Figure 2.1 (c), have proven to push the TEM resolution below 50 pm [76] and even at ultra-low accelerating voltages of 15 kV atomic resolution has been demonstrated [55].

Alongside this bold developments of C_s - and C_c -correctors and their technological refinement, other very interesting developments in EM took place. These were emergences of high brightness field emission electron sources (XFEG and ColdFEG), corrector and monochromator automation routines, high-resolution tomography [77], superresolution and light element contrast enhancement via imaging scanning transmission microscopy (ISTEM) [78] as well as ptychography [79], differential phase contrast (DPC) imaging [80], enabling atomic field measurements, approaches towards mapping orbitals and the dynamics of single atoms [81] and the evolving whole new approach to temporal dynamics in the TEM using ultra-short-photon pulses in pump-probe arrangements [82–84].

After this rather broad motivational and historic introduction in EM the following will give a more technical view on the TEM by following the path of electrons from their emission in the electron gun to their detection on the screen or charge-coupled-device (CCD) camera and the most important parts of the (non-aberration-corrected) microscope that interact with the electrons on this path, see Figure 2.2. This part of the section is primarily based on [85–88].

The electron emission takes place in the electron-source or -gun (small red cone), located at the very top of the TEM, which is a sharp metal tip, usually a W hairpin filament, a LaB₆ crystal needle mounted on a W hairpin filament for thermionic guns or a very sharp W (100) crystal coated with ZrO, also mounted on a W hairpin filament for *Schottky* FEG emission sources. C-nanotubes, *Bose-Einstein* condensates and single atom emitters have also been tested as an electron emission source [89, 90], but up to now no commercial implementation could be achieved. Recently, it has

³ *Walter Glaser* actively tried to find a loophole but did not succeed. Recent attempts to do so can also be found [72], but to no avail [73].

been shown that LaB₆-nanowires can also be utilized to build ultra-high-brightness and monochromatic electron sources [91]. The emission process determines the energy spread (monochromaticity, longitudinal or temporal coherence) of the emitted electrons and strongly depends on the temperature, the work function of the emitter material, which is also depending on the crystal orientation, and, in case of a field emitter, the electric field, that is applied to lower the shape and height of the potential barrier. Typical parameters for field emission sources are a field strength of 0.5 V nm⁻¹ to 1.5 V nm⁻¹ and a temperature of 1800 K obtained from resistive heating, which yield an energy spread (full-width at half maximum (FWHM)) of 0.3 eV to 1 eV, and 0.2 eV to 0.7 eV for cold field emission sources. Typical energy spreads for a thermionic source are 1 eV to 3 eV. Before C_C -correctors became available, the only way to reduce the detrimental effect of chromatic aberrations on the imaging capabilities of the TEM, was to use highly monochromatic (cold) FEG sources (and higher beam energies). When working in the STEM mode, the temporal coherence of the emitted electrons slightly blurs the minimal achievable spot size according to $d_{C_c} = C_c \Theta \Delta E/E$, where C_c is the chromatic aberration coefficient (typically of the order of 1.2 mm), Θ the field limiting aperture semi-angle, ΔE the FWHM energy spread of the electron gun and E the primary beam energy, see Figure 2.3. The tip geometry or, more precisely, the electron emission region strongly influences the source size and thus plays a crucial role in achieving small spot sizes and high spatial coherence needed for high-resolution imaging as well as holography and the usage of holographic masks. Figure 2.3 shows, that this contribution (source size, d_{source}) to the achievable probe-size is the most dominant one, at least for analytical beam currents of 500 pA and medium convergence angles Θ . The lateral or transverse coherence length can be described by $\lambda_C = \lambda/2\pi\alpha_{source}$ [92]⁴, with λ being the electron wavelength and α_{source} the effective angular source size. For FEG tips the lateral coherence is of the order of 65 μm at 200 kV as compared to thermionic electron sources, where only 12 nm to 65 nm can be reached. Thus, only FEGs provide electrons, which are coherent all over HVMs which are typically smaller than 50 μm in diameter. Another representative value for the quality of an electron source is given by the brightness, that is, how much current per surface area is emitted into a certain solid angle. For example, using a thermionic source (LaB₆) TEM, this value amounts to $5 \times 10^{11} \text{ A m}^{-2} \text{ sr}^{-1}$. For FEG TEMs it reaches $5 \times 10^{12} \text{ A m}^{-2} \text{ sr}^{-1}$ to $10^{13} \text{ A m}^{-2} \text{ sr}^{-1}$ and thus illustrates how much current one can put into a given beam size.

On their way down the column, it is absolutely essential to prevent electron collisions with gas molecules in the TEM column as well as the generation of arcs between the cathode and the extraction and acceleration anodes. Therefore the column must be evacuated to high vacuum, better than 10^{-4} Pa (10^{-6} mbar) using pre-vacuum, turbo-molecular, oil-diffusion and ion-getter pumps. If the TEM is equipped with

⁴Note that this estimation is based on the *van Cittert-Zernike* theorem, assuming a round shaped incoherent source. Recently, it has been argued that a more sophisticated approach, including a partially coherent source, leads to a correction [93], which out of scope in this thesis.

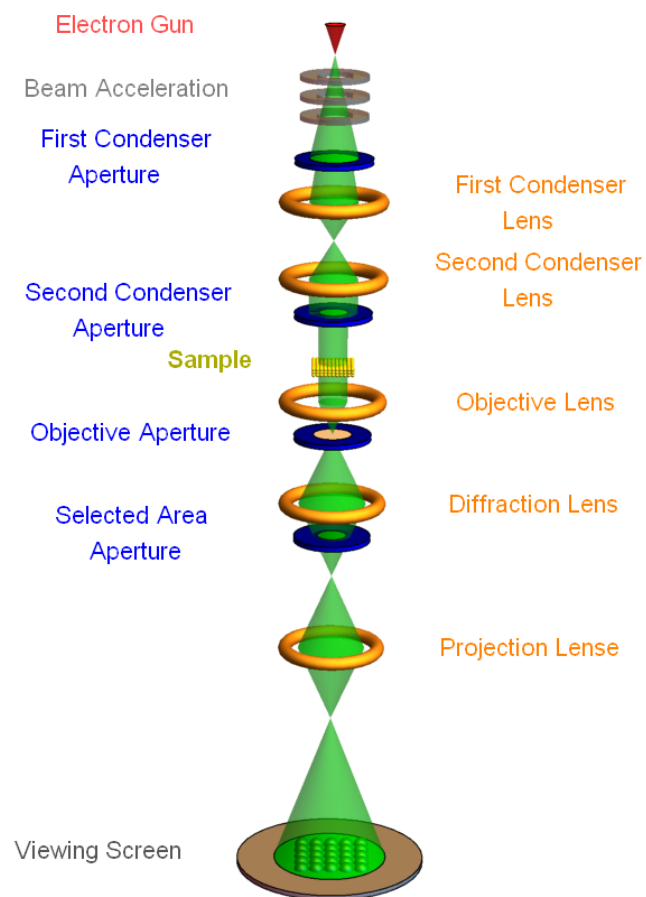


Figure 2.2: Schematic (simplified) representation of a non-aberration-corrected TEM (comparable to the one at the TU Wien), shown in Figure 2.1.

a FEG, the region surrounding the source has to be kept in ultra high vacuum in the range 10^{-6} Pa to 10^{-9} Pa (10^{-8} mbar to 10^{-11} mbar), depending on the type of the FEG source (cold FEGs need a better vacuum). W and LaB₆ electron sources are much easier to operate, since they only need a high vacuum. Once the electrons leave the extraction region, they get accelerated by electrostatic fields, applied by evenly spaced rings (grey disks in Figure 2.2) with successively increasing positive potential relative to the electron. Typical acceleration voltages are 60 kV to 300 kV, but acceleration voltages up to a few MeV and down to 6 kV have been used. There are multiple reasons to adjust the acceleration voltage (AV), to name a few, higher AVs increase the resolution and penetration depth but also *Cerenkov* losses and beam damage increase, e.g., graphene (a single layer of graphite) and biological samples suffer from beam damage above ≈ 80 kV⁵. Also, the elastic- and inelastic scattering cross-sections increase with lower AVs, and thus improves the SNR.

200 kV electrons travel with 70 % of the velocity of light down the column, where several magnetic dipoles (not shown in Figure 2.2) are used to align their path to the optical axis before they enter the condenser system of the TEM. Very much like in optical microscopes this collection of magnetic lenses and apertures is used to shape the electron bundle. A typical condenser system consists of two to three lenses (see Figure 2.2, yellow tori). In a two-condenser lens system the first and uppermost one (called C1 in FEI microscopes) basically controls the spot size and current, while the second one (C2) can be used to vary the beam diameter in the specimen plane. Depending on the experimental setup, a (nearly) parallel beam with diameters up to a few microns can be formed for standard (HR)TEM imaging applications and for convergent beam techniques, like STEM, or convergent beam electron diffraction (CBED), the electrons can be focused down to roughly 2 Å, in state-of-the-art aberration-corrected machines even down to 50 pm [76, 94, 95].

21 mm below the second condenser lens, the C2-aperture/diaphragm is placed, which is also called beam-forming- or condenser aperture, see Figure 2.2 (blue disk). This aperture, typically between 30 μm to 200 μm in diameter, enables the TEM user to change the illumination convergence angle Θ and thus control the spot size, according to Figure 2.3. There, contributions proportional to the inverse convergence angle, like the source size and diffraction of the beam limiting C2 aperture ($d_{diff} = (1.22\lambda)/\Theta$), and contributions showing a direct proportionality, like C_c and C_s are summed up, and results in an optimal convergence angle, where a minimal spot- or probe-size can be achieved. Here it amounts to roughly 8 mrad. The C2 aperture is placed in an aperture holder that can typically handle four apertures. This opens up the possibility to replace one (or some) of the standard apertures by holographic masks in order to gain access to a new degree of freedom, apart from (simply) changing the convergence angle of the illumination, that is, to arbitrarily structure the illuminating beam [23].

After passing the C2 aperture, the electrons enter the objective lens (OL), which is the strongest ($B \approx 2$ T) and by far the most important lens for image formation in

⁵Conversely, adjusting the AV too low can also induces severe sample degradation via radiolysis

2 Fundamentals

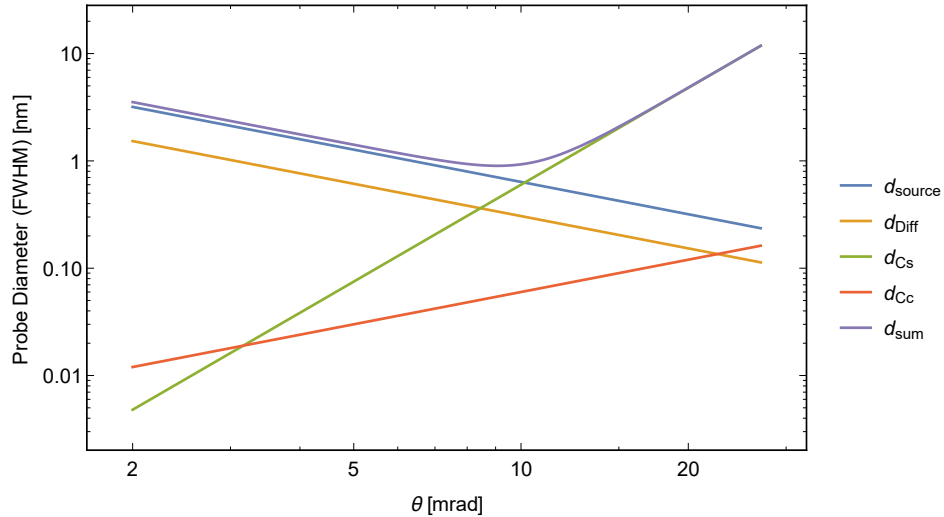


Figure 2.3: Showing the different contributions and limiting factors to the achievable spot size in a typical non-aberration-corrected FEG TEM running at 200 keV and a screen current of 500 pA. For low convergence angles Θ the most dominant contributions are the source size d_{source} and diffraction from the condenser aperture d_{diff} . At higher convergence angles spherical- and chromatic aberrations take over, d_{Cs} and d_{Cc} respectively.

both operation modes TEM and STEM as it produces the strongest, roughly 50-fold, magnification of the object's image. The OL in the *Tecnai* microscope is a so-called super-twin-OL: an immersion lens. Electron optical lenses are in fact extremely bad lenses and their most prominent aberration, which is blurring the otherwise focused fine spot to an extended disk of least confusion of a size of $d_{Cs} = 0.5 C_s \Theta^3$, is the spherical aberration C_s . In the super-twin-OL, it is of the order of 1.2 mm. The OL can be represented by two thin lenses, a condenser-OL above the specimen and an image-OL right beneath it. In STEM, the aberrations of the condenser-OL degrade the electron phase and thus limit the achievable minimal spot size. Machining errors, inducing deviations of the perfect roundness of the OL bore, of the order of a few tens to hundreds of nanometres, and material inhomogeneities lead to axial astigmatism of the same dimension, and thus, can be easily corrected using weak quadrupole coils. Smaller probe-sizes demand higher convergence angles and by that the influence of apparent spherical aberrations increases, necessitating the use of a probe-corrector, which is therefore placed between the last condenser lens and the condenser-OL. In the TEM mode, it is the image-OL, which induces unwanted aberrations. For highest resolution TEM imaging, a so-called image-corrector has to be installed beneath the OL.

The specimen, typically 10 nm to 300 nm in thickness⁶, is placed in the object

⁶Using energy-filtered TEM, it has been shown that dislocation networks in extremely thick specimen, up to 10 μm , can be imaged [96].

plane of the image-OL, which is approximately in the centre of the OL pole-piece: a 5.4 mm gap in an iron-cobalt yoke (see Figure 2.2, yellow block of small spheres). It is mounted on a 3 mm ring in the sample holder, which is inserted into the sample-stage (goniometer). The sample-stage can be moved in the x,y,z -direction using electric servo- and/or piezo-drives with sub-micron and even sub-nm precision, respectively. Depending on the specific holder model, it can also be tilted by roughly $\pm 40^\circ$ around the long axis of the holder (α -tilt) and some tens of degrees around the direction perpendicular to it (β -tilt). The sample-stage and its α -tilt-axis defines the so-called eucentric height of the microscope. It is essential to bring the specimen to this z -position, as all the magnification calibrations are only valid for objects placed at this height. And more practically, the sample does not move laterally, while using the α -tilt. Most of the standard TEM work is carried out with the sample at the eucentric height. However, in some techniques, like CBED or large-angle CBED, the specimen is intentionally lifted above the eucentric height, quite similar to the proposed vortex filter EMCD technique. Approximately 2.7 mm further down the TEM column, in the back-focal-plane (BFP), diffraction- or *Fourier*-plane of the image-OL, the objective apertures, which are placed on an apertures stripe with eight hole apertures, with diameters ranging from 10 μm to 100 μm , can be inserted in the electron beam path. These apertures can be used to block electrons, that have been scattered to certain angles, in order to enhance the TEM image contrast. Therefore they are also called ‘contrast apertures’. E.g., in the case of bright-field imaging, where all scattered electrons, except the transmitted (also called ‘direct’) electrons, are apertured, absorption (or mass-thickness) and diffraction contrast is enhanced. Alternatively, one can choose to select specific diffraction spots either via physically centring the contrast aperture around the desired spot, or via tilting the incident beam on the sample, which translates to a shift in the BFP, called dark-field imaging. Apart from mere apertures, also Zernike-, Hilbert- and Volta-phase-plates have been successfully used in the BFP, in order to enhance the contrast transfer of low spatial frequencies, as commonly needed in imaging of biological samples [97–99].

Approximately 14 cm further down the column, the first intermediate image of the specimen is obtained. As the magnification is defined as the ratio between the image- and object distance, a fifty-fold magnified image is observed. Placing apertures, as small as 10 μm , in this plane (in a standard four position aperture holder), basically limits the field of view to areas as small as 200 nm. Switching now to diffraction, one can obtain diffraction patterns of the selected region of interest. Because of that, these apertures are called ‘selected area diffraction (SAD)’ apertures.

Right below the SAD aperture, or first intermediate image plane, the diffraction lens is placed. Depending on its excitation, it transfers either an image of the BFP (diffraction mode), or an image of the SAD plane to the following projection system. The task of the projection system, which is a set of three magnetic lenses (one intermediate- and two projective-lenses) and represented by a single lens in Figure 2.2, is to further magnify the image, delivered by the diffraction lens, by a factor of hundred to twenty-thousand.

Finally, after traversing the specimen and a multitude of electron-optical, after

around two metres of flight distance or 10 ns, the electrons impinge, one by one⁷, on a fluorescent copper-activated zinc sulphide screen, yielding a greenish light where the electron density is high. The screen is primarily used for microscope alignment, region of interest identification and pre-recording sample inspection purposes. The recording of the electron distribution is done, depending on the operation mode and investigation's purpose, on a multitude of different electron detectors, varying in read-out-speed and spatial pixel distribution. For example, a high-angular annular dark field (HAADF) detector is frequently used in STEM imaging, to generate mass-thickness contrast. It consists of one pixel that collects all electrons scattered to an annular ring-shaped region, and is read out within a few microseconds, allowing fast STEM scanning across the sample. In contrast to that, a CCD, or complementary metal-oxide-semiconductor (CMOS) detector, collects the two-dimensional electron intensity distribution, using a (typically, 2K by 2K or 4K by 4K) pixel array with a pixel-size of about 15 μm at rather low read-out-speeds of 40 ms per frame. These CCDs and CMOS sensors are fibre-optically coupled to a scintillator crystal, to collect the photons which are produced when high energy electrons hit the scintillator. An upcoming and powerful alternative to these conventional fibre-optically coupled cameras, are direct detection cameras, which detect an electron charge redistribution inside the semiconductor pixel array of the camera, without any scintillator or fibre-optic, and thus show much higher detective quantum efficiency, a measure to describe the capability of the camera to discriminate noise from a real impinging electron, compared to conventional CCD or CMOS camera systems [100, 101]. Using this new class of electron detectors in the TEM, 4D-STEM (two dimensions in real-space and two in the reciprocal space) techniques, like strain-mapping and electric- and magnetic-field mapping using DPC, quite like high-resolution transmission electron microscopy (HRTEM) imaging of beam-sensitive materials, cryo-TEM of complex organic structures and in-situ applications can be dramatically improved, for some recent advancements see: [102–105].

2.2 Electron-Energy-Loss Spectrometry

This section is based on [106–108] and [88].

After the functional (and historical) introduction to the field of TEM, with its means to ever-increasing spacial resolution power and tricky contrast methods in the preceding section, in the 1970s and 80s a parallel development took place. – Electrons, with their strong coulombic interaction with matter, do produce a multitude of signals, apart from the plain trajectory or phase change, given in elastic scattering events, when incident on a specimen. E.g., electron back-scattering and secondary electron emission takes place, two processes mandatory for image formation in SEM,

⁷At rather high beam currents of $I \approx 10\text{ nA}$ the distance d between successive electrons can be estimated by $d \approx v_e/(n_e I)$ which is of the order of 3.4 mm for 200 keV, thus, justifying the notion of ‘one by one’ electron hits.

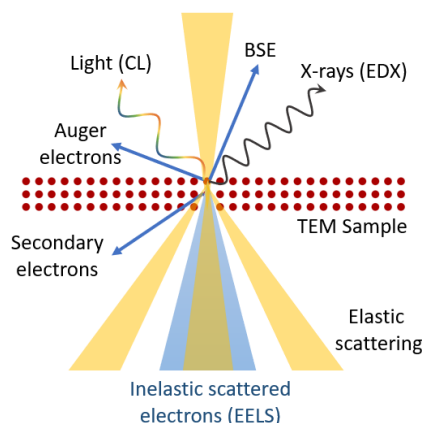


Figure 2.4: Schematic of the different interactions and signals that are induced when a swift incident electron hits the TEM sample.

Auger-electrons leave the sample and are extensively used in surface science analytics and visible light in the form of cathodoluminescence and high energetic x-rays are produced, see Figure 2.4. – Atop on all of these signal channels, it was possible to build a practical detector system for the TEM, that exploits the energy-loss of the swift electron, when subject to inelastic scattering in the sample. This so-called electron-energy-loss spectrometer, opened up the door to numerous electron-sample interaction phenomena and invoked a new dimension of how we see samples in the TEM.

When doing EELS, nowadays, the most common way is to employ a post-column spectrometer⁸, that is fixed right under the viewing screen or CCD/CMOS or direct detection 2-D pixel array, used for TEM imaging. – A brief and (most probable incomplete and strongly biased) historical evolution of EELS spectrometers, of that kind, can be seen in Figure 2.5. – In that case the electron’s journey does not end at the viewing screen, it practically enters a second microscope, which opens up astonishing new possibilities, like the acquisition of atomically resolved quantitative EELS maps [110] and the detection of a single La atom, buried within a CaTiO_3 matrix [111]. Senga and Suenaga were able to acquire maps of very beam-sensitive single light-element atoms, encapsulated in C-nanorods, using their 60 kV STEM/TEM, which was corrected for coherent and incoherent aberrations [112]. Not only single atoms may be probed, but also parts of them in the form of atomic orbital mapping [113, 114]. Recently, impressive results, concerning the attainable energy resolution in EELS, were presented. On a *Titan* (ThermoFisher/FEI) instrument, using an alternative monochromator setup, it was possible to get an energy resolution of 24 meV [118]. And a new generation of *Nion* STEMs, was employed as a nanoscale thermometer, able to probe the local nanoscale temperature (energy-gain

⁸In-column omega filters are less practical for EELS spectroscopy, but do have advantages in energy-filtered transmission electron microscopy (EFTEM), and are sometimes also used as impressively powerful monochromators [109].

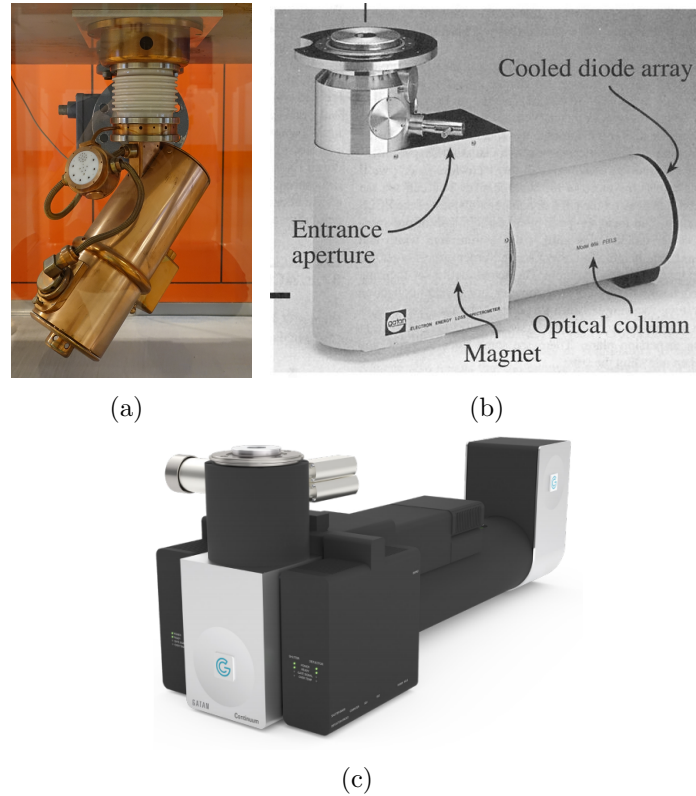


Figure 2.5: A historic evolution of TEM post-column filters. (a) Electrostatic electron-energy-loss spectrometer prototype, developed from 1972 to 1977 by Siemens, working on the basis of Möllenstedt's electrostatic lens energy filtering principle [115], and reaching an energy resolution of 0.2 eV at 50 kV and single-electron detection sensitivity. (b) The *Gatan* PEELS revolutionized the spectrum acquisition, using parallel detection of the energy channels, instead of a serial acquisition. A three orders of magnitude improved count rate was achieved. Taken from [116]. (c) State-of-the-art imaging filter from *Gatan* (GIF Continuum) high-speed sub-ms spectra acquisition, an energy resolution below 20 meV, fast automated tuning and large lateral- and spectral field of view, taken from [117].

and -loss phonon peaks) of h-BN flakes. The most recent record on an experimental machine lies at 4.2 meV FWHM, at a primary voltage of 30 kV and a recording time of 16 ms [109]. Surely, these examples pose only the top of the iceberg and there could be much more to say about outstanding EELS results but this is not the scope of this work. The bottom line is that EELS, for instance compared to energy dispersive x-ray spectrometry (EDX), is exceptionally suited for light element detection and that it provides a very high signal collection-efficiency, at a typical energy resolution of 1 eV compared to ~ 130 eV in EDX.

Similar to the principle of magnetic TEM lenses and the *Lamor*-rotation of the electrons traversing them, as well as *Landau*-states, that can be produced inside of them [119], the basic working principle of spectrometers can be described using the *Lorentz*-force F :

$$F = e \cdot (\mathbf{E} + \mathbf{v} \times \mathbf{B}), \quad (2.2)$$

with e being the electric charge of the electron, \mathbf{E} and \mathbf{B} the electric- and the magnetic-field, that the electron experiences, respectively, and v the electron's velocity. Magnetic sector magnets are nowadays the most commonly used dispersion element in EELS spectrometers, such that Equation 2.2 can be reduced to:

$$F = e \cdot (\mathbf{v} \times \mathbf{B}). \quad (2.3)$$

With that, its easy to see how the electron deflection in a constant magnetic field, that is oriented perpendicular to the direction of electron motion, is solely depending on its velocity. Hence, such a field can not only be used to tilt and shift the electron beam back to the optical axis⁹, it also acts as a magnetic prism for electrons, comparable to optical glass prisms for photons. Slower electrons (green and red trajectories) feel a weaker *Lorentz*-force and get less deflected in the sector magnet of a spectrometer, see Figure 2.6. Using the centrifugal force $F_{cf} = \frac{mv^2}{R}$, the deflection radius R , of electrons entering the spectrometer prism, can be calculated to be,

$$R = \frac{\gamma \cdot m_e}{e \cdot B} \cdot v, \quad (2.4)$$

where m_e has been replaced by the relativistic electron mass $m = \gamma m_e$, with $\gamma = 1/\sqrt{1 - (v/c)^2}$ being the *Lorentz*-factor for swift electrons¹⁰. Typically this deflection leads to a dispersion of the order of $2 \mu\text{m eV}^{-1}$. In the schematic principle of a (post-column) spectrometer, depicted in Figure 2.6 (a), electrons e^- diverge from the last projection lens crossover, point P_{object} , quite as if in diffraction mode, to the magnetic prism or sector magnet, which is drawn in Gray. At the entrance of the spectrometer, there is an angle-limiting aperture, the spectrometer entrance aperture (SEA), which determines the collection angle in spectroscopy-mode and reduces aberrations. The sector magnet, as already mentioned above, disperses the electrons by kinetic energy. Its special shape accounts for the time-of-flight differences

⁹Dipoles are commonly used in TEMs to correct for beam-shift and -tilt

¹⁰At a typical AV in the TEM of 200 kV the electron has a relativistic mass that is 39.1 % higher than its rest mass.

2 Fundamentals

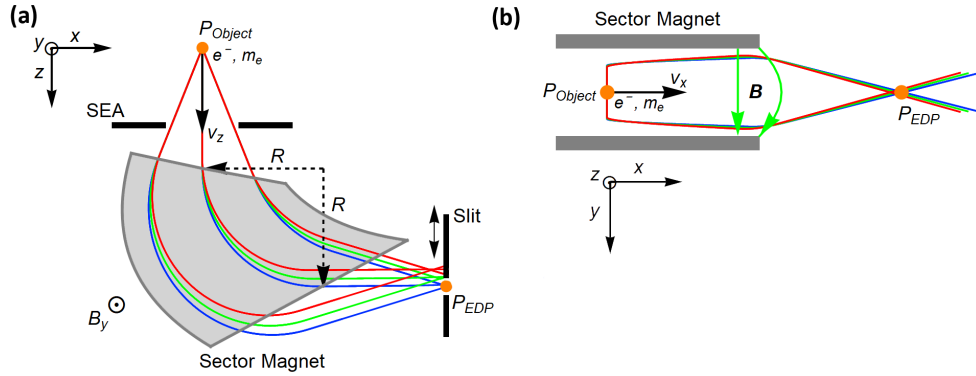


Figure 2.6: (Post-column) magnetic prism schematics. (a) Side-view: Electrons e^- diverge from point P_{Object} (the last protection lens cross-over, diffraction-mode) to the magnetic prism or sector magnet (Gray) limited by the SEA. The sector magnet disperses the electrons by kinetic energy and its special shape refocuses them again to a point P_{EDP} that lies within the EDP (vertical focusing). A movable slit can be inserted that selects electrons of a certain energy. Using post-slit electron optics (not drawn) these electrons can be used for EFTEM. Removing the slit and imaging the EDP on a e.g. CCD produces a electron-energy-loss spectrum, as it is shown in Figure 2.7. (b) Top-view: While a constant magnetic field in the y -direction is responsible for the energy dispersion, the sector magnets' fringe fields at the entrance and exit are responsible for the lateral focusing effect. (Note that the trajectories are simulated and to scale the z -distance from P_{Object} to the prism is 200 mm).

of electrons, entering the magnet at different points under different angles, and thus, refocuses them in the vertical direction to a point P_{EDP} that is located within the energy dispersive plane (EDP). A movable slit ($5\ \mu\text{m}$ to $250\ \mu\text{m}$) can be inserted, to select electrons with a certain energy width ΔE . By shifting the spectrum in the EDP up or down, the energy-loss E of interest can be chosen. Using post-slit electron optics (not drawn), these electrons can be used for EFTEM. Fully opening the slit and imaging the magnified EDP on a ,e.g., CCD, produces an electron-energy-loss spectrum, as it is shown in Figure 2.7. The top-view sketch (b), in Figure 2.6, shows the double focusing behaviour of the sector magnet. While a constant magnetic field in the y -direction is responsible for the energy dispersion (in x -direction), the sector magnet's fringe-fields at the entrance and exit are responsible for the lateral focusing effect (together with pre- and post-prism quadrupoles). There are three ways to shift the spectrum in the EDP: the first, by applying a positive voltage to an electrically isolated drift tube, that is installed inside the sector magnet, the second, by changing the excitation of the magnetic prism and the third, which is primary used in EFTEM,

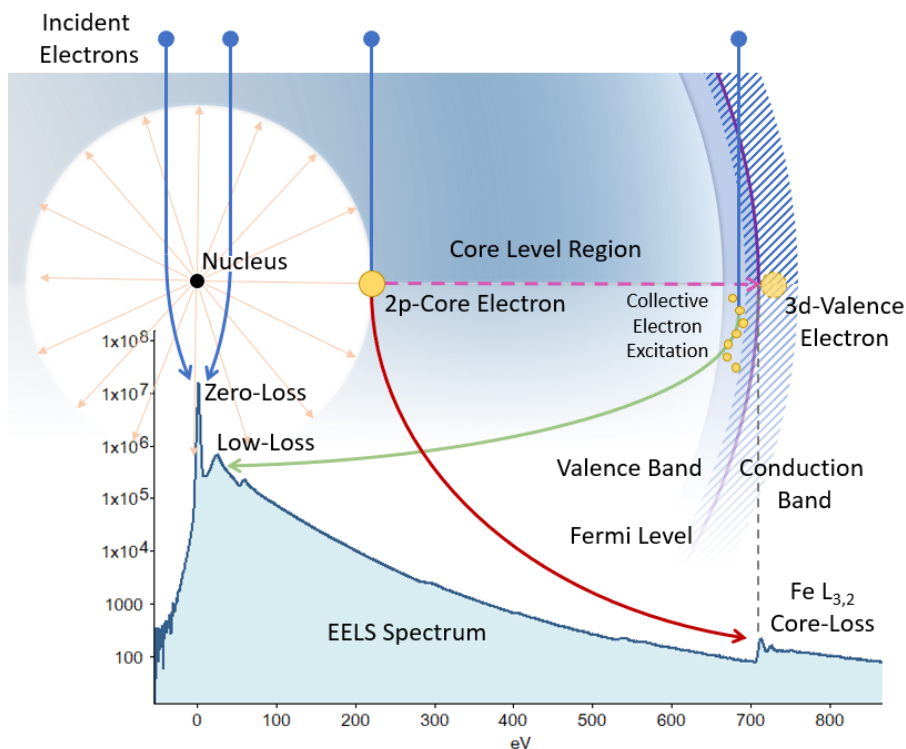


Figure 2.7: Typical EELS spectrum of 50 nm Fe sputtered on 5 nm SiNx, showing zero-loss, low-loss and core-loss features and a graphical explanation of its physical origin. A logarithmic scale was used to emphasize the large discrepancy in the scattering probability of EELS features. Note that due to the logarithmic scale, the faint Si-L and N-K edges are not clearly visible.

by adding the energy-loss of interest to the high-tension.

A typical EELS spectrum, and its connection to the physics behind, is shown in Figure 2.7. The, by far, most intense and prominent feature in such a spectrum is the *zero-loss*, which includes all electrons that did not lose a significant amount of energy, leastways less than the energy spread of the electron source. This is the case in elastic scattering events at the partially screened coulomb potential of the atomic nuclei. And, except for the TEMs described in the beginning of this section, this is also the case for phonon scattering. Its FWHM (sometimes also its full-width at tenth maximum (FWTM) is of interest) is an indication of the attainable system energy resolution. The second most intense region, starting at the zero-loss and extending to ~ 50 eV, represents the *low-loss* region. Here, the electron undergoes inelastic coulomb scattering on the valence band electrons of the atom. There is a multitude of different effects responsible for the intensity distribution in that region. But foremost, it is a collective oscillation of free electrons in the bulk of the sample, which is excited when a swift probe electron comes by. This so-called bulk plasmon

is an indicator for the free-electron density in the material and, e.g., a shift of the C plasmon peak allows for the identification of different chemical coordinations [120]. Typical plasmon energies range from 15 eV to 35 eV. Additionally, the electron can also excite surface plasmons and surface plasmon polaritons at lower energies, as well as inter- and intra-band transitions. Even *Cherenkov* light leaves a footprint in the low-loss part of the spectrum, if the electron velocity in the sample is higher than the speed of light therein, i.e. $v > c/n$. Moreover, relating the integral intensity under the zero-loss I_{ZLP} to the one of the low-loss/core-loss regions I_P ,

$$\frac{t}{\lambda} = \log \frac{I_P}{I_{ZLP}}, \quad (2.5)$$

represents a quick-and-easy method to measure the local sample thickness, which is called *Log-ratio method*. λ , the electron mean free path (MFP) in the sample can be estimated by $\lambda = 0.8E_0$, where E_0 is the primary beam energy. More realistic values for λ have to be calculated, using scattering theory. Recent pump probe experiments also showed the possibility to transfer quantized energy to the electron beam, which signifies itself as a peak or a series of peaks at the energy gain side [121].

When the electron experiences inelastic coulomb scattering on core electrons, as schematically illustrated in Figure 2.7, it loses a significant amount of energy, corresponding to the energy it takes to lift the core-electron to the first available and free states above the Fermi level. In the case of, e.g., Fe $L_{3,2}$ ¹¹, the probe electron excites a transition of the target electron in the atom, from the 2p-core electron state to a 3d-valence state¹². These *core-losses* lead to a distinct fingerprint of the elements hit by the electron in the spectrum at energies above ~ 50 eV (708 eV in the case of the iron edge) and they are sitting on a plasmon tail background, which can be described and removed using power law fitting. In EFTEM imaging, in order to fit and remove the background, it is necessary to acquire three energy-filtered images, two pre-edge ones and one post-edge image, which is known as ‘three-window-method’. Apparently, core-loss features are three to five orders of magnitude less intense than the zero-loss peak, which reflects the fact, that their scattering cross-sections are tiny, compared to those from elastic scattering. The onset of the core-loss edges and their distinct features and shapes, up to roughly 50 eV above the edge-onset, the so-called ‘energy-loss near edge structure (ELNES)’, bears rich information on the chemical state of the probed atom, e.g., oxidation, bonding and coordination.

2.3 Energy-Loss Magnetic Chiral Dichroism

As already pointed out above, EELS provides insights on not only the kind of atoms present in the sample, but also on its chemical environment. Though, one important

¹¹Note that EELS edges are named by their initial state.

¹²It thus represents the unoccupied density of states weighted by the wave-function overlap between the initial and the final state. Note that also multiple scattering effects have to be considered, and ideally removed, using the so-called *Fourier-Log* method.

property has not been covered so far: the magnetic state of the sample. Nowadays, it is quite common to quantitatively measure volumetric magnetic properties, such as the magnetization, magnetic anisotropies and coercivity as well as switching fields by employing vibrating sample- or superconducting quantum interference device (SQUID) magnetometers. Averaging over relatively large areas or surfaces, it is also possible to determine spin structure, e.g., complex magnetic ordering, like ferro-/ferri- and anti-ferromagnetic states, and spin- and orbital-magnetic moments with element specificity, by using large-scale facilities, where neutron diffraction or XMCD experiments can be carried out [122, 123]. There, typical resolutions of the order of 25 nm to 50 nm can be achieved. Alternatively, 40 nm small magnetic structures have been imaged, using high-harmonic-generation [124]. Also, spin-polarized scanning tunnelling microscopes can be employed [125], even up to atomic resolution [123, 126]. The common drawback of all of these techniques, except for the neutron scattering, is that they are mainly sensitive to the surface.

The TEM, with its inherent nanometre and sub-nm resolution, is an ideal candidate for overcoming both limitations. Holography, for example, utilized a Möllenstedt-biprism to probe the electron's phase shift, due to in-plane magnetic fields of the sample, and reaches nanometre resolution [127, 128]. STEM-DPC uses a fast readout pixelated array detector to determine the characteristic beam deflection in magnetic samples [129], which can probably be done with atomic resolution soon [80, 130]. It has also been pointed out that detecting magnetic signatures in the elastic scattering signal of incident electron vortices could be feasible [131, 132]. Moreover, taking a defocus series to reconstruct the (magnetic) deflection of the electron in the atom's potential, employing the transport of intensity formalism, has proven to be another promising route [131].

The discovery, in 2006, that EMCD can be observed in the TEM [6], provided an unexpected alternative to XMCD in the synchrotron and, to some extent, also to the aforementioned non-element specific and in-plane sensitive methods. Both EMCD and XMCD are based on the fact, that in spin-polarized (magnetic) samples, the interaction of the probe beam with the target electrons depends on the transfer of OAM between the two [133]. This has its origin in the spin-orbit-interaction of the target electron's initial states. By means of sum rules [134], it is even possible to determine the spin and orbital magnetic moments, upon close inspection of the ELNES. EMCD has seen tremendous progress since its inception in 2006 [10, 11, 135, 136], achieving nanometre resolution [14], sub-lattice resolution [12, 16, 17] and most recently, using a chromatic aberration-corrected TEM, also atomic resolution EMCD maps of double perovskites [137]. Typically, only the out-of-plane component of the magnetic field is probed, using EMCD, but recently also in-plane geometry measurements have been shown [138].

In Figure 2.8 a schematic explanation of the EMCD effect is given. There, an incident electron e^- interacts with the electronic system of the target atom via coulomb interaction and produces a virtual circularly polarised photon γ , which shows either left- or right-handed helicity. The formal equivalence of the polarisation vector ϵ in XMCD and the momentum transfer $\hbar\mathbf{q}$ in electron scattering is a key-aspect of

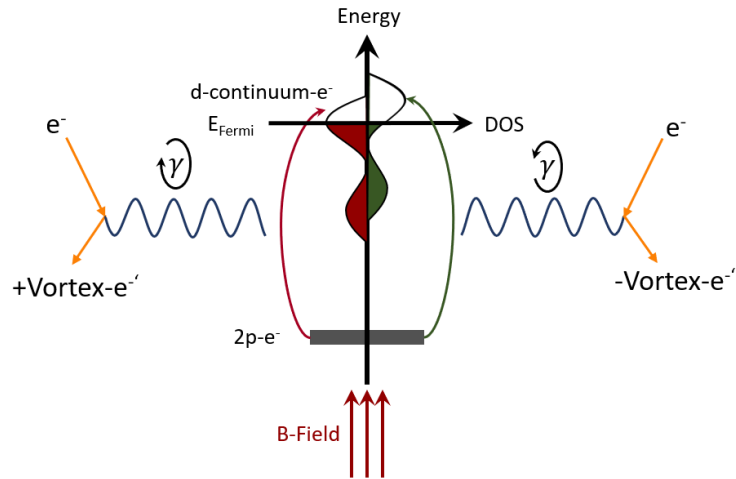


Figure 2.8: A schematic explanation of the EMCD effect. An incident electron e^- interacts with the electronic system of the target atom via coulomb interaction and produces a virtual circularly polarised photon γ , which shows either left- or right-handed helicity. The outgoing electron has been turned into a vortex. A magnetic field B spin polarizes the system, such that there is an asymmetry in the density of states (DOS) for unoccupied spin-up/-down states above the Fermi level E_{Fermi} . γ excites the 2p-electron to the 3d-continuum valence states, but as the absorption cross-sections for right- and left-handed photons are different, there is also an asymmetry for the electron scattering into the respective vortex state. The difference between the respective scattering cross-sections, is the dichroic signal aimed for.

EMCD, already pointed out in the 90s [6]. Due to angular momentum conservation, the outgoing electron, that had no OAM before, carries now OAM [133, 139]¹³. The magnetic field B spin polarizes the system, such that there is an asymmetry in the partial DOS for unoccupied spin-up/-down states above the Fermi level E_{Fermi} ¹⁴. γ excites the 2p-electron to the 3d-continuum valence states, but as the absorption cross-sections for right- and left-handed photons are different in such a spin-polarised system, there is also an asymmetry in the probability for electron scattering into the respective vortex state. The difference between the respective scattering cross-section is the dichroic signal searched for in EMCD experiments.

In the TEM, the phase structure of these vortex states and, thus, an EMCD signature, is accessible by employing the crystal lattice itself as a beam splitter and retarder, while at the same time, using a clever interference setup, see Figure 2.9. I.e., the sample is tilted to a systematic row condition, such that only two or three beams are excited in the diffraction pattern ($0, g$ or $0, \pm g$) and a phase shift of $\pi/2$, relative to each other, is given¹⁵. This is in close analogy to the fact, that the circularly polarized photon γ in XMCD can be described by the superposition of two linearly polarised photons with a fixed phase relation of $\lambda/4$, which makes a phase difference of $e^{\pm ik\lambda/4} = i$ ($\pm\pi/2$) and polarisation vectors standing normal to each other.

Describing the scattering process in a mathematical manner, based on [6, 141], starts from taking the double differential cross-section for transitions from a core electron initial state $|i\rangle$, to a final (unoccupied) valence band state $|f\rangle$, when hit by a swift incoming electron, going from its initial (incoming) state $|\varphi_i\rangle$ to the final (outgoing) state $|\varphi_f\rangle$, in first-order Born approximation¹⁶:

$$\frac{\partial^2 \sigma}{\partial E \partial \Omega} = \frac{2\pi}{\hbar} \cdot \frac{1}{j_0} \langle \varphi_i | \otimes \langle i | \hat{V} | f \rangle \otimes | \varphi_f \rangle |^2 \times \delta_{\nu f} \delta(E + E_i - E_f). \quad (2.6)$$

E and j_0 denotes the incident electron's energy-loss and current density, respectively, while \hat{V} is the *Coulomb*-potential operator between the projectile- and target-electrons. The ionization energy is given by $E_f - E_i$. In the one-particle approximation, assuming that the probe electron can be represented as plane waves states, having a wave vector k_i before the inelastic scattering process and k_f after it, Equation 2.6 can be written as [141, 142]:

$$\frac{\partial^2 \sigma}{\partial E \partial \Omega} = \frac{4\gamma^2}{a_0^2 q^4} \cdot \frac{k_f}{k_i} \sum_{i,f} | \langle i | e^{i\mathbf{q}\hat{\mathbf{R}}} | f \rangle |^2 \times \delta(E + E_i - E_f), \quad (2.7)$$

with $\hbar\mathbf{q} = \hbar(\mathbf{k}_i - \mathbf{k}_f)$ being the momentum transfer from the probe electron to the target, γ the *Lorentz*-factor, a_0 the *Bohr*-radius and $\hat{\mathbf{R}}$ representing the position

¹³OAM exchange with the sample may be neglected here.

¹⁴In a TEM, the sample is immersed in a objective lens field of roughly 2 T, which saturates most of common magnetic samples.

¹⁵Recently, it has been shown that, even without the tedious orientation of the sample to the two- or three-beam case, zone axis EMCD signals are present in the diffraction plane [140].

¹⁶Single electron scattering is a reasonable approximation for core-level scattering in thin samples.

2 Fundamentals

operator of the target electron. Using the dipole approximation $\mathbf{q} \cdot \mathbf{R} \ll 1$, $e^{i\mathbf{q}\mathbf{R}}$ can be expanded as $e^{i\mathbf{q}\mathbf{R}} \cong 1 + i\mathbf{q} \cdot \mathbf{R}$. Due to the orthogonality of the initial and final states of the target, the matrix element of the first term in the expansion vanishes and Equation 2.7 simplifies to:

$$\frac{\partial^2 \sigma}{\partial E \partial \Omega} = \frac{4\gamma^2}{a_0^2 q^4} \cdot \frac{k_f}{k_i} \sum_{i,f} |\langle i | i\mathbf{q}\mathbf{R} | f \rangle|^2 \times \delta(E + E_i - E_f). \quad (2.8)$$

If the crystal is now used as a beam splitter and sets the incident electron wave into the coherent state $|\varphi_i\rangle = A_1 |\mathbf{k}_i\rangle + A_2 |\mathbf{k}'_i\rangle$, with their respective complex amplitudes $A_{1,2}$ inserting into Equation 2.6, the double differential cross-section, Equation 2.8, becomes:

$$\frac{\partial^2 \sigma}{\partial E \partial \Omega} = \frac{4\gamma^2}{a_0^2} \cdot \frac{k_f}{k_i} \cdot \left(|A_1|^2 \frac{S(\mathbf{q}, \mathbf{q}, E)}{q^4} + |A_2|^2 \frac{S(\mathbf{q}', \mathbf{q}', E)}{q'^4} + 2\Re \left[A_1 A_2^* \frac{S(\mathbf{q}, \mathbf{q}', E)}{q^2 q'^2} \right] \right), \quad (2.9)$$

using the vector transfer $\mathbf{q} = \mathbf{k}_i - \mathbf{k}_f$ and $\mathbf{q}' = \mathbf{k}'_i - \mathbf{k}_f$ for the two incident waves \mathbf{k}_i and \mathbf{k}'_i into the outgoing wave vector \mathbf{k}_f ($k_f = k'_f$). Equation 2.9 is now a sum of two direct terms, which consist of the dynamic form factor (DFF),

$$S(\mathbf{q}, \mathbf{q}, E)_{Dipole} = \sum_{i,f} \langle i | \mathbf{q} \cdot \mathbf{R} | f \rangle \delta(E + E_i - E_f), \quad (2.10)$$

that is, describing inelastic scattering of an incoming plane wave into an outgoing plane wave. And an interference term, called mixed dynamic form factor (MDFF):

$$S(\mathbf{q}, \mathbf{q}', E)_{Dipole} = \sum_{i,f} \langle i | \mathbf{q} \cdot \mathbf{R} | f \rangle \langle f | \mathbf{q}' \cdot \mathbf{R}' | i \rangle \delta(E + E_i - E_f), \quad (2.11)$$

where the sum is taken over the initial (occupied) core and final (unoccupied) band states with initial- and final-energy E_i and E_f , respectively. It is a complex quantity (hermitian), obeying $S(\mathbf{q}, \mathbf{q}, E) = S^*(\mathbf{q}, \mathbf{q}, E)$. As a result, its diagonal elements, the DFFs, are real. In analogy to the circularly polarised X-rays, the incident electron can be prepared in a way that $\mathbf{q} \perp \mathbf{q}'$, which is basically done by placing the SEA midway between the *Bragg* spots on the Thales circle connecting them, see Figure 2.9. In addition, $|\mathbf{q}|$ should be equal to $|\mathbf{q}'|$ and there should be a phase shift of $\lambda/4$ between both partial waves, e.g., by selecting $A_1 = 1$ and $A_2 = \pm i$. Using this setting, Equation 2.9 becomes:

$$\sigma_{\pm}(E) = \frac{\partial^2 \sigma_{\pm}}{\partial E \partial \Omega} = \frac{4\gamma^2}{a_0^2} \cdot \frac{k_f}{k_i} \cdot \left(|A_1|^2 \frac{S(\mathbf{q}, \mathbf{q}, E)}{q^4} + |A_2|^2 \frac{S(\mathbf{q}', \mathbf{q}', E)}{q'^4} \mp 2\Im \left[\frac{S(\mathbf{q}, \mathbf{q}', E)}{q^2 q'^2} \right] \right). \quad (2.12)$$

The dichroic signal, as stated above, can now be written as the difference between the cross-sections σ_{\pm} :

$$\frac{\Delta \sigma(E)}{\sigma(E)} = \frac{\sigma_+(E) - \sigma_-(E)}{\sigma_+(E) + \sigma_-(E)} = \frac{2\Im[S(\mathbf{q}, \mathbf{q}', E)] / (q^2 q'^2)}{S(\mathbf{q}, \mathbf{q}, E) / q^4 + S(\mathbf{q}', \mathbf{q}', E) / q'^4}. \quad (2.13)$$

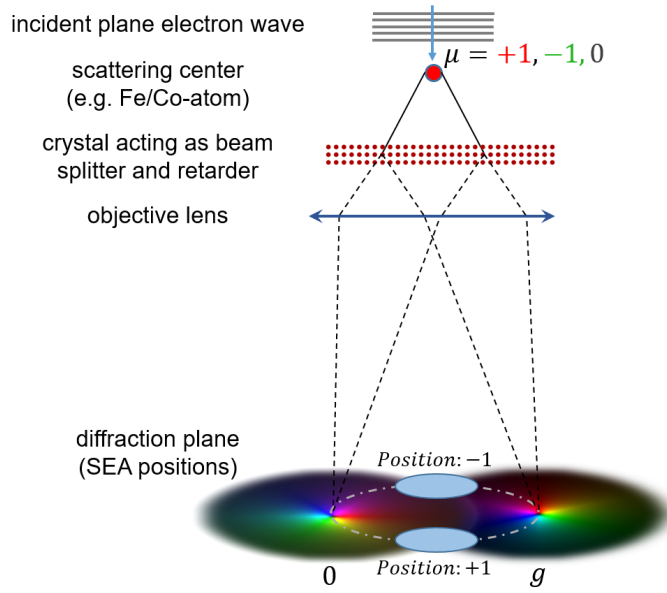


Figure 2.9: Schematic classical EMCD measurement setup in a TEM. The scattering centre (one atom) is drawn outside the crystal for better understanding.

Practically, the EMCD signal is defined as,

$$I_{EMCD} = 2 \frac{I_{Pos+1} - I_{Pos-1}}{I_{Pos+1} + I_{Pos-1}}, \quad (2.14)$$

where $I_{Pos\pm 1}$ is the accumulated electron intensity, positioning the SEA at position +1 and -1, respectively, see Figure 2.9. A finite size SEA needs to be accounted for by integrating the k_{fs} over the aperture radius. The same is true for non-parallel incident beams, where k_i has to be integrated up to the convergence angle.

EMCD combines the analytical capabilities of EELS with the coherent electron propagation through crystalline materials. It utilizes interference effects of the inelastically scattered partial electron waves in the crystal lattice and is thus a variant of interferometric EELS [143], a technique that is also known as ‘ALCHEMI’, where inelastic channelling effects change the intensity of the energy-loss edge. It strongly depends on the wave-splitting action of the crystal lattice.

2.4 Electron Vortex Beams

This section is mainly based on [144] and the electron vortex beam review articles [145–148].

The term ‘electron vortex beam’ has been used quite often so far, but a closer inspection and definition is still missing. This section aims at giving a short overview

on the field of structured electron waves and wavefront engineering with the focus set to a subclass, that has gained a lot of attention in the last few years since its invention in 2010, due to some peculiar attributes, inherent to electron vortex beams.

2.4.1 Wavefront Engineering

When a plane electron wave, structureless by definition, is incident on a thin crystal slab, the strong electrostatic interaction of the electron with the atomic potentials modifies the electron wavefront in such a way, that, on the exit surface of the crystal, a massively structured electron wave can be observed. This HRTEM image can be rich in details on the atomic structure, metastructures, precipitations, dislocations, strain, etc..¹⁷ Generally, wavefront engineering can be understood as the intentional production of arbitrary structures or electric- or magnetic-field configurations, that impart structure to an otherwise structureless wavefront. A very basal example for that process in microscopy is the round aperture, used to confine the electrons near to the optical axis, in order to reduce the influence of spherical aberrations on the electron beam. In an ideal aberration-less world, imaging a plane wave in the far-field, would result in a delta peak, but introducing the aperture changes the image dramatically to the well known *Airy* disk. Using *Fourier* optics, the *Airy* disk can be calculated, using the *Fourier* transform of the aperture function, $\psi^{Airy}(x, y) = FT(\psi^{Aperture}(k_{x,y}))$. Another example employing magnetic fields instead of material, are the stigmator coils in the TEM, which are typically used to reduce the wavefront deformation induced by imperfections in the round lenses in the microscope. In biology, contrast enhancement at low and intermediate spatial frequencies is achieved by using *Zernike* and *Hilbert* phase-plates [98]. With the advent and the massive improvement of micro- and nano-machining devices like electron beam lithography and focused-ion-beam machines, it became possible to produce much more complex arrangements, such, that it is now possible to arbitrarily shape the electron beam phase and amplitude structure in two dimensions [23], as well as in three dimensions [149], using practically the same *Fourier* optics based principle as mentioned above.

Aside from the study of fundamental beam properties, e.g., self-accelerating *Airy* beams [150], or the observation of free-electron LS in the TEM [32, 34], wavefront engineering can have also very practical applications. For example, experimental evidence was presented, that aberrations (beam tilt, two-fold astigmatism, three-fold astigmatism and spherical aberration) can be reduced, using structured membranes, either on-axis [28] or off-axis [151], opening up the route for a cost-efficient alternative to magnetic multipole correctors. Sculpturing the wavefront according to specific symmetries, e.g., of localized surface plasmon resonances, enables the research on otherwise hidden phenomena [26]. Also, linear phase contrast in STEM imaging has been reported using a structured illumination in combination with a high speed pixelated detector, such that light elements could be resolved in close proximity

¹⁷In principle the specimen is the hologram for a target wavefunction that resembles the diffractogram using a plane wave reference.

to high-Z elements with atomic resolution [152]. Recently, an interesting super-resolution scheme has been put forward by Remez et al. [153]. Employing binary amplitude masks, that produce a superposition of two *Bessel* beams, lead to the formation of sub-diffraction limited spots. The drawback with such a scheme is, that the central sharp spot is very weak and surrounded by multiple bright rings.

2.4.2 General Introduction

The advances made using electron wavefront engineering are closely related to the inception of EVBs, because with the seminal papers of *Uchida* and *Tomomura* [4] and *Verbeeck* et al.[5] it was shown, that light optical approaches can be transferred to EM or matter wave physics, relatively straightforward. At that time, the field of singular optics was already well established, and up to now inspires the field of electron matter waves. As vortex waves are an ubiquitous phenomenon, it is not surprising that long before EVB entered the stage, optical vortex beam (OVB) have already been observed [154–156]. *Hans Wolter* in 1950 kind of dismissed or downplayed the importance of his discovery by saying: ‘Die zirkulierende Welle ist eine in der Optik zwar neue, aber durchaus unkomplizierte Erscheinung (The circulating wave is indeed a new phenomenon in optics, but definitely an uncomplicated phenomenon.)’. Nevertheless, a systematic theoretical description of this ‘uncomplicated phenomenon’ was delivered nearly a quarter of a century later by *Nye* and *Berry* [19] who tried to understand radio echoes from the bottom of the *Antarctic* ice sheet, and quasi simultaneously for quantum matter waves by *Hirschfelder* [157]. The first intentional experimental realization with light waves happened in the 1990’s [20, 21]. Today, there are many applications of optical vortices ranging from tweezers exerting a torque [158], over optical micromotors [159], cooling mechanisms [160], toroidal *Bose–Einstein* condensates [161], communication through turbulent air [162] to exoplanet detection [163] ¹⁸.

Recently, *Arthur Ashkin* and his invention of the optical tweezers and their application to biological systems have been honoured with the *Nobel prize* in physics [166].

Helical spiralling electron beams were already produced in the 1970s by *Beck*, *Mills* and *Munro* [167–169], as a by-product of millimetre wave radiation generation. *McCullough* et al., who did simulations of H/H₂ reaction kinetics, coined the term ‘quantum whirlpool effect’ [170] and a few years before the holographic realization of EVB in the TEM took place, large-scale electron vortex structures have been observed in a electrostatic plasma lens [171].

All these phenomena have in common, that their probability current density $\mathbf{j} \propto \Im(\psi^* \nabla \psi) = |\psi|^2 \nabla \text{Arg}(\psi)$ swirls around phase singularities. That are points in 2D or lines in 3D space of indeterminate phase, appearing in regions \mathbf{r}_s of destructive interference $|\psi(\mathbf{r}_s)|^2 = 0$. The phase around such singular points is well-defined, and it has a non zero increment for a contour enclosing it of $\oint \nabla \text{Arg}(\psi(\mathbf{r})) d\mathbf{r} = 2\pi m$ with

¹⁸Additional information on OVB can be found in the two review articles ‘Advances in optical angular momentum’ and ‘Tweezers with a twist’ [164, 165].

2 Fundamentals

$m = 0, \pm 1, \pm 2, \dots$ being an integer winding number, called ‘topological charge’¹⁹. A general free-space vortex wavefunction, propagating in the z -direction, can be given in a cylindrical coordinate system (r, φ, z) as,

$$\psi(r, \varphi, z) \propto f(r, z)e^{ik_z z}e^{im\varphi}, \quad (2.15)$$

with φ representing the azimuthal angle, k_z the longitudinal wave number and $f(r, z)$ being a radial distribution function. It is quite intuitive, that such wavefunctions could possess OAM, and indeed vortex wavefunctions in the form $\psi \propto e^{im\varphi}$ are eigenmodes of the z -component of the quantum mechanical OAM operator, $\hat{L}_z = -i\hbar\partial/\partial\varphi$, which has eigenvalues $\hbar m$. So, every single particle carries $\langle L_z \rangle = \hbar m$ along its propagation direction, independent of the choice of the coordinate system, which is also called intrinsic OAM, as opposed to the extrinsic OAM, valid for classical particles, given by $L = \mathbf{r} \times \mathbf{p}$. Note that one could also say that the vortex producing device, e.g., a hologram, which will be described later on, is designed in a way that it imparts OAM in units of $\hbar m$ to the incoming electrons, independent of their distance to the centre of the hologram, i.e. it compensates for the r -dependence in the classical equation of angular momentum $\mathbf{L} = \mathbf{r} \times \mathbf{p}$.

Typically, free electrons do carry quantized spin angular momentum (SAM) in units of $\pm 1/2\hbar$, EVB can, in principle, carry arbitrary high values of OAM. It has been shown that, vortex phase masks can be fabricated, that produce EVB carrying OAM of up to $1000\hbar$ in the first diffraction order, with no overlap of the opposing vortex orders [54]. Contrary to OVB, electrons carry charge $|e|$, and thus a swirling probability current is associated with a magnetic moment of $\boldsymbol{\mu} = g\mu_B m \mathbf{e}_z$, with $g = 1$ being the g-factor for orbital motion, \mathbf{e}_z being the unit vector in z -direction and $\mu_B = \frac{e\hbar}{2m_e}$ being the *Bohr*-magneton.

2.4.3 Theory

Depending on the symmetry and constraints of the problem at hand, the choice of the coordinate system is essential and determines the kind of modes that solve the Schrödinger equation. For example, in atomic physics, spherical coordinates result in spherical modes for atomic orbitals or if a Cartesian coordinate system is chosen *Hermite-Gaussian* modes are solutions of the Schrödinger equation. For the case of swift electrons travelling in the z -direction and isotropic conditions in the transverse direction, it is convenient to choose a cylindrical coordinate system (r, φ, z) .

Bessel beams

The fundamental equation describing a quantum system is the Schrödinger equation,

$$\hat{H}\psi = E\psi, \quad (2.16)$$

¹⁹Often also called l , referring to the orbital quantum number, here, m is chosen, reminiscent of the magnetic quantum number and the inherent magnetic moment of an EVB.

where the Hamiltonian \hat{H} for an electron in a field free region can be given as $\hat{H} = \frac{\hat{\mathbf{p}}^2}{2m_e}$ with $\hat{\mathbf{p}} = -i\hbar\nabla$ being the quantum mechanical (linear) momentum operator. Putting this into the Schrödinger equation 2.16 yields:

$$-\frac{\hbar^2}{2m_e}\nabla^2\psi = E\psi. \quad (2.17)$$

The natural choice of a cylindrical coordinate system leads to the following representation:

$$-\frac{\hbar^2}{2m_e}\left[\frac{1}{r}\frac{\partial}{\partial r}\left(r\frac{\partial}{\partial r}\right) + \frac{1}{r^2}\frac{\partial^2}{\partial\varphi^2} + \frac{\partial^2}{\partial z^2}\right]\psi = E\psi, \quad (2.18)$$

with axially symmetric solutions of the form,

$$\psi_m^B(r, \varphi, z) \propto J_{|m|}(\kappa r)e^{i(k_z z + m\varphi)}. \quad (2.19)$$

J_m represents the *Bessel* function of the first kind and $m = 0, \pm 1, \pm 2, \dots$ is the azimuthal quantum number. $\kappa = p_\perp/\hbar$ and k_z are the transverse radial- and the longitudinal wave number, respectively. The solutions in Equation 2.19 satisfy Equation 2.18 only if the following dispersion relation is met:

$$E = \frac{\hbar^2}{2m_e}k^2 = \frac{\hbar^2}{2m_e}(k_z^2 + \kappa^2). \quad (2.20)$$

The wave number k is defined as $k = p/\hbar$.

For $m \neq 0$, solutions of the form given in Equation 2.19 are called *Bessel vortex beams*, showing a distinct intensity drop in the centre of their radially symmetric intensity distribution, see Figure 2.10, indicative of their OAM content. The zero-order, $m = 0$, does not carry OAM, and, contrary to the vortex orders, peaks in intensity in its centre. Notably, *Bessel* beams do not show a z -dependence of their radial beam profile, i.e., they are non-diffracting solutions to the Schrödinger equation. Similar to plane waves they cannot be normalized $\int_{\mathbb{R}} |\psi_m^B|^2 d^3r$, which renders them quite unphysical. This issue has been resolved by using a radial limiting aperture, restricting the wavefunction to a finite interval [144]. A property that is often uniquely assigned to *Bessel* (and *Airy*) beams, is their ‘self-healing’ ability [172]. But, aside that ‘self-healing’ can be understood using geometric ray optics, it has been shown that this property can also be seen in *Gaussian* beams [173].

Diffracting Laguerre-Gaussian modes

Based on [32, 34, 119, 145].

The above *Bessel* modes do not contain a z -dependence and are not localized (square-integrable) in the transverse direction. Hence, to cover the z -dependency of a convergent electron beam, a set of solutions of the paraxial²⁰ Schrödinger equation, namely *DLG* modes, will be described in the following. Using the substitution

²⁰The paraxial approximation reads: $p_\perp \ll p$ and $\mathbf{p}_\parallel \simeq \mathbf{p} \cdot \mathbf{e}_z$ and $(k_z \simeq k)$.

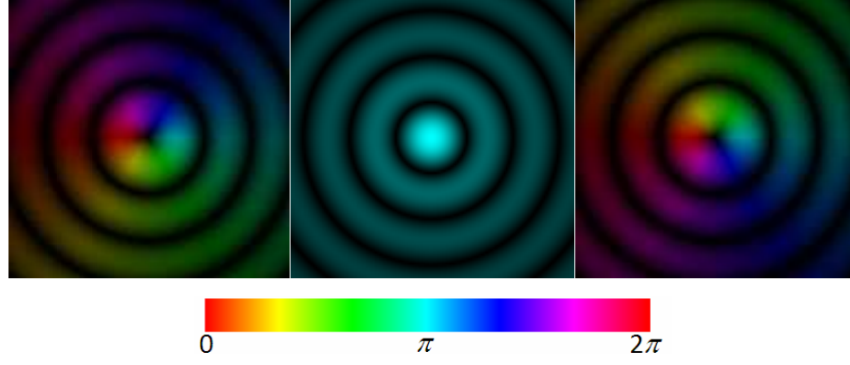


Figure 2.10: Probability density $\rho^B = |\psi_m^B|^2$ of *Bessel* beams using Equation 2.19. The $m = \pm 1$ states show the central intensity drop and a either right- or left-handed azimuthal hue colour-coded phase ramp running from 0 to 2π , whereas the $m = 1$ order has a flat phase and no dip. Taken from [119].

$\partial^2/\partial z^2 \simeq -k^2 + 2ik\partial/\partial z$, the Schrödinger Equation 2.18 reduces to the paraxial wave equation, also known as the paraxial Helmholtz equation ($\nabla_{\perp}^2 \psi + 2ik \frac{\partial \psi}{\partial z} = 0$):

$$\left[2ik \frac{\partial}{\partial z} + \frac{1}{r} \frac{\partial}{\partial r} \left(r \frac{\partial}{\partial r} \right) + \frac{1}{r^2} \frac{\partial^2}{\partial \varphi^2} \right] \psi = 0. \quad (2.21)$$

Well behaved (properly localized and normalizable) solutions to Equation 2.21 are DLG modes, which can be expressed as:

$$\begin{aligned} \psi_{m,n}^{DLG}(\mathbf{r}) = & \sqrt{\frac{n!}{\pi(n+|m|)!}} \frac{1}{w(z)} \left(\frac{r}{w(z)} \right)^{|m|} \times \\ & L_n^{|m|} \left(\frac{r^2}{w^2(z)} \right) e^{-\frac{r^2}{2w(z)^2}} e^{i\frac{kr^2}{2R(z)}} \times \\ & e^{-i(2n+|m|+1)\zeta(z)} e^{i(m\varphi+kz)}. \end{aligned} \quad (2.22)$$

$L_n^{|m|}$ represents generalized Laguerre polynomials with $n = 0, 1, 2, \dots$ being the radial quantum number, defining the number of nodes in the transverse probability density ($\rho = |\psi|^2$) profile. See Figure 2.11 (a) for a representation of the modes $(n, m) = (0 - 3, 0 - 2)$. The dispersion relation of DLG modes is given by $E = \frac{\hbar^2 k^2}{2m_e}$. The beam-waist $w(z)$ is defined as:

$$w(z) = w_0 \sqrt{1 + \left(\frac{z}{z_R} \right)^2}, \quad (2.23)$$

illustrating the transverse beam size evolution over z . See Figure 2.11 (b) for a schematic cross-section of a DLG mode, indicating the different parameters given

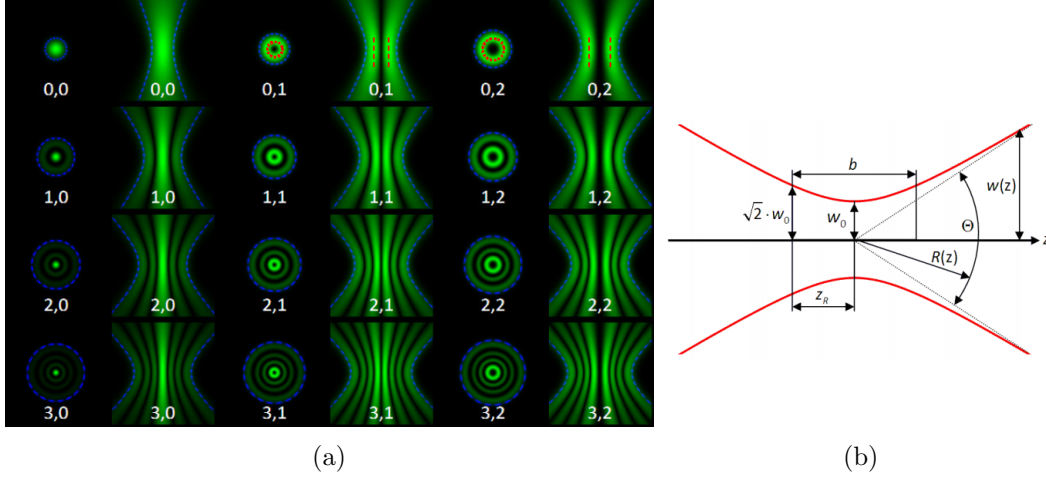


Figure 2.11: (a) Plane views and cross-sections of the probability density of DLG modes. The dashed red lines indicate the position of the maxima according to Equation 2.25, whereas the dashed blue lines indicate the DLG mode's spot size defined by Equation 2.26. (b) Schematic drawing of the fundamental DLG beam parameters. Taken from [119].

herein. w_0 is the narrowest ‘beam-waist-radius’ (of the $m = 0$ beam)²¹ at the focal plane $z = 0$ and

$$z_R = \frac{\pi w_0^2}{\lambda} = k w_0^2 \quad (2.24)$$

is the *Rayleigh*-range, denoting the position where the illuminated area doubles, and thus $w(z) = \sqrt{2}w_0$. The acquired phase shift stemming from the *Gouy* phase, which is given by $\zeta(z) = \arctan(z/z_R)$, reaches the value of $\pi/2$ at that z -position. $R(z)$ represents the curvature of the DLG beams and is defined as $R(z) = z(1 + (z/z_R)^2)$. It happens to be that $R(z)$ is greatest at the point $z = z_R$ and the region between $z = \pm z_R$ is called the confocal parameter or depth of focus of a DLG beam. The position of the vortex beam's maxima for the radial mode $n = 0$ have been found to lie at,

$$r_{max}^{m,n=0} = \sqrt{\frac{|m|}{2}} \cdot w(z) \quad (2.25)$$

and the spot size, where the intensity dropped to $\sim 13.5\%$ ($\frac{1}{e^2}$ value) of the beam's maximum intensity, can be given as:

$$w^{m,n}(z) = w_0 \cdot \sqrt{2n + |m| + 1} \cdot \sqrt{1 + \left(\frac{\lambda z}{\pi w_0^2}\right)^2}. \quad (2.26)$$

At this radial distance to the beam centre, the beam contains approximately 86.5% of its total transported energy. Similar to the *Bessel* beams, $m = 0, \pm 1, \pm 2, \dots$

²¹ $w(z)$ is not the maximum intensity radius of a vortex, which is given by $r_{max}(z, m) = w(z)\sqrt{|m|}$ for $n = 0$.

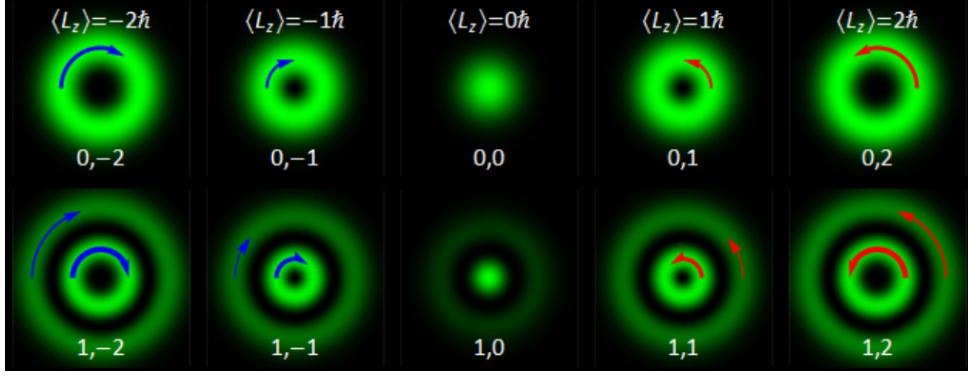


Figure 2.12: Plane views of the probability density of DLG vortex modes ($m = \pm 1, \pm 2$) and non-vortex modes ($m = 0$), together with their probability density current indicated as red and blue arrows. The length and thickness of the arrows increases with increasing azimuthal probability density current j_φ and their positions coincide with the position of the maxima according to Equation 2.25, whereas the dashed blue lines indicate the DLG mode's spot size defined by Equation 2.26. Taken from [119].

represents the azimuthal quantum number and is therefore an indicator for the vortex character of the respective mode. Not only the transverse probability density ρ changes dramatically for higher m -values, but also the probability density current, which are defined for the general case as:

$$\rho = |\psi|^2 \quad \mathbf{j} = \frac{1}{m_e} \Re[\psi^* \hat{\mathbf{p}} \psi] = \frac{\hbar}{m_e} \Im[\psi^* \nabla \psi]. \quad (2.27)$$

Using the canonical momentum operator $\hat{\mathbf{p}} = -i\hbar \nabla$ and substituting the wavefunction Equation 2.19 in Equation 2.27 yields the probability density and probability density current of a *Bessel* beam:

$$\rho_{|m|}^B(r) \propto |J_{|m|}(\kappa r)|^2 \quad \mathbf{j}_m^B(r, \varphi) = \frac{\hbar}{m_e} \left(\frac{m}{r} \mathbf{e}_\varphi + k_z \mathbf{e}_z \right) \rho_{|m|}^B(r), \quad (2.28)$$

where \mathbf{e}_φ is the azimuthal unit vector. For $m \neq 0$ the combined azimuthal and forward motion resembles a spiralling probability current in *Bessel* beams, Equation 2.28, and DLG beams given by,

$$\rho_{|m|,n}^{DLG}(r, z) \propto \left(\frac{r^2}{w^2(z)} \right)^{|m|} \left| L_n^{|m|} \left(\frac{r^2}{w^2(z)} \right) \right|^2, \\ \mathbf{j}_{m,n,\varphi}^{DLG}(r, z) = m \frac{\hbar}{m_e r} \rho_{|m|,n}^{DLG}(r, z). \quad (2.29)$$

Notably, DLG beams show an additional radial component of the probability density and probability density current associated to their diffracting behaviour. The spiralling current in those modes is responsible for their z -directed OAM content, which

can be calculated, using either the expectation value of the OAM operator or the circulation of the probability current. For the longitudinal component of the OAM in 2D-localized beams, using a normalization to one electron, this becomes:

$$\langle L_z \rangle = \frac{\langle \psi | \hat{L}_z | \psi \rangle}{\langle \psi | \psi \rangle} = \frac{m_e \int \mathbf{r} j_\varphi d^2 \mathbf{r}_\perp}{\int \rho d^2 \mathbf{r}_\perp}, \quad (2.30)$$

with $\hat{L}_z = -i\hbar\partial/\partial\varphi$. Now, any vortex wavefunction containing the azimuthal phase factor $e^{im\varphi}$ and $j_\varphi = m(\hbar/m_e r)\rho$ put into Equation 2.30, leads to:

$$\langle L_z \rangle = \hbar m. \quad (2.31)$$

Which is a well-defined, quantized and longitudinal content of OAM in a vortex state, solely determined by the topological charge m . The independence of the choice of the coordinate system, justifies the notion of an intrinsic OAM. Contrary to that, an extrinsic OAM can be calculated by:

$$\langle L^{ext} \rangle = \langle \mathbf{r} \rangle \times \langle \mathbf{p} \rangle, \quad (2.32)$$

using the definition for the expectation value for \mathbf{r} :

$$\langle \mathbf{r} \rangle = \frac{\langle \psi | \hat{\mathbf{r}} | \psi \rangle}{\langle \psi | \psi \rangle} = \frac{\int \mathbf{r} \rho d^3 \mathbf{r}}{\int \rho d^3 \mathbf{r}}, \quad (2.33)$$

which is basically the electron's centroid. And the one for the electron momentum is:

$$\langle \mathbf{p} \rangle = \frac{\langle \psi | \hat{\mathbf{p}} | \psi \rangle}{\langle \psi | \psi \rangle} = \frac{m_e \int \mathbf{j} d^3 \mathbf{r}}{\int \rho d^3 \mathbf{r}}. \quad (2.34)$$

For radial symmetric EVB, the centroid coincides with the z -axis, $\langle \mathbf{r}_\perp \rangle = 0$, and the expectation value for the momentum is aligned parallel to the propagation direction z , $\langle \mathbf{p} \rangle \parallel \mathbf{e}_z$. As a result, the expectation value for the extrinsic OAM is zero: $\langle L_{ext} \rangle = 0$.

Note that, even though DLG modes represent a powerful analytical solution to describe EVB, as well as OVB, there are still distinct differences to the *Fourier* optically simulated wave-field of vortex beams, see Figure 2.13, such that care has to be taken when comparing experiments to theory for defocus values exceeding the z_R .

Moreover, this treatment does not account for the realistic case in a typical TEM of a present longitudinal magnetic field, which alters the canonical OAM of vortex beams, as described above, in a peculiar way. This topic will be covered in Section 5.2. Also, the effect of an incoherent source size was not included here but will be elaborated in Section 5.1. Throughout this section it was assumed that a non-relativistic scalar electron picture is sufficient to describe the propagation of 200 keV electrons. Recently, a couple of publications addressed that issue [174–179], but this is beyond the scope of this work. It is very likely that spin-related effects are not observable under the given experimental parameters [180, 181].

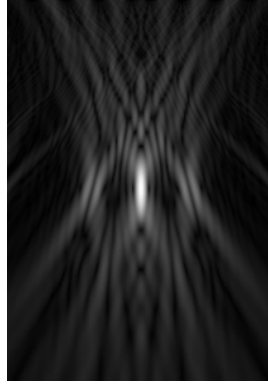


Figure 2.13: Cross-section of a wavefunction, propagating through vacuum after passing a binary HVM, using *Fourier* optics and a multi-slice simulation code. Compare to the cross-sections in Figure 2.11.

2.4.4 Electron Vortex Production

Already Dennis Gabor, back in 1948, realized the potential of electron holography in the TEM [182], and first realizations were seen a few years later [183, 184]. A lot of holography schemes have been tested from that on [185] in EM, but it took a while until it was realized that computer generated holograms can also be used in the TEM to manipulate the amplitude and phase of the electron beam [5]. Since the inception of HVMs, in 2010, the field rapidly evolved and a lot of different holographic structures have been presented, see, e.g.: [23–25, 53, 54, 149, 172, 186, 187], and the review articles [145, 188].

The basic principle of EVB production, using a holographic device has already been shown in Figure 1.2, in Section 1.2. Here, it will be shown how a two-dimensional (nanoscale) structure, the hologram, that produces a well defined (helical) phase pattern in the electron beam when illuminated with the proper reference wave, can be calculated.

Details on the production of the thin metal membranes will be given in Section 2.9 and Chapter 4.

The holographic reconstruction works, as follows, a desired target wavefunction, in our case the aperture limited vortex wave,

$$\psi_{target}(r, \varphi, z) = \Pi(r/r_M)e^{im\varphi+ik_zz}, \quad (2.35)$$

propagating in the z -direction, has to be brought to interference with a tilted reference wave, in our case an aperture limited plane wave,

$$\psi_{ref}(r, \varphi, z) = \Pi(r/r_M)e^{ik_x x + ik_z z + i\phi}, \quad (2.36)$$

with $\Pi(x)$ being the radial step function,

$$\Pi(x) = \begin{cases} 1, & x \leq 1 \\ 0, & x > 1 \end{cases} \quad (2.37)$$

and k_x the reference wave's in-plane deflection vector, given by $k_x = \frac{2\pi}{g}$. r_M is the limiting aperture's radius and g is the periodicity of the interference pattern or holographic grating, respectively. ϕ is an arbitrary phase offset between the target and the reference wave, which is used to adopt the shape of the pattern, e.g., to align the edge-dislocation in the centre of the fork-like interference pattern. Without this, most of the time unmentioned, phase factor, an HVM built upon this model, would have unstable grating bars around the edge-dislocation, that could easily break away. The interference of ψ_{ref} and ψ_{target} in the reference plane $z = 0$ leads to interference pattern,

$$\begin{aligned} \rho_{int}(r, \varphi) &\propto |\psi_{target} + \psi_{ref}|^2 = \Pi(r/r_M) [2 + 2 \cos(k_x x + \phi - m\varphi)] = \\ &= \Pi(r/r_M) \left[4 \cos^2 \left(\frac{k_x x + \phi - m\varphi}{2} \right) \right] \propto T(r, \varphi). \end{aligned} \quad (2.38)$$

A hologram, having the transmission function $T(r, \varphi)$, is now produced, imitating this interference pattern as good as possible. See Figure 2.14 (a) for the ideal sinusoidal HVM. When this hologram is now illuminated with a non-tilted plane wave, as it is the case in the TEM, the transmitted or reconstructed wavefunction looks like:

$$\psi_{reconstructed}(r, \varphi, z) = T e^{ik_z z} \propto \Pi(r/r_M) e^{ik_z z} [e^{ik_x x + i\phi - im\varphi} + 2 + e^{-ik_x x - i\phi + im\varphi}]. \quad (2.39)$$

This is basically the superposition of the aperture limited, tilted target wavefunction, a non-tilted reference wave and the complex conjugated target wave, being tilted in the opposite direction. The phase factor ϕ adds only a global phase difference of 2ϕ between the two tilted target waves. At $z = 0$ the components of Equation 2.39 are not distinguishable, which changes drastically upon propagation to their *Fourier* plane (far-field), by applying the *Fourier* transform to the wavefunction Equation 2.39:

$$\tilde{\psi}_{reconstructed}(\mathbf{k}_\perp) \propto \tilde{\Pi}((k_M/|\mathbf{k}_\perp|)) \otimes [\tilde{\psi}_{target}(\mathbf{k}_\perp + k_x \bar{x}) + 2\tilde{\Pi}(k_M/|\mathbf{k}_\perp|) + \tilde{\psi}_{target}^*(\mathbf{k}_\perp - k_x \mathbf{e}_x)]. \quad (2.40)$$

Technically and physically, it is impossible to produce a sinusoidal pure amplitude hologram for electrons, like it is shown in Figure 2.14 (a). Hence, a common used approximation to the problem is to binarise the transmission function $T(r, \varphi)$,

$$T_{Binarised}(r, \varphi) = \begin{cases} 0, & \text{for } T(r, \varphi) \leq A_{Threshold} \\ 4, & \text{for } T(r, \varphi) > A_{Threshold} \end{cases}, \quad (2.41)$$

where $A_{Threshold}$ is typically chosen to be two for a barwidth-to-vacuum ratio (duty-cycle) of one, or slightly lower, in order to compensate for over-cutting and instabilities while the FIB production process. The binarised hologram is shown in Figure 2.14 (b), as well as its realisation, using a FIB to mill the structure, having $r_M = 10.3 \mu\text{m}$ and $g = 1065 \text{ nm}$ in a 1200 nm AuPd membrane deposited on 200 nm SiNx, Figure 2.14 (c). The according far-field simulation, Figure 2.14 (d), agrees very well with the measured intensity distributions, given in Figure 2.14 (e). Note that the

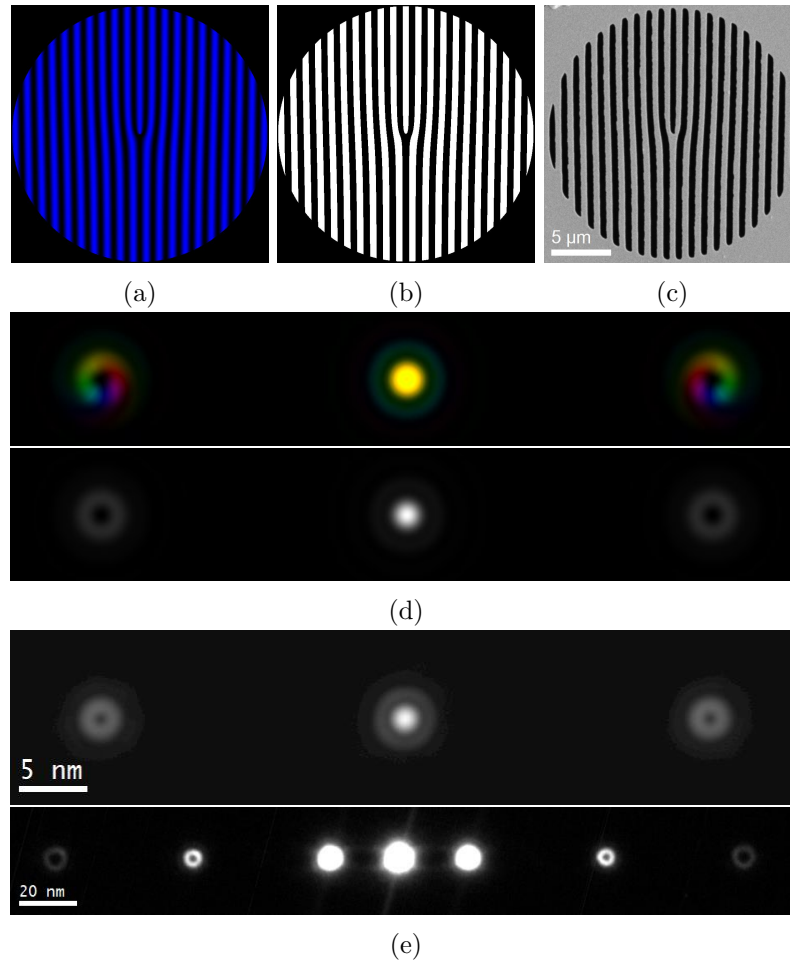


Figure 2.14: (a) Representation of the sinusoidal transmission function $T(r, \varphi)$ that produces laterally separated EVB. (The blue colour-coding has no physical meaning but a technical, it's actually needed to control the FIB dwell time). (b) Shows the binarised hologram and (c) the FIB milled result in a 1200 nm AuPd membrane, deposited on 200 nm SiNx ($r_M = 10.3 \mu\text{m}$ and $g = 1065 \text{ nm}$). (d) Simulation results, showing the hue colour-coded phase and intensity of the wavefunction propagation, using an in-house *ImageJ* plug-in. Note that the hue image was brightness adopted. (e) shows the experimental result when the hologram in (c) is placed in the condenser system of a *Tecnai F20* FEG-TEM and illuminated by a practically plane wave. The upper image of (d) shows the first two orders ($m = \pm 1$), adjacent to the central spot, whereas in the lower image the higher orders are also visible, e.g., $m = \pm 5, \pm 3$.

central dark spot in the vortices, indicative of the vortex phase singularity, is less pronounced in the experimental images, due to incoherent source size broadening [189], which was not included in the simulation. The sharp edge onset, introduced by the binarisation, leads to higher harmonics in the vortex order spectrum, as can be seen in the lower panel of Figure 2.14 (e). The intensity envelope of the vortex spectrum is given by the duty-cycle of the grating bars.

The calculated transmission function, the hologram, is then converted to a 24-bit bitmap image for the FIB milling step. It is recommended by the FIB manufacturer to use black $(r, g, b) = (0, 0, 0)$ for none milling points and white $(r, g, b) = (255, 255, 255)$ for milling points. Details on the milling parameters and strategy will be described in Section 2.8 and Chapter 4.

An import figure of merit of diffractive elements, like the HVMS described above, is their DE, i.e., the amount of electrons distributed to a certain diffraction order m . Depending on the application, there are different definitions of the DE, e.g., for STEM-EELS measurements well-separated beams are important and, thus, the relative DE $\eta_m^{(m')} = \frac{I_m'}{I_m}$, with I_m being the electron counts in the m diffraction orders. When studying solely structural effects of the hologram to the electron distribution, without caring for the electron loss in the mask material, the transmitted DE, given by $\eta_{(t)}^m = \frac{I_m}{I_{trans}}$, where $I_{trans} = \sum_m I_m$, is of interest. The absolute DE can be given by [25]:

$$\eta_{(i)}^m = \frac{I_m}{I_{in}}, \quad (2.42)$$

where I_{in} is the intensity incident on the hologram [25]. Especially in low electron count applications, like core-loss EELS measurements, this figure of merit is of great importance.

The DE of a hologram structure can be given analytically in the form [24],

$$A_m = \frac{1}{g} \int_0^g T_H(x) e^{-i\alpha} dx, \eta_m = |A_m|^2, \quad (2.43)$$

using $\alpha = 2\pi\frac{x}{g} + m\varphi$ for a pitchfork hologram, with g being the periodicity of the grating, m the topological charge and T_H being the transmission function [24].

$$T_H(x) = e^{-t(\mathbf{r}_\perp)/\lambda_{mfp}} \cdot e^{iC_E \bar{V}t(\mathbf{r}_\perp)} \quad (2.44)$$

similar to Equation 2.45, given in Section 2.5, but with the addition of an amplitude damping term, describing high-angle- and inelastic scattering in the hologram (excess) material [25, 190]. The electron mean free path is defined as $\frac{1}{\lambda_{mfp}} = \frac{1}{\lambda_{el}} + \frac{1}{\lambda_{inel}}$. Values for the elastic and inelastic contributions can be found in, e.g., [191–194]. Table 2.1 lists the absolute DE values for various hologram structures, using Equation 2.43, with the according transmission functions [24]. Note that high-angle- and inelastic-scattering in the hologram (excess) material has not been included. Using blazed phase holograms, the theoretical maximum absolute DE is 100 %. For vortex filter EMCD measurements, a symmetric distribution of intensity in the $m = \pm 1$

Table 2.1: Theoretical DE of different kinds of phase and amplitude HVMS, according to [24], without amplitude damping due to high-angle- and inelastic-scattering.

	Amplitude hologram		Phase hologram	
Grating geometry	Diffraction orders	$\eta_{(i)}^{\pm 1}$ [%]	Diffraction order	$\eta_{(i)}^{\pm 1}$ [%]
Sinusoidal	0, ± 1	6.25	All	33.85
Binary	Odd	10.13	Odd	40.52
Blazed	All	2.53	First order	100

orders is needed, such that the most favourable alternative seems to be the binary phase hologram with maximal 40.5 % of the incident current in the two first diffraction orders. However, the focus in this work lies on amplitude HVMS, only at the end of the Optimization chapter, first experimental tests to produce binary phase vortex masks will be shown.

2.5 Alternative Electron Vortex Production Methods

This section is based on the review articles [145, 188].

This section aims at giving a concise overview of different alternative vortex production methods that came up after *Verbeeck* et al. [5] for the first time produced EVB in the TEM in a reproducible manner, using binary absorption HVM, as described above.

Even though binary absorption HVM proved to be a robust and straightforward method to impart OAM to the electron beam in a controlled way with high mode purity [47] and regardless of the high voltage used, there are some drawbacks that render them unpractical for certain applications. Unlike in the applications described in Chapter 5, the presence of three or multiple vortex orders at the same time is not beneficial in STEM imaging or, generally, experiments done in the STEM-mode. Moreover, TEM experiments often suffer from a lack of electron intensity, especially core-loss EELS measurements, and, thus, every loss or blocking of electrons in the mask material is detrimental, i.e. only $\sim 10\%$ of the beam current incident on the aperture are transferred to one of the two first-order EVBs.

Soon after *Verbeeck* et al. published in 2010, the first modification of the original fork dislocation grating was presented in the form of a spiral binary holographic structure [187]. By using a spherical wave, instead of a tilted plane wave, as reference wave, it was possible to separate the resulting vortex orders in the z -direction, the propagation direction of the electron, such that opposing vortex orders can be selected by changing the defocus value. This is indeed more practical for STEM imaging and high resolution STEM, as shown in [187]. The fact that this vortex

production method does not yield a pure OAM state, as all produced vortex orders are overlapping along the z -direction [38], and that the structure also blocks half of the incoming electrons, forms definite drawbacks.

A means to avoid losing half of the electrons, due to high-angle scattering in the mask material, has been put forward two years later by Grillo, Shilo and Harvey and their respective colleagues [23–25]. They use phase masks that utilize the fact that the electron acquires a phase shift (deflection) in thin materials, depending on the space-averaged electrostatic potential \bar{V} of the (homogenous) material in the form of,

$$\Delta\Phi = C_E \int_0^{d(\mathbf{r}_\perp)} V(\mathbf{r}) dz = C_E \bar{V}(\mathbf{r}_\perp) t(\mathbf{r}_\perp), \quad (2.45)$$

where $C_E = \frac{2\pi e(1+U/U_0)}{\lambda 2U(1+U/2U_0)}$ is a microscope and experimental specific constant. This is a global phase shift, not to be confused with the microscopic atomic potentials $V(\mathbf{r})$, e.g., leading to complex changes in the phase structure of the electron, exploited in, e.g., HRTEM imaging. Typically only ~ 50 nm shallow grooves have to be milled for phase shifts of the order of π . As a result, using FIB milling, much finer structures can be produced, compared to the much thicker absorption or amplitude masks. Even though phase masks are milled into a low- Z material like SiNx, the electron loss due to high-angle scattering, can be quite pronounced. Optimizing the SiNx support thickness leads to a diffraction efficiency of 25 % [25]. Using the possibility of milling very fine trenches, phase mask with $m = 1000$ EVBs have been produced, that are well-separated in the lateral direction [54].

Shilo et al. [23] and B  ch   et al. [195] picked up the original approach used by Uchida and Tonomura [4] and intentionally produced a spiral staircase phase mask to produce an azimuthal phase shift of 2π , which theoretically leads to a single on-axis $m = \pm 1$ vortex mode, depending on the sense of rotation. Concerning the diffraction efficiency of such holograms, the B  ch   group reported an average OAM of ~ 0.8 per electron, with almost 60 % of the beam’s intensity transferred to the $m = 1$ state. But the azimuthal- and radial intensity profiles shown did not beautifully resemble the expected intensity distribution of an EVB like in Figure 2.14 (d,e). They also did not discuss the effects of high-angle scattering as well as beam broadening in the amorphous material and defocus spread, due to inelastic scattering. Estimating the mean thickness of the structure to be ~ 50 nm, the diffraction efficiency would be around 30 %. Shilo did not make any comments on the beam intensity distribution, but, given the fact that they used 50 nm to 100 nm SiNx and a comparable OAM distribution (probably better), the overall diffraction efficiency can be estimated to be of the order of 12 % to 30 %.

Another route of producing electron vortices was to use electric- or magnetic-fields instead of materials to modify the electron phase.

Clark et al. [196] realized that the linear variation of the azimuthal angle φ from $-\pi$ to π indicative of a vortex phase can be reproduced by *detuning an aberration corrector*, and an angle-limiting annular aperture. The outcome of a feasibility study showed, that 15.6 % of the incident beam current could be transferred to an $m = 1$

2 Fundamentals

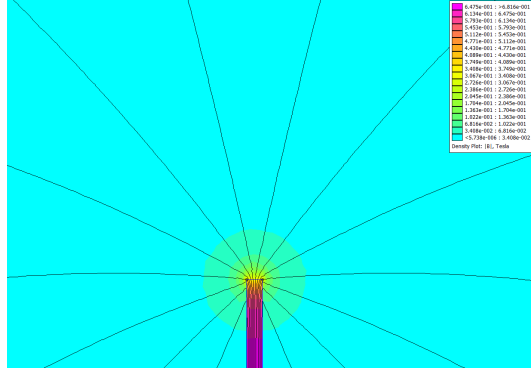


Figure 2.15: Finite-elements simulation (femm4.2) showing the radial flux lines (black lines) and the magnetic flux density (color coding) of a nanoscale magnetic needle, which should approximate a monopole field. The azimuthal deflection of an electron passing this magnetic field distribution produces an EVB. The needle is 310 nm wide.

vortex state, nevertheless the beam profile was very asymmetric and showed a lot of azimuthal variations along the vortex’s maximal intensity radius.

An apertured tip of a miniature *magnetic needle*, sometimes referred to as a magnetic monopole, has been successfully used to impart OAM to the electron beam [39, 197]. The magnetic field lines of that configuration head radially outward of the needle tip, which is positioned in the centre of an aperture, as can be seen in Figure 2.15. The *Lorentz-force* for such a field distribution predicts an azimuthal deflection of the incident electrons at a certain radius r , in the form of: $\beta = \frac{v_\varphi}{v_z} = \frac{e}{m_e v} \int B_r(z, r) dz$, leading to a vortex phase structure. The needle was made out of a 60 nm Ni thin film by carefully removing material from the needle, using a FIB, it was possible to tune the azimuthal phase shift to a value close to 2π . Thus, a single mode high-brightness vortex beam has been produced, where almost 90 % of the incident beam intensity were transferred to the $m = 1$ state. Using this probe, it was possible to acquire high-resolution scanning transmission electron microscopy (HRSTEM) images [39]. Via externally applied magnetic fields, the magnetisation direction of the magnetic needle can be switched, such that the TEM operator can toggle between $m = \pm 1$ vortex states in an instant of time.

Opposed to the magnetic needle method, proof-of-principle experiments show that the generation of electron vortices is also possible by using electrostatic line charges. Via changing the applied voltage to the device, dynamical control over the amount of OAM content in the electron beam is possible [198–200]. Though not yet proven, realizing a scheme similar to the magnetic jump approach, mentioned in the vortex introduction, may lead to the formation of extremely high OAM states with nearly arbitrary control of the OAM state by simply changing the excitation of the magnetic jump current loops. The production methods which have been successfully employed to produce vortex beams in the optical- and electron-optical field, have been shown

to be also applicable to other matter waves, like neutrons [22], air molecules (acoustic vortices) [201], and (broadband) THZ radiation [202, 203]. Also, the development of the ultra-fast TEM opens up the possibility to transfer OAM to the electron beam, using pump-probe experiments which employ chiral photonic excitation fields [204, 205].

The above methods aimed at introducing an azimuthal phase component, a quite specific wavefront, to the electron beam. A more general approach has been shown by Verbeeck and co-workers. They managed to build a *dynamic phase plate*, using a two by two array of controllable miniature drift tubes [206]. Further improving this concept may lead to a fully programmable spatial electron modulator, with the ability to form arbitrary wavefronts quasi instantaneously.

2.6 Vorticity Filtering in a TEM

Since the introduction of the possibility to produce (nearly) arbitrary OAM states, the question of their qualitative and more importantly their quantitative measurement became apparent.

The first method to discern the OAM content of an electron beam, which will also be used in this work, was the binary fork dislocation grating [45, 207], see Figure 2.16 (a). There, a post specimen HVM is illuminated by an electron vortex state, carrying an OAM of $\mu\hbar$. Upon interaction with the hologram the orbital angular momenta add up to $m' = \mu + m$. This in turn modifies the radial intensity distribution of the outgoing vortices observed in the intermediate image plane. For example, an intensity rise in the centre of the $m = -1$ vortex is indicative of an incident $\mu = +1$ vortex state and vice versa, see Figures 2.16 (b-d). A simple pinhole detector could be used to detect the OAM state of the incoming wave. Note that the overall intensity does not change significantly upon different incident OAM to the filtering HVM, i.e, less than $\sim 0.2\%$ for $m = \pm 1$ and an incident $\mu = \pm 1$) [207]. Therefore it is crucial to compare radial intensity distributions, not the overall intensity, in the opposing vortex orders to discern the OAM content of the incoming electron wave. If the incident wave consists of an arbitrary superposition of vortex states, which is, e.g., the case in core-level excitations and EMCD experiments, the analysis is more complicated, as will be shown in Section 5.1.

Apart from this straightforward method, meanwhile, a multitude of other clever OAM filtering ideas came up, e.g., triangular shaped apertures, knife edges, astigmatic phase shifts [45, 46] and multi-pinhole arrangements [47]. The multi-pinhole interferometer consists of n small holes evenly distributed on a circle. A far-field pattern of a wave that is projected on such a structure depends on the relative phases between the pinholes. This can be used to determine the value of m of the incident wave field. By calculating the autocorrelation function, which can be found by applying a Fourier transform (FT) to the diffraction pattern as stated in the Wiener-Khinchin theorem, a quantitative measurement of mixed OAM states is possible [47].

Recently, it has been shown that OAM sorters, quite similar to the optical OAM

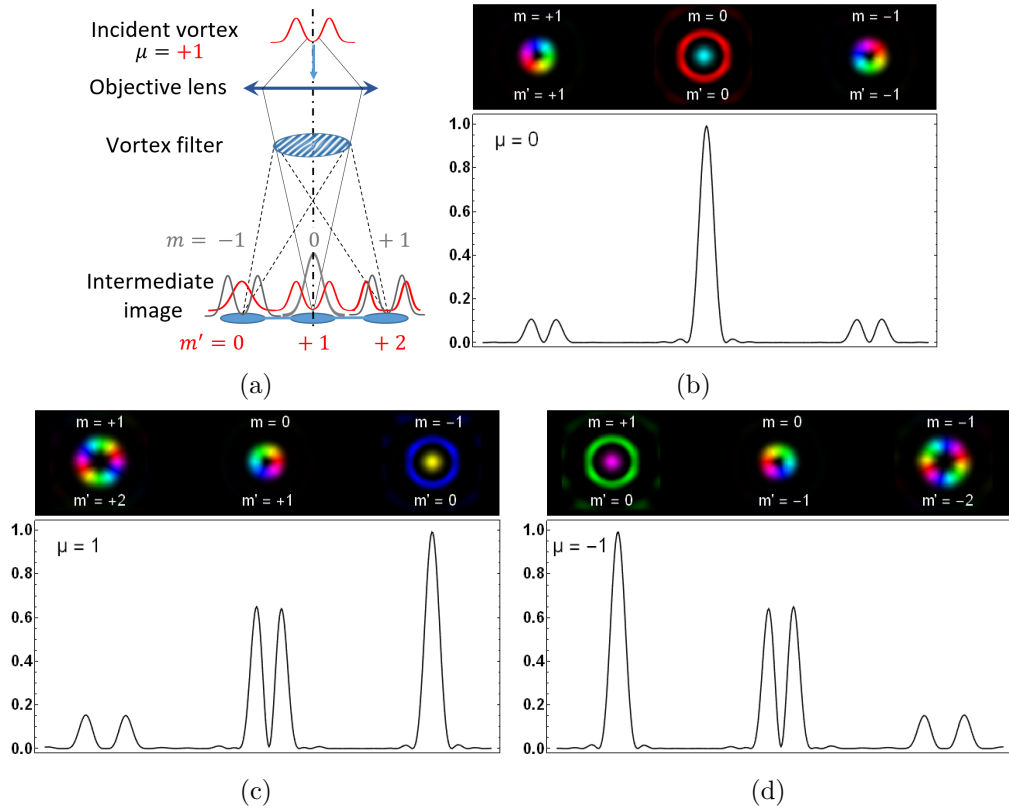


Figure 2.16: Vorticity filtering principle using a binary HVM. (a) A post specimen HVM is illuminated by an electron vortex state that carries an OAM of $\mu\hbar$. Upon interaction with the hologram the orbital angular momenta add up to $m' = \mu + m$ which modifies the radial intensity distribution of the outgoing vortices, e.g., the intensity rise in the centre of the $m = -1$ vortex is indicative of an incident $\mu = +1$. (b-d) Profiles and 2D-representation of simulated diffraction patterns of the vortex filter setup in (a) for $\mu = 0, 1, -1$.

sorting schemes [48], can also be built for electrons in a TEM [49]. The OAM sorter consists of two structures milled in SiNx membranes that manipulate the electron phase. The first one is used to perform a log-polar coordinate transformation of the wavefunction. It maps the azimuthal variation of the electron's phase to a Cartesian coordinate, whereas the second structure acts as a correction element for the introduced defects produced by the first element. This method is able to decipher arbitrary superpositions of OAM states. There is also a proposal dealing with the possibility of a fully electrostatic OAM sorter [50] of this kind. And there are proposals for non-destructive OAM sorting schemes, incorporating a magnetic field only in a Stern-Gerlach-like approach [51], as well as utilizing the presence of induced eddy-currents in a conducting loop, which has been found to be OAM-dependent [52]. Both schemes have not yet been realized.

2.7 Multi-Slice Simulation Technique

This section is based on [208, 209].

Numerical simulations have become a powerful tool in the field of EM to model the propagation of the electron wave through the sample and calculate TEM as well as STEM images in order to better understand the material structure underlying the recorded image intensity. Traditionally there are mainly two methods that have been developed and improved throughout the last decades: MS and the Blochwave formalism. While the Blochwave formalism works well for small perfect crystals, the MS method can be employed to simulate elastic and inelastic scattering in any structure, e.g., amorphous materials. First the MS approach for elastic scattering will be introduced and further expanded to inelastic scattering.

When the electron enters the material, (multiple or dynamical) scattering occurs on the electrostatic potential $V(x, y, z)$ of the atoms. As a result the eigenfunction ψ_f has to be computed for a Hamiltonian that includes the potential energy as:

$$\left[-\frac{\hbar^2}{2m_e} \nabla^2 - eV(x, y, z) \right] \psi_f(x, y, z) = E\psi_f(x, y, z). \quad (2.46)$$

For swift 200 kV electrons it would be necessary to account for relativistic effects using the Dirac wave equation including the electron spin, but by using the electron's relativistic mass $m = \gamma m_e$ and, later on, also the relativistic wavelength λ , it is possible to use the non-relativistic Schrödinger equation and account for relativistic effects. $e = |e|$ and E are the modulus of the electron charge and the total energy of the electron, respectively. For swift 200 kV electrons the primary direction of motion is along the z -direction, which justifies an ansatz that splits ψ_f into a product of a wave, moving in z -direction and a small slowly moving 'perturbation' wavefunction due to the elastic scattering:

$$\psi_f(x, y, z) = \psi(x, y, z) \cdot e^{\frac{i2\pi z}{\lambda}}, \quad (2.47)$$

2 Fundamentals

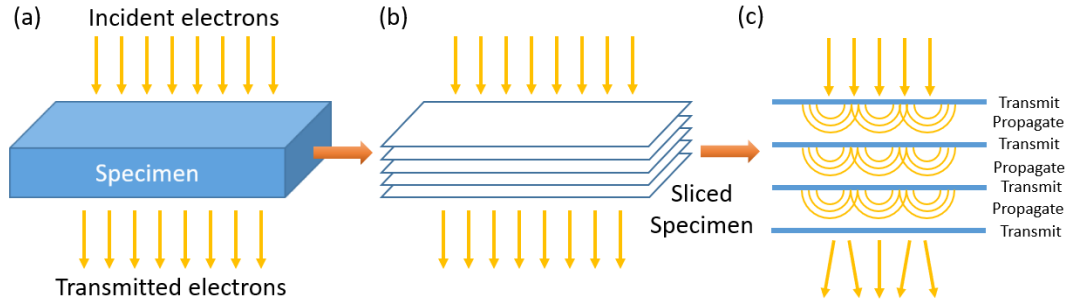


Figure 2.17: Multi-slice simulation principle. The multi-slice-approximation splits a TEM specimen (a) up in multiple slices (b) which contain the projected atomic potentials of the sample atoms. The slice thickness is chosen such that each slice of the specimen can be approximated by a simple phase shift of the electron wave, which is propagated from slice to slice in vacuum (c). Adopted after [208].

where λ is the incident electron's wavelength. As we are only dealing with elastic scattering and transverse momenta are small compared to k_z , E can be given by $E = \hbar^2/2m\lambda^2$. Inserting Equation 2.47 in Equation 2.46 gives the second-order partial differential equation:

$$-\frac{\hbar^2}{2m} \left[\nabla_{xy}^2 + \frac{\partial^2}{\partial z^2} + \frac{4\pi i}{\lambda} \frac{\partial}{\partial z} - \frac{2meV(x, y, z)}{\hbar^2} \right] \psi_f(x, y, z) = 0, \quad (2.48)$$

where the factor $e^{\frac{i2\pi z}{\lambda}}$ has been dropped. Because the electron motion is predominately in the z -direction, changes in ψ will be relatively small. Thus, one can estimate that the second term in Equation 2.48 will be much smaller than the third term, which could be coined a paraxial approximation to the Schrödinger equation:

$$\left| \frac{\partial^2 \psi}{\partial z^2} \right| \ll \left| \frac{1}{\lambda} \frac{\partial \psi}{\partial z} \right|. \quad (2.49)$$

Now, using Equation 2.49 and the abbreviation $\sigma = \frac{2\pi m e \lambda}{\hbar^2}$, a term that describes the interaction between the incident electron and the atom, the Schrödinger Equation 2.46 can be rewritten to be a first-order differential equation,

$$\frac{\partial \psi(x, y, z)}{\partial z} = \left[\frac{i\lambda}{4\pi} \nabla_{x,y}^2 + i\sigma V(x, y, z) \right] \psi(x, y, z). \quad (2.50)$$

For the numerical calculation the specimen is split into multiple thin slices, see Figure 2.17 (a-b). If the initial value is now offset to z and the integration is done over z up to $z + \Delta z$ the following expression can be found,

$$\psi(x, y, z + \Delta z) = \exp \left[\frac{i\lambda}{4\pi} \Delta z \nabla_{x,y}^2 + i\sigma \int_z^{z+\Delta z} V(x, y, z') dz' \right] \psi(x, y, z). \quad (2.51)$$

This can be further simplified by using the Zassenhaus theorem [210],

$$\psi(x, y, z + \Delta z) \approx \exp\left(\frac{i\lambda\Delta z}{4\pi}\nabla_{x,y}^2\right)t(x, y, z)\psi(x, y, z), \quad (2.52)$$

with $t(x, y, z)$ being the transmission function:

$$t(x, y, z) = \exp\left[i\sigma\int_z^{z+\Delta z}V(x, y, z')dz'\right] = \exp[i\sigma\nu_{\Delta z}(x, y, z)], \quad (2.53)$$

where $\nu_{\Delta z}(x, y, z)$ is the projected potential in one slice. The atom potentials are calculated from a relativistic Hartree-Fock calculation for isolated atoms, using Slater type orbitals. The entity $e^{\frac{i\lambda\Delta z}{4\pi}\nabla_{xy}^2}$ can be thought of as,

$$\exp\left(\frac{i\lambda\Delta z}{4\pi}\nabla_{x,y}^2\right) = p(x, y, \Delta z)\otimes, \quad (2.54)$$

with \otimes being a two-dimensional convolution in the (x, y) sample plane and $p(x, y, \Delta z)$ being the real-space propagator function for an z -increment of Δz . The propagator function and its FT now read:

$$\begin{aligned} P(k, \Delta) &= e^{-i\pi\lambda k^2\Delta z} \\ p(x, y, \Delta z) &= FT^{-1}[P(k, \Delta z)] = \frac{1}{i\lambda\Delta z}\exp\left[\frac{1}{i\lambda\Delta z}(x^2 + y^2)\right], \end{aligned} \quad (2.55)$$

which basically resembles *Fresnel* diffraction, describing near-field propagation of a wavefunction for a distance Δz . As shown in Figure 2.17 (b), the thin slab of material is discretized along the beam propagation direction (z -direction) and the resulting slices are labelled $n = 0, 1, 2, 3, \dots, N$ and $z = n\Delta z$. Hence, combining Equations 2.52, 2.53 and 2.54 gives the *multi-slice equation*:

$$\psi_{n+1}(x, y) = p_n(x, y, \Delta z_n) \otimes [t_n(x, y)\psi_n(x, y)]. \quad (2.56)$$

The propagation of a known incident electron wavefunction $\psi_0(x, y)$ can be calculated numerically by applying the convolution theorem to the multi-slice Equation 2.56,

$$\psi_{n+1}(x, y) = FT^{-1}\{P_n(k_x, k_y, \Delta z_n) \cdot FT[t_n(x, y)\psi_n(x, y)]\}. \quad (2.57)$$

The propagation of the electron wavefunction now takes place by successive steps of transmission through a slice (by multiplying the transmission function $t(x, y)$ with the wavefunction $\psi(x, y)$) and vacuum propagation, as illustrated in Figure 2.17 (c). As input-data the initial wavefunction $\psi_0(x, y)$, the atom positions in each slice and imaging conditions like spherical aberrations C_s and defocus Δf have to be defined. Lens aberrations and defocus are taken into account by applying the contrast transfer function $\chi(\mathbf{k})$,

$$\chi(\mathbf{k}) = \frac{2\pi}{\lambda}\left[\frac{1}{4}C_s\lambda^4\mathbf{k}^4 - \frac{1}{2}\Delta f\lambda^2\mathbf{k}^2\right], \quad (2.58)$$

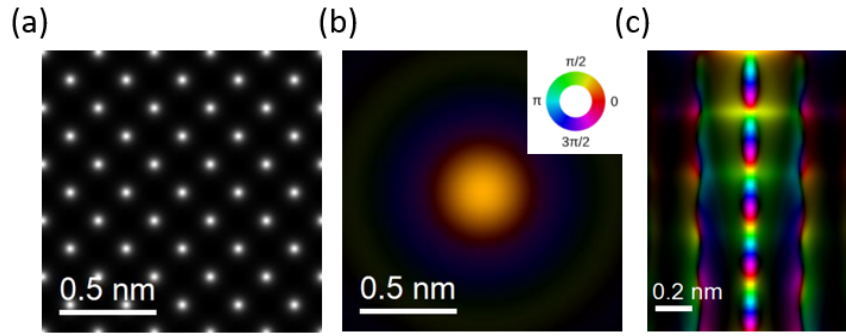


Figure 2.18: An example for a MS simulation result of 50 nm bcc-Fe in [001] zone-axis orientation with (a) showing the atomic potentials, (b) the incident complex wavefunction with an inset showing how the Hue colour relates to the electron waves' phase and (c) a cross-section of the simulated beam propagation through the crystal (Gamma-adopted).

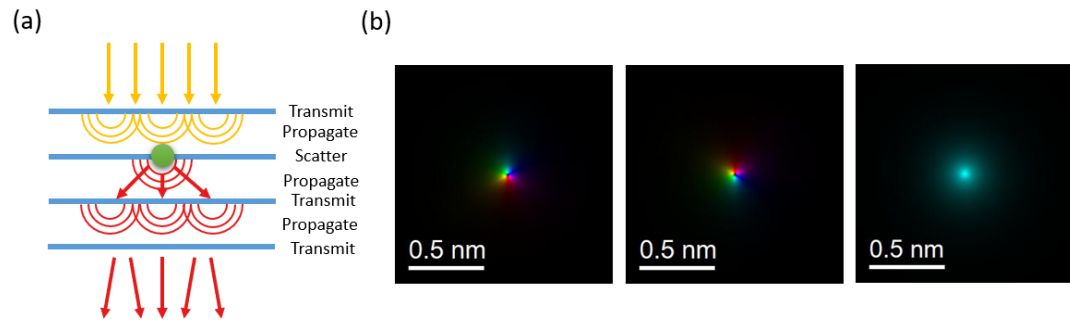


Figure 2.19: (a) Principle of the implementation of inelastic scattering in the MS code. (b) Depicts the three components of the inelastic scattering kernels for the $\text{Fe}L_3$ -edge.

to the calculated outgoing wavefunction $\psi_N(x, y)$. A typical example of the projected atomic potentials, an incident focused beam and the resulting simulation result of a bcc-Fe crystal cross-section, respectively, using the in-house MS code IXCHEL, are presented in Figure 2.18. IXCHEL combines the MS approach with inelastic scattering, using the density matrix formalism and the MDFE established in a series of works, see [211–213]. It is thus capable of simulating energy-filtered diffraction patterns as well as HRTEM images. In principle, for a single atom at position $z = d$ in the crystal or generally in the sample slab (green dot in Figure 2.19a), this is done by propagating the incoming wavefunction $\psi_0(x, y)$ to the thickness d , using the MS approach described above, see Figure 2.19 (a). Then an inelastic scattering kernel, containing the FT of the mixed dynamic object spectrum (MDOS) see Figure 2.19 (b), is applied to the wavefunction at depth $z = d$. This process splits the electron wave into an incoherent sum of three components, which are separately propagated

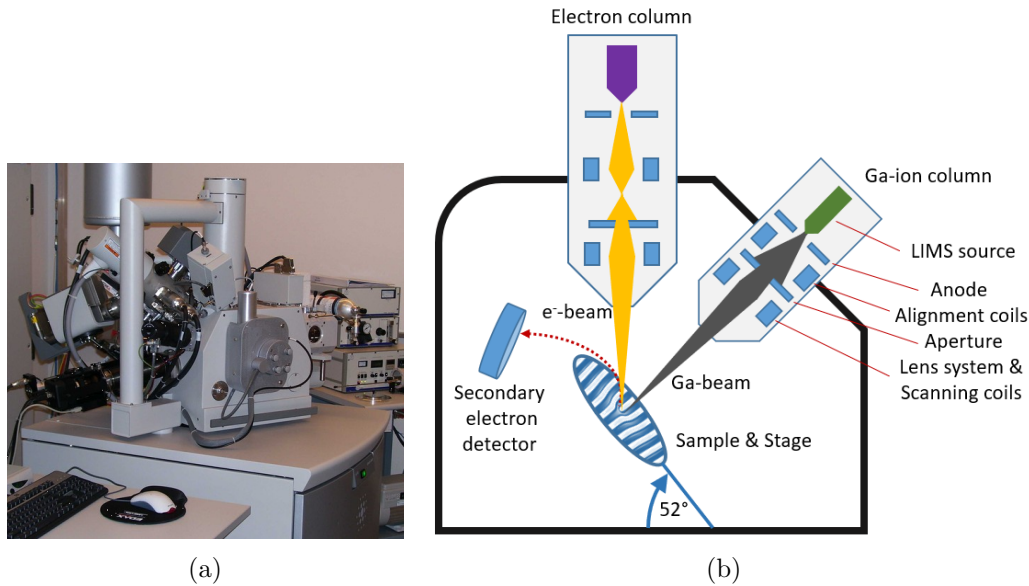


Figure 2.20: The dual beam instrument: (a) Image of the dual beam device located at the TU Wien University Service Centre for Transmission Electron Microscopy (USTEM) (FEI Quanta 200 3D) and (b) schematics of such a dual beam device.

to the exit surface of the specimen, only subject to elastic scattering. Finally, the intensities of *all atom positions* in *all slices* from $z = 0$ to $z = t$ are summed up to yield the energy-filtered image in the detector plane. Mind, that in STEM only such atoms that are hit by a significant amount of intensity are included in the calculation, reducing the computational effort.

2.8 The Dual Beam Machine and Focused-Ion-Beam Milling

This section is based on the review article [214–216].

In 1937 *Manfred von Ardenne* invented the SEM where a focused electron beam is raster-scanned over the sample. In contrast to the TEM it took nearly thirty years for the first commercial SEM to enter the stage. But soon after, FIBs or when combined with an electron column, dual-beam machines, exemplified in Figure 2.20 (a), have been introduced in the semi-conductor industry for fault diagnostic purposes. Nowadays, FIB milling evolved to a mature micro-machining or nano-device prototyping technique, capable of producing, e.g., 100 μm *Fresnel* zone plates with 100 nm outermost zones width, using high-accuracy drift correction [217], few nanometre-sized features of plasmonic bow-tie antennae and complex three dimensional structures by using predictive patterning strategies [218].

Figure 2.20 (b) shows a schematic overview of a FIB/dual beam system. In prin-

2 Fundamentals

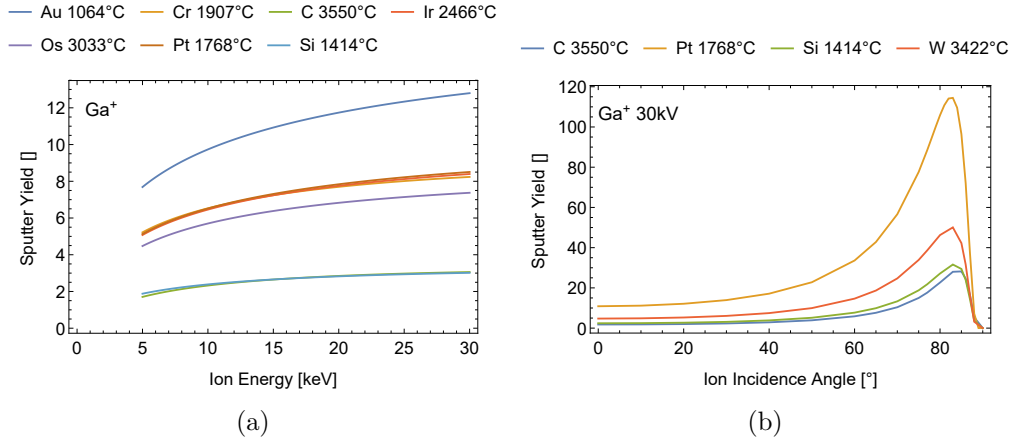


Figure 2.21: Sputter yield dependencies for Ga. (a) Calculated sputter yields for different Ga-ion energies and different target materials using a calculator [220], based on [221]. Above a certain sputtering threshold energy the sputtering yield increases for higher incident ion energies and is strongly depending on the target material, an inverse relation to the materials melting point is apparent (see the values next to the element symbol). (b) Calculated sputter yield dependence on the incident angle (0° represent normal incidence), based on an empirical formula [222]. The grazing incidence of the ions massively enhances the sputter yield.

inciple a FIB is comparable to a STEM, but instead of electrons an ion-beam is sent through a beam-forming column and raster-scanned over the sample, where it removes material from a nanoscale region. Ions deposit orders of magnitude more energy in the sample, compared to electrons, which is reflected in the achievable sputter rate or sputter yield Y defined by:

$$Y = \frac{\langle n \rangle}{n^+}, \quad (2.59)$$

with n^+ being the mean number of ions incident on the target and $\langle n \rangle$ being the mean number of atoms that are removed from the surface under the ion bombardment. E.g., 60 keV electrons have a sputter yield of the order of $Y_e \approx 1 \times 10^{-9}$ for carbon atoms in graphene [219], while typical sputter yields for Ga-ions are of the order of 2 to 12. The sputter yield depends on many parameters like the energy of the incident ion, ion mass, atomic mass of the target, see Figure 2.21 (a), and the crystallinity of the sample. With increasing ion-energy (at least for the ion-energies used in typical FIB systems) and angle of incidence the sputter yield raises, see Figure 2.21 (a, b). Notably, each material has a certain threshold energy, below which no sputtering occurs, which is typically in the range of 10 eV to 30 eV. FIB milling results are strongly influenced by the sputter yield, e.g., uneven surfaces change the angle of incidence to the Ga-ions and thus, with a changing sputter yield ($\cos^{-2}(\varphi)$), irregularities, ripples, etc. are produced in the hologram. Additionally the crystallinity

and, thus, ion channelling reduce the sputter yield, which would also destroy the homogeneous thickness of the milled structure.

Typically, Ga-ions are used, but a multitude of other materials have been shown to work as well. As a source of Ga-ions, a liquid metal ion source (LMIS) is used, which consists of a reservoir of liquid Ga, heated to its melting point at 29.8 °C. A sharp tungsten needle is placed in the centre of a reservoir of liquefied Ga. The Ga flows to the apex of the needle and forms a sharp meniscus, where Ga-atoms are ionized and extracted by applying a high electric field to the needle apex. The Ga-ion current is set by blocking apertures in the range 1 nA to 20 nA. A sample (the HVM) is placed on a five-axis stage and typically moved to the coincidence point where the electron beam, coming from the vertical electron column, intersects with the ion-beam. Because the ion column is tilted by 52° with respect to the horizontal axis, the sample has to be tilted to that angle for milling. Simultaneously an e-beam image can be acquired. Typically, a dual beam machine is also equipped with a gas injection system (with gas pre-cursors for W, Pt and C) to produce protective layers on the region of interest on a sample by using electron beam-induced deposition (not drawn in Figure 2.20 (b)). Additionally, an Omniprobe device, which is basically a very sharp needle that can be moved with nanometre precision to manipulate and lift out FIB lamellae, is mounted on a dual beam device (not drawn in Figure 2.20 (b)).

The achievable spot sizes (FWHM) in FIB machines range from ~430 nm, for high beam currents of 20 nA, to ~7 nm at 1 pA and even less for state-of-the-art machines. As the energy- and angular-spread of the LMIS are much higher than that of field emission sources, and the chromatic- and spherical aberrations of electrostatic lenses are also higher than that of magnetic ones, the achievable spot sizes will always be larger than that of electron-optical systems. Generally the beam current distribution follows a *Gaussian* profile, but has larger tails than electron beams, because of the high energy spread in a Ga LMIS (≈ 15 eV) [223]. Typically a serpentine raster-scan strategy is employed to remove material where the distance between each successive scan point, also called pitch, is ideally half the spot size or even less. On each scan point the beam is parked for a certain amount of time, the dwell time, ranging from a few hundred nanoseconds, for fast imaging purposes, to a few microseconds, for standard material removal recipes, up to milliseconds. Due to redeposition effects the dwell time cannot be chosen arbitrarily high, meaning, that the ion dose has to be distributed during multiple passes over the same scan area.

The secondary electrons (SE), emitted by the sample upon impinging Ga-ions, are collected by an Everhart-Thornley detector. This kind of detector consists of a Faraday cage where a low positive voltage (300 V) is applied, in order to attract the rather low energy (≤ 50 V) SE. Behind the Faraday cage the electrons are accelerated towards a scintillator by applying a high positive voltage of the order of 12 kV to the scintillator. The imping electrons on the scintillator produce photons that are sent through a light guide to a photomultiplier tube for amplification and signal conversion. As the Ga-ion stopping power is one to two orders higher than that of electrons, their penetration depth in materials is much lower than for electrons of

the same incident energy, resulting in a more confined SE yield region. Electrons have their SE yield maximum at approximately 1 kV, whereas for Ga-ions it lies at much higher energies, leading to a very different imaging contrast in SIM images. As opposed to SEM images, light elements appear bright and high-Z materials appear dark in SIM images, and the channelling contrast is enhanced.

2.9 Thin Film Production

Production of HVM, as described in Section 2.4.4, is to a great extent depending on the ability to produce dense membranes, that are intransparent to electrons, ideally electron-absorbing or -blocking, but in reality high-angle scattering is the primary electron ‘route’, but at the same time have to be sufficiently thin for the FIB following processing step, where in a reasonable period of time fine features of nanoscale size shall be milled. In addition, these membranes should show a high electrical conductivity, in order to avoid charging, show a relatively fine-grain-size for a homogenous sputter yield and the resolution of fine details and, as will be shown later, should be low in inner stresses.

Nowadays there is a whole zoo of methods available, in order to produce thin films that could, in principle, be used for that purpose. Ranging from chemical vapour deposition (CVD), and physical vapour deposition (PVD) techniques, like evaporation, ion-plating and pulsed deposition layer (PLD). Given its availability at USTEM, the physical vapour deposition method, direct current (DC)-magnetron sputtering, is the method of choice and, thus, will be described in the following. Closely related to a successful deposition of a thin film are the cleanliness and high-vacuum capabilities of the deposition system, hence, this section will also contain a little introduction to vacuum physics and technology. Last but not least, the thin film characterisation techniques used, will be described.

2.9.1 Magnetron Sputtering

Based on [224–226] and the review article [227].

In 1852 *Grove* made an, at that time probably rather inconspicuous, observation, one of that kind, where its importance and significance for our everyday life is only revealed after decades. When operating a glow discharge system, the walls, made out of glass, turned opaque after some time of operation. An analysis of the material, that was built up on the inner glass tube walls, showed that it was the same material as the cathode was made of. This was kind of the starting point of physical thin film deposition by sputtering. A method that is nowadays widely used for the production of semiconductors, CCDs, hard disks, displays, ultra-hard coatings, anti-reflex coatings, catalysts and solar cells, to name only a few. This multitude of applications is a direct result of the benefits of this method, like its low deposition temperature, high deposition rates, superior thin film properties and a large range of commercially available sputtering devices. Magnetron sputtered thin films typically show the same

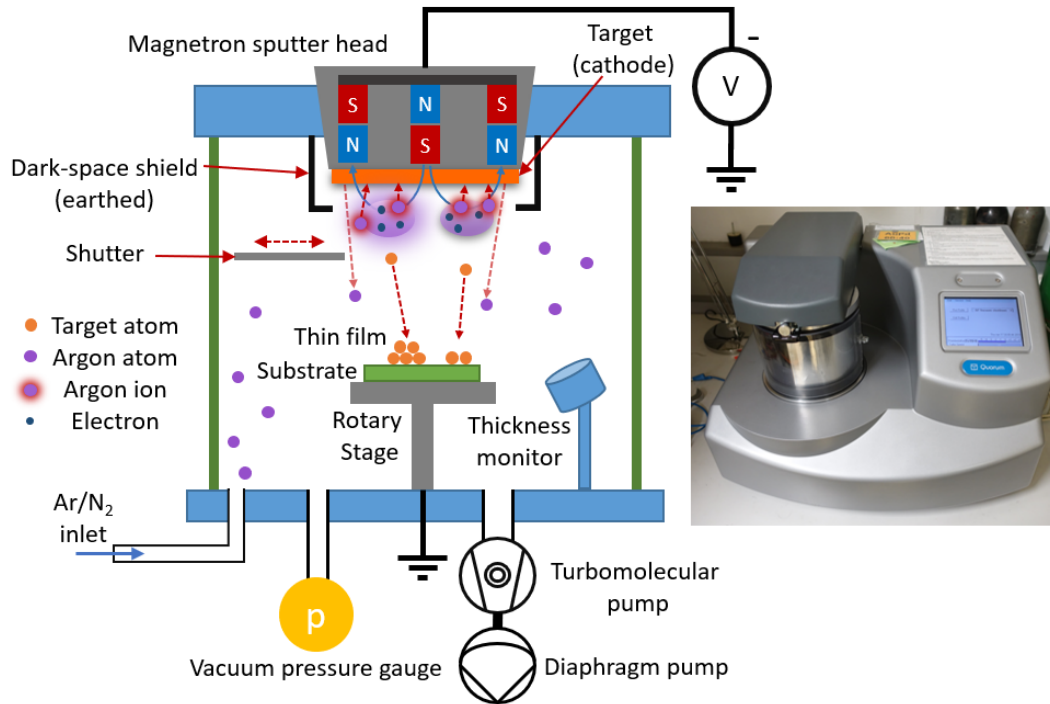


Figure 2.22: Principle of the magnetron sputtering thin film deposition method and the schematic apparatus together with an image of the Q150T (Quorum Technologies) sputter coater. For the description see the text.

chemical composition as the target, are well adhered to the substrate and show interesting properties, e.g., giant magneto-resistance [228]. The thin film deposition process can be split up in material vaporization at the target material, its transport to the substrate and the final adsorption and growth on the same. Due to the separation of these processes, magnetron sputtering allows a wide and convenient control of the thin film properties by varying the process parameters, like sputter power density, the working gas pressure p_{Ar} , the base pressure p_B , working distance or sputter working distance (SWD), substrate orientation, rotation, temperature and biasing.

A schematic description of the working principle of DC-magnetron sputtering is given in Figure 2.22. There, it can be seen that a process vacuum chamber is evacuated using a TMP and a diaphragm pre-vacuum pump to the desired base-/working pressure p_B in the range from $\sim 1 \times 10^{-4}$ mbar to $\sim 5 \times 10^{-7}$ mbar, which is monitored using a vacuum sensor (a combined Pirani/cold-cathode cell) (yellow). The working gas (Ar) is introduced to the chamber and a negative high voltage, ranging from 280 V to 600 V, is applied to the target material (orange). The high electric field between the anode (Stage and dark-space shield) and the cathode ionizes the Ar-gas atoms. A magnetic field in front of the target is produced by magnets placed in the magnetron sputter head directly behind the target. Due to the *Lorentz-force*, Equation 2.2, the electrons are forced on spiral paths around the magnetic field lines (cyclotron mo-

2 Fundamentals

tion), increasing their collision probability with Ar atoms. The degree of ionization is typically 1% to 10% in magnetron devices, which is ten to hundred times higher compared to non-magnetron sputtering devices. Thus, the ignited plasma can be sustained at very low Ar pressures p_{Ar} , typically in the range 0.1 Pa to 5 Pa, and still provides a high amount of Ar-ions, which are accelerated towards the target by the electric field, leading to Ar-ion energies up to 600 eV. Due to their low velocity, the magnetic field acts mainly on the electrons not on the Ar-ions. Ar-ions hit the target and induce a linear collision cascade that ejects a certain number of target atoms per incident ion. Comparable to the sputter yield of Ga-ions in FIB milling, the sputter yield of Ar-ions shows dependencies on target species, ion-energy, see Figure 2.23, incident angle and crystallinity. Typically it ranges from 0.5 to 4 and its practical consequence is, that deposition rates drastically drop for high melting point materials. The energy distribution of the emitted target atoms follows a Sigmund-Thomson distribution and peaks at half the surface binding energy of the sputtered material, which is in most cases anywhere between 1 eV to 4 eV [229]²². Due to this relatively inefficient energy transfer, the target is heating up and water cooling is sometimes necessary/included in the sputter head. The neutral ejected target atoms fly towards the substrate (green), which is placed directly beyond the target in a certain distance, the WD. A shutter placed between target and substrate can be used to pre-sputter the target, in order to remove contamination and oxide layers from it, without affecting the sample. Depending on the actual Ar-gas pressure, the target atoms collide with the working gas atoms and lose some or most of their kinetic energy before they reach the substrate, depending on the working gas pressure. There, they are adsorbed to the surface and rapidly transfer their thermal energy to the substrate lattice, with cooling rates as high as $1 \times 10^7 \text{ K s}^{-1}$ for very high deposition rates of 50 nm s^{-1} and low working gas pressures, yielding highly amorphous metal layers. For complex surface structures, often seen in EM samples, there is a rotary stage to enhance the substrate-/sample coverage and uniformity. Furthermore, upon movement of the substrate, relative to the target, the morphology, structure, hardness, grain-size, internal stresses, reflectivity and electrical properties of a thin film can change [231–234]. The thin film thickness is monitored using a quartz-based film thickness monitor (FTM).

The thin film structure properties, like density, grain-size and shape are crucially determined by the kinetic energy and angular distribution of the incident target atoms, as well as their mobility on the substrate. *Thornton* mapped those parameters onto the working gas pressure p_{Ar} and the ratio between the deposition temperature and the melting point of the deposited material $\frac{T}{T_M}$ and condensed his findings in an instructive drawing, see Figure 2.24 [235, 236]. This structure zone model shows four different regions. For low kinetic energies of the target atoms and low mobility at the substrate, which is equivalent to low working gas pressures and low substrate

²²Note that a few percent of the high energy Ar-ions can be neutralised at the target and be reflected towards the sample with relatively high kinetic energy [230]. Those reflected Ar neutrals may cause changes in the thin film's structure.

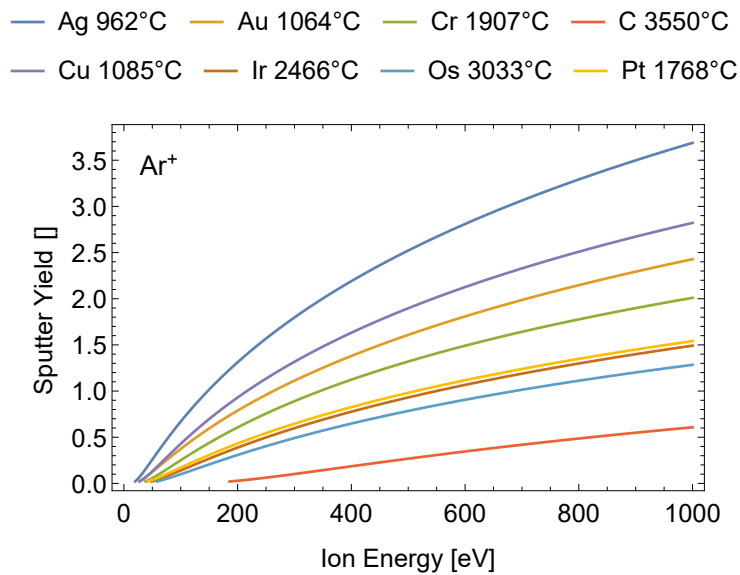


Figure 2.23: Calculated sputter yields for different Ar-ion energies and different target materials, using a calculator [220] based on [221]. Above a certain sputtering threshold energy the sputtering yield increases for higher incident ion energies and is strongly depending on the target material, an inverse relation to the materials melting point is apparent (see the values next to the element symbol).

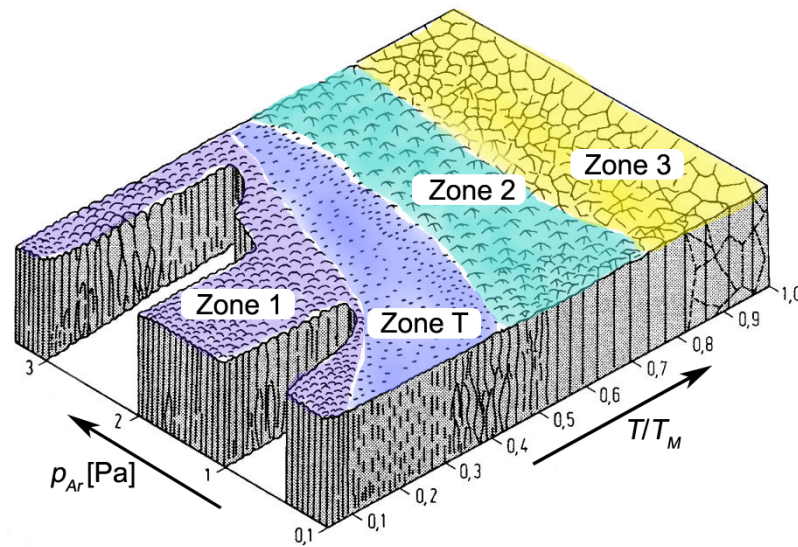


Figure 2.24: Structure-zone model of *Thornton*, showing the influence of the working gas pressure and the deposition temperature on the structural characteristics of a thin film. Figure adopted from [224]. Inner stresses in the violet zone are predominantly tensile, while in the blue zone there are compressive stresses and in the yellow and turquoise zones both stress states can in principle be possible.

Table 2.2: Summary of the structure zone model according to *Thornton*.

Zone	T/T _m	Mechanism	Characteristics	Inner Stress State
1	<0.2	Shadowing	Fibres, porous	Tensile
T	<0.4	Particle energy	Nano-grains	Compressive
2	>0.8	Surface diffusion	Columnar grains	Variable
3	>0.8	Volume diffusion	3D-grains	Variable

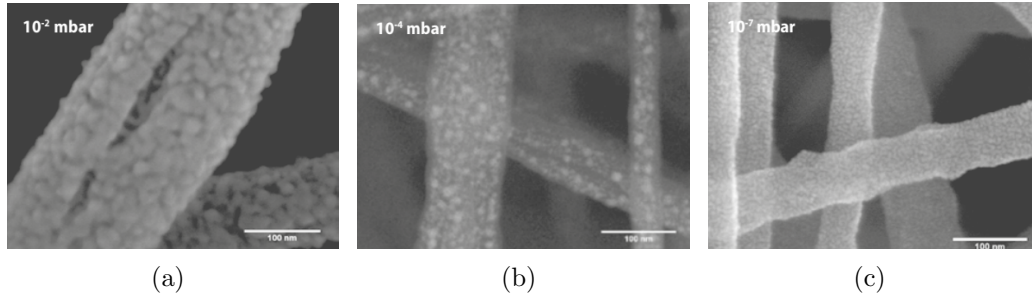


Figure 2.25: Illustrating the influence of the base pressure before sputtering on the thin film morphology. A 2 nm film of Au was deposited on electrospinning fibres, using the same sputter coater model as is present at USTEM, at a current of 20 mA and a working gas pressure of 1 Pa. See (a) for a base pressure of 1×10^{-2} mbar, (b) for a base pressure of 1×10^{-4} mbar and (c) for a base pressure of $\sim 1 \times 10^{-7}$ mbar. Better base pressure clearly improves the thin film grain-size. The scale bar is 100 nm. Taken from [237].

temperatures, the thin film structure is porous and spongy, consisting of fibres and voids. Inner stresses, apparent in this regime, are tensile. In the second zone, zone T (for transition), the structure completely changes. As a result of the higher kinetic energies and atom mobilities, a dense fine- or even nano-crystalline packing occurs. The target atoms are literally peened into the lattice (atomic peening), occupying interstitial lattice sites and, with that, causing compressive inner stresses. For even higher temperatures surface- and volume-diffusion is predominant, leading to the formation columnar grains in zone 2 and even large 3D-grains in zone 3, with varying inner stress states, depending on, e.g., a lattice misfit between the substrate and the target atoms and grain growth. Table 2.2 summarizes the different growth regimes shown in the structure zone model from *Thornton*. Note that for a certain T/T_M ratio, going from zone 1 to zone T, there is a distinct working pressure (kinetic energy and angular distribution), where the inner stress state of the thin film vanishes. This working gas pressure is called *critical pressure*. *Thornton* found a linear relation between critical pressure and target density [235].

The residual gases in the deposition chamber, like oxygen, hydrogen, nitrogen and carbon monoxide (O_2 , CO , H_2O , H_2 and N_2), or in other words the base pressure

before the actual sputtering process is started, can also have significant influences on the thin film morphology, inner stresses and resistivity [238, 239], see Figure 2.25.

Due to the variety of sputtering parameters, it is not trivial to figure out a working combination, but this complexity also bears the opportunity to tune the characteristics of the thin film to the desired needs. In this work, it is sought for highest possible density, in order to absorb electrons, even at relatively moderate film thickness, a good adhesion to the SiNx membranes and a fine-grain-size. Additionally, the influence of the internal stress state on the FIB milling will be investigated.

2.9.2 Vacuum Technology

As the thin film purity and, thus, its density as well as its inner stress state are crucially determined by the base pressure of the deposition system, this section includes a bit of basic and background information on the topic.

The mean free path of an energetic gas particle, being the mean distance between collision events, is a fundamental property in vacuum physics and is, thus, also used to structure the section. It can be given by:

$$\lambda(n, r) = \frac{1}{n\sigma} = \frac{1}{4\pi nr^2}, \quad (2.60)$$

with n, σ, r being the particle density, the collision cross-section and particle radius, respectively. Using the basic thermodynamic equation $p \cdot V = N \cdot k_B \cdot T$ and $\frac{N}{V} = n = \frac{p}{k_B \cdot T}$, where p is the gas pressure, N the number of particles, k_B the Boltzmann constant and T the absolute temperature, Equation 2.60 can be written as:

$$\lambda(p, T, r) = \frac{k_B \cdot T}{4\pi pr^2}. \quad (2.61)$$

For typical atomic radii of the scale of 1.5 \AA and under room temperature, $\lambda \cdot p = 5 \text{ mmPa}$ can be given as a rule of thumb for the mean free path. Table 2.3 gives the mean free paths for 1 Pa to $1 \times 10^{-7} \text{ Pa}$. With the definition of the mean free path λ and the diameter of the vacuum vessel or tubing d , three distinct gas flow regimes can be defined, according to the ratio $Kn = \lambda/d$. Kn is called Knudsen number and for $Kn < 0.01$, the *laminar flow* regime is present. Here, collisions between gas particles are dominant, the mean free path is much smaller than the tubing diameter. Diaphragm pumps are typically used in this low vacuum regime for pumping down to $\sim 1 \text{ mbar}$. A *Knudsen flow* is given for $0.01 < Kn < 0.5$, which is kind of a transition region between the laminar and molecular flow region. Here, most commonly, a rotary vane pump or scroll-pump is used to reach medium vacuum pressures, down to $\sim 1 \times 10^{-3} \text{ mbar}$. Typically gas type dependant Pirani measurement cells or gas type independent capacitance manometers are used for the vacuum measurement in this regime. When the mean free path gets significantly higher than the vacuum chamber dimensions, i.e. $Kn > 0.5$, collisions between gas particles are much less probable than those with the chamber walls, and the notion of *molecular flow* is justified. The molecular flow regime is reached at pressures below

Table 2.3: Influence of the background gas pressure on monolayer formation times. The arrival ratio compares the number of film particles hitting the surface to the number of residual gas atoms/molecules, at a given deposition rate of 1 nm s^{-1} .

p		Z(p, T, m) [$\text{cm}^{-2}\text{s}^{-1}$]	Time [s]	ML/s [s^{-1}]	λ [cm]	Arrival ratio []
[mbar, Torr]	[Pa]					
10^{-2}	1	2.7×10^{18}	0.0004	2700	1.5	10^{-3}
10^{-3}	10^{-1}	2.7×10^{17}	0.004	270	15	10^{-2}
10^{-4}	10^{-2}	2.7×10^{16}	0.04	27	150	0.1
10^{-5}	10^{-3}	2.7×10^{15}	0.4	2.7	1.5×10^3	1
10^{-6}	10^{-4}	2.7×10^{14}	4	0.27	1.5×10^4	10
10^{-7}	10^{-5}	2.7×10^{13}	40	0.027	1.5×10^5	100
10^{-8}	10^{-6}	2.7×10^{12}	400	0.0027	1.5×10^6	10^3
10^{-9}	10^{-7}	2.7×10^{11}	4000	0.00027	1.5×10^7	10^4

$\sim 1 \times 10^{-3}$ mbar. This high vacuum regime can be reached using TMP, oil-diffusion or cryogenic vacuum pumps. Down to 1×10^{-8} mbar, vacuum measurement is done by using cold cathode-penning cells, which are gas dependent, due to their working principle, based on gas ionization.

When dealing with thin film purity the areal impingement rate $Z(p, T, m)$, that is the number of gas atoms or molecules hitting a surface inside the vacuum system per second, is of utmost importance. It can be given by [224]:

$$Z = Z(p, T, m) = \frac{p}{m} \sqrt{\frac{m}{2\pi k_B T}}, \quad (2.62)$$

with m being the mass per atom or molecule of the gas species of interest, p the base pressure, T the substrate temperature and k_B the Boltzmann constant. Using Equation 2.62, it is possible to estimate the time, needed to form a complete monolayer of oxygen on the sample surface. For example, at a base pressure of 1×10^{-3} mbar, it takes only ~ 4 ms to form a monolayer of oxygen, leading to 270 ML/s, see Table 2.3. In this case a sticking ratio of one was assumed. The sticking ratio is defined as $\alpha_{stick} = 1 - \frac{Z_{Des}}{Z}$, with Z_{Des} being the atom-/molecule desorption rate. It is an indicator of how much particles adhere to a surface after impingement. For highly reactive gases, like O_2 or H_2O , it is approximately one, whereas it is much less for inert gases, like He, Ar or N_2 .

In Table 2.3 the arrival ratio of deposited atoms, incident with a rate of 3 ML/s, relative to the oxygen molecules' areal impingement rate, is calculated, using:

$$\frac{Z_x}{Z_{\text{O}_2}} = R_x \frac{m_{\text{O}_2}}{p} \sqrt{\frac{2\pi k_B T}{m_{\text{O}_2}}}, \quad (2.63)$$

with R_x representing the deposition rate. For a base pressure of 1×10^{-5} mbar,

Table 2.4: Gas desorption rates q_{Des} for different materials, taken from [241, 242].

Material	Surface	Surface treatment	Desorption rate @ 1 h [$\frac{\text{mbar}\cdot\text{l}}{\text{s}\cdot\text{cm}^2}$]
Stainless steel	shining	cleaned	2.7×10^{-7}
Stainless steel	polished	cleaned	2.0×10^{-8}
Stainless steel	pickled	1 h bake-out	1.4×10^{-9}
Al		cleaned	6.0×10^{-8}
Cu		cleaned	3.5×10^{-7}
Glass		cleaned	4.5×10^{-9}
FPM			1.2×10^{-6}
FPM		4 h bake-out at 100 °C	1.2×10^{-7}

there is one oxygen molecule for each and every deposited target atom, underlining the importance of decent vacuum conditions during thin film deposition.

In order to reach high-vacuum conditions – as a means for high-purity thin film deposition – the sum of all gas load sources Q :

$$Q = Q_{Leak} + Q_{Des}(t) + Q_{Perm}, \quad (2.64)$$

has to be minimized [240]. Q_{Leak} represents the leakage into the vacuum chamber, $Q_{Des}(t) = q_{Des} A f(t)$ stands for the out-gassing/desorption of water and spurious gasses, like CO, from vacuum chamber surfaces and Q_{Perm} is the gas permeation through the chamber walls. The gas load rates are commonly given in $\frac{\text{mbar}\cdot\text{l}}{\text{s}}$ ($10 \text{ Pa}\cdot\text{m}^3 \text{ s}^{-1}$). q_{Des} is the desorption rate and A represents the surface area, while $f(t)$ is the temporal evolution of the gas desorption.

In high-vacuum systems the gas load Q is typically balanced by a TMP. Assuming a typical pumping speed of a TMP of 50 l s^{-1} , a descent high-vacuum can only be achieved, if the leakage rate into the vacuum system is lower than $5 \times 10^{-5} \text{ mbar l s}^{-1}$. Interestingly, at a leakage rate of $1 \times 10^{-7} \text{ mbar l s}^{-1}$, the total area of all leaks is equivalent to a hole of only $\text{Ø}3 \mu\text{m}$ [241]. The detection of such rather low leakage rates is carried out by using TMP based leakage testing devices connected to the vacuum chamber and a He tracer gas, which is sprayed over the chamber.

Given, that the leakage rate of a vacuum system is sufficiently low, desorption characteristics of the vacuum system and possible gas permeation crucially determine the pump-down behaviour. There are a few sources of out-gassing/desorption like the vaporisation of the vacuum chamber material itself, desorption of water and other spurious gases, diffusion and also permeation. Table 2.4 lists gas desorption rates q_{Des} of typical materials in vacuum technology. It is evident from Table 2.4 that the material choice and even the surface treatment can significantly alter the vacuum performance of a system. Polished and compacted metal surfaces as well as glass show two to three orders of magnitude lower out-gassing rates than common fluoro-elastomer materials (FPM), used as rubber sealing. Therefore, rubber and other

Table 2.5: Gas permeation values for different gases and typical tubing materials at or around room temperature, taken from [241–243].

Material	Gas	Gas Permeation [$\frac{\text{mbar l}}{\text{s}} \frac{\text{mm}}{\text{m}^2 \text{bar}}$]
Silicone	CO ₂	1.5
	H ₂	0.5
	O ₂	0.6
	N ₂	0.2
Tygon E Lab	CO ₂	2.7×10^{-2}
	H ₂	7.3×10^{-3}
	O ₂	6.0×10^{-3}
	N ₂	3.0×10^{-3}
C-Flex Ultra	CO ₂	1.6×10^{-4}
	O ₂	8.3×10^{-5}
	N ₂	2.6×10^{-4}
FKM/Viton	CO ₂	6×10^{-3}
	H ₂	3.5×10^{-3}
	Air	5×10^{-3}
Pyrex Glas	H ₂	5×10^{-9}
Steel	H ₂	1×10^{-6}
	N ₂	2×10^{-15}
Copper	H ₂	1×10^{-11}

materials, showing high out-gassing rates, should only be used rarely and if so, their surface area should be kept low, because the gas load, stemming from out-gassing, scales with the surface area. Additional bake-out cycles can further reduce the out-gassing rate by an order of magnitude. Note that the temporal evolution of $Q_{Des}(t)$ is markedly different for plastic materials, compared to metals or glass. This will be covered in Section 3.1.2.

The gas permeation gas load Q_{perm} can be calculated by:

$$Q_{Perm} = q_{Perm} A \frac{\Delta p}{d}, \quad (2.65)$$

with q_{Perm} and A being the gas permeation rate of a material and its surface area, respectively. $\Delta p = (p_{outside} - p_{inside})$ represents the pressure drop along the wall thickness d . It is clear from Equation 2.65 that the vacuum system containers and tubing should be constructed under use of high wall thicknesses and low surface areas. Table 2.5 lists some permeation rates q_{Perm} of typically used materials in vacuum technology. From Table 2.5 the strong influence of the chosen wall or tubing material is evident. For example, the permeation rates of silicone and steel for N₂ differ by 14 orders of magnitude. Thus, the material choice in the vacuum system components is highly relevant.

2.9.3 Thin Film Characterisation Techniques

In the following section those methods, relevant for the characterisation of thin metal films, used for the production of HVMS, will be presented. As an example, the thin film thickness and its density crucially determine the electron absorption and electron scattering behaviour, as well as the FIB milling results.

One may argue that there is no explicit need for an additional thickness characterisation, as there is already an online thin film thickness measurement device included in the QT150 sputter coater: the FTM. However, an FTM is an oscillating Quartz-crystal-based indirect thickness measurement device, that only yields reliable thickness and sputter rate results, if it is properly calibrated. It crucially relies on the correct placement height of the sample and the knowledge of the thin film density. Parameters, that are either unknown in the first place or are subject to changes when testing different sputter deposition conditions.

Thin film purity or density could also be measured, e.g., using EDX in a SEM, but, as the electrical conductivity measurement station represents a fast, inexpensive and readily available alternative, this one was used here.

The inner stress measurement station built in the course of the thesis will be described in Chapter 3.

The following subsections are mainly based on [224].

Thickness Measurement Using a Stylus Profilometer

There are multiple direct and indirect methods to measure thin film thicknesses. Direct thickness measurements can be separated into invasive and non-invasive methods, e.g., using a stylus based contact profilometer, is an invasive technique. There, a sharp diamond or sapphire stylus is moved laterally over the thin film surface, and its vertical motion, due to surface roughness, curvature and steps, is fed to the read-out electronics via inductive coupling, quite similar to the principle of a vinyl record player. This method relies on the stability and hardness of the thin film as the sharp stylus would otherwise sink into it, underestimating the given thickness. As the materials used in this thesis are Os, Cr, Ir and Pt, this condition is definitely fulfilled. The stylus profilometer method is the oldest and most widespread surface topography characterisation method. More sophisticated contact or pseudo-contact methods are atomic force microscopy or scanning tunneling microscopy.

Non-invasive thickness measurements can be carried out by optical non-contact profilometers employing, e.g., digital holographic microscopy [244], or relatively straightforward, using light- or electron-optical observation in the SEM. In the case of electron-optical investigations (especially in the TEM) a cross-section preparation of the sample is necessary, so this would be a very powerful direct but invasive thickness measurement method. Non-invasive optical thickness measurements are nowadays able to sample two-dimensional thickness changes in-situ, with frame rates of the order of 1000 frames per second. Indirect thickness measurement methods, like measuring the resistance or capacity of deposited thin films, yields thicknesses of

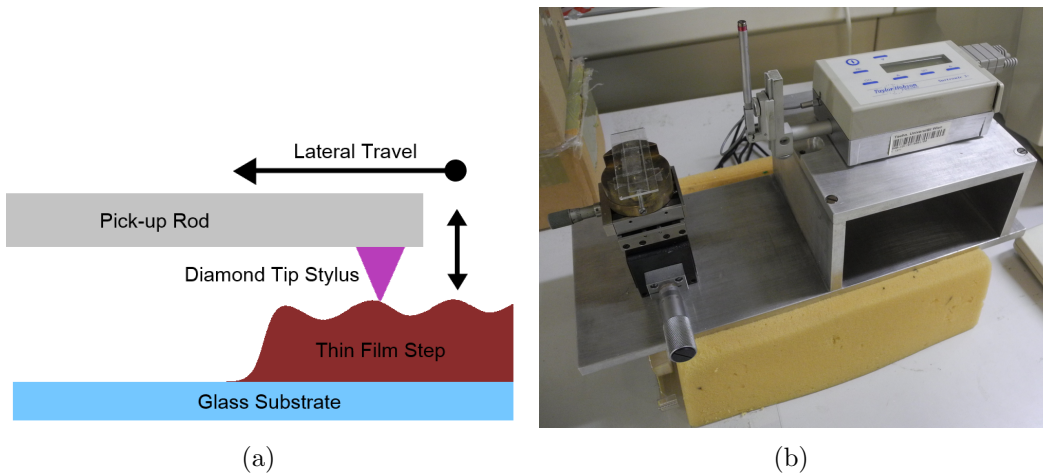


Figure 2.26: (a) Schematics of a stylus profilometer which employs a electromechanically coupled sharp diamond stylus to scan across a sharp step in the thin film in order to measure its thickness. (b) Image showing the thin film stylus profilometer from Taylor Hobson Surtronic 3+ that was used to determine thin film thicknesses greater than ~ 50 nm.

conductive and isolating thin films, respectively. For non-iron materials, paints and plastics on ferritic steel substrates, one can measure the holding force of a magnet, placed onto the thin film, and by that deduce its thickness. For non-iron substrates the formation of eddy currents can be used to derive thickness information. The FTM method belongs to the very powerful and widespread micro-balancing thickness determination techniques, it can be used to monitor the thin film thickness in-situ by observing the resonance frequency change in the Quartz crystal upon deposition of the thin film material on its surface.

Coming back to the stylus profilometer, there, all critical dimensions as step (height), curvature, flatness and surface roughness are computed from the surface topography, which is recorded upon pulling the stylus over the surface, see Figure 2.26 (a). Its lateral resolution is limited by the diamond tip radius, which can be of the order of 20 nm to 50 μm . In the vertical direction the measurement range for state-of-the-art devices under ideal conditions is 5 nm to 5 mm with sub-nm resolution. Here, the minimal film thickness, that can be reasonably resolved is roughly 50 nm. For a successful thickness determination, it is of utmost importance to have a sharp onset or step of the thin film on a flat substrate, as depicted in Figure 2.26 (a). To achieve this, microscopy glass slides (Thickness: ~ 100 μm , $\text{Ø}18$ mm) were not only used as a (very flat) substrate for the thin film deposition, but also as a partial cover of the substrate, leading to half-moon-like structures with a very defined step.

A typical measurement routine consists of the following steps:

- Set the lateral travel to 5 mm to 10 mm and the height resolution according to the expected thin film thickness.

2 Fundamentals

- Then load the sample into the sample holder using adhesive tape.
- Gently place the stylus on the sample surface and take care that the stylus is oriented perpendicular to the surface.
- Now the measurement can be started and has to be validated after acquisition.
- Afterwards the operator manually corrects the levelling of the measurement, as there are always some residual tilts present from the sample mounting.
- Then the step height can be deduced by selecting the ‘Step’ entry in the ‘Studies’ menu.
- When the measurement is finished, move the sample stage to a new position and repeat the upper steps or remove the pick-up/stylus from the sample and the sample from the sample holder.

Typically one sample was measured on three to six different positions, in order to get a little bit of statistics and an indication if the film is uniformly deposited over the substrate. The acquired thickness values were also used to calibrate the FTM.

Thickness Measurement using Optical Transmission Measurements

For thin film thicknesses below ~ 50 nm a practical alternative to the direct determination of the thin film thickness as described above, is the measurement of the optical transmission through the deposited layer.

Using Beer-Lambert’s law, where the material’s transmittance T is related to its optical depth τ via,

$$T = \frac{\Phi_{e,\lambda}^t}{\Phi_{e,\lambda}^i} = e^{-\tau}, \quad (2.66)$$

with $\Phi_{e,\lambda}^t$ being the spectral radiant flux in wavelength, transmitted by that surface, and $\Phi_{e,\lambda}^i$ being the spectral radiant flux in wavelength, incident to that surface. Using the attenuation coefficient $\mu(z)$, the optical depth τ can be expressed as:

$$\tau = \int_0^l \mu(z) dz, \quad (2.67)$$

with l being the propagation length in the material. In the case of uniform attenuation, which is a reasonable assumption for homogenous thin films, $\tau = \mu l$ and thus,

$$T = e^{-\mu l}. \quad (2.68)$$

Using κ , the extinction coefficient, which is indicating the amount of attenuation when an electromagnetic wave propagates through a material, μ can be expressed as: $\mu = \frac{4\pi\kappa}{\lambda_0}$. Thus, Equation 2.68 can be rewritten to yield an expression for the

Table 2.6: Extinction coefficient κ and attenuation values μ for materials used in this work at $\lambda_0 = 530$ nm, extracted from [245], except * is taken from [246]. † Os values for that wavelength could not be found, instead the values from Ir were taken [247].

Material	κ []	μ [m^{-1}]
Ti	3.3418	$7.923\,45 \times 10^7$
Cr	3.33	$7.895\,47 \times 10^7$
α -C	0.70782	$1.678\,25 \times 10^7$
ta-C*	0.379585	9×10^6
ta-C	0.024919	$5.908\,33 \times 10^5$
Fe	2.9164	$6.914\,82 \times 10^7$
Fe ₂ O ₃	0.564	$1.337\,25 \times 10^7$
Ir	5.0	$1.185\,51 \times 10^8$
Os†	5.0	$1.185\,51 \times 10^8$

thin film thickness, depending on the wavelength of the incident light λ_0 and the material's extinction coefficient:

$$l(T, \kappa, \lambda_0) = \frac{\text{Log}(T^{-1}) \cdot \lambda_0}{4\pi \cdot \kappa}. \quad (2.69)$$

Values for κ at specific wavelengths can be found at [245]. Table 2.6 lists κ - and μ -values for the materials used in this work. Note that extinction values critically depend on the chemical coordination, e.g., amorphous carbon and its tetrahedral coordinated counterpart and iron versus iron(III)oxide (rust).

Alternatively to the approach given above, it is also possible to directly look up the transmittance values in tabulated curves, see Figure 2.28.

One has to consider, that Equation 2.69 is only valid, if the chemical composition of the thin film over the integration range is homogeneous and the absorption coefficient for that specific composition/material, or even electronic coordination, is known. As stated above, Fe and Fe_xO_y do have totally different μ , as well as C, which can show a large variation of its absorption coefficient upon changing its chemical bonding states.

Another aspect of the above relations is, that they only hold true if the sample illumination is parallel and homogeneous, which is the case in commercially available slide scanners. For thin film thickness measurements a Nikon Super Cool Scan 9000 device was used, according to the setup depicted in Figure 2.27 (a). An incident flux of parallel white light Φ_e^i is incident on microscopy glass slides (Thickness: ~ 100 μm , $\varnothing 18$ mm). The outgoing flux Φ_e^t is detected by an RGB-CCD-detector pixel array. As the extinction value κ is wavelength-dependent, a wavelength selection was achieved, using only one, e.g., the green, colour channel of the RGB-CCD image, thus justifying the notion of spectral radiant flux Φ_{e,λ_0}^t from above. In order to correct for the (rather small) absorption of the microscopy slide, a non-coated reference slide was inserted

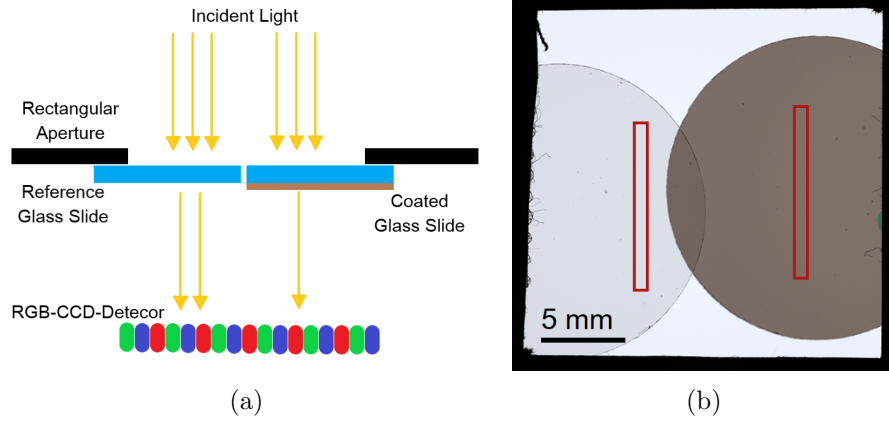


Figure 2.27: Optical transmission thickness measurement principle in (a) and typical measurement image of a 25 nm α -C film deposited on thin microscopy slides (right side) and non-coated reference slide on the left side taken with a Nikon Super Cool Scan 9000 slide scanner (b). The red boxes show the signal integration range of 20 pixels.

next to the coated slide, such that the outgoing flux $\Phi_{e,coated}^t$ could be correlated to the outgoing flux $\Phi_{e,non-coated}^t$, instead of relating it to Φ_e^i .

The flux values were evaluated by taking the mean value of a 20 pixel wide line profile over homogeneous regions of the samples, see Figure 2.27 (b). Putting these transmittance values together with the attenuation values μ from Table 2.6 into Equation 2.69, the film thickness l can be calculated.

Electrical Conductivity Measurements, using a Four Point Probe Measuring Station

In order to estimate the density and purity of thin films, produced by magnetron sputtering for the use as HVM, it is possible to determine the electrical conductivity as an indirect marker.

Electrical conductivity or electrical resistivity measurements are an easy and straightforward way to determine on the one hand side the density of states at the Fermi level, or in other words the amount of free charge carriers available for conduction, and on the other hand how much electron scattering occurs within the thin film material. The macroscopic relation for the resistance R of a material, given by the Ohm's law, $R = U/I$, with U being the applied voltage and I the current through the resistor, does not tell much of the origins and deeper causes of the material's resistance. Contrary to that, the microscopic explanation of resistance, given by the Drude's law

$$\mathbf{j} = \frac{n_e e^2 \tau}{2m_e} = \sigma \mathbf{E}, \quad (2.70)$$

expresses the electrical current, using fundamental physical entities like n_e , e and

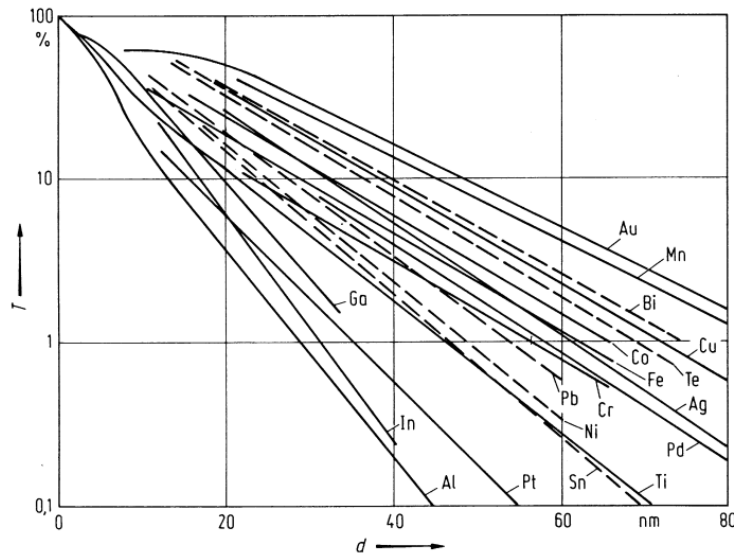


Figure 2.28: Optical transmittance T curves over thin film thickness d for various materials on a glass substrate for a wavelength of 550 nm, taken from [248], p. 39.

τ , being the number of charge carriers, the electron charge and the mean free time between scattering events, respectively. These quantities are summarized under the term σ : the electrical conductivity (not a scattering cross-section). \mathbf{E} represents the electrical field applied. The *Matthiessen* rule states, that the inverse of τ is the sum of different scattering contributions $1/\tau = 1/\tau_L + 1/\tau_{GB} + 1/\tau_I + 1/\tau_{IF}$, where τ_L , $1/\tau_{GB}$, $1/\tau_I$ and $1/\tau_{IF}$ describe the mean free times between scattering on the lattice atoms, on grain boundaries, on impurities and interfaces, respectively. Thus, an increase of electrical conduction is directly connected to an increasing contribution of one, some or all of these processes. E.g., with decreasing film thickness the contribution of scattering on the film interfaces increases, relative to the other contributions, and reduces its conduction.

For the case of a homogeneously distributed material, having a uniform cross-section along the current path, and a constant electric field and current density across the sample and parallel orientation to each other, the electrical resistance can be given by:

$$R = \rho \cdot \frac{l}{d \cdot b}, \quad (2.71)$$

where d is the thin film thickness and l and b are the current path length and width, respectively, according to Figure 2.29 (a), and ρ is the electrical resistivity, which is the inverse of the electrical conductivity σ . For $l = b$ the resistance simplifies to $R = R_{\square} = \rho/d$, which is the sheet or surface resistance of a material. For the linear four-point probe geometry, given in Figure 2.29 (b), $R_{\square} = 4.532 \cdot (U/I)$ and with

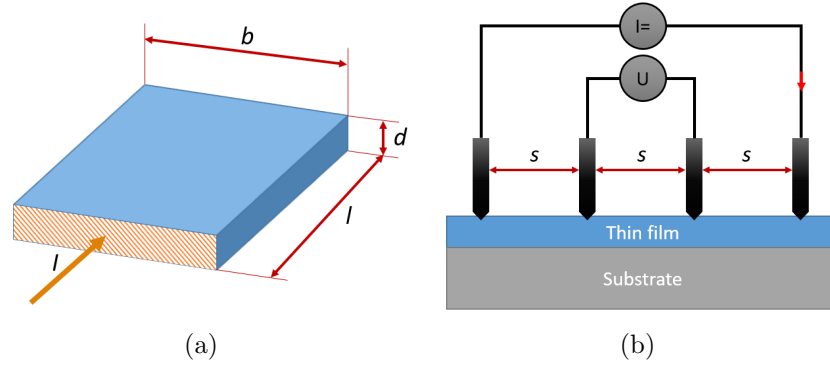


Figure 2.29: Four point probe measuring principle. (a) Geometry of a thin film resistor (b) four-point probe linear geometry. A constant current is applied at the two outer electrodes, while the according voltage drop at the two inner electrodes is measured.

that Equation 2.71 can be written as,

$$\rho = R_{\square} \cdot d = 4.532 \cdot \frac{U}{I} \cdot d. \quad (2.72)$$

The electrical resistivity ρ , as opposed to the electrical resistance R , is a material intrinsic property, meaning that, irrespective of the conductors size and shape, ρ can be compared to tabulated values. This is why it is also known as specific electrical resistance. With decreasing film thickness the electrical resistivity departs dramatically from the bulk values and can give insights in the thin film purity and grain-size distribution.

The measurement routine on the thin film resistivity measurement station, shown in Figure 2.30, can be described as follows: When the sample is mounted on the sample stage, see Figure 2.30 (b) it has to be centred under the four-point probe head (a), using the (x, y) -stage movement screws, afterwards contacting of the thin film is done by slowly moving the stage up in z -direction under continuous observation of the force value indicated on the *LabView* computer control system, Figure 2.30 (e). The contact force is determined by using a load cell, which is attached to the four-point probe cell²³. Typical contact forces are in the range of 1 N to 3 N. When the contacting is finished, the measurement routine, implemented in *LabView*, needs to be configured in order to account for the expected resistivity range of the thin film and for measurement result accuracy. Here the predefined values have been used. Geometric parameters, like the thin film thickness d and the substrate shape and size, have to be entered before starting the routine. The program ramps up the DC-current I from 10^{-7} A to 10^{-5} A in thirty steps, using a DC- and alternating current (AC) pico-ampere current source (Keithly model 6221), Figure 2.30 (c). The current

²³Note that the load cell has to be reset to zero (tare), before the four point probe touches the thin film, to give a valid force value.

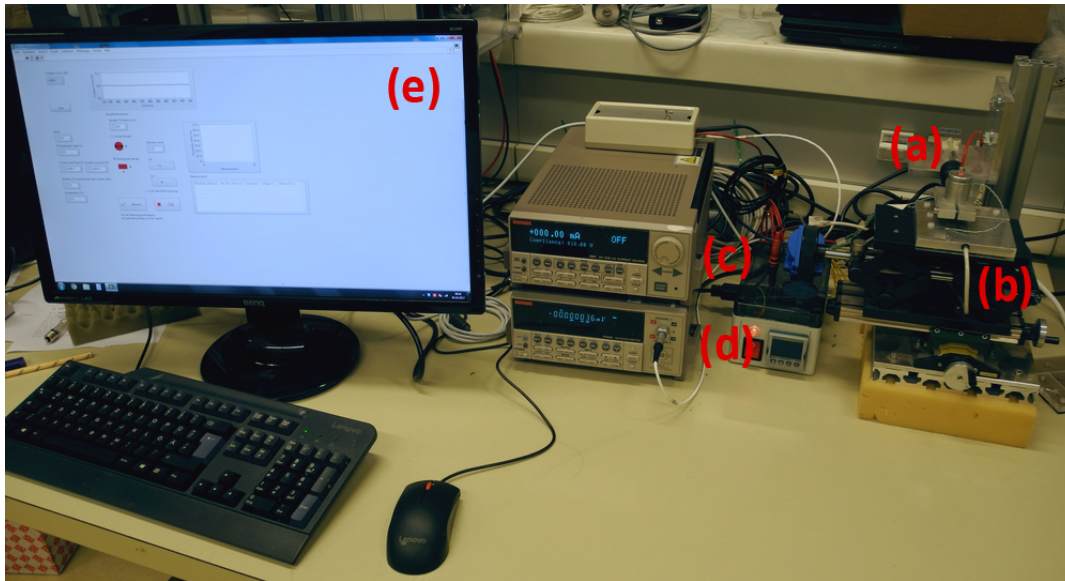


Figure 2.30: Image of the four point probe measuring station. (a) Four-point probe head attached to a load cell to determine the force used to contact the thin film. (b) (x, y, z) -moveable sample stage used to position the thin film/substrate centred under the (a). The contacting is done by slowly moving the stage up in z -direction under continuous observation of the force value, indicated on the *LabView* computer control system (e). The constant current is provided by a pico-ampere current source (c) and applied at the outer two electrodes of (a), while the nano-voltmeter (d) measures the voltage drop along the inner two electrodes of (a).

2 Fundamentals

is applied on the outer electrodes, of the four-point probe head, Figure 2.30 (a) and Figure 2.29 (b). At every step the voltage drop along the inner two electrodes is measured twenty times with a nano-voltmeter (Keithly model 2182A), Figure 2.30 (d), and the resistivity ρ is calculated by using Equation 2.72 and written to a semicolon-separated text file, together with its standard deviation of the mean (STD). *Wolfram Mathematica* is then used to import these data files, reformat and calculate an average value of the measured thin film resistivities, using the measured STD of each and every current step as weights.

3 Device Modifications and New Measurement Tools

Not only that numerous measurement tools and devices have been employed in the course of this thesis, at some points it was also necessary to improve the performance of given devices, to build a new characterisation tool and to build extensions to already existing ones. This chapter aims at describing those specific additions and devices, needed to produce and improve HVMS employed in vortex EMCD measurements.

3.1 Sputter Coater Vacuum System

In order to be able to produce own magnetic samples, e.g., of the strongly oxidising materials Fe, Ni and Co, for vortex filter EMCD measurements with the desired properties like thickness, crystallinity and orientation at any time, the vacuum performance of the in-house sputter coater (Quorum Q150T) had to be further improved. Especially, with the long-term goal of epitaxial grown layers the demands on the vacuum are very stringent [249]. The influence of impurities and, thus, to great extent the base pressure of the sputter system before sputtering, and the process gas supply, on thin film properties, like its density, granularity, inner tensions, mechanical stability and even the degree of amorphicity have been observed [237, 250]. Even for the same metal and the same film thickness, different film structures have been seen, under the use of different deposition devices [251], emphasizing the impact of a ‘clean’ vacuum on the production of dense and oxygen-free electron-absorbing heavy metal films used for binary HVM¹.

Therefore, the weak points in the vacuum system of the in-house sputter coater were quantified by using a He-leakage tester (Leybold UL200). Additionally, the vacuum-pump-down behaviour, depending on its leakage, out-gassing and gas permeation, was modelled, using the methods described in the vacuum theory part, Section 2.9.2. Afterwards the practical implementation of these findings will be described, e.g., in the form of a redesign of the high-vacuum backing line and sealings and the development of a cooling and bake-out system. In order to get a more reliable and convenient control over the impact of the diverse measures to improve the vacuum performance of the system, a vacuum logging possibility was devised.

¹Note that the manufacturer of the sputter coater realized the importance of the vacuum system’s performance too and adopted the vacuum system in his newest series [237, 250].

3.1.1 Vacuum Logging

The *Quorum Q150T* sputter coater (SC), is equipped with a full range (5×10^{-9} mbar to 1000 mbar) vacuum gauge from Pfeiffer (Model PKR 251), which combines a Pirani measurement cell and a cold cathode system according to the inverted magnetron principle (Penning). This vacuum sensor has a measurement range of 5×10^{-9} mbar to 1000 mbar. Unfortunately, the Q150T software outputs the measured vacuum level in the scientific notation but only with single digit precision, which is not appropriate for a decent assessment of vacuum improvement measures or leakage estimations. Also, logging was only possible by manually reading and writing down the vacuum level value, indicated on the device's display, which rendered the detection of subtle changes in the high vacuum range below 1×10^{-4} mbar impossible. Therefore, a self-built lead-through from the combined vacuum gauge to a multimeter with logging capabilities (Meterman XR38) has been built. The lead-through can also be used by the system described in Section 3.2.

According to the technical data sheet [252], the measuring signal is output as a logarithm over the whole measurement range. To get access to this output signal, a three metre long extension cable with a standard nine pole sub-D male plug was connected in parallel to the vacuum gauge's signal output. Pin 1 on the sub-D connector is the signal common and pin 2 is the signal output (measuring signal). Care must be taken, that the connected load is not less than $10 \text{ k}\Omega$ and the analog-to-digital converter (ADC) can handle the voltage range from 0 V to 10.5 V. An error signal is given if the measured voltage drops below 0.5 V (no supply) or if it exceeds 9.5 V (Pirani measurement element defective; filament rupture), 0.5 V to 1.82 V indicates an under-range, whereas 8.6 V to 9.5 V represents an over-range value. If the measured voltage signal U lies within 1.82 V to 8.6 V, it can be converted to a pressure value p by:

$$p(U) = 10^{(1.667 \cdot U)/V - d}, \quad (3.1)$$

where $d = 11.33$ yields the pressure value in *mbar*, and vice versa, a pressure value can be converted to a voltage value by:

$$U(p) = c + 0.6 \cdot \log_{10}(p/\text{mbar}), \quad (3.2)$$

with $c = 6.8$ for a pressure value given in *mbar*. With the data logging ability described above and Equation 3.1, it was possible to acquire a correspondence table, that connects the indicated vacuum values on the SC's display with the measured ones.

Note that the measured vacuum pressure value crucially depends on the measurement position, e.g., placing the vacuum sensor at the end of a long and narrow tube and connecting the other end to the vacuum chamber will inevitably give a wrong and higher value. The thermal management system, as described below, includes a heating/cooling sample stage that has to be electrically connected to the control system of the thermal management system. This electrical connection is realized via an electrical feed-through (Pfeiffer Vacuum, DN16 ISO-KF, 9 pin, 2 A/pin), that is

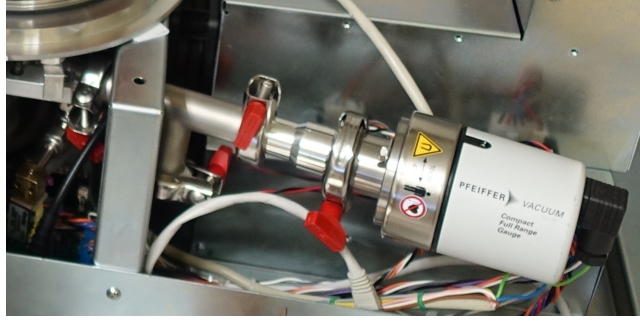


Figure 3.1: DN16 ISO-KF T-piece added to the Q150T sputter coater in order to be able to add an electrical feed-through to the system.

connected to the lower port of a T-piece (Pfeiffer, DN16 ISO-KF), see Figure 3.1, which has been added in between the chamber port and the vacuum measurement cell. This T-piece increases the distance between the vacuum sensor and the chamber. Thus, for comparing the measured values after including the T-piece and before, a correction of the indicated pressure value has to be applied.

Using the definition for the conductance of vacuum tubing parts and apertures $C = q_{pV}/\Delta p$, with q_{pV} being the gas flow rate and $\Delta p = p_1 - p_2$ the pressure difference at the respective ends of the tube, yields $q_{pV} = C\Delta p$ [241]. Together with the definition of the gas flow rate $q_{pV} = S_{eff} p_2$ with S_{eff} , representing the effective pumping speed at the entrance of the tube [241], one can write the actual pressure value or at least the value comparable to the original position of the vacuum sensor as a function of p_1 , which is the pressure measured at the end of the tube:

$$p_2(p_1) = \frac{C_{tube} \cdot p_1}{S_{eff} + C_{tube}}. \quad (3.3)$$

In the molecular flow regime for air at 293 K, the conductance of an aperture is given by: $C_{ap} = 11.6 \cdot A$, with A being the area of the aperture. The conductance of a tube in the molecular flow regime for air at 297 K is given by $C_{tube} = C_{ap} \cdot P_{tube} = 12.1 \cdot \frac{d^3}{L}$, where P_{tube} is the mean probability of particle passage, and has been determined by *Monte-Carlo* (MC) simulations [241]. The effective pumping speed can be calculated by $\frac{1}{S_{eff}} = \frac{1}{S} + \frac{1}{C}$, with C representing the conductance of the vacuum system between the TMP and the tube entrance, under use of the system parameters $S_{eff} = 2.41 \text{ s}^{-1}$ and $C_{tube} = 4.91 \text{ l s}^{-1}$.

3.1.2 Modelling the pump-down behaviour

In this section it is sought to estimate the effect of different vacuum improvement measures on the pump-down behaviour of the sputter coater. Upon this estimation and accompanying He-leakage measurements, it is possible to decide what measures may lead to an effective reduction in the pump-down times.

3 Device Modifications and New Measurement Tools

Starting with the volume flow rate or theoretical pumping speed S of a vacuum pump, given by [242]:

$$S = \frac{Q}{p}, \quad (3.4)$$

where Q is the gas load, typically given in $\frac{mbar \cdot l}{s}$ and p is the system's vacuum level or equilibrium pressure, given in $mbar(10^{-2}Pa)$, it is possible to set up a gas load balance including the most important gas load sources. Typical units of S are $\frac{m^3}{h}$ and, especially for TMP, $\frac{l}{s}$. Due to additional tubes, valves or apertures between the vacuum chamber and the TMP, the pumping speed given in Equation 3.4 is reduced. This effective pumping speed can be calculated by,

$$S_{eff} = \frac{1}{\frac{1}{S_{nom}} + \frac{1}{C}}, \quad (3.5)$$

with C representing the conductance value of the elements blocking the molecular particle flow to the pump. Formulae to calculate the conductance of pipes and apertures have been already given in the preceding section.

The gas load of a vacuum system typically consists of the gas volume in the chamber, which is removed within seconds or a few minutes, for a small chamber like the given one ($V = 3.2l$), the leakage through micron and sub-micron sized holes or surface roughness imperfections, the gas desorption of the chamber walls and the permeation through the chamber walls, e.g., through rubber hose walls. Using Equation 3.4, the combination of all these effects can be summarized and leads to a description of the temporal pressure evolution $p(t)$,

$$p(t) = \frac{Q_{Leak}}{S} + \frac{Q_{Des,M}(t)}{S} + \frac{Q_{Des,P}(t)}{S} + \frac{Q_{Perm}}{S}. \quad (3.6)$$

with Q_{Leak} being the total leakage rate, $Q_{Des,M}(t) = \sum_i q_{Des,M}^{(i)} A_M^{(i)} \frac{t_0}{t}$ being the total gas desorption of all metallic and glass chamber walls with their respective areas $A_M^{(i)}$ and desorption rates $q_{Des,M}^{(i)}$, whereas $Q_{Des,K}(t) = \sum_i q_{Des,P}^{(i)} A_P^{(i)} \frac{\sqrt{t_0}}{\sqrt{t}}$ represents the total gas desorption of all plastic material surfaces in the vacuum system and $Q_{Perm} = \sum_i q_{Perm}^{(i)} A_{Perm}^{(i)} \frac{\Delta p}{d_{Perm}^{(i)}}$ is the total permeation leakage rate, due to different materials $q_{Perm}^{(i)}$ with their respective thicknesses $d_{Perm}^{(i)}$ and areas $A_{Perm}^{(i)}$.

Using the respective measured and estimated areas², as well as the values for the gas desorption, taken from Table 2.4, and for the gas permeation, taken from Table 2.5, it is possible to model the pump-down behaviour of the Q150T sputter coater for various conditions, see Figure 3.2. The influence of different permeation values of various high-vacuum backing line tubing materials is shown in Figure 3.2 (a). It gets clear that the gas permeation through the backing line tubes alone does

²The areas used for the rubber tubing permeation and desorption have been weighted by the trespassing probability for long and narrow pipes $\frac{4}{3} \frac{d}{l}$, where d is the inner tube diameter and l its length, according to [253].

3.1 Sputter Coater Vacuum System

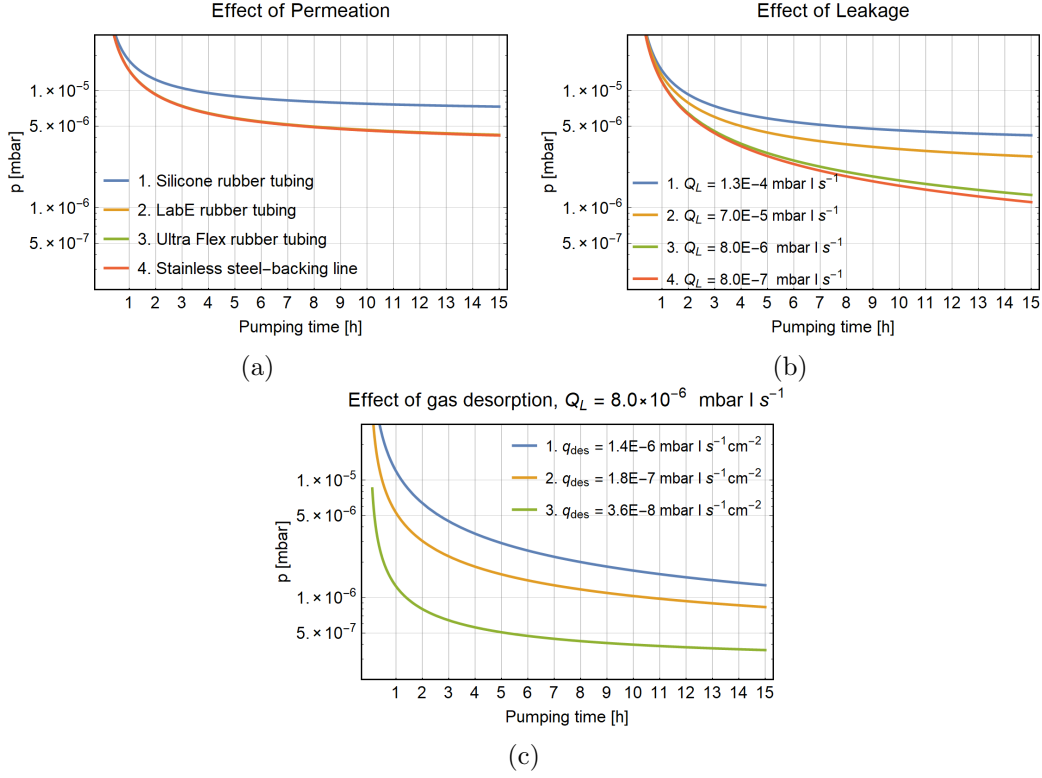


Figure 3.2: Panel of calculated pump-down curves for the Q150T, according to Equation 3.6, showing the influence of (a) gas permeation through rubber tubing, (b) leakage reduction, and (c) gas desorption of the chamber walls. For comparison the same scales is used in all diagrams.

not pose a problem, except really leaky silicone tubing is used (the other curves do overlap). Originally, the ‘LabE’ rubber tubes were used in the Q150T. Note that gas permeation through the Al and glass chamber walls is even more improbable, and that the rubber tube connections consist of pressing the rubber tube over small metallic barbs, which is probably a source of gas leakage.

Looking at the influence of leakage, given in Figure 3.2 (b), gives a different picture. Here, strong improvements of the final pressure can be expected, starting from an estimated initial leakage rate of the system (based on vacuum pump-down observations) of $1.3 \times 10^{-4} \frac{\text{mbar l}}{\text{s}}$, going down to $8.0 \times 10^{-6} \frac{\text{mbar l}}{\text{s}}$. A further improvement of the leakage rate by an order of magnitude has no significant effect on the pump-down behaviour, as the relative strength of the other terms in Equation 3.6 outweighs the leakage term. Thus, it is evident from Figure 3.2 (c) that major improvements in pump-down time and final pressure can only be expected from a significant reduction in the out-gassing rate of the inner chamber walls. Notably, the gas desorption values, given in Figure 3.2 (c), are estimated values for a very rough Al surface, found in the connection tube in between the TMP and the main chamber. For the Al top-

and bottom-plates and the glass cylinder the tabulated values were used. The values $1.4 \times 10^{-6} \frac{\text{mbar}\cdot\text{l}}{\text{s}\cdot\text{cm}^2}$ and $1.8 \times 10^{-7} \frac{\text{mbar}\cdot\text{l}}{\text{s}\cdot\text{cm}^2}$ correspond to the gas desorption before and after a polishing step. The last value of $3.6 \times 10^{-8} \frac{\text{mbar}\cdot\text{l}}{\text{s}\cdot\text{cm}^2}$ corresponds to an estimated value, reached after a bake-out cycle. There, of course, all the desorption values were reduced by 80 % mimicking a bake-out of the whole chamber.

3.1.3 Vacuum System Improvements Measures

The above considerations and He-leakage measurements (Leybold UL200) revealed three major weaknesses of the vacuum system. First, the high-vacuum backing line out of rubber tubes with their non-optimal connection, second, high out-gassing rates, e.g., due to rough surfaces and third, the glass cylinder sealing. The integral leakage rate of the ‘L’-gaskets out of FPM, used as a sealing between the glass chamber and the aluminium top- and bottom-plate, were roughly two orders of magnitude higher than leakage rates for other FPM O-ring based sealings in the system.

In Figure 3.3 the adoptions made to the high-vacuum backing line are shown. In a first step the original rubber tubing, Figure 3.3 (a), was removed by a high-end rubber tubing (C-Flex Ultra, Cole Parmer) and a stainless-steel T-piece, see Figure 3.3 (b). The overall length of the backing line tubes stays the same. This adoption showed only minor effects on the pump-down time and the final pressure. This could be expected from the modelling in the preceding section. The slight improvement in vacuum performance is most likely due to the fact that cable ties were used in order to reduce the leakage at the connection points. Hence, the backing line was rebuilt, as illustrated in Figure 3.3 (c), using full stainless-steel tubing and cutting ring fittings (Swagelock). It was tried to keep the tube length as short as possible in order to reduce the volume and surface area of that part of the system. As there was no commercial solution available, to connect the stainless-steel tube to the Ar-bleeding valve barbs, a custom-built variant was devised, see Figure 3.3 (e) and mounted to the system, see Figure 3.3 (d).

This intervention improved the final vacuum³ by $\sim 4 \times 10^{-6}$ mbar to better than 1.4×10^{-6} mbar and reduced the pump-down time to reach, e.g., 4×10^{-6} mbar, from ~ 14 h to ~ 1.5 h, see Figure 3.6 (blue line compared to magenta coloured line).

One of the main components responsible for the gas load in high-vacuum systems is out-gassing in the form of desorbed water, and carbon monoxide molecules [240]. In order to reduce the out-gassing of surfaces in the vacuum chamber, typically the surface roughness is reduced via polishing or etching and, ideally, also densified by using shot peening [240]. As already mentioned above, the surface of the one-quarter elbow tube, connecting the TMP and the vacuum chamber, which has a relatively large area, was in the as-cast state, as can be seen in Figure 3.4 (a, c). Thus, the device was completely taken apart and the connection tube was then manually polished, to the state shown in Figure 3.4 (b, d). The polishing procedure was as follows:

³Which means in this case, the vacuum after ~ 21 h to 24 h. This is the software limit for keeping the system under TMP pumping.

3.1 Sputter Coater Vacuum System

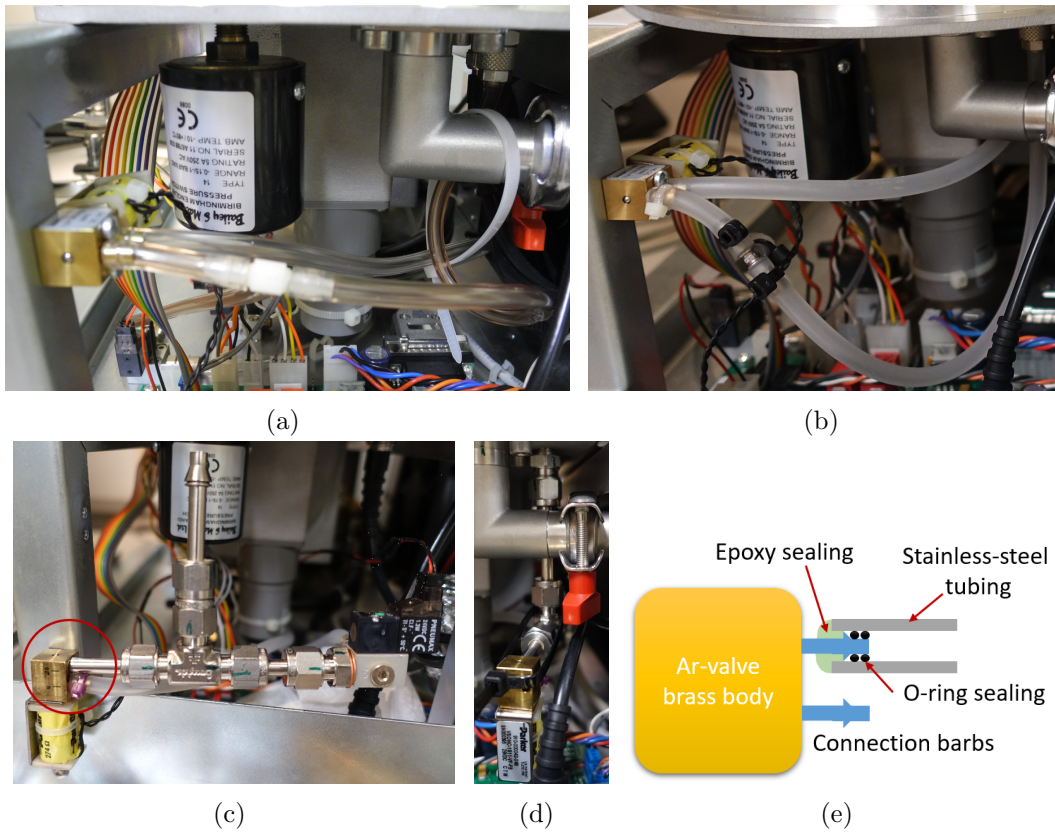


Figure 3.3: High vacuum side backing line. (a) As it was, *Tygon-E-Lab* or similar rubber tubing with a plastic T-piece, (b) intermediate state, using a high-end rubber tubing (*C-Flex Ultra*, Cole Parmer) and a stainless steel T-piece, (c) full stainless steel tubing, T-piece and connections (*Swagelock*), before mounting and (d) after mounting. (e) schematics of the sealing solution for connecting the Ar-bleeding valve to the stainless-steel backing line, marked by a red circle in (c), using miniature O-rings and an epoxy resin seal (*UHU*, *Endfest 300*).

3 Device Modifications and New Measurement Tools

- The sputter coater was carefully disassembled, as well as the TMP was removed, in order to get access to the pipe without contaminating more parts than absolutely necessary with grinding particles, etc..
- For the first grinding step, an FEPA P#220 silicon carbide sand paper was used to remove coarse cast Al grains.
- Using a multifunction rotary tool (similar to a Dremel), equipped with an Aluminium-oxide grinding stone, the extremely rough protrusions on both sides of the channel were removed or at least strongly reduced.
- The first polishing step was done using ultra fine microgrid P#2000 sand paper (grain-size 10.3 μm) and distilled water. This polishing step was done by hand.
- The last polishing step was done using an ultra-fine P4000 microgrid silicon-carbide abrasive paper with a grain-size of 5 μm and distilled water. This polishing step was done by hand and in between the grinding/polishing steps the pipe was rinsed with H_2O dest. in order to get rid of Al and sand paper particles.
- Cleaning with Methanol, H_2O dest. and pressurised air and final reassembly.

This step resulted in a further improvement of the pump-down characteristics, shown in Figure 3.6 (orange line), i.e., the final pressure decreased to 8.7×10^{-7} mbar and the pump-down time for reaching, e.g., 4×10^{-6} mbar, decreased from ~ 1.5 h to ~ 0.5 h. Note that no specific surface densification step was undertaken or possible with the equipment at hand, so the achieved degassing rate reduction is still rather on the lower side of possible out-gassing rates for Al surfaces⁴.

The ‘L’-gasket sealing, depicted in Figure 3.5 (a), marked by the two red arrows, has not only a relatively high leakage rate, as seen in He-leakage tests, it also protrudes ~ 10 mm into the vacuum chamber, as it was designed to hold an implosion guard on the outside and to centre the glass vessel on the base-plate, as well as to centre the top-plate over the base-plate. As shown above, gas desorption plays an important role in the high-vacuum regime and the out-gassing of FPM is at least two orders of magnitude higher than the one of Al or stainless-steel parts. Therefore, the ‘L’-gasket was removed by an FPM O-ring sealing, which is held in place by an Al-ring in order to reduce both, leakage and gas desorption, see Figure 3.5 (b). The O-ring mounting geometry is shown in Figure 3.5 (b) as an inset. Even though this solution may seem unideal for O-ring mounting, it can easily be added and removed from the system, such that other users can still use the original sealing. The O-ring cross-section (3 mm) was chosen, such that the deformation under vacuum conditions is of the order of 25 %, to guarantee leak tightness [253] and the Al-ring was designed, such that the thermal expansion of Al, which is nearly ten times larger than that of glass, does not cause damage to the glass cylinder.

⁴A degassing rate that is three times higher than the one of Al was chosen for modelling the polished state of the elbow tube in the preceding section.

3.1 Sputter Coater Vacuum System

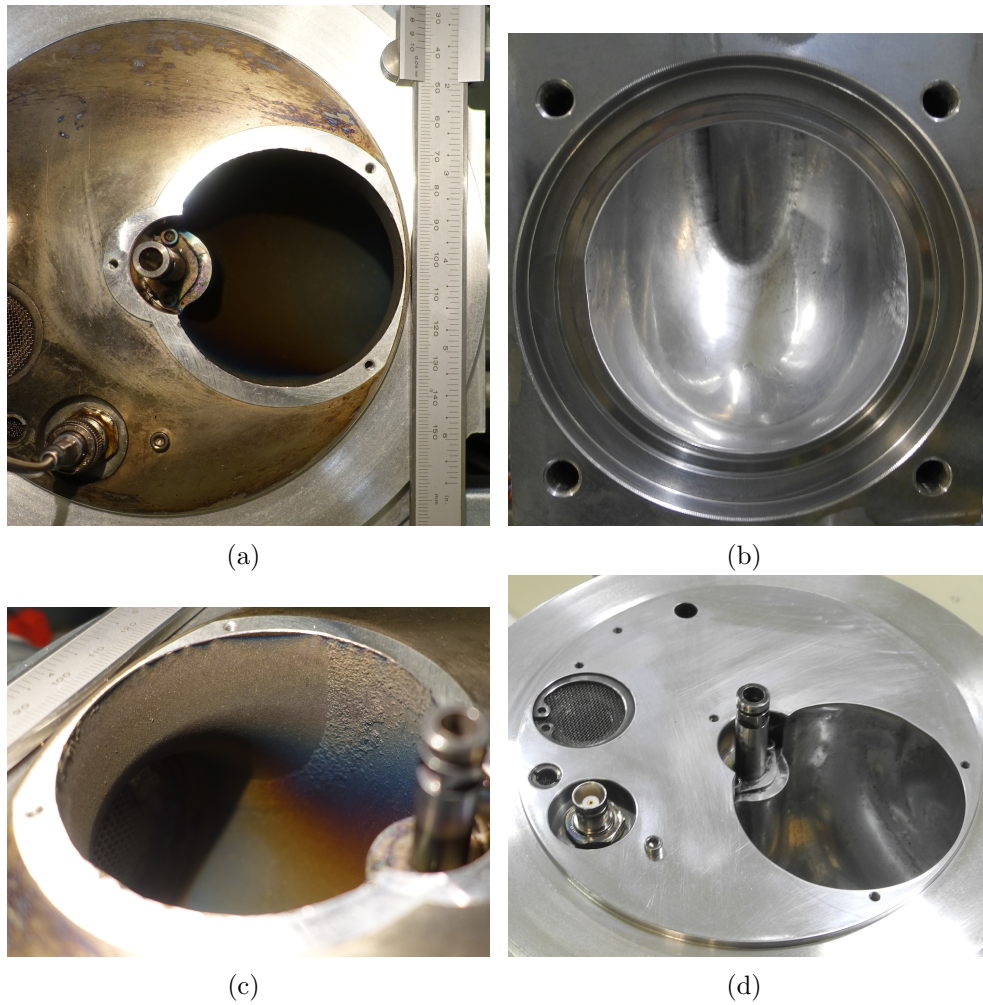


Figure 3.4: Gas desorption reduction by surface roughness improvement. Before (a,c) and after (b,d) polishing, comparison of the elbow tube connection between the TMP and the vacuum chamber of the sputter coater.

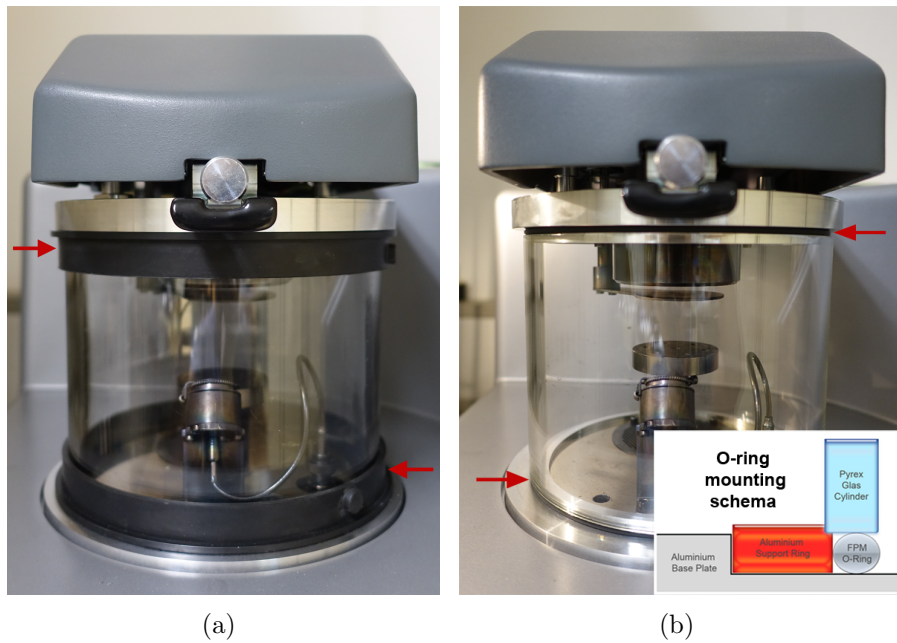


Figure 3.5: Before (a) and after (b) replacing the 'L'-gasket of the sputter coater's vacuum chamber with an Al-ring supported O-ring ($3 \times \text{Ø}157$ mm, FPM, Shore hardness: 80, red arrows) sealing. The inset schematically shows the O-ring mounting.

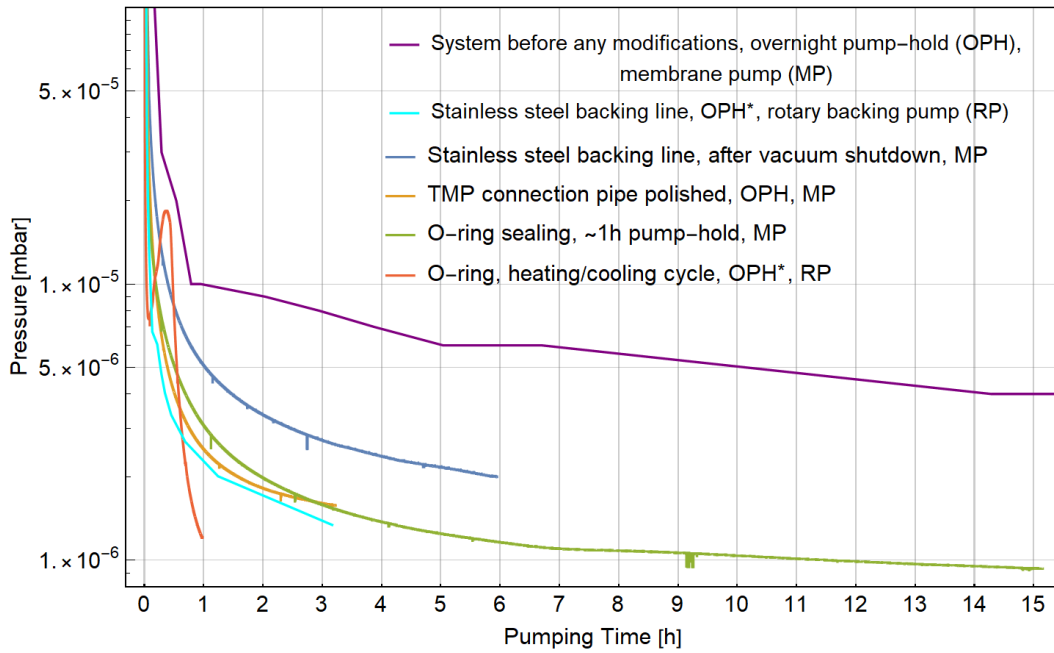


Figure 3.6: A logarithmic plot of the pump-down curves of the Q150T after various vacuum improvement measures. Overnight pump-hold stands for ~ 12 h TMP pumping before the test, whereas vacuum shutdown is the typical standby state of the sputter coater, with the chamber valve closed and no TMP pumping. Before each test the chamber was vented with N_2 and was ~ 1 min on air, except in the OPH* measurements, where the chamber was vented with N_2 but not opened. Note the different backing pump configurations and pre-pump-down states. The position change of the penning cell and the resulting pressure difference, was corrected by using Equation 3.3.

Despite the green curve in Figure 3.6 not being acquired after an overnight pump-down cycle, it descends stronger than the orange one in the high-vacuum regime, indicating an improvement against the state before. After 15 h of pumping, a pressure of 9.3×10^{-7} mbar was reached, comparable to the final pressure reached after 21 h using the “L”-gasket.

For all the above tests the backing pump of the TMP was a membrane vacuum pump (Vacuum Brand, MD1, $S = 1.2 \frac{m^3}{h}$). A TMP has a given compression ratio for a certain gas species, e.g., $> 1 \times 10^{-11}$ for N_2 , hence, given that the gas leakage into the vacuum chamber is not the limiting factor, the final vacuum can be reduced by reducing the outlet pressure at the TMP. As the final pressure of a rotary vane pump is two to three orders of magnitude better than that of a membrane pump and has also a roughly five-fold higher pumping speed than the membrane pump in use, it was tested to replace the membrane pump by a two stage rotary vane pump. A

first test was promising, as can be seen in the turquoise line in Figure 3.6. But as the chamber was not opened after N₂ venting, this strong improvement could also (partly) be due to reduced out-gassing in the chamber.

The above measures ensure clean and oxygen free conditions in the vacuum chamber before sputtering in not too long pumping times.

It should be noted that the process- and venting gas lines are made out of rubber, which could be problematic when a high-purity in the Ar-gas supply is needed. Additionally, on the low-vacuum side of the Q150T, there are three different plastic hoses, used to connect the TMP outlet to the pre-vacuum pump, probably leading to permeation of H₂ and CO₂ through the hoses and subsequent back-streaming into the vacuum chamber.

3.2 The Sputter Coater Vacuum Chamber and Sample Heating- and Cooling System

As already pointed out in the theory Sections 2.9.2 and 2.9.1, the background- or base pressure before and during thin film deposition crucially determines, e.g., the structural, compositional, electrical and mechanical properties of the layer [237]. In the preceding section multiple passive measures to improve the vacuum performance of the Q150T were described. A self-built system or upgrade for the Q150T, that employs a commonly used method in high- and ultra-high vacuum applications to significantly reduce the out-gassing rate in order to reach a decent high-vacuum in a reasonable time, which is baking out the vacuum chamber, will be illustrated [240]. Additionally to thermally controlling the vacuum chamber, the possibility to control the substrate temperature was also included in the system. This may be used to produce large grain crystalline magnetic samples, using high temperatures [249, 254, 255] and nano-crystalline Os/Ir thin films at low temperatures. Furthermore, the cooling function of the new sample stage could be used to improve the C film diamond-like properties [120] for robust phase HVM⁵. Heating cycles may be used to reduce the thin film inner stresses of Os/Ir/Pt-layers [224].

Because the term ‘sputter coater vacuum chamber and sample heating and cooling system’ is relatively unhandy, it will further on be called sputter coater thermal management (SCTM) or bake-out and cooling system.

The first version of this system can be seen in Figure 3.7. Basically, the sputter coater vacuum chamber can be split into three separate regions, the top plate out of Al holding the magnetron cathode and the shutter, the bottom Al plate where the sample holder, film thickness monitor, process- and vent-gas supplies, vacuum sensor and the TMP are situated and the middle part, which is a borosilicate glass cylinder (Ø160 mm × 140 mm), see Figure 3.5 and 3.8. Since the basic idea was to have both options, heating and cooling, available, at least for the two Al parts, traditional heating devices like resistive heating, ceramic heaters or heat lamps could

⁵Notably, with increasing substrate thermal conductivity the density and sp^3/sp^2 ratio increases as well [120].

3.2 The Sputter Coater Vacuum Chamber and Sample Heating- and Cooling System

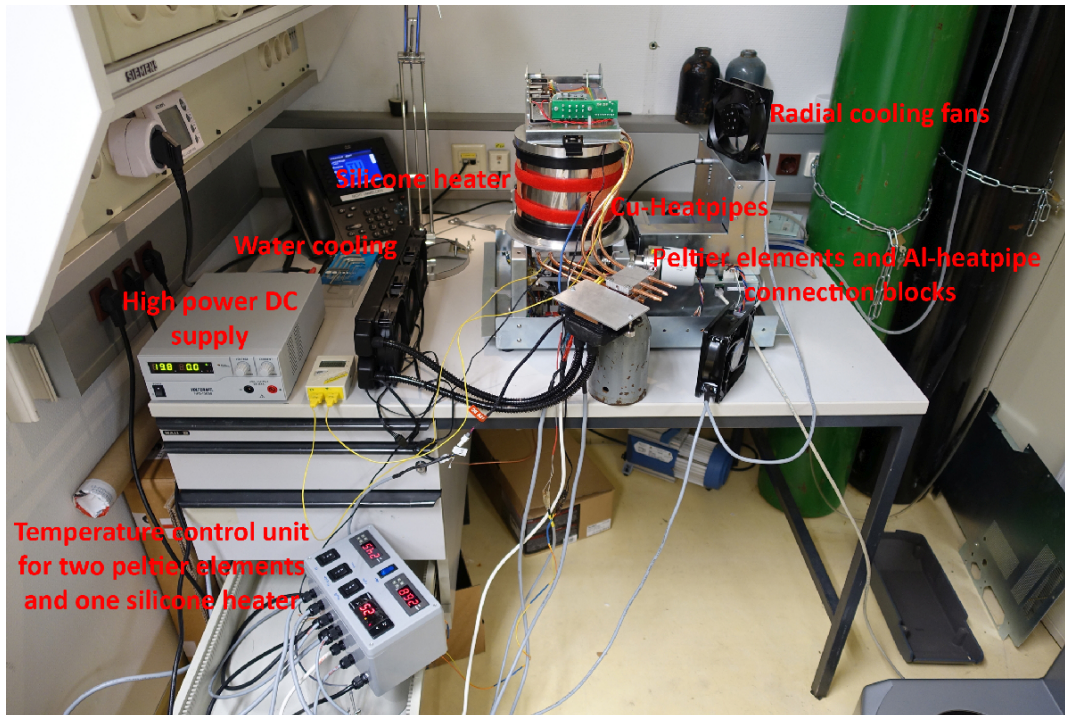


Figure 3.7: The first version of the Q150T sputter coater *Peltier* heating/cooling upgrade, used to improve vacuum and thermal stability during sputtering. Many parts are loosely hanging or standing around, which complicated the operation a lot.

not be employed. Using *Peltier* elements which utilize the *Peltier* effect, that is the possibility of transferring heat by flowing an electrical current through a thermocouple, provide the possibility to heat and cool devices by simply inverting the current direction through the element. No moving parts are needed and the power density is reasonably high, e.g., $\sim 10 \text{ W/cm}^2$. Two 40 mm by 40 mm *Peltier* elements (Quick-Ohm) were used, yielding a maximal heat dissipation of 160 W ($U_{max} = 19 \text{ V}$ and $I_{max} = 15 \text{ A}$), and were powered by a 900 W DC switching mode power supply (Votcraft, HPS-13030). Glass has a very low thermal conductivity of $0.76 \frac{\text{W}}{\text{mK}}$, which, combined with its cylindrical shape, made cooling impractical. Thus, this part is only resistively heated using a silicone rubber heating foil (thermo Technologies, 230 V AC, 800 W, 400 mm \times 100 mm), wrapped around the vessel, using two *Velcro* bands for good thermal contact. The problem of commercial sputtering machines (like the Q150T) is that most of the (vacuum) parts are enclosed in a moulded housing and are, thus, hardly reachable with heating or cooling devices. Therefore, heat-pipes were used to connect difficult-to-reach regions with a heat dissipation device. Heat-pipes are sometimes also referred to as ‘heat superconductors’, due to the fact that a temperature variation on one end of the a heat-pipe nearly instantaneously

3 Device Modifications and New Measurement Tools

leads to thermalisation on the other end. They exploit the fact that the latent heat of the phase transition between liquid and vapour and vice versa, as well as the heat transfer rate, of, e.g., water, is very high. Their thermal conductivity can be of the order of $100 \frac{\text{kW}}{\text{mK}}$ for long heat pipes, compared to $0.4 \frac{\text{kW}}{\text{mK}}$ for Cu, the metal with the second highest thermal conductivity. The working medium inside is chosen according to the application temperature range, but, typically it is water, working from 0°C to 250°C . Each heat-pipe, 6 mm in diameter (Quick-Ohm), can transfer 40 W of heat energy. A standard connection block for heat-pipes can carry three heat-pipes, thus, roughly 120 W of heat can be transferred, which is sufficient for the cooling of the sputter coater cathode, which has a maximal dissipated power of roughly 100 W.

A water cooling device (beQuiet!, Silent Loop 360 mm, 450 W), typically found in high-performance personal computers, is used as both: a heat sink, in the case the system needing to be cooled and a heat reservoir, if the *Peltier* elements are used to bake-out the chamber. The relatively high heat dissipation capacity of the water cooling is needed, because not only the heat that is removed from the magnetron cathode has to be taken into account, but also *Joule* heating of the *Peltier* element.

Three two-point temperature regulation units, using *PT100* (silicone heater) and *NTC* thermocouples, have been assembled in a custom-made housing. Temperature logging was only possible with an external logger.

Testing the system revealed that with a starting vacuum level of 1×10^{-5} mbar, after ~ 1.5 h of pumping and heating up to 90°C and a subsequent cool-down to 22°C , the vacuum level got down to 4×10^{-6} mbar. Without the thermal cycle, the vacuum level would be of the same order after ~ 14 h of pumping. If the vacuum chamber would have been kept under high vacuum, using the TMP and the pump-hold function, a comparable vacuum level would be reached after ~ 3.5 h. Thus, this first version already shows promising results concerning the vacuum improvement and quality of, e.g., carbon thin films, but soon some drawbacks became apparent, necessitating a redesign. E.g., one water cooling device for both *Peltier* elements was clearly not enough, temperature regulation was unhandy and could not be automated (cycle length and temperature, heating/cooling rate) and many parts of the setup were loosely hanging or standing around, which complicated the operation a lot, see Figure 3.7.

The redesigned system has a much more compact footprint and is more practical in usage, it can be controlled and automated by a *Linux*-based miniature computer (*Raspberry Pi* (RPI)) and it also includes a substrate heating (and cooling) stage for testing on the one hand side, if inner tensions of the sputtered thin films can be reduced by vacuum heating cycles, and on the other if epitaxial grown Fe, Ni or Co samples can be produced using temperatures as high as 800 K during sputtering and thereafter. A schematic overview of the system architecture can be seen in Figure 3.8. The system is controlled via a graphical user interface (GUI), either by touching the screen or classically using mouse and keyboard, see Figure 3.10, running on a *Linux*-based miniature computer, see Figure 3.9 (f). Most of the temperature readings, e.g., from the hot and the cold side of the *Peltier* elements (green) and the vacuum pressure value, are sent to the electronics box (orange), where a 16 bit ADC (Joy-it,

3.2 The Sputter Coater Vacuum Chamber and Sample Heating- and Cooling System

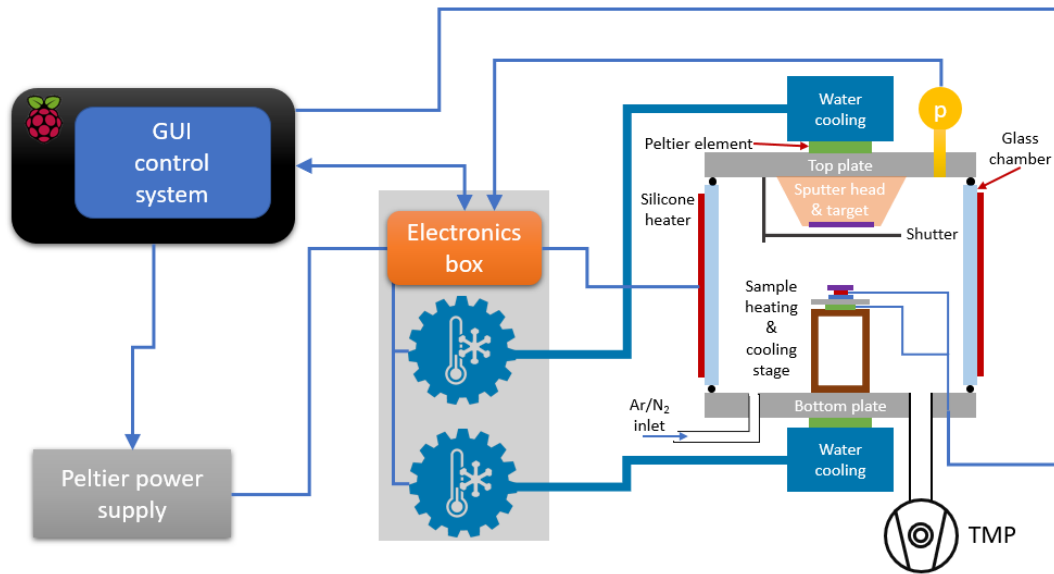


Figure 3.8: Schematic of the new thermal management system for the Q150T sputter coater.

I2C ADS1115), a 12 bit digital-to-analog converter (DAC) (Adafruit, MCP4725) and three 4-channel power switching relays (Seeed Studio, RPI relay board v1.0, 30/250 VDC/VAC, 15 A) are situated, see Figure 3.9 (c). The electronics box, and an additional 5 V power supply, wiring and the water-cooling heat dissipation elements are mounted in an adapted personal computer housing (light-grey shaded box), see Figure 3.9 (a, b).

The two *Peltier* elements (green) are powered by their own power supplies (grey, Manson, HCS3402, 32 V, 20 A, only one is drawn) which can be activated and voltage-controlled in the GUI, using the DAC. Thus, enabling the possibility to use a *PID* temperature regulation algorithm, where the *Peltier* current is smoothly tuned from zero to $I_{max} \sim 15$ A. As compared to the formerly used two-point regulation, this method provides a gentle *Peltier* operation. The temperature regulation of the silicone rubber heater foil is still realised as a two-point regulation based on a *PT100* that is mounted on the foil. What has changed is that the temperature control is now done by the control software, with the possibility to automatically start and stop the temperature control for some or all heating/cooling elements at once and specify the duration or sequence of heating. Theoretically, also the rate of heating and cooling could be controlled, but in practice this is not necessary. Additional Cu heat pipes for the bottom-plate heating and cooling (not drawn in Figure 3.8) were used to effectively transfer the heat from and to the sputter coater and to gain more space for the *Peltier* element water cooling device (Alphacool, Eisbär 420 mm). Both Al plates can thus be heated to 95 °C to 110 °C for bake-out and also be cooled down to

slightly above the dewpoint ($\sim 8^\circ\text{C}$), acting as a mild cryo-pump. The glass cylinder can, in principle, be heated up to 200°C , but, in order not to damage the FPM sealings, temperatures lower than 150°C are used. The sample heating and cooling stage (brown frame in Figure 3.8) consist of a Cu frame that thermally connects a *Peltier* element to the (cooled) bottom plate, see Figure 3.9 (f). On top of the *Peltier* element sits an Al plate. In normal operation this plate is kept cool, such that it also acts as a mild cryogenic-pump in close vicinity to the substrate/sample. Atop of this Al plate there is a thermal and electrical isolator, e.g., a 1 mm thick glass slide, which separates the ceramic heating element, with a diameter of 7 mm (Zhuhai 4U electronic ceramics, 5 V, $0.4\ \Omega$ to $0.62\ \Omega$), from the Al plate. On that ceramic heater the sample is placed for sputtering, having a working distance of 40 mm to the magnetron cathode. To monitor and regulate the temperature of the ceramic heater, a miniature *PT1000* temperature sensor (Heraeus Nexensos M222, -70°C to 500°C) is mounted at the downside of the heating element, using a high-temperature resistant glue (Hark, Thermic 1100°C), whereas the *Peltier* temperatures are controlled using digital one-wire temperature sensors (DS18B20) and the wiring is done by using low out-gassing cables (VACOM). Figure 3.10 shows the whole system assembled and in operation. A pump-down curve with simultaneous heating to 110°C for ~ 20 min and subsequent cooling down to 8°C shows the improvement against no heating. Instead of taking 3 h to 6 h, a descent high-vacuum was reached after ~ 1 h, Figure 3.6 (red line).

3.3 A Basic Thin-film Tensiometer to Estimate Thin Film Stresses

In Section 2.9.1 thin film growth mechanisms and the influence of sputtering parameters on the film characteristics have been described. The bottom line is that there were multiple parameters that can be controlled (and some others that are harder to control) to change thin film tension. Curiously, in the work of Luhmann et al. stress value measurements of stoichiometric silicon nitride (Si_3N_4) membranes and a systematic study on the oxidation behaviour of Si_3N_4 under O_2 plasma treatment, lead resulted in the finding that the O_2 plasma treatment leads to the formation of an SiO_2 film on the Si_3N_4 , which counteracts the intrinsic tensile strength of the films by adding compressive stress to the membrane [256]. A similar strategy is sometimes used to balance compressive stresses of metallic thin films in adding a tensile stressed adhesion layer between the target layer and the substrate.

In the Optimizations Chapter the question if the stress state and the amount of inner tension are responsible for structural imperfections appearing in the FIB milling process of HVM will be addressed. Therefore, a basic home-built thin film stress measurement tool was devised.

Typically, there are three sources of thin film stresses, mechanical stress σ_M during the deposition process, due to clamping of the substrate, thermal stress σ_T , due to high deposition temperatures and different thermal expansion coefficients of the film

3.3 A Basic Thin-film Tensiometer to Estimate Thin Film Stresses

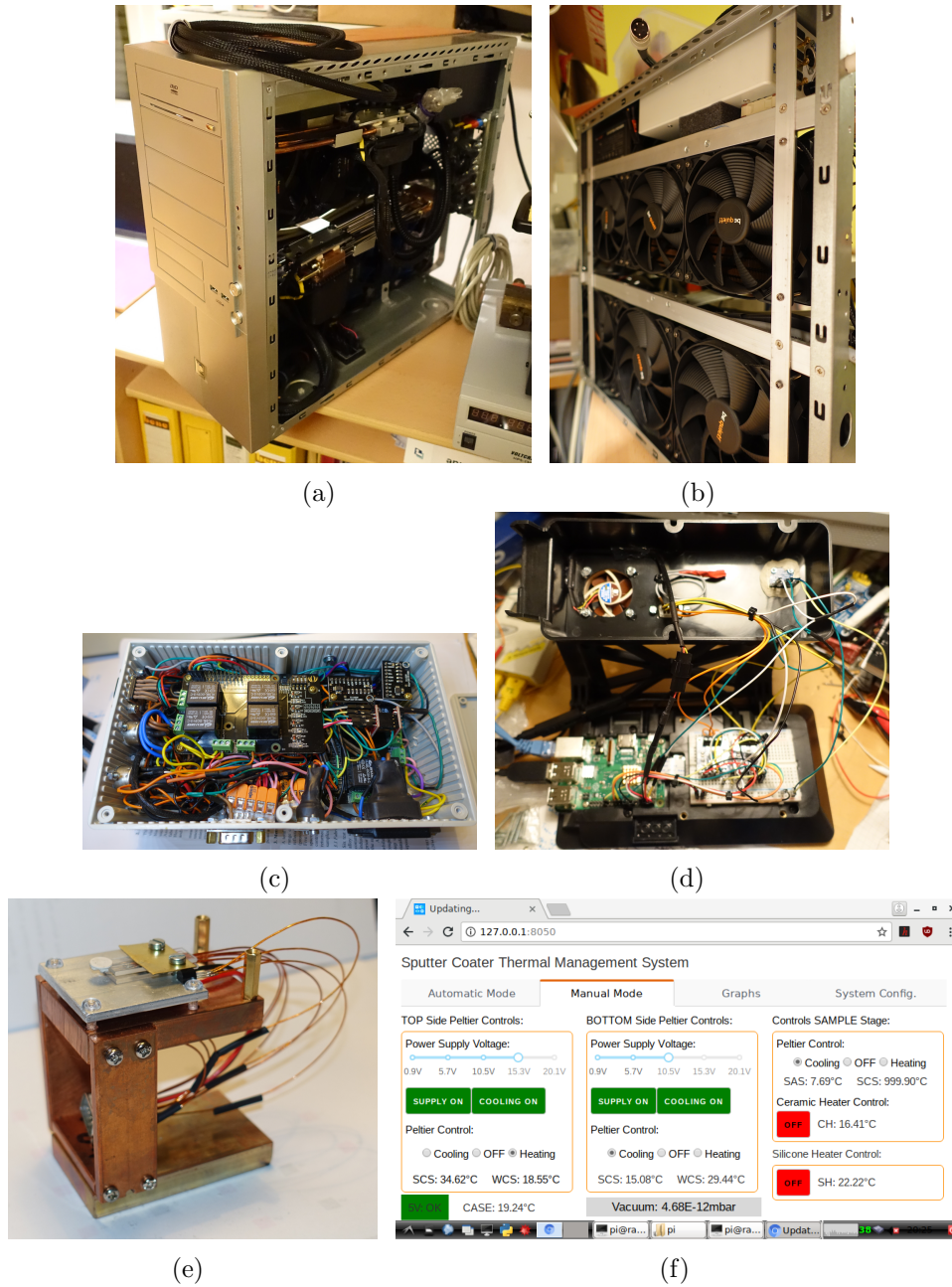


Figure 3.9: Images of the SCTM system. (a) shows the modified personal computer housing containing the two water cooling units, the *Peltier* elements and their heat-pipe connection pieces as well as the electronics box. (b) shows the back-side. (c) depicts the dense packaging of the interior of the electronics box containing the wiring, multiple relays, DACs and ADCs. Panel (d) shows the interior of the RPI with its modified housing and additional ADCs to read out a *PT1000* temperature value from the heating stage. In (e) the home-built heating and cooling stage is shown. A ceramic heater element (white) is placed on top of an Al plate, which is directly mounted on a *Peltier* element and a Cu-frame. (f) is a screenshot of the control program's browser-based GUI.

3 Device Modifications and New Measurement Tools

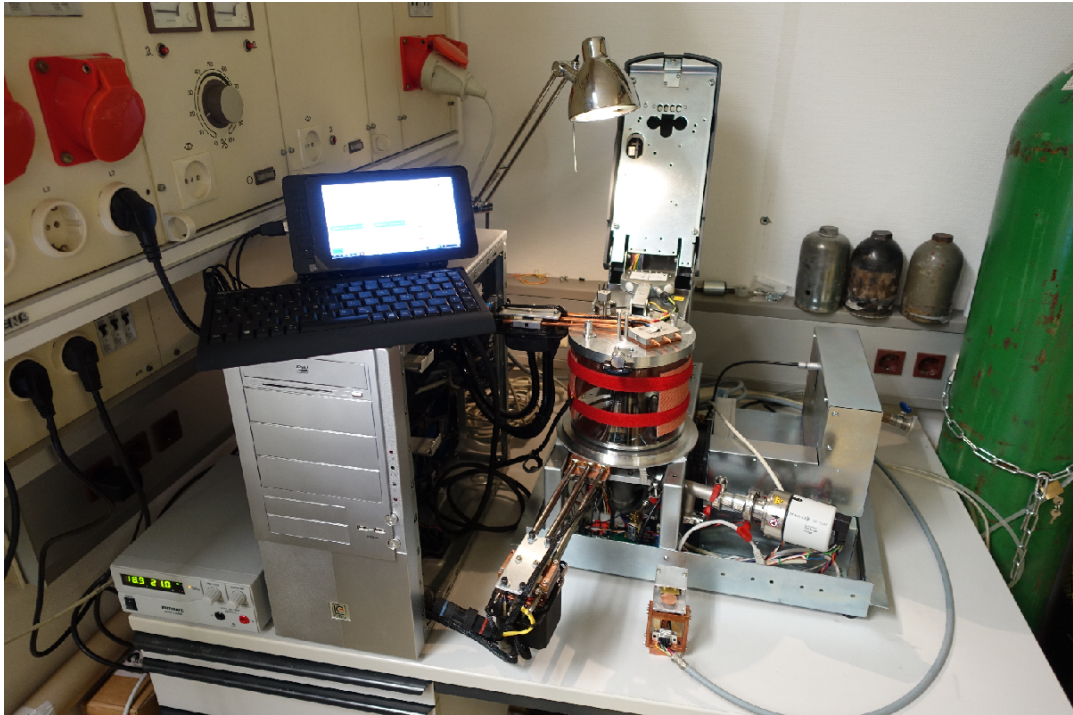


Figure 3.10: Image of the new SCTM, fully assembled and in operation, heating the in-house sputter coater. The heating and cooling stage (lower right corner) was placed outside the coater for better visibility.

3.3 A Basic Thin-film Tensiometer to Estimate Thin Film Stresses

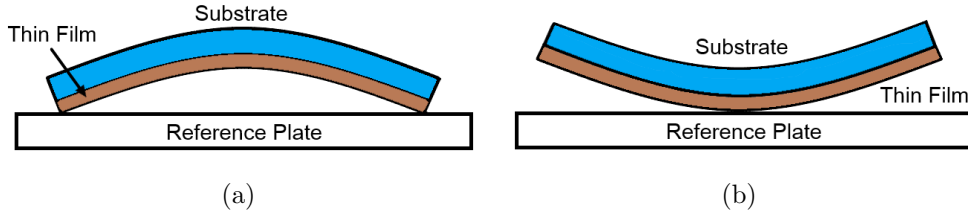


Figure 3.11: Effects of thin film stresses. (a) Tensile stresses in the thin film lead to inward bending of the substrate, while compressive stresses bend the substrate outward (b).

material and the substrate and thin film intrinsic (inner) tensions σ_I , due to lattice misfit, impurities and growth conditions [235, 257]. The sum of these contributions yields the final thin film stress level: $\sigma = \sigma_M + \sigma_T + \sigma_I$. As all the depositions done throughout the thesis were made with a non-clamped substrate at room temperature, $\sigma_M = \sigma_I \approx 0$ can be assumed. The inner stresses of thin films, especially for high melting point materials, can easily reach a few Gigapascal. In combination with relatively thin substrate plates (70 μm to 500 μm), this can lead to a measurable deformation of the substrate, see Figure 3.11.

Besides the more intricate thin film stress measurement methods, which are CCD based, like geometrical optics or an interferometric approach, there is the possibility of using a simple cantilever based method. There, the substrate itself is used as a flexible cantilever that is bent upon tensile or compressive inner stresses in the thin film deposited on it. Additionally, the metallic thin films show very high reflectance, comparable to a high quality mirror, and thus, it was tempting to use a home-built cantilever beam technique, capable of detecting changes in the curvature of the coated 18 mm diameter glass cover slips [258].

Using the Stoney Equation 3.7, which relates the stress of the film σ to the curvature radius R_S of the substrate and some geometrical parameters of the setup, it is possible to determine the stress state and quantity of the deposited thin films [259]. The Stoney equation reads,

$$\sigma = \frac{E_S t_s^2}{6(1 - \nu_S) t_f} \cdot \left(\frac{1}{R'_S} - \frac{1}{R_S} \right), \quad (3.7)$$

where $\frac{1}{R_S}$ and $\frac{1}{R'_S}$ are the curvature of the substrate before and after thin film deposition, and E_S and ν_S are the respective Young's modulus and Poisson's ratio of the substrate. d_s and d_f are the thickness of the substrate and the deposited metallic film, respectively. For $\sigma > 0$ the films show tensile stress, and if $\sigma < 0$, the films exhibit compressive stress. The elastic modulus and the Poisson ratio of the cover slip was taken from the manufacturer's homepage: $E_S = 64 \text{ GPa}$ and $\nu_S = 0.2$ [260]. The substrate thickness was measured by observing the defocus change from the upper to the lower surface of the glass slide with a light microscope and the thin film thickness was determined by using the methods described in Section 2.9.3.

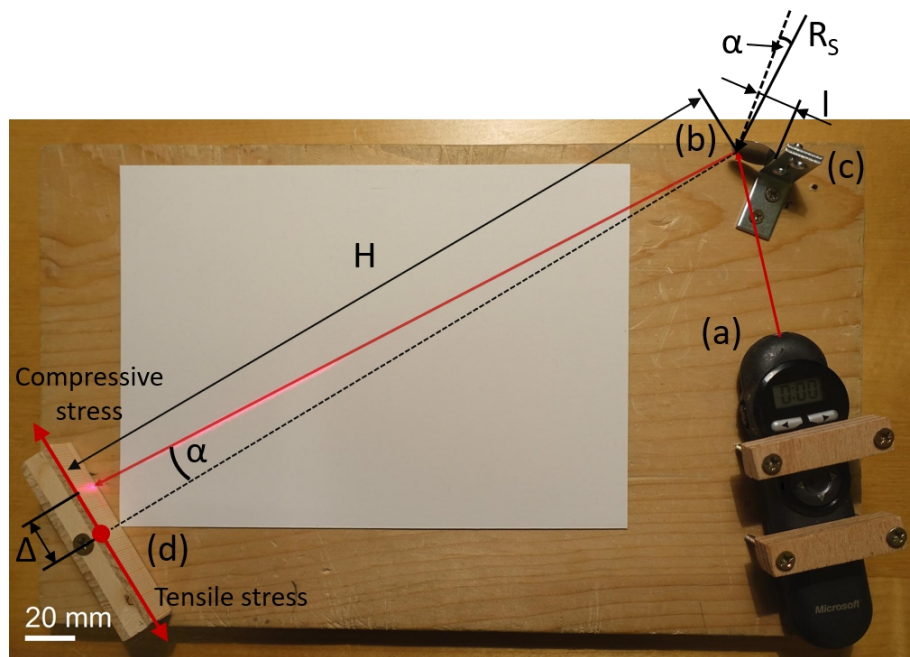


Figure 3.12: Image of the self-built reflection tensiometer with the schematics overlaid. A red laser is used (a) to illuminate the thin films deposited on a $\varnothing 18$ mm and $100 \mu\text{m}$ thick glass slide (b) which is held by a sample holder (c). The reflected beam position Δ is read from a millimetre paper stripe (d), positioned in a distance of $H = 290$ mm. α is given by the beam deflection of a stressed glass slide, relative to the reflected beam of a flat reference glass slide, and can be related to the curvature of the stressed glass slide R_S using the free-standing length of the glass slide l . The whole measurement setup is mounted on a 15 mm thick wooden plate.

3.4 Focused Ion Beam Milling at a Reduced Working Distance

Now the curvature of the substrate had to be measured. This is done by a home-built bending beam reflection tensiometer, as it is depicted in Figure 3.12, together with the schematics, shown as an overlay. It is mounted on a 15 mm thick wooden plate and consists of a red laser emitter (Microsoft Presenter) (a), used to illuminate the thin films deposited on a $\varnothing 18$ mm, and an ~ 100 μm thick glass slide (b). The glass slide has a free-standing length of $l = 15$ mm and is held in place by a sample holder (c). Inner tensions in the thin film bend the glass slide, and the incident collimated beam of light changes its deflection angle α . The change of the deflection angle, relative to a flat reference glass slide, can be determined by reading the reflected beam position Δ on a millimetre paper stripe (d), positioned in a distance of $H = 290$ mm from (b). The deflection angle α can be related to the curvature R_S for the specific setup shown in Figure 3.12 with the relation,

$$\frac{1}{R_S} = \frac{\alpha}{l} = \frac{\Delta}{Hl}. \quad (3.8)$$

Equation 3.8 is an approximate result, only valid for small angles α , which is clearly fulfilled in the present case. As the measurement of the substrate curvature is done relative to a flat reference sample, the term $1/R_s$ in Equation 3.7 vanishes.

A measurement routine consists of five individual measurements, where the rotation of the sample is changed in steps of 90° , to get an indication of the scattering of the deflection angles. Using this basic setup with an estimated mean error of 0.38 GPa, inner stresses of thin films between ± 2.5 GPa have been measured. This value could be further improved by a redesign of the sample holder.

3.4 Focused Ion Beam Milling at a Reduced Working Distance

The available FIB instrument at USTEM is a somewhat out-dated machine. To improve its milling resolution, a rather simple approach can be utilized, consisting of reducing the distance between the sample (hologram-membrane) and the FIB column, i.e., reducing the (free-)WD. This measure increases the convergence angle of the ion-beam and, thus, decreases the spot size, assumed that lens aberrations do not alter the beam profile.

In order to reach a WD of 10 mm⁶ at the FIB column, the sample, placed on a 12.7 mm SEM sample holder stub, has to be moved very close to the SEM column (~ 1.5 mm). In normal operation the instrument's software does not allow for such small WD of the SEM column, because of the danger of a pole touch. In order to circumvent this safety measure, the WD is intentionally set to a feature that is situated way lower than the actual surface of the sample holder, or in other words, the image has to be massively defocused while linking the z-value to the WD. Then, under permanent visual inspection, using the IR-camera in the chamber, the sample can

⁶Note that this is the indicated value in the software, its also the lowest possible value, but the physical WD is ~ 15 mm.

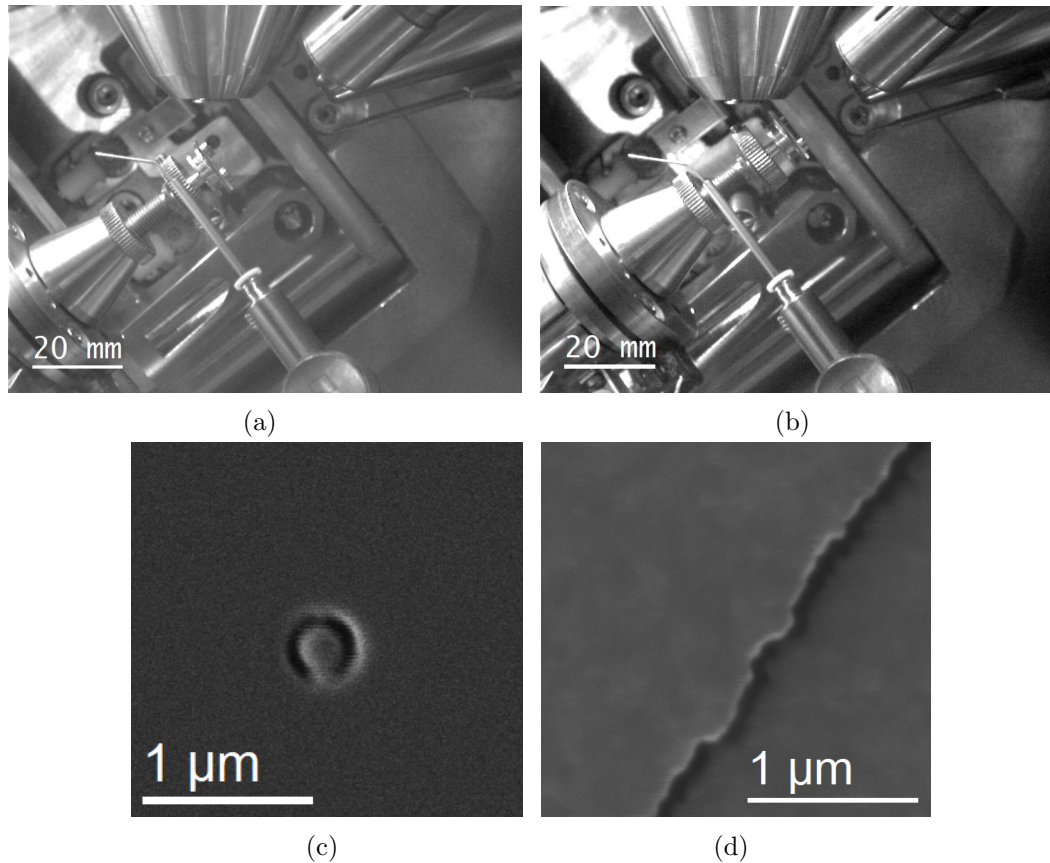


Figure 3.13: Comparison of the stage positioning and the achievable resolution of the two FIB working modi WD 30 mm (a) and 10 mm (b). For standard applications and parallel SEM inspection the sample is brought to the point of coincidence (eucentric height) at a WD of 30 mm yielding a resolution of 30 nm to 38 nm at 30 pA as estimated from the SIM image in (c) using the knife-edge method. Whereas for high-resolution milling a reduced WD of 10 mm yields a resolution of 24 nm to 29 nm for a beam current of 100 pA, estimated from (d). Parallel SEM imaging is no longer possible.

be lifted towards the FIB column, until the minimal WD value of 10 mm, or slightly more for focusing purposes, is reached. Figure 3.13 (a) shows the IR-chamber camera image the sample at the eucentric height and in (b) it is moved to the reduced WD.

SIM images, taken at a WD of 30 mm and at a WD of 10 mm, are shown in Figure 3.13 to illustrate the resolution-gain of that simple measure⁷. There are sophisticated methods to determine the spot size of ion-beams, e.g., using dose arrays in 2D materials [261]. Here, a simple sharp-edge (knife-edge) scan method was

⁷Note that modern instruments use a WD of 4 mm (FEI *Helios* 600i).

used [262, 263] to estimate the spot size, as only the relative spot size change is of interest instead of the absolute value. Also, it is clear that imaging resolution is not the milling resolution, but from milling results obtained (showed in the next chapter), a spot size improvement is evident. In Figure 3.13 (c) an SIM image of a 400 nm annular aperture is shown, taken with an ion current of 30 pA at a WD of 30 mm and compared to an image of a surface feature on an Os membrane, taken at 100 pA at a WD of 10 mm, Figure 3.13 (d). Qualitatively, the image resolution is comparable even though a three-fold higher ion current was used. The respective estimated image resolutions are 30 nm to 38 nm for the higher WD and 24 nm to 29 nm for the shorter WD.

3.5 A Focused Ion Beam Sample Stage for TEM Grids and Membranes

Milling fine structures with periodicities of 200 nm to 1000 nm in the FIB, with outer dimensions ranging from 5 μm to 100 μm , and material thicknesses of a few hundred nanometres can easily last dozens of minutes, or even multiple hours. This puts high demands on the instrument's stability. Drift is thus a major concern in the production of amplitude HVM. There are multiple sources of drift like beam-drift, due to, e.g., sample charging and/or time varying magnetic stray fields, and mechanical sample-drift, originating, e.g., from thermal instabilities, mechanical vibrations and stage instabilities. For example, in order to reduce the influence of thermal instabilities, the sample is allowed to settle down for ~ 1 h, prior to milling critical structures.

The samples, $\text{\O}3$ mm thin Si-chips with the thin film membranes on it, are typically mounted on a Al stub with sticky tapes out of C or Cu. Especially when the sample is tilted towards the FIB column (52°), it may move slowly down. In order to avoid this mechanical drift, a direct and firm connection between the sample and the stage has to be established. Additionally, such a direct connection assures good electrical contact and reduces any charging-induced beam-drift. Milling experiments of HVMs, carried out in Brno at the Institute of Scientific Instrumentation at the Czech Academy of Science (ISI-CAS), in the course of an informal collaboration, showed the beneficial influence of a mechanical firm membrane-mounting.

Therefore, a custom-made sample holder for the FIB was fabricated, especially suited for the 3 mm TEM aperture- and membrane-disks, used for HVM production. Figure 3.14 (a) shows a schematic cross-section of the new holder. The basis is a standard $\text{\O}12.7$ mm Al SEM sample holder stub (light blue), where a central bore of $\text{\O}1.8$ mm \times 3.0 mm is placed. This bore ensures that no part of the fragile hologram membranes, located in the centre of the Si chip (red), touches the stub when mounted from upside down. A step $\text{\O}3.5$ mm \times 0.1 mm was added to centre the aperture or Si frame on the stub and to hold it in place laterally. Note that the frame thickness of a SiNx membrane is typically 200 μm , compared to the thickness of an aperture with 250 μm . For the vertical fixation a 0.2 mm thick Al sheet (dark blue in Figure 3.14 (a)) was cut to the size of the stub. Five holes were drilled into that sheet, a central,

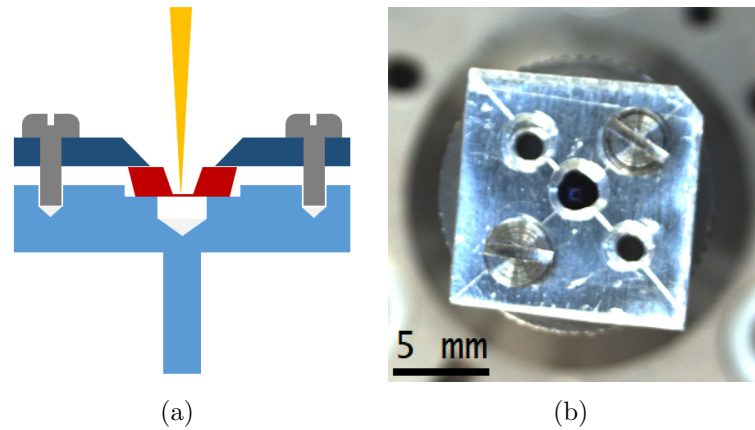


Figure 3.14: (a) Schematic cross-section of the self-built FIB holder for $\text{\O}3$ mm TEM apertures and membranes and a navigation camera top view of it in (b). (c) Navigation camera image of the self-built TEM membrane holder. A 0.2 mm Al sheet is fixed to a standard 12.7 mm SEM sample holder stub by two M2 screws. The SiNx membranes are mounted in a central hole and the two additional bores are needed for sample loading. Due to its slim design there is no acute danger of a pole touch, when working at a WD of 10 mm.

$\text{\O}2.0$ mm, bevelled one, which provides access for the Ga-ion-beam, drawn in yellow, to the membrane area, two alignment holes, that are only used when the sample is loaded, and two fixation holes, that are used to press the Al sheet onto the aperture/membrane via two M2 screws (grey). When building the sample holder, care was taken that no parts protrude beyond the $\text{\O}12.7$ mm stub more than ~ 1.5 mm, because of the danger of a pole touch while moving the sample towards the WD 10 mm position, as illustrated in Figure 3.13 (b). Figure 3.14 (b) shows a top view of the holder, loaded with a SiNx membrane. The results on milling Os HVM, presented in the next chapter, were made employing this sample holder.

3.6 Focused Ion Beam Milling Drift Correction Script for the Production of Holograms

The high-stability stage, described in the preceding section, guarantees a minimal mechanical drift of the sample, while other sources of drift, especially the variation of the electromagnetic environment, still complicate the situation and add undesired milling artefacts to the hologram structures. Measurements of the Ga-ion-beam-drift rate, made by a colleague, imaging a fiducial marker every 12 s for up to 14 min, show drift rates up to 50 nm/min at night, with a characteristic monotonic and single-directional behaviour. Measurements done at daytimes show a reduced drift rate of

3.6 Focused Ion Beam Milling Drift Correction Script for the Production of Holograms

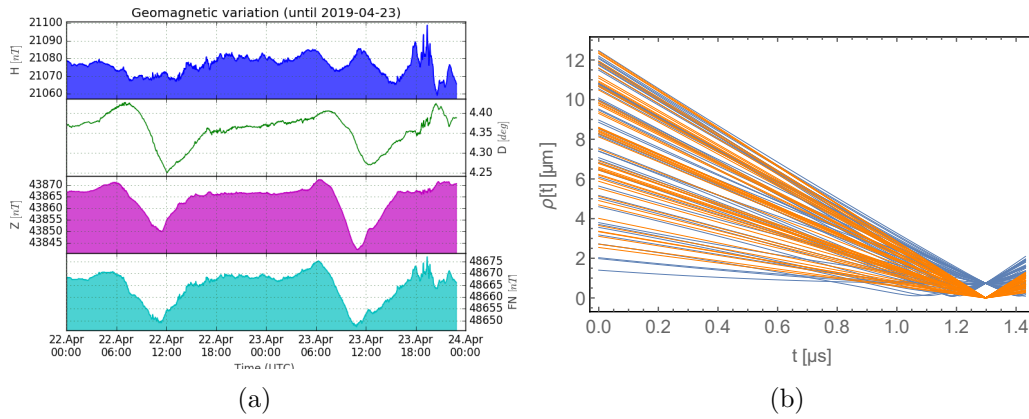


Figure 3.15: (a) Typical geomagnetic variation in Vienna, as obtained from the *Conrad Observatory* [264]. The uppermost plot shows the horizontal magnetic field component (H), below the declination (D) and vertical component (Z) are shown. The bottom plot represents the total field intensity (FN). From the plots, field variations of the order of $\sim 0 \text{ nT h}^{-1}$ to 30 nT h^{-1} are possible. (b) MC particle trajectories calculation, showing the radii ($\rho(t)$) of fifty trajectories of 30 keV Ga-ions over the course of 41 cm ($1.4 \mu\text{s}$) when subject to no field (orange lines), and inside a weak magnetic dipole field, oriented perpendicular to the page plane and of the order of 6.5 nT (blue lines). The beam deflection is of the order of 1 μm , exemplifying the principal possibility of an earth magnetic field influence on the ion-beam trajectory.

$\sim 15 \text{ nm/min}$, but with a clearly more erratic and non-predictable pattern. While the daytime drift pattern could be understood as affected by artificial sources, like elevator-, metro- and tram power-lines in close vicinity, the night time drift behaviour is somewhat strange⁸. One could speculate that this behaviour is a consequence of variations in the earth magnetic field strength, which amounts to tens of nanoteslas over an hour [265], see Figure 3.15 (a). Such variations, either of artificial- or natural-origin, result in a beam-shift of a few hundreds of nanometres for a 30 keV Ga-beam, see Figure 3.15 (b). A more in-depth study would be needed to clarify this issue.

Independent of what is causing the beam-drift (and sample-drift), its presence is detrimental for the goal of producing large-scale high periodicity diffraction gratings. Therefore, the scripting option and an included visual matching routine⁹ of the FIB instrument were employed to correct for any deviations of the beam and/or sample

⁸Notably, the best milling results for complex holograms could be achieved in the time slot after eight o'clock in the evening and before half past six in the morning. This is true for work done at USTEM and also seen by our informal collaboration partners at the Leibnitz Institute for Solid State and Materials Research Dresden (IFW-Dresden).

⁹Details on the scripting language can be found in the document's 'runscript.pdf' and 'auto-script_technical_note.pdf', located at the instrument's control computer.

position while the milling is in progress.

The drift correction routine (DCR) is based on a visual matching routine that searches for fiducial markers after each stream-file-pass. The fiducial markers have been milled into the thin film membrane prior to the actual milling of the hologram structure. If there is a difference between the actual- and the former-position of the fiducial markers, larger than a preset threshold value, the script adjusts the beam-shift according to the measured difference vector. The stage is not moved by the script.

Now some details on the DCR operation and typical parameters will be given. Figure 3.16 gives an overview of the drift dialogues and the available options. Assuming that the sample area of interest has been found and the beam is aligned, the first step is to start ‘runscript xT’, to load the main file for the drift correction script (*.psc file) Figure 3.16 (a). Note that the name of the stream file(s), containing the actual milling points, etc., has to be manually written to the main script file before loading it. Up to now, no better solution was found. Also, the ‘Visual Match’ option must be checked, for the drift routine to work¹⁰.

The drift routine is split into three main dialogues, see Figure 3.16 (b, c, d). In the first dialogue, panel (b) of Figure 3.16, ‘Premilling Options’ are summarized, e.g., the beam-shift calibration, which is the relation between shift excitation and actual shift distance, can be started. It changes from time to time and, especially when working at massively reduced WD, this automated routine ought to be run before milling. Second, via the ‘Drift Corr’ button a ‘Drift Correction Routine’-dialogue opens, as depicted in Figure 3.16 (c). There, the user can either deactivate the DCR or change the kind of image-feature, that is sought by the visual match routine, from being a circular- or a cross-marker, or a certain image-feature, nearby the desired hologram region, as well as the mask hologram itself. So far, the circular markers yielded very good results, while the two other options could not yet be tested thoroughly. When pressing the ‘MarkersDC’ button, various options to define the markers can be set. For example, the shape of the marker can be changed from one, which represents circular markers, to two, representing cross markers. Also, their radius/size and z-depth can be chosen together with the number of markers. In Figure 3.16 (e) four markers with a radius of 0.3 μm and a z-depth of 0.3 μm ¹¹ have been milled into a C-coated Os/SiN_x thin film. These parameters turned out to work well for this material combination. In case that the hologram structure is not yet finished after the predefined number of passes, the number of extra passes to mill can also be defined, in this option panel. Third, in the pre-milling options dialogue important parameters for the milling and drift correction process have to be entered. For example, entering the magnification determines the actual hologram size, while

¹⁰Mind that the drift correction algorithm, together with the *Cognex Vision Pro* visual match window, only works if the quadrant, which is used to display the SIM image, is set to ‘Default’ in the ‘Color’-tab, which is located in the ‘Enhanced Image’-panel and the checkbox in that panel is disabled. The panel can be found on the right hand side of the FIB control software.

¹¹This value assumes a Si sample, so it does not represent the actual z-depth milled, because of differences in the sputter yield.

3.6 Focused Ion Beam Milling Drift Correction Script for the Production of Holograms

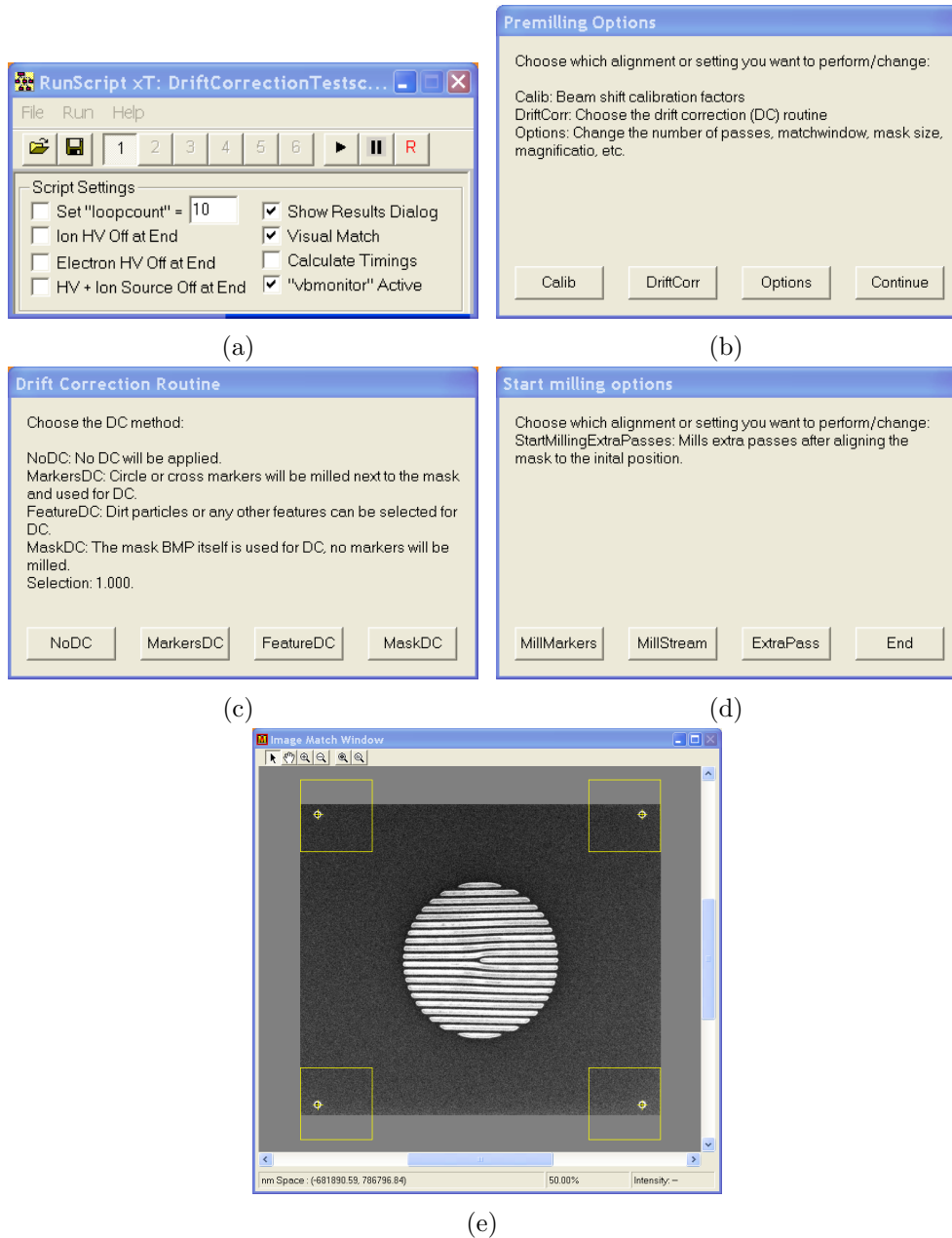


Figure 3.16: Panel of the FIB drift correction routine dialogues. (a) The ‘runscript xT’ program is used to load and start the drift correction script. (b) In the ‘Pre-milling Options’ dialogue the beam-shift calibration routine can be started, the drift correction options dialogue, shown in (c), can be opened, drift correction relevant options are accessible via the ‘Options’ button and the milling options, shown in (d), are accessible via the ‘Continue’ button. (c) In the ‘Drift Correction Routine’-dialogue the kind of drift correction used can be chosen, and marker associated parameters are accessible via the ‘MarkersDC’ button. (d) The ‘Start Milling Options’-dialogue contains the possibility to start milling the fiducial markers, to start milling the stream file using the DCR and, if necessary, to start milling of extra passes. (e) The matching window always appears or is updated when the drift correction is active or some user input is needed, e.g., the manual position determination of the markers.

the number of passes depends on the membrane thickness, material, ion-beam current and dwell time. Note that there is a, so far inexplicable, factor of 2.331 between the indicated magnification and the actual magnification used for milling, e.g., for a 10 μm hologram stream file, the indicated magnification is 15 kx, whereas a value of 6434.32 kx has to be entered in the option-panel. For the visual matching routine a threshold level can be set, which defines the sensitivity of the match command, i.e., specifying the allowable amount of difference between the source bitmap and the matched images. The preset value is 0.5, while a value of 0.3 worked well in the case of Os-layers. The matching window-size, see the yellow squares in Figure 3.16 (e), can be defined in units of ‘the field of view’. Mind that the matching windows should not overlap with the hologram structure, as this would complicate the feature identification for the matching routine. The maximal allowed absolute drift distance in microns (drift control level) can also be adjusted. A value of 0.015 μm worked reasonably well. If values larger than that are measured after a drift correction attempt, the DCR starts another drift correction loop and continues, until either the measured drift is lower than the preset drift control level, or the preset maximal number of loops is reached. The last set of options deals with various ‘sleep times’, e.g., it can be defined how long the system waits for the stage to stabilize before milling.

When the pre-milling adjustments are done, pressing ‘Continue’ opens the ‘Start Milling Options’, see Figure 3.16 (d). Before starting the actual stream file milling, using the ‘MillStream’ button, the markers have to be produced by using the ‘Mill-Markers’ button. After pressing the ‘MillStream’ button, the user has to tell the program the position of the markers. For that the ‘Image Match Window’, Figure 3.16 (e), pops up and the user is asked to manually click on the centre of the first marker, marked by the small yellow crosses in Figure 3.16 (e). If there is more than one marker, this is repeated for all markers. In principle this procedure could also be done automatically by the visual match routine, but it turned out that this results in a non-optimal identification of the feature position. The DCR now loads the stream file and starts to mill the points given therein. When milling of the stream file is finished, a drift correction loop starts, grabbing an image with the same dwell time and pixel-size, as was used prior to starting the script. This is important because the image contrast and with that the pixel dwell time for imaging, as well as the pixel-size, needs to be sufficient for a successful image matching process and for an accurate drift correction. On the other hand, a too high dwell time and pixel density may remove too much of the thin film layer and alter the image contrast. Therefore, trial runs have to be conducted to figure out a working set of parameters. Ideally, the image contrast in the marker region is conserved throughout the whole milling process, otherwise the visual match routine may fail if the image contrast significantly reduces or changes while milling the hologram. Then the coordinates of the markers are determined by the matching routine, and beam-shift is changed according to the drift vector. If more than one marker is used, a mean drift vector is calculated. Before going on milling the next pass, another frame is grabbed in order to check the result of the beam-shift action, in case the absolute drift value is

3.6 Focused Ion Beam Milling Drift Correction Script for the Production of Holograms

larger than the preset value, another drift correction loop is started. The process is halted, if it is not possible to reach the desired drift correction within the predefined number of loops, or the drift was too high, such that the markers moved outside the matching window search region. Otherwise the predefined number of passes will be executed and additional extra passes can be milled through the according option in the ‘Start Milling Options’ dialogue.

When starting the DCR automatically, a logfile named ‘autolog.n’ is created. n can be defined in the options panel in the pre-milling options dialogue. There, all the measured drift correction values are stored, e.g., for later inspection.

4 Optimization Strategies for the Production of Binary Holographic (Amplitude) Vortex Masks

A prerequisite for the successful application of EVBs, either in vacuum or incident on a sample, is a clearly defined HVM geometry, delivering as pure as possible OAM eigenstates. The same is true for HVMs, used as vorticity filtering devices in a TEM. Additionally, in order to achieve high vortex order separation, the grating periodicity should be very fine and, as a means to improve the SNR of both, incident and vorticity filtering EMCD experiments, the dimensions of the HVMs need to be large. To achieve these design criteria, various optimization routes have been tested. Ranging from testing alternative scan strategies, over looking at the influence of material properties, like density and inner stresses, to testing the diffraction efficiency of binary phase masks.

4.1 Vector Scan Approach for Focused-Ion-Beam Milling of Holographic Vortex Masks

Generally, FIB milling proved to be a robust and reliable technique to produce HVMs, with ever-increasing demands on structure size and fidelity, methods to improve the ordinary milling strategy, using raster- or serpentine scanning, were sought [266]. In this paper a ‘vector-scan’-technique, using spiral paths instead of the raster-scan approach, has shown to be beneficial for the repair process of semiconductor circuits, as it provided precise and more arbitrary control over the ion-beam. Here, it will be tested if such a vector-scan-strategy improves the milling results of HVM over the raster-scan approach.

Therefore, a *Mathematica*-based program has been devised that is able to calculate spiral vector paths for the milling areas in binary hologram bitmaps and converts them into FIB readable stream-files. These stream files were tested and optimized at the in-house FIB instrument and sent to our collaboration partners at the IFW-Dresden. There they were used to mill finely structured large-scale HVM and were compared to the raster-scan method.

Typically, the binarised hologram is stored as 24 bit RGB bitmap (BMP). Its green component determines if the beam is blanked; any other value than 0 will unblank the beam. When this BMP is loaded into the scan engine of the FIB instrument, its pixel arrangement is converted into a raster-scan pattern, as illustrated in Figure 4.1 (a). The ion-beam is moved over the whole area of the BMP, line by line, and depending

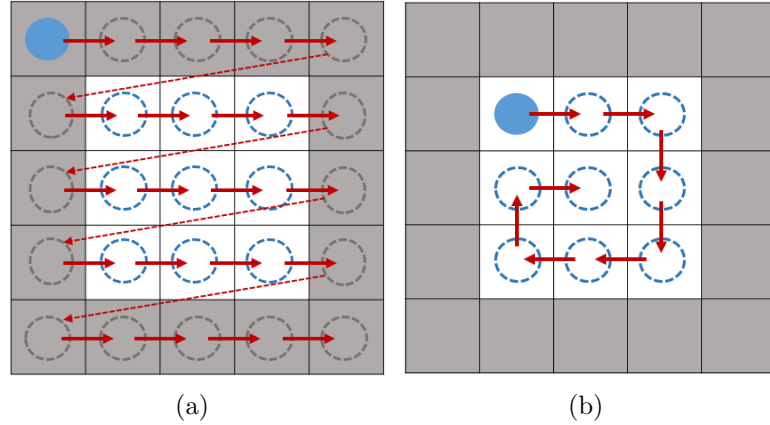


Figure 4.1: Comparison of ion-beam (blue circle) movement strategies. (a) For ordinary raster-scanning the beam scans over the whole image, line by line, with intermediate fly-backs. The ion-beam is also moved over black pixels, but blanked (grey broken line circles). (b) Vector-scanning strategy, following a spiral path only on white pixels where the beam is unblanked (blue broken line circles).

on the pixel value, the beam is blanked or not. The blue channel determines the dwell time, whereas for binary holograms always a value of 255 is used, being equal to the maximal dwell, which is entered in the user interface. Lower values are linearly interpolated from a fixed dwell time table. Typically black and white images are generated, where white pixels represent the milling points. Contrary to that, the vector-scan approach guides the ion-beam along arbitrary paths, e.g., along spiral paths, as shown in Figure 4.1 (b). Notably, the beam is only moved over milling regions. Evidently, other scan strategies could be envisaged like random walking, zick-zack or intermittent scanning, etc., but only the spiral paths will be tested in this work, as they seem plausible from a physical point of view.

To realise the vector-scan approach, *stream files* are used to tell the FIB instrument the exact position, milling sequence and dwell time of the ion-beam. A stream file, is an ASCII text or binary file that addresses the patterning 12 bit (16 bit for a *Helios* instrument) DAC directly. Because a 12 bit DAC is used, the patterning field of view is divided into 4096 steps (65 536 for a 16 bit DAC). The x -range is, thus, 0 to 4095 and in the vertical direction it is approximately 280 to 3816, as the data bar is overlaid to the image in that region¹. Figure 4.2 shows an example of a stream file. The file must begin with an ‘s’, indicating a stream file. For a *Helios* machine it should be ‘s16’. The second line defines the number of passes, here 40, and the third line indicates the total number of x, y -coordinates (pixels) in one pass, in this example 25. Note that for the Quanta FIB the maximum number of milling points is 1 MP and for *Helios* instruments, e.g., used at the IFW-Dresden and Central European

¹In fact the whole y -range is accessible, as has been tested with large-scale masks.

4.1 Vector Scan Approach for Focused-Ion-Beam Milling of Holographic Vortex Masks

s	96 2867 2867	96 1639 2048	96 2457 1639
40	96 1229 2457	96 2048 2048	96 2867 1639
25	96 1639 2457	96 2457 2048	96 1229 1229
96 1229 2867	96 2048 2457	96 2867 2048	96 1639 1229
96 1639 2867	96 2457 2457	96 1229 1639	96 2048 1229
96 2048 2867	96 2867 2457	96 1639 1639	96 2457 1229
96 2457 2867	96 1229 2048	96 2048 1639	96 2867 1229

Figure 4.2: An example of a stream file, with the first character indicating the string, the second line defining the number of passes, the third indicating the total number of milling points. The following strings are the dwell time and x, y -coordinates.

Institute of Technology, Brno, (CEITEC), it can be 8 MP^2 . Each coordinate tuple is prefixed with the dwell time in units of $0.1 \mu\text{s}$, thus, 96 means $9.6 \mu\text{s}$. The dwell time range is $0.1 \mu\text{s}$ to $4600 \mu\text{s}$, with 124 values distributed, approximately logarithmically, within this range.

The spiral vector-scan paths, as sketched in Figure 4.1 (b), for any binary HVM and in principle for any structure that consists of connected regions, are generated and converted to the stream structure (described above) by a custom search algorithm which has been implemented in *Mathematica*. As an input, this program needs the hologram BMP, which is calculated using Equation 2.38, given in Section 2.4.4, and an according text file with some structure- and milling informations. Both are produced with a self-made Gatan Digital Micrograph (DM) script. The routine then loops through every pixel P_i of the binarised image, as illustrated by the blue dot in Figure 4.3 (a), starting in a corner of the image. If a white pixel P_{i+1} is detected, this pixel is added to a list that contains the paths and a vector $\mathbf{v} = P_{i+1} - P_i$, and its perpendicular vector \mathbf{v}_\perp is calculated. Using these vectors, the routine defines a seven-pixel-long U-shaped search path, indicated by the black arrows in Figure 4.3 (a) and searches for other white pixels in the nearest neighbours of P_{i+1} . When another white pixel is found on that path, it is also added to the list of vector-scan points. Additionally, these found path pixels are set to zero in a copy of the initial image, as means to control that there are no duplicates in the scan paths. The algorithm thus finds the hull of a connected region in the image and adds path points, going in circles from outside in. The routine can also handle very narrow elongated regions (corners) of the structure, where so-called undercutting occurs. After the paths are found the routine rearranges and sorts the paths according to the user's choice, depending on the specific hologram geometry, see Figure 4.3 (b) as an example. There, the paths are overlaid to the hologram, where the numbering and colour-coding indicates the milling sequence of each path/region. Additionally, the green and red dots represent the starting- and end-points of the milling paths, respectively.

Figure 4.4 (a) shows the result of an early milling test of a $m = 250$ *Bessel* HVM

²Note that when producing the stream file, there must not be spaces at the end of the file, otherwise the FIB will not load it.

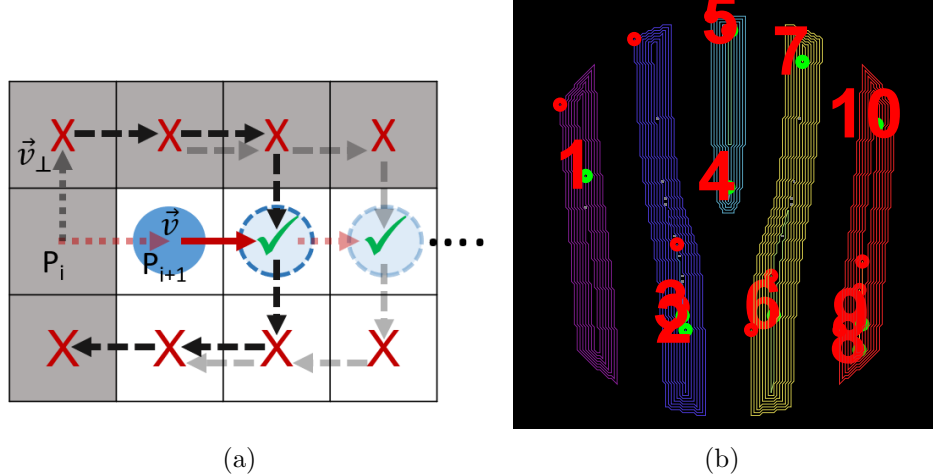


Figure 4.3: (a) Schematics of the search algorithm, used to detect the outer boundaries of a connected region, i.e., holes or vacuum areas in a HVM. (b) Example of the spiral vector paths found for a fork dislocation mask. Milling is done starting at region or path one and so forth. The green and red dots indicate the respective starting- and endpoints of the paths.

($\text{Ø}50 \mu\text{m}$, $g = 2.5 \mu\text{m}$), using the above described method to produce stream files. The substrate was a 310 nm Pt thin film, deposited on 200 nm SiNx and the milling was done using inward spiral paths, just like shown in Figure 4.1 (b), using the in-house Quanta 3D FIB, operated at 30 kV.

Massive redeposition, that is material that was removed at one site is not completely removed from the structure but rather deposited on sites in close proximity to the milling site, can be observed. Redeposition strongly reduces the rate of material removal and, thus, the voids between the grating bars, typically free of any material, are totally obstructed. Milling the same structure using an outward milling scan-strategy³, see Figure 4.3 (c), yields a completely different picture, Figure 4.4 (b). Now, the hologram structure is well reproduced and, as shown in the inset, redeposition is minimized. This clearly shows that the milling strategy can dramatically influence the milling outcome.

Thus, for the following milling tests the outward-spiral-paths scan-strategy will be used. Moreover, after each pass the milling sequence of the single regions is reversed as well as the handedness of the spiral paths, as a potential means to reduce milling artefacts stemming from using only a single scan direction [25]. To test if there are differences in the hologram structure between the ordinary BMP or raster-scan strategy and the spiral paths scanning, two very large $m = 1$ HVM structures with the same outer diameter of $50 \mu\text{m}$ and nearly the same grating periodicity of $g = 630 \text{ nm}$ and $g = 600 \text{ nm}$ were produced at the IFW-Dresden, using a state-of-the-art FIB

³A Ga-ion current of 50 pA, a dwell time of 270 μs and 50 passes were used. To reduce the influence of drift, the milling was done overnight (2:00 a.m. to 4:55 a.m.).

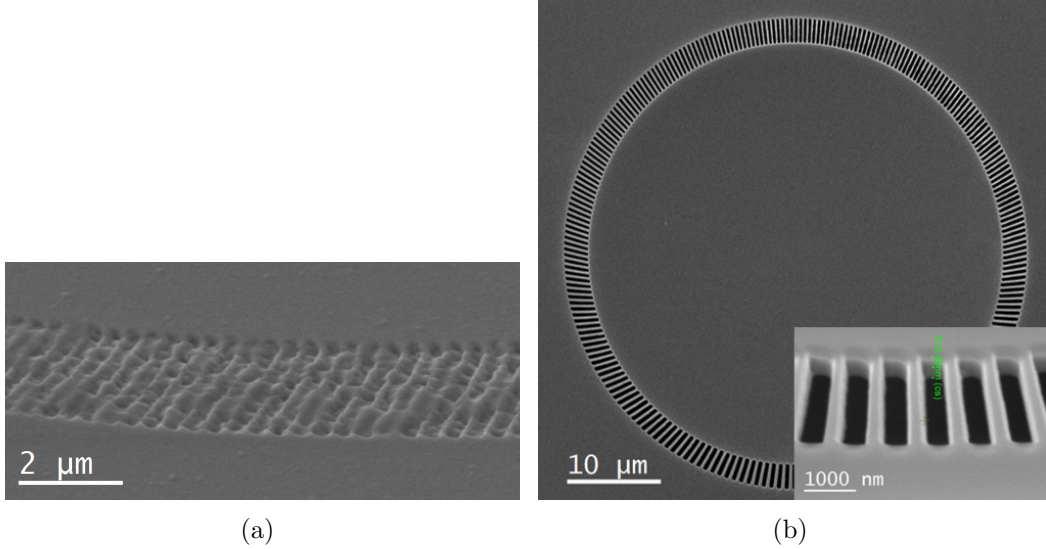


Figure 4.4: Influence of the milling direction. (a) Massive re-deposition found after inward spiral stream file milling on a $m = 250$ Bessel vortex mask. (b) The same structure as in (a) using outward spiral milling.

(FEI, *Helios* nanolab i600 operated at 30 kV) on the same thin film, see Figure 4.5⁴. The substrate was a 310 nm Pt free standing thin film, that was deposited using radio-frequency sputter deposition, and floated off a NaCl crystal. For the FIB milling a Ga-ion current of 230 pA was used and the BMP, as well as the stream file pitch, was 19 nm. In order to stabilize the grating structure, a second-order grating had to be added to the hologram structure with a periodicity of 5 μm and a bar width of 145 nm and 420 nm for the BMP and stream file hologram, respectively. The duty cycle, i.e., the void to bar-width ratio, in the BMP was chosen to be 50 %, such that the milling region is half the width of the bar, while in the stream file it was 88 %. These values resulted in a duty cycle of 83 % and 122 % for the HVM shown in Figure 4.5 (a) and (b), respectively. Note that achieving an ideal duty cycle of close to 100 % is a matter of trial and error, and while the BMPs files were already optimized before this comparative run, the stream file was generated upon experiences from in-house milling tests, which is also true for the stabilisation bar width. The differences between the achieved and the chosen duty cycle are practically the same for the BMP and stream milling strategies, being 33 % and 34 %, respectively. This could be expected as the same beam current, and, thus, the same beam profile, was used in the test. Besides the apparent differences between the raster-, Figure 4.5 (a) and the vector-scan-test, Figure 4.5 (b), due to the different duty cycle and stabilisation bar width, the overall grating quality is the same. There are no significant differences visible between the two milling strategies (see the insets), at least not larger than the

⁴A disk of 20 μm in the centre was left out, as means to increase the detected EMCD signal, which will be described in the vortex EMCD section.

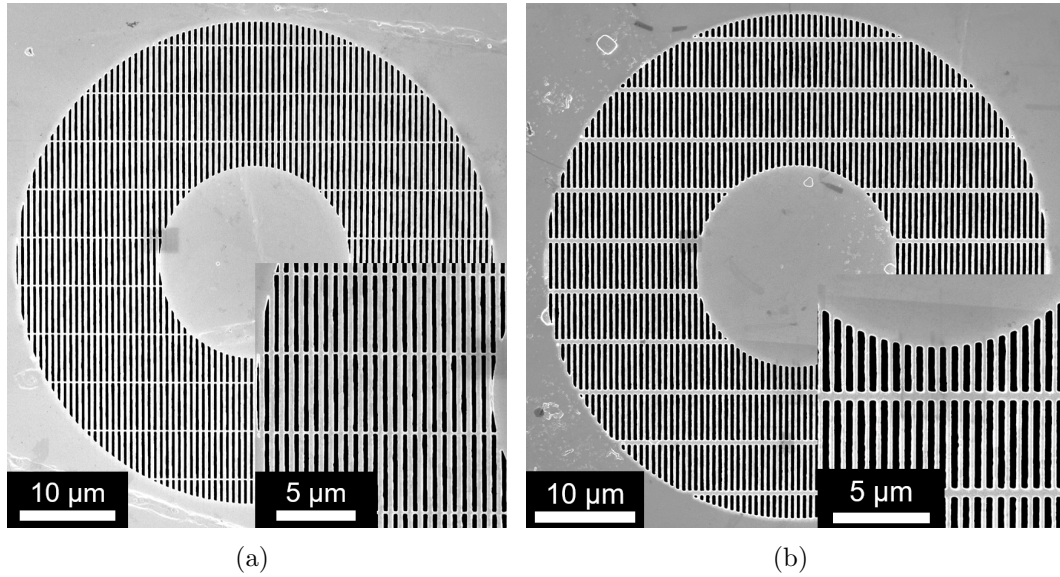


Figure 4.5: Comparison of HVM milling results using (a) raster-scanning and (b) vector-scanning. Besides the apparent differences in the stabilization grating bar width and the duty cycle, there are no differences in the general fidelity of the grating.

thin film inhomogeneities. This coarse granularity, of the order of 20 nm to 50 nm, could be a result of sputter yield variations across the thin film, as a result of different crystal grain orientations.

A second milling test, using the same instrument and full HVMS with a grating periodicity of $g = 623$ nm for the BMP milling and $g = 600$ nm for the stream file milling with the same film thickness and material, but a more homogenous thin film quality, has been conducted at the IFW-Dresden. The same ion current as in the first test was used, but the stream file pitch was reduced to 11.5 nm and a dwell time of 200 μs with 8 passes was used, including 4 passes with a positive and 4 passes with a negative chirality of the spiral paths. The second-order grating bar width was 100 nm and 190 nm for the BMP and stream file hologram, respectively, and the duty cycle, for the BMP milling test, Figure 4.6 (a, c), was measured at 103 % (initially: 50 %). For the stream file test, given in Figure 4.6 (b, d), it is 113 % (initially: 54 %). The resulting SEM images, shown in Figure 4.6, do again not show any significant differences, apart from the second-order grating bar width and the stream file test missing ~ 5 % of the structure, which is probably due to the higher pixel density, such that the number of milling points was too high. Though, looking at the magnified images of the holograms, given in Figure 4.6 (c, d), there are faint differences, e.g., the BMP milled grating bars in (c) show small steps (marked by the left red arrow) of 20 nm to 30 nm height, which are not visible in (d). There, structural defects are smaller than 10 nm. Also, there are slight asymmetries apparent at the end of each

4.1 Vector Scan Approach for Focused-Ion-Beam Milling of Holographic Vortex Masks

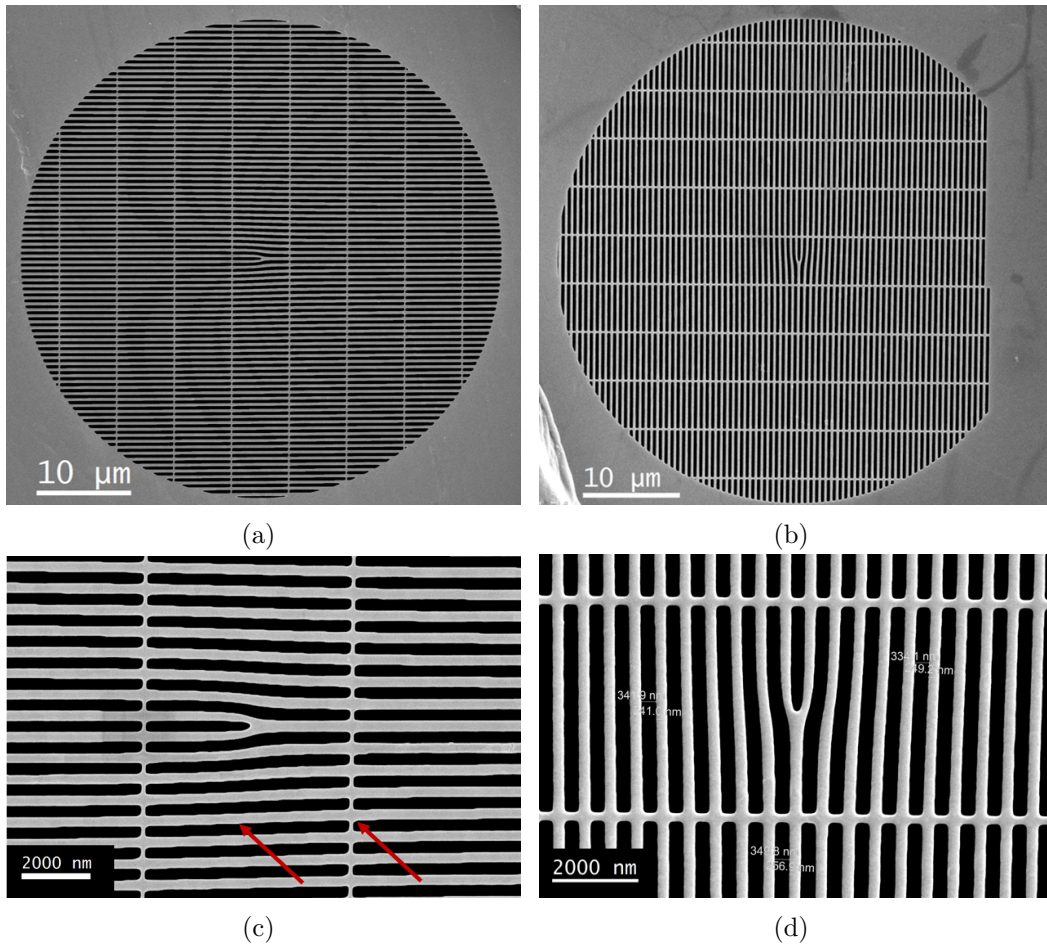


Figure 4.6: Comparison of HVM milling results using (a) raster-scanning and (b) a vector-scanning strategy with improved thin film quality and a higher pixel density of the stream file. Only faint differences, marked by the red arrows, are observable in the zoom in images between the BMP-milled (c) and the stream-file-milled structure (d).

void region (marked by the left red arrow), whereas the stream file mask is perfectly symmetric.

So, in principle, the vector-scanned hologram reproduces the calculated structure slightly better, but the asymmetries observed, stem most likely from drift while milling the structure, and could also be present in vector-scanned masks. Also, the steps are an artefact, that is not a scan-strategy-related effect, but is due to the achievable pixel density using BMP as opposed to stream files. Using stream files is, thus, not so much a matter of the scan-strategy, but rather a possibility to increase the achievable pitch parameter way below half the ion-beam spot size, which was in the present case 38 nm. As already mentioned in the beginning of this section, every pixel in a BMP counts as a ‘milling’ point, including the black pixels, whereas stream files only contain the actual milling points, which is a fraction of $\sim 25\%$ for the present structures, and, thus, $\sim 75\%$ more pixels can be packed into a stream file. Note that the slightly higher duty cycle of the stream file milling test is a matter of adjusting the initial duty cycle, but not a principal drawback.

Another issue, when milling holographic structures of that size and/or in thick (heavy) metal membranes, is the achievable milling rate, defined by:

$$R = \frac{Ad}{It}, \quad (4.1)$$

with A being the whole milled area, I the ion current, $t = t_{Dwell}N_P N_{MP}$ the total beam dwell time, with t_{Dwell} being the dwell time on one pixel and N_P the number of passes needed to mill through the thin film of thickness d , and N_{MP} being the number of milling points. Using the relation $N_{MP} = A/l_{Pitch}^2$, where l_{Pitch} is the pixel pitch length, Equation 4.1 can be written as,

$$R = \frac{dl_{Pitch}^2}{It_{Dwell}N_P}. \quad (4.2)$$

The higher the milling rate, the faster the hologram is produced and, thus, drift is less influential. Estimating the milling rate for the cases given above, yields a milling rate of $0.08 \frac{\mu\text{m}^3}{\text{nC}}$ for a raster-scanning milling test (not shown), where 200 nm of Pt were used with a dwell time of 800 μs , 5 passes and an ion current of 230 pA. For the vector-scan milling test, given in Figure 4.6 (b, d), a milling rate of $0.11 \frac{\mu\text{m}^3}{\text{nC}}$ is calculated, which would be an impressive improvement of 37% in the milling rate. But this number has to be treated with caution, because there are multiple error sources, e.g., the beam current varies with aperture usage time, older apertures show higher than nominal currents, another thin film was used, the high dwell time may cause re-deposition, reducing the effective milling rate, and additionally drift could have minimised the milling rate as well.

So there are some benefits of stream file milling over BMP milling, but their effects are weak and most likely not directly associated with the scan-strategy per se, but rather a result of the higher pixel density and the higher milling rate and, thus, a lower milling time consumption could reduce drift issues, but has to be further

analysed. Another aspect, pointed out by these results, is the influence of the thin film characteristics on the milling outcome, which will be covered in more detail later on.

4.2 Testing a Spatial Dwell Time Modulation as a Means to Improve the Grating Cross-Sections

The above experimental tests showed, that the hologram structure can be well reproduced in the lateral direction, using state-of-the-art FIB milling. In the vertical direction, high-aspect ratios, that is the relationship between depth and the width of a milled structure, are synonymous to sharp and clearly defined edges of HVM structures, which are crucial for the production of the desired pure OAM states of EVB. The Ga-ion milling parameters, like beam current, dwell time, the number of passes, beam shape, angle of incidence and redeposition, alter the rectangular shape of the grating bars in a way that is shown in Figure 4.7. Typical aspect-ratios, seen in FIB milling are of the order of three, and, under extremely low beam current conditions, also up to 25 [214]. Here the notion of an aspect ratio is less practical, compared to taking the bevel angle or slope s of a bar edge, that is related to the aspect-ratio AR , as $s = \arctan(AR^{-1}) \frac{1}{2} \frac{180}{\pi}$, e.g., for an aspect ratio of $AR = 3$ the bevel angle is 9° . It is well known that milling of high-aspect ratio structures is achieved by increasing the number of passes to minimize the re-deposition rate (while keeping the total dose constant). On the other hand, too low dwell times lead to swelling and amortization. For effective material removal a certain threshold dose, being in the range of 1×10^{16} ions/cm² to 1×10^{17} ions/cm², has to be used [214, 267], meaning that there is an optimum range for the combination of beam current, dwell times and number of passes. In earlier tests on the in-house FIB, it was found that a dwell time range within $75 \mu\text{s}$ to $300 \mu\text{s}$ for beam currents of 50 pA to 300 pA , leading to pass numbers between 10 and 50, works well for the given application. Also, for very low film thicknesses, single pass milling tests, done at the CEITEC, gave very good results.

Assuming that the dose/current/passes balance has thus be optimized, the question was, if the full vector control of the milling position and dwell time, provided by the stream file milling, can be used to improve the cross-sectional shape of HVM gratings, see Figure 4.7. Inspired by the publication [59], that found, using the electron beam-induced deposition (EBID) technique, that a spacial dependent dwell time can improve the edge fidelity of deposited structures, a similar approach was tested for the ion milling of holographic gratings. The *Mathematica* routine (described before) to generate the stream files was adopted, such that a spatial dependent dwell time reduction in the proximity of the voids' edges is produced. A subroutine determines the number of void pixels surrounding the scan point and classifies it according to the three different cases given in Figure 4.8 (a-c). Void points (a) are surrounded by other void or milling points to 100% and are assigned the highest dose/dwell time. Whereas, when the beam is reaching the edges of the grating bars, the number of

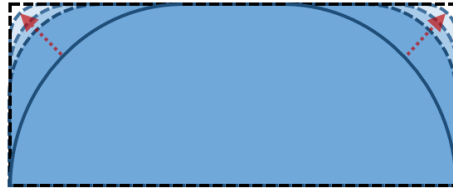


Figure 4.7: Schematic cross-section of one grating bar, showing the rounded shape (blue filled shape) as a result of the ion-beam etching procedure and possible stages of improvement (opaque dashed shapes), reducing the roundness towards the ideal rectangular cross-section (black dashed line).

surrounding milling points is reduced by 37.5 % and, thus, these edge points (b) are assigned a lower fraction of the dose. For corner points (c), where the amount of neighbouring milling points is reduced by 62.5 %, the dwell time reduction is also highest. Additionally to the neighbouring milling points classification, the proximity to the edge is also determined for every scan point, reducing the dwell time accordingly. Both parameters are then used to weight the reduction of the nominal dwell time, as depicted in Figure 4.8 (d). To test whether this kind of dwell time adoption has an influence on the cross-section of diffraction grating bars, a series of test structures was milled, using the *Helios* machine at the IFW-Dresden, operated at 30 kV, into a 310 nm Pt thin film, where only the amount and sign of the EDT adoption was changed. See Figure 4.9, for a plane-view overview. The structure had the same periodicity as was used for the stream milling test, but the milling current was 80 pA, the pitch was reduced accordingly to 6 nm and a dwell time of 75 μ s with four passes (two left-handed ones and two right-handed ones) used. The duty cycle was set to 67.5 %.

To inspect the edge structure, cross-sections were prepared, using the FIB and an EBID C protection layer. Figure 4.10 shows the result of the milling series. The EDT parameters were varied from an edge-dwell-time decrease of -20 % over to practically no change and ranging up to an increase of 20 %. Besides the obvious change in the grating cross-sections' duty cycle, the slopes and rounding radii seem to be very similar, except for the test structure, cut at a much higher beam current of 230 pA and on another thin film sample.

To further analyse the edge shapes, the image processing capabilities of *Mathematica* were used to extract the edges from the 80 pA SEM images. In the following the edge shape extraction procedure using *Mathematica 10.1* is described in bullet points:

1. The images were binarised using the function *MorphologicalBinarize* with a threshold of 0.55.
2. Edge Detection was done employing the function *EdgeDetect*, using a pixel-range of 10 pixels.

4.2 Testing a Spatial Dwell Time Modulation as a Means to Improve the Grating Cross-Sections

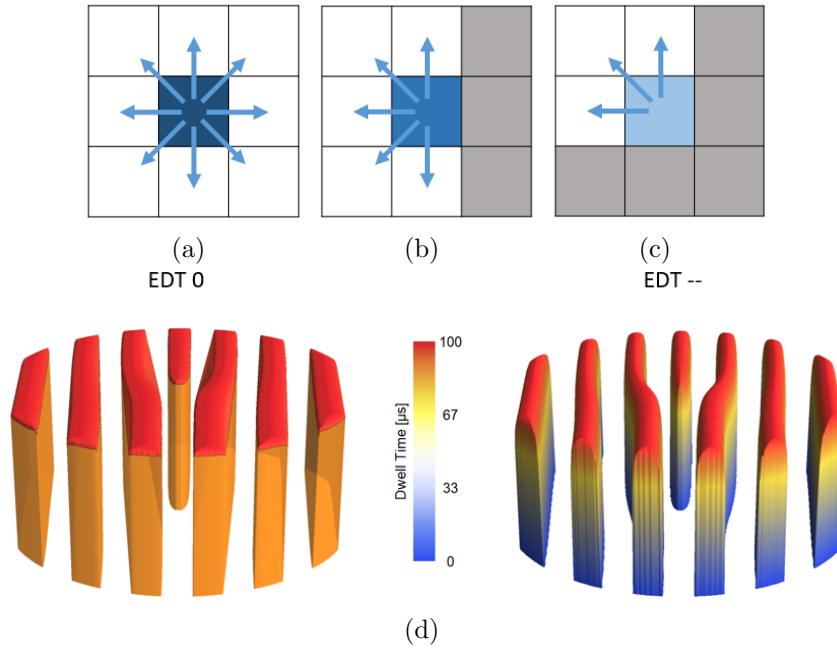


Figure 4.8: (a) Principle of the beam position-dependent dwell time adaption, inspired by the work [59]. (a) Void points are surrounded by other milling points, the highest dose is assigned to them. (b) edge point have less milling point neighbours, such that their received dose is reduced. (c) corner point having the least number of surrounding milling points and the highest dwell time reduction. (d) Three dimensional representation of the spatial depend dwell time of a HVM structure before adoption, left (EDT 0) and, right, after adoption (EDT -).

3. Then components in the sense of connected regions are detected, using the function *MorphologicalComponents*.
4. Getting the pixel positions of each edge region, using the function *Position*.
5. Afterwards the edges are rotated and rescaled to nanometres. The bottom line is removed and the edge pixels are sorted by their respective mean x -value.
6. Separating the left and right edge of the central bars.
7. Shifting the odd/even edges to the same starting value in x for better comparison.
8. Fitting the odd/even edges, using a Fermi distribution function and the non-linear model fit function.

Different fit functions were tested, but it was found that a Fermi-distribution function

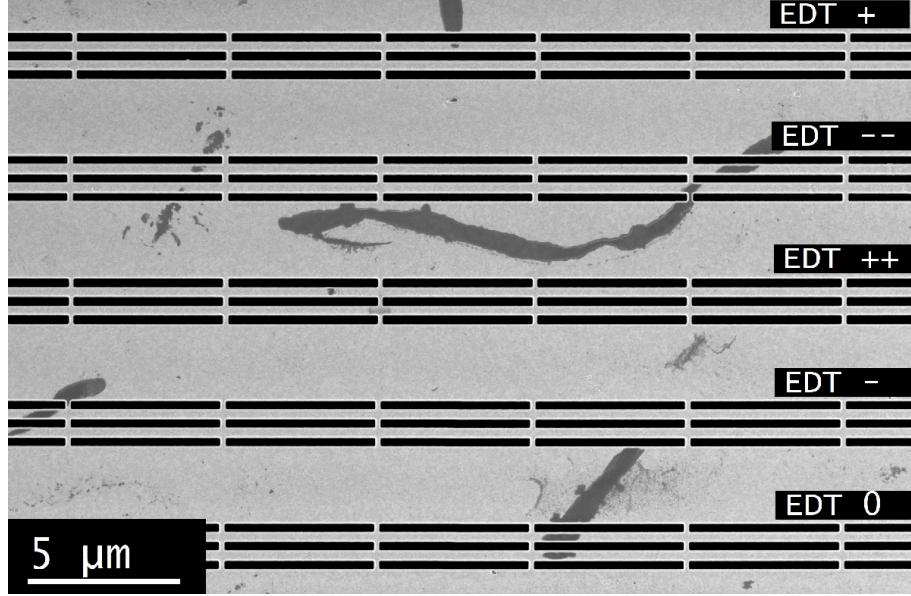


Figure 4.9: Plane-view overview of the EDT test structures for different EDT parameters.

in the form of:

$$f(x) = a + \frac{2 y_{max}}{1 + e^{\frac{x-b}{r}}} + d(x - b), \quad (4.3)$$

can be used to fit the edge-shape, with y_{max} , being the highest point of the respective edge in the vertical direction, and a, b, r, d being fit parameters. The extracted edges 1 to 6 can now be directly overlaid and compared, using the extraction procedure. The results are shown in the graphical panel given in Figure 4.11. Additionally to the duty cycle variations, there is now also an asymmetry between the left- and right-side edges visible. The right side edges are systematically more rounded and show a higher slope angle, which is most likely due to drift. Considering the EDT-dependent variation in the edge form, there are no clear distinctions discernible in Figure 4.10. Utilising the fit function, Equation 4.3, values for the edge radii and their respective slope values were extracted and summarized in Table 4.1. For the moderate EDT reduction, the lowest edge radius and, together with the EDT 0, lowest slope, as well as the highest aspect ratio can be observed. This could hint at the possibility, that a moderate EDT reduction improves the edge quality slightly, compared to no EDT and higher EDT values. The uncertainties of the fits are reasonably low. But looking at the STD values of the edge radii and acclivities clearly indicates that one cannot infer an improvement of the edge quality from these results. The observed variations are smaller than the measurement accuracy and possibly due to instrument instabilities, misalignments and/or drift.

These results suggest that the most significant parameter for low bevel angles of the grating side-walls is the beam current, see the lowermost panel of Figure 4.10.

4.2 Testing a Spatial Dwell Time Modulation as a Means to Improve the Grating Cross-Sections

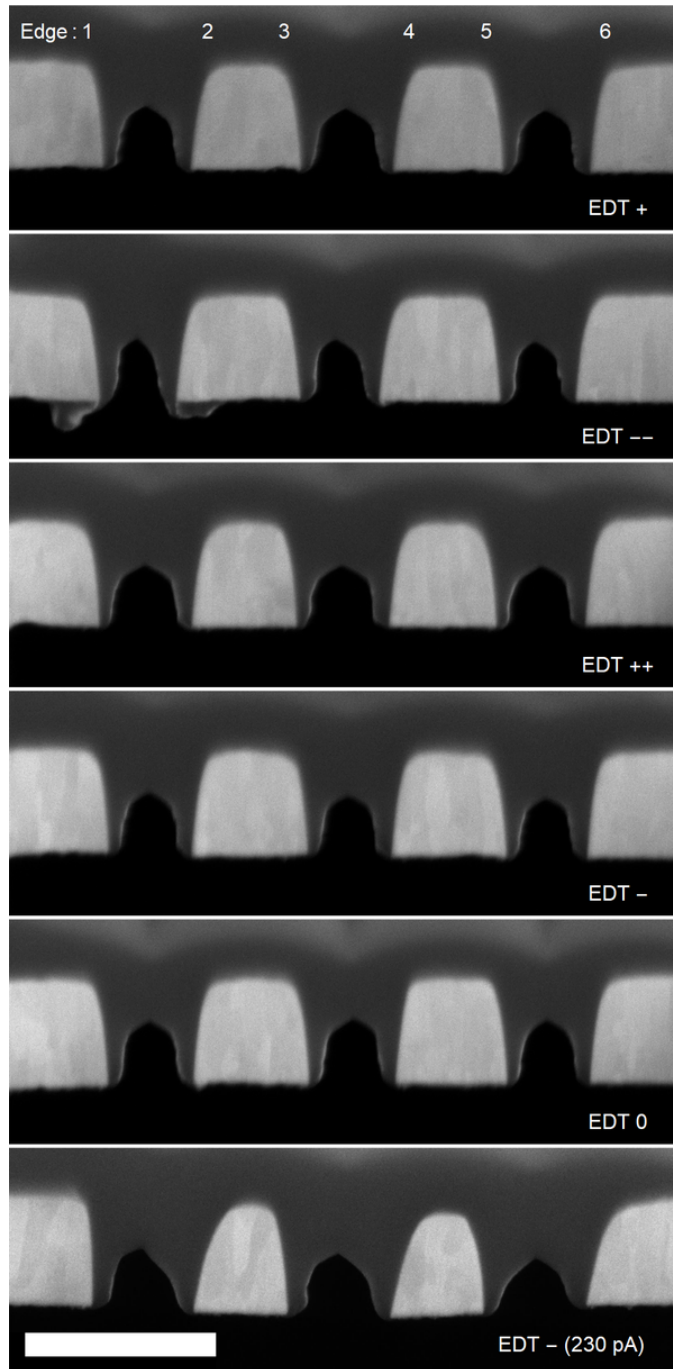


Figure 4.10: Comparison of different EDT parameters showing FIB prepared cross-sections of a diffraction grating test structure cut at 80 pA. Note that the darker structure partially filling the grating voids is a EBID protection layer out of C. In the EDT + image the EDT increase was +7%, in EDT - enhanced EDT decrease -20% was used, in EDT ++ an enhanced EDT increase +20% was applied, in EDT - a moderate EDT decrease of $\approx -7\%$ was tested and in EDT 0, the EDT was not adapted at the edges. The lowermost image was cut, using a higher beam current of 230 pA and the scale bar is 500 nm.

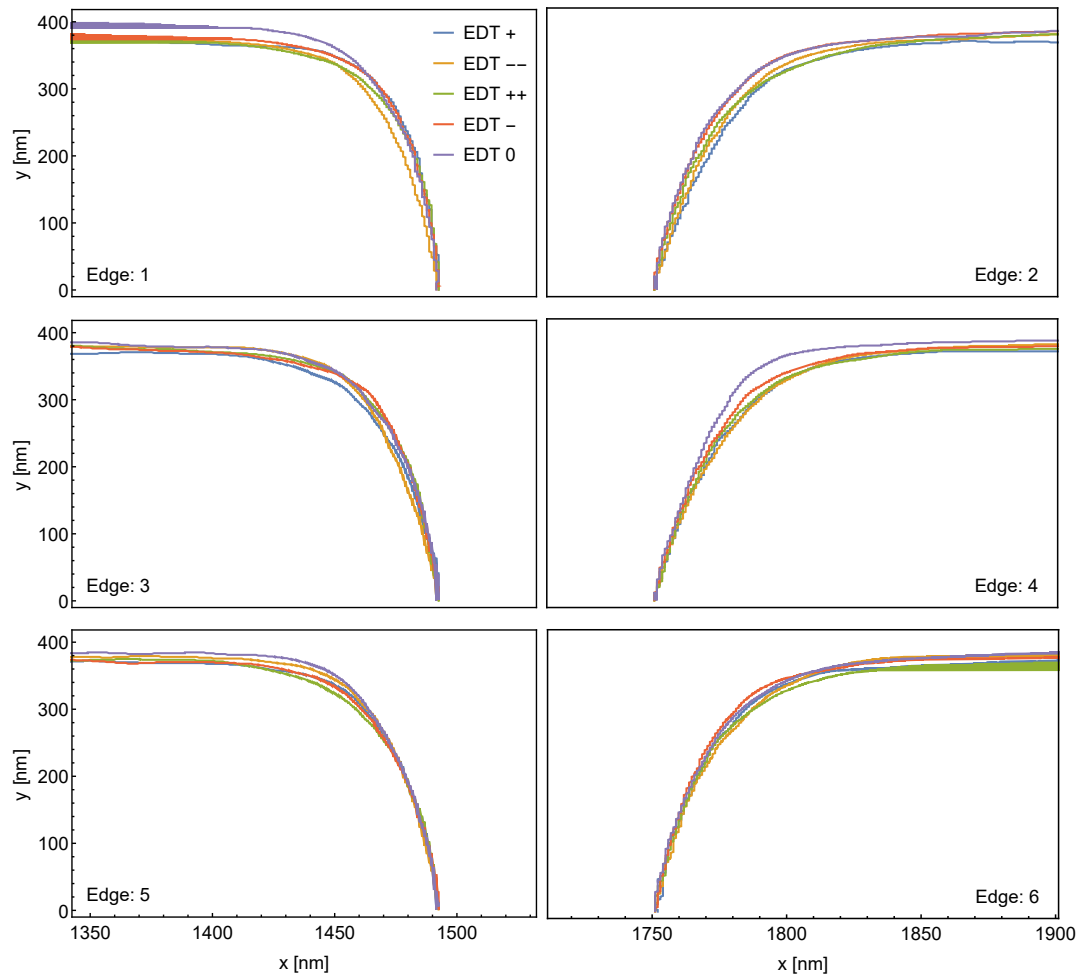


Figure 4.11: Direct comparison of the different EDT parameters, extracted from the images shown in Figure 4.10 of Edge 1 to 6. The edge onsets have been aligned to each other for better comparability. No significant influence of the EDT adoption, besides the apparent duty cycle change, visible in Figure 4.10, can be observed.

Table 4.1: Results of the SEM image analysis of Figure 4.10. Mean values and the absolute and the relative standard error of the mean of the fitted edge radius, its slope/bevel angle and aspect ratio.

EDT	Mean Edge Radius [arb]				Mean Slope [deg]			Mean Aspect Ratio []		
	r	σ_{fit}	σ_{edges}	σ_{edges}^{rel}	s	σ_s	σ_s^{rel}	AR	σ_{AR}	σ_{AR}^{rel}
+	13.8	± 0.16	± 2.9	$\pm 21\%$	4.5	± 0.9	$\pm 20\%$	6.5	± 1.6	$\pm 24\%$
- -	15.0	± 0.23	± 1.8	$\pm 12\%$	4.9	± 0.4	$\pm 9\%$	5.8	± 0.5	$\pm 9\%$
++	12.8	± 0.25	± 2.2	$\pm 17\%$	4.3	± 0.7	$\pm 15\%$	6.8	± 1.1	$\pm 17\%$
-	12.7	± 0.15	± 1.9	$\pm 15\%$	4.1	± 0.5	$\pm 12\%$	7.0	± 0.9	$\pm 13\%$
0	13.2	± 0.13	± 1.0	$\pm 8\%$	4.1	± 0.3	$\pm 7\%$	7.0	± 0.5	$\pm 7\%$

This negative result can be understood considering that the idea of using a spatial dependant dwell time adoption originated from a different technique, where other physical processes are involved, e.g., in the EBID method, the edge improvement due to an EDT increase, can be understood as being due to a secondary electron deficiency at the edges of the structure, which leads to a lower deposition yield. Here, the milling rate is primarily defined by the beam dose and, thus, by the lateral beam profile.

4.3 Improving the Thin Film Production

On the one hand, only little attention was paid to the deposition process and properties of the thin metal films, used for absorptive vortex masks. This is reflected in the lack of information on that issue in publications dealing with the production of the HVM [5, 207]. On the other hand, the presented results in the preceding sections do point out, that there is a significant influence of the thin film characteristics, like grain-size and crystallinity, on the actual milling result.

In numerous milling tests, it could be observed that the grating bars tend to stick together, when trying to mill, e.g., $\text{\O}20\ \mu\text{m}$ HVMs with grating periodicities lower than $g < 1000\ \text{nm}$. Therefore, a low frequency (large periodicity) second-order grating, lying perpendicular to the primary high frequency (small periodicity) grating was introduced to avoid a grating collapse, as exemplified in Figure 4.12. It was found that, in order to avoid the grating collapse, the second-order stabilizing grating should have a periodicity of $g_2 \approx (6 - 8) \cdot g_1$, where $g_1 < 1000\ \text{nm}$ is the primary-, and g_2 the secondary grating periodicity. For $g_1 > 1000\ \text{nm}$, g_2/g_1 -ratios of 20 are feasible. See for example Figure 4.9 and Figure 4.6 in the preceding sections.

These second-order stabilizing or supporting gratings were added under the tacit assumption that there is no influence on the waveform. Experimental far-field images, shown in the Applications chapter, see Figure 5.17 (b), prove this assumption to be wrong. The influence of second-order gratings on the far-field distribution is of significance. They introduce artefacts visible as azimuth intensity variation of the

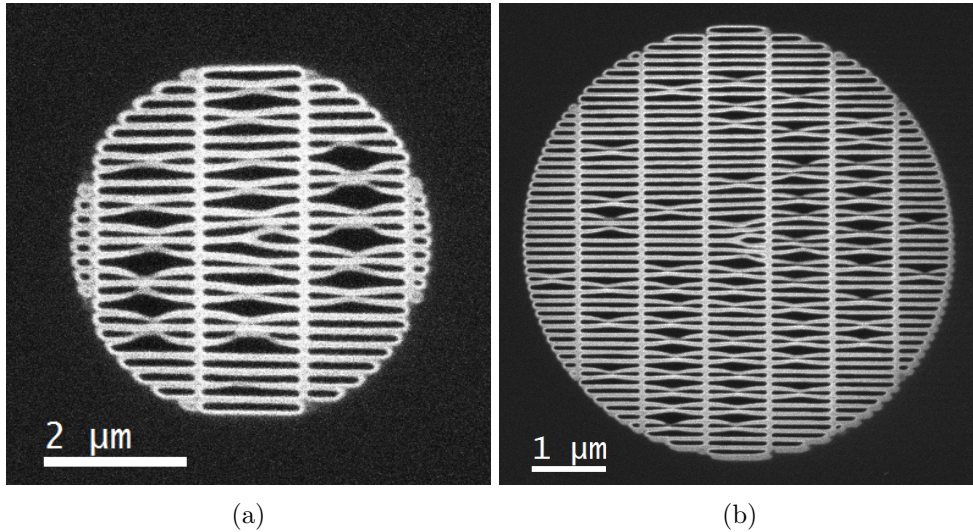


Figure 4.12: Typical examples of grating collapses observed when the g_2/g_1 -ratio gets too high.

single vortex orders. Moreover, every square micron of an amplitude mask, that is blocked by a stabilizing grating, further reduces its DE via electron loss, due to absorption and high angle scattering. Not only absorption, but also diffraction at the second-order grating reduces the amount of electrons delivered to the $m = \pm 1$ vortex orders. To estimate the effect of the introduction of a second-order grating on the DE, image simulations were undertaken. Figure 4.13, shows that a reduction of $\sim 16\%$ in DE can be expected for a typical stabilization grating, having $g_2 = g_1/2$ (orange line) and a g_2/g_1 -ratio of five, up to 70% in the worst-case-scenario. Therefore, measures to reduce the need for a second-order grating (and/or its thickness) are needed, in order to improve the DE of HVMS.

Another point, that is made in Figure 4.13, is the influence of the primary grating transmission on the DE. To be able to mill fine-grating periodicities, of the order of 600 nm and below, the thin film thickness plays an essential role, due to the limited aspect ratio that is achievable with a FIB instrument. The thinner the film, the more important the thin film's density gets, and with that the material choice and the thin film deposition conditions, which both influence its density.

To tackle the aforementioned issues, the thin film properties have to be engineered. The expended efforts to understand and optimize the deposition process of high density metals, like Os and Ir, via DC-magnetron sputtering, will be presented in the next three subsections. Before, there will be a short introduction on the used principal thin film layer structure, together with some details on how the factory settings of the sputtering machine were adapted to increase the systems cleanliness and sputtering performance.

In contrast to the already mentioned thin film preparation method in the stream

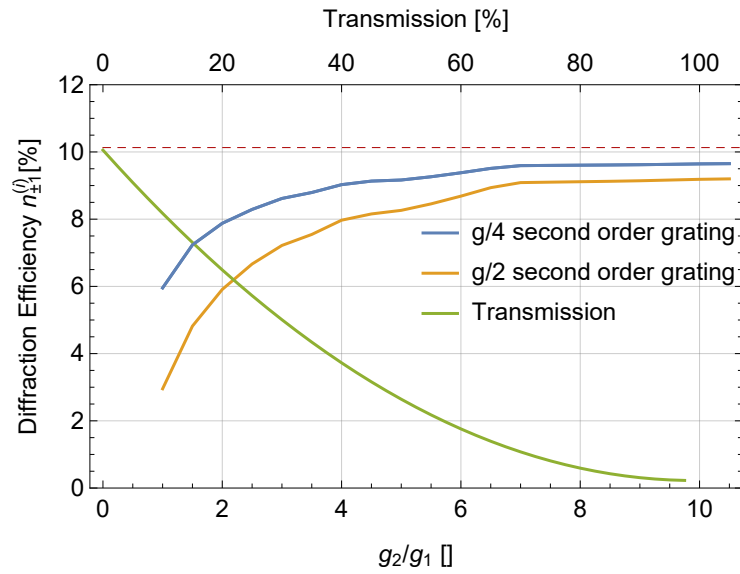


Figure 4.13: Showing the influence of the HVM primary grating transmission (green line) and the presence of a second-order grating, with a grating bar width of $g_1/4$ (blue line) and a grating bar width of $g_1/2$ (orange line) on the DE of the hologram. Both of which can massively reduce the effectiveness of the holographic structure on distributing electrons to the desired vortex orders $m = \pm 1$.

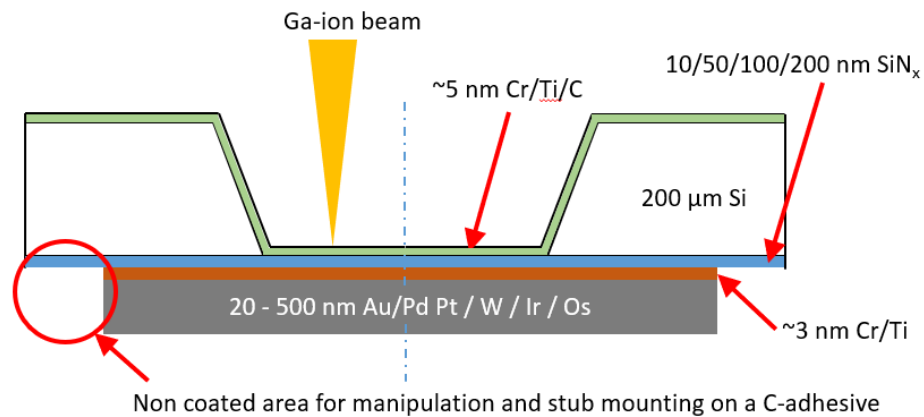


Figure 4.14: Schematic drawing of the layer structure of holographic amplitude masks. The metal layer is deposited on top of a typically 100 nm to 200 nm thick SiN_x support membrane, after a thin adhesion layer has been sputtered onto the substrate membrane. FIB milling is done from the back-side, as it has turned out that milling through the amorphous SiN_x first is beneficial. Moreover, a few nanometre thick low sputter yield cover layer is added on the milling side, as a kind of protection layer.

file milling section (water bath floating-off a NaCl crystal), the thin film production method employed here comprises low-stress SiN_x membranes (SPI, Norcada) as a substrate, see Figure 4.14. Before coating, no chemical or mechanical cleaning is applied to the membranes. Instead, He-plasma is used for cleaning for 3 min (on both sides), using a radio-frequency plasma cleaner at a base pressure of ~ 0.05 mbar, and a He partial pressure of 0.2 mbar (Gala Instrumente, Plasma Prep 5). After the plasma cleaning step, the membranes are directly transferred to the sputter coater vacuum chamber.

Ti and Cr are commonly used as adhesion layers in thin metal film deposition. Therefore, the substrate is coated by a 3 nm to 25 nm thick adhesion layer out of Cr or Ti. Cr as well as Ti oxidises rapidly, within a few seconds to minutes, when exposed to air. Ideally, the deposition system is equipped with two sputter sources, such that both materials can be deposited without the need for breaking the vacuum. The in-house Q150T sputtering device is a single sputter target machine, and thus, the vacuum has to be broken upon changing the sputter target, and by that (partial) oxidation occurs, reducing the adhesive strength of the Cr or Ti layer. To reduce the oxidation of the adhesion layer until the actual (precious) metal film is deposited, the N₂ vent time was increased from 30 s to a few minutes, such that the sample stays immersed in an N₂ atmosphere, while the sputter target is changed.

The adhesion layer is then coated with the actual electron-blocking heavy metal layer, e.g., Au/Pd or Pt/Ir/Os/W with a thickness of 20 nm to 500 nm, depending on

the utilised application and electron AV. FIB milling is done from the back-side, as it has turned out that milling through the amorphous SiN_x first is beneficial. Moreover, a few nanometre thick low sputter yield cover layer is added on the milling side, to function as a kind of protection layer for the metal film during FIB milling.

The sputter process is either terminated by using a fixed sputtering time, or by using the FTM. Both methods need to be thickness-calibrated first: For thin layers below 20 nm to 50 nm, this was done with the light transmission measurement approach and the thin film Profilometer was used for thicker layers, both described in the Fundamentals section.

The Q150T is designed as an easy-to-use sputter machine for SEM users, standard recipes can be saved for a fully automatic deposition process. These recipes are optimized to yield a sufficiently fine-grained and conductive 1 nm to 10 nm metal layer within a relatively short time (a few minutes). They are in no way optimized for producing dense, high purity thin films, which was also realized by the manufacturer [237]. Thus, additionally to the changes to the vacuum system, described in the Modifications chapter, one has to modify the vacuum-, material- and recipe-specific settings as follows, in order to improve the thin film characteristics.

For example, the base pressure can be drastically lowered by simply increasing the ‘extra pump time’. This is the time delay between the system’s ready to sputter signal and the actual beginning of the deposition process. Typical ‘extra pump times’ are 0 s to 60 s, yielding a base pressure in the 10⁻⁴ mbar regime. Increasing this time to the allowed maximum value of 600 s leads to a base pressure in the 10⁻⁵ mbar region. Sometimes this time delay is not sufficient, but one turn on the ‘pump-hold’ function in the recipe file, enabling an extended extra pump time of up to 24 h. Pressures reached with this mode are plotted in Figure 3.6 in the Modifications section. Also, N₂ flushing is used for every coating run and the N₂ flushing time, prior to the pump-down, is increased from 0 s to 60 s (the allowed maximum value). Similarly, the process gas (Ar) flushing time and -repetitions are increased to the maximum of 60 s and five times, respectively. A sputter target cleaning step, consisting of sputtering against the closed shutter for a certain period of time, is used not only for oxidising materials like Cr or Ti but for all metals. The cleaning time and the -current are again set to the allowed maximum values of 60 s and 150 mA, respectively. The stage rotation, typically set to 70 %, is, either left there, or increased to 100 %.

Additionally to the parameters described above, the working gas pressure p_{Ar} , SWD and the sputtering current (power or power density) I have to be modified. Their influence on the thin film characteristics will be covered in the following.

4.3.1 Influence of the Mask Material on Focused Ion Beam Milling of Holographic Vortex Masks

Up to now, Pt [5, 38, 40, 147], PtPd [207], Au [153], AuPd (previous HVMS made in-house) and Cr [139] membranes or coatings were utilized in the production of binary amplitude HVMS. None of these publications vindicates the use of a certain material or compares milling results of the same structure on different material membranes.

Table 4.2: Amplitude HVM materials with some of their mechanical, electrical and thermal properties sorted by material density.

Material	Density [g/cm^3]	Elastic Modulus [GPa]	Resistivity [$\mu\Omega cm$]	Heat Conductivity [W/mK]
Cr	7.14	279	11.44	94
W	19.3	411	5.5	170
Au	19.32	78	2.2	320
Pt	21.45	168	10.6	72
Ir	22.56	528	5.07	150
Os	22.59	559	9.17	88

An attempt to close this gap will be given in the following.

The materials used so far, except for Cr, show a very low mechanical strength or elastic modulus, see Table 4.2 and they are very ductile, i.e., susceptible to deformation. The observations of the grating collapse could be due to a mechanical instability and therefore the FIB milling tests were conducted comparing the conventionally used materials, like Pt and Au, to the extraordinary robust materials, like W, Ir and Os. Cr was not further analysed, as its density is far below the values of the refractory metals.

Ir is an outstanding metal: it is very hard and brittle, making it very hard to machine, form, or work, it has the second highest density of all known materials, it can sustain high temperature annealing, high positive electric fields and it is the most corrosion-resistant material known [268, 269]. Also, it was tested for phase plate applications and turned out to be one of the most beneficial materials for use [270]. It shows the lowest transmission with only slight charging and excellent dose tolerance. In such applications it was only overruled by Al, as it shows less electron absorption, which is beneficial in the case of absorption masks. It shows half the resistivity and twice the heat transfer capability of Pt.

Os also shows some very interesting material properties, which render it probably a superior material in the production of absorption holographic masks. Together with Ir it has the highest density of all natural elements, somewhat competing for the title of the densest element, see [269]. It also has a very low compressibility, which is even comparable to that of diamond [271]. Even under extreme pressures it does not change its crystal structure, but rather shows peculiar pressure-induced interaction with core electrons [272]. Contrary to that, in a fine powder or spongy form, Os can easily oxidize to OsO_4 in contact with air, even at ambient conditions, forming a low boiling point, dangerous and highly toxic compound. But in the dense metallic state it has the highest melting point among noble metals, not taking Rhenium into account [271].

The thin films, used to test the influence of the material on the milling result, were deposited on custom-made 50 nm SiNx membranes, provided by the ISI-CAS, using

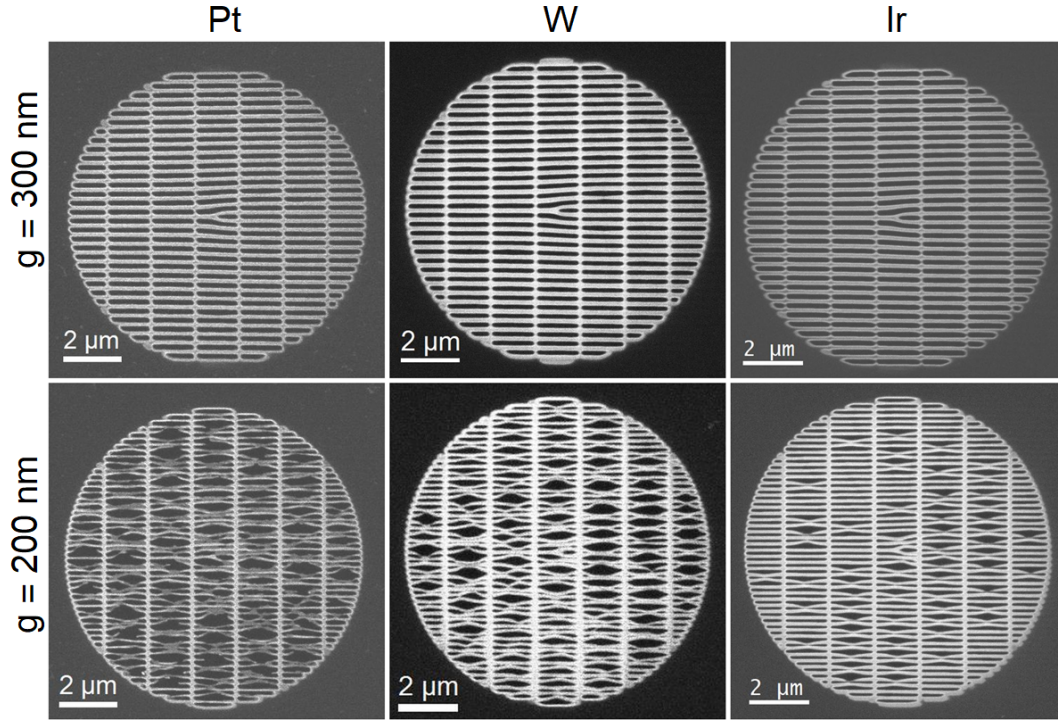


Figure 4.15: FIB milling results using the Quanta 3D, comparing different sputtered materials with approximately the same thickness of 20 nm, deposited under similar conditions on the same substrate (50 nm SiN_x membranes provided by the ISI-CAS collaboration partners) and two different grating periodicities: $g = 300$ nm and $g = 200$ nm, both with a diameter of $\text{\O}10$ μm . While for the coarser grating all materials yield comparable and good results, for the fine grating the Ir thin film clearly yields the best milling result.

DC magnetron sputtering with the following parameters: a process gas pressure of $p_{Ar} = 0.7$ Pa to 1.4 Pa, with the currents ranging from 10 mA to 50 mA, leading to deposition times of 240 s to 480 s. Sputtering was started after the base pressures reached $p_B = 4 \times 10^{-5}$ mbar, except for the Os layer where $p_B = 5 \times 10^{-6}$ mbar was used. The working distance was either set to 45 mm or 50 mm. The $\text{\O}57$ mm Os and Ir targets have a purity of 99.9% and 99.99%, respectively. Note that these sputtering conditions, except for the base pressure of the Os layer sputter run, represent the non-optimized state, yielding relatively low density, low-stressed, but fine-grain-size thin films. However, all films in this comparison were deposited under the same non-optimized conditions. Figure 4.16 shows the FIB milling result using the Quanta 3D instrument for Pt/W/Ir for two different grating periodicities.

It should be noted that, besides the interest in the material milling properties, this kind of very fine-grating HVMs are of interest for the ISI-CAS collaboration partners

for use in a SEM to produce electron vortex beams. There, a very high vortex order separation is needed, but due to the low AV typically used in a SEM, phase masks can only be used under massive electron loss.

The holograms with a diameter of 10 μm were milled using stream files, as described in the preceding sections, with a beam current of 30 pA, a working distance of 19 mm and 9 to 12 passes. While for the 300 nm grating all materials yield comparable and good results for a g_2/g_1 -ratio of 5, without any degraded grating bars sticking together, the Ir thin film clearly yields the best milling result for the 200 nm grating and a g_2/g_1 -ratio of 7.5. This is even more striking, as there was drift in the Ir mask's milling test, visible as a broadened bright seam on the lower right section of the hologram. Though, none of the structures is free of grating collapses. This indicates that, indeed, material properties, either inherent to the material or possibly due to the deposition parameters, play a role for and can change the ion-beam milling outcome.

Further tests to extend the size of the hologram to $\sim 15 \mu\text{m}$ and to try additional materials were conducted at the *Helios* NanoLab 660 machine at the CEITEC. The results are shown in Figure 4.16. For the FIB stream milling a dwell time of 75 μs was used with two passes (one left- and one right-handed) and a current of 31.5 pA to 40 pA. The initial duty cycle was 33 % and a pitch value of 4.1 nm was used. The Ir and Os thin films were produced in-house and the Pt and Au films were made at the CEITEC. All of them under non-optimized deposition conditions.

It is clearly visible that the Ir, Os and Au membranes yield more homogenous and regular results. Using a reduced g_2/g_1 -ratio of 4.5 effectively avoided the grating collapse for all materials shown. Os shows the desired duty cycle value of 100 %. Though this is not a material characteristic but a matter of finding the right ion-dose. Pt membranes seem to be less favourable, under the given conditions.

In additional milling tests (not shown) it was found, that the quality of the SiNx substrate influences the milling results as well. Also, the milling strategy and drift are strong factors, affecting the production of a hologram. Using a high number of passes and BMP milling brought the worst outcome, while single- or low-pass-number stream file-milling results are comparable to the BMP-milling results. If drift was present, none of the materials nor milling strategies was successful. For the results given in Figure 4.16, the drift was very low, but cannot be excluded for the Pt milling test. The substrate quality was sufficiently homogenous for all material tests shown.

Note that Pt membranes repeatedly showed milling results much worse than the ones shown in Figure 4.16, with completely over-etched masks, while the Os/Ir membranes worked just fine. It was also tried to mill HVMs with a grating periodicity of 100 nm, a g_2/g_1 -ratio of 4 and an initial duty cycle of 25 %, at a current of 10 pA. Even though the attempts were not successful, Os/Ir membranes, again, were superior to the Pt, as well as the Au membrane milling tests.

This supports the idea of a material-dependent influence on the FIB milling result and that, indeed, high melting point and high stiffness materials, like Os/Ir, can improve the milling results of holographic structures.

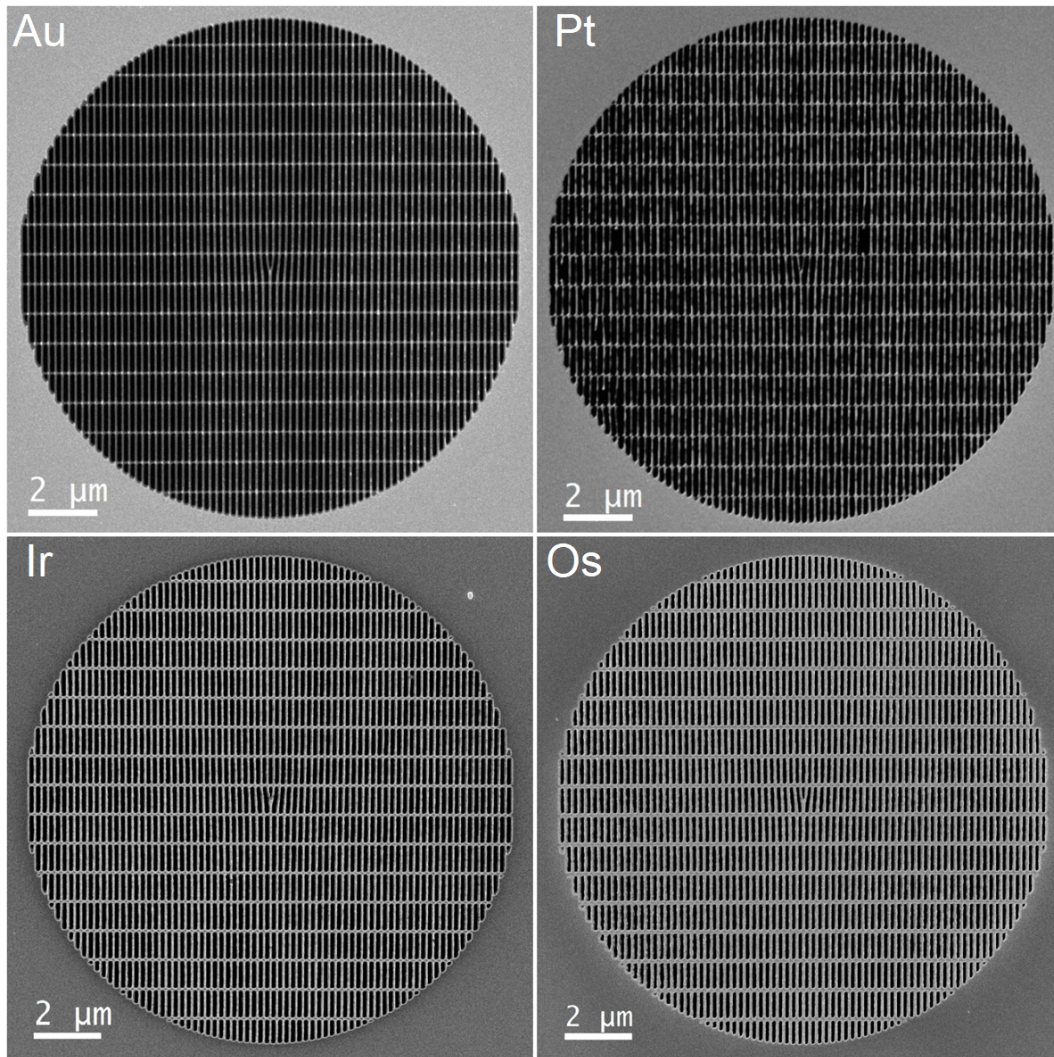


Figure 4.16: FIB milling results comparing different membrane materials for $\text{Ø}14.45\ \mu\text{m}$ and $g = 192\ \text{nm}$ HVMS. They were cut using stream files with the same milling parameters and the same substrate of $50\ \text{nm SiN}_x$. The materials were $30\ \text{nm Au}$, $30\ \text{nm Pt}$, $20\ \text{nm Ir}$ and $30\ \text{nm Os}$ thin films. Au, Ir, Os deliver very good milling results for this very low grating periodicity. Note that a duty cycle of 100% was achieved only for the Os grating, and that the Au layer was practically removed in the hologram area.

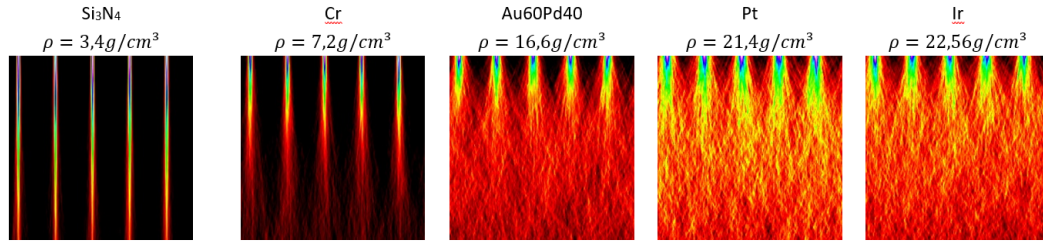


Figure 4.17: Monte-Carlo-Simulation of the scattering strength of a 200 nm thick layer, consisting of materials of different density ρ for 200 keV electrons. The distance between the single electron beams is 10 nm. The highest density material, Ir, scatters and absorbs the electrons strongest, while Si_3N_4 is only a weak barrier.

4.3.2 Optimizing the Thin Film Density

The superior density of the two platinumoid *5d* transition elements Os and Ir makes them perfect candidates for highly electron-scattering and -absorbing layers, as can also be deduced from MC simulations of electron energy deposition/scattering in different thin film materials, as shown in Figure 4.17. Obviously, there are strong differences between high density and low density materials. Also, for $\text{Au}_{60}\text{Pd}_{40}$ and Pt/Ir there are differences in absorption and high angle scattering evident. But this is only true, if the deposited film density is comparable to the bulk density of the thin film. According to the structure zone model, shown in Figure 2.24 and Table 2.2 in the Fundamentals chapter, it can be seen that this is only fulfilled in zone T, 2 and 3, whereas in the zone 1 sputter regime, given at low substrate temperatures relative to the melting point of the material (T/T_M -values below ~ 0.2), this is not the case. In this sputtering regime the thin film density can deviate drastically from the bulk value while producing fibrous and spongy thin films. Note that Os has a melting point of 3333 K [269] and, thus: $T/T_M = 0.09$. Heating to temperatures of 1000 K could be used to increase the mobility of adsorbed atoms on the substrate surface to the expense of grain growth. Another possibility would be to use low process gas pressures, but that would yield extremely high compressive stresses for such high (elastic, bulk) modulus materials [273].

Additionally, the inclusion of light element rest gas species, like O/CO/H₂O, in the thin film can modify the density considerably. Notably, fresh surfaces of noble metals immediately form a monolayer of oxygen, which is not an oxide [270]. So even for noble metals the considerations on the arrival ratio of sputtered atoms to oxygen, given in Section 2.9.2, have to be kept in mind and will be used later on.

To optimize the density of the thin films, one has to have a parameter at hand that acts as an indicator for this quality. Even though there are few publications regarding the Os thin film growth using PVD [273, 274], it can be seen from what is published, that the thin film resistivity is a viable marker to give an indication of dense Os [273] and Ir [275] thin films. To back up the resistivity measurements EDX

was used to quantify the composition of the deposited Os thin films⁵. The resistivity values were measured on 200 nm Os films deposited on carefully cleaned Ø18 mm microscopy glass slides. Acetone, ethanol, deionized water, and, finally, compressed air was used in order to clean the glass slides. A Cr adhesion layer, with a thickness of 5 nm to 25 nm, was used.

In order to improve the thin film purity, first and foremost, the base vacuum of the sputter system has to be improved, as already described in the Modifications chapter, and for all measurements given in Figure 4.18 and Figure 4.19, extended pump-down times were used in order to reach a decent base vacuum between 5×10^{-6} mbar to 3×10^{-5} mbar before sputtering.

However, the attained resistivity value of in the sputter run ‘OsCr16’ was ~ 20 times higher than the bulk value of Os, see Figure 4.18, and clearly higher than the expected resistivity value of $21.7 \mu\Omega \text{ cm}$ (indicated by the brown dashed line). This resistivity value was calculated by using the empirical thickness dependence of ρ_{el} , given in [275], in the form of $\rho_{el} = 13.0 + 1.74/t$ in $\mu\Omega \text{ cm}$ with the thin film thickness given in microns.

Figure 4.19 shows the EDX measurements of most of the Os films, measured in Figure 4.18, and indicates that the higher resistivity value of ‘OsCr16’ is due to O impurities. In this sputter run the sample was placed 60 mm away from the sputter target, which is approximately 10 mm more than the standard working distance, recommended by the manufacturer. Looking at the average number of collisions of the target atom with process gas atoms on its way to the sample, regarding the rule of thumb for the mean free path given in the Vacuum Technology section, it is evident that for a working gas pressure of, e.g., 2.8 Pa, ~ 34 collisions can be expected for a SWD of 60 mm, and only ~ 22 for a SWD of 40 mm⁶. A higher number of collisions slows down the target atoms and increases the probability of getting hit by residual gas atoms, and with that an increase of impurities and a less dense thin film can be explained. Therefore the SWD was reduced, as a means to compensate for the non-optimal base pressure or other sources of impurities. See, for example ‘OsCr10’, where the reduction of the working distance to a value of 50 mm also resulted in a reduction of the resistivity. The same tendency can be seen in the Cr layer depositions, e.g., in ‘Cr04’, ‘Cr05’, ‘Cr08’, compared to ‘Cr03’ and ‘Cr06’, where the SWD was reduced from 50 mm to 40 mm.

But, still, the resistivity value of ‘OsCr10’ is ~ 3 times higher than the expected value. Another hint on what can be done in order to resolve this discrepancy can be found in Table 2.3, in the Vacuum Technology section, which lists the monolayer formation times. For a certain base pressure there is a given monolayer formation time. Thus, to increase the arrival ratio of target atoms, relative to residual gas atoms, the sputter rate has to be increased. This can be easily done by increasing the

⁵The focus is set to Os thin films, not only because it yielded very promising results in the material tests above, but also as a consequence of the higher sputter target thickness, which allows more sputter runs.

⁶This formula neglects effects like the change of the scattering cross-section for slower atoms and, thus, most likely underestimates the number of collisions for the higher SWD.

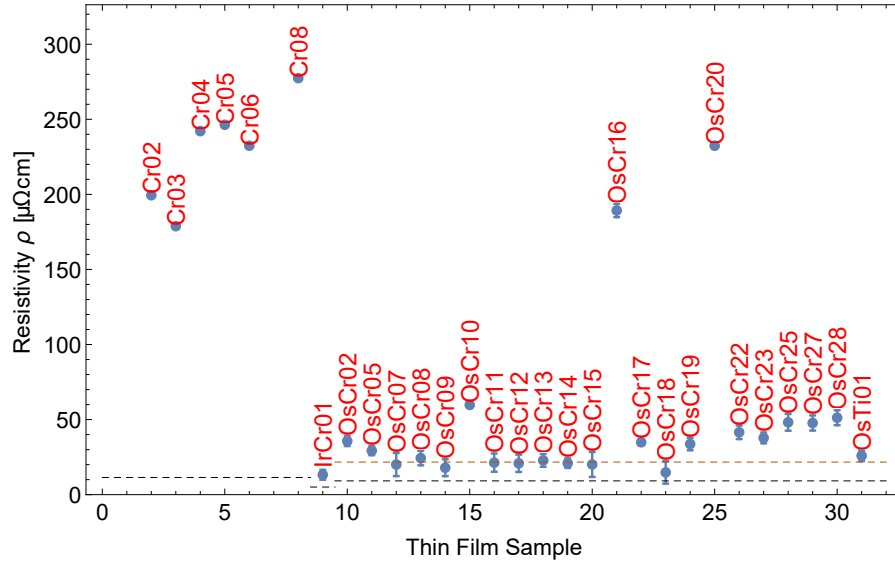


Figure 4.18: Measured thin film resistivity values of the sputtered Os/Cr/Ir thin films together with their respective bulk resistivity (dashed lines) using the four-point probe station, showing the high purity achieved for the precious metals when sputter conditions are optimized.

sputter power density or current. In the sputter test ‘OsTi01’, the sputter current was increased from 10 mA in ‘OsCr10’, where a sputter rate of 0.04 nm s^{-1} was measured, to 150 mA, which yielded a nearly 16 times higher sputter rate of 0.63 nm s^{-1} . The sample was at a SWD of 50 mm. This measure resulted in a further decrease of the resistivity to a value of $26 \mu\Omega \text{ cm}$, which is close to the expected value given by [275].

It was also tested if, by further decreasing the SWD to 40 mm, the thin film resistivity can be pushed to values at or below the reference value. The reduction in the SWD by 10 mm resulted in a sputter-rate-increase of another 16% to 0.73 nm s^{-1} . See, for example, ‘OsCr11’ to ‘OsCr15’ and ‘OsCr18’ where resistivity values of $21.7 \mu\Omega \text{ cm}$ and below were reached, pointing out that the density of the produced thin films is now comparable to the bulk density values of Os. Note that these findings are also supported by the EDX measurements, given in Figure 4.19 (a) and (visually less pronounced) (b). The thin film O-content was reduced to less than 8%. Due to the high density of Os, this oxygen content can be considered negligible for the thin film density, see Figure 4.19 (b).

There is also another class of resistivity values (‘OsCr17 and ‘OsCr19’ to ‘OsCr28’), showing twice as high to more than ten times higher resistivity values, but no increase in the O-content (Figure 4.19), which has yet to be explained: this is due to a grain-size refinement measure, further described in the next section. Note that the AV for the EDX measurements was set to 10 kV, such that the electron penetration depth

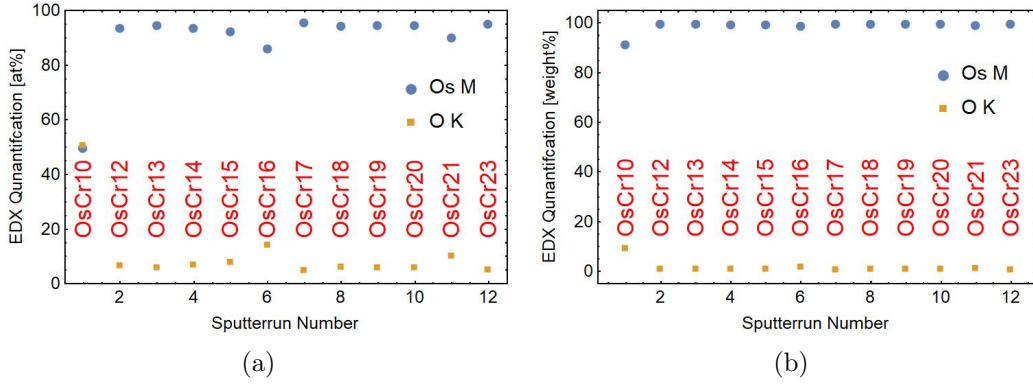


Figure 4.19: EDX analysis results of some of the sputtered Os thin films (plane-view), using a FEG-SEM, equipped with a silicon drift detector (SDD) (EDAX, Octane Elite 55), showing the high purity (except ‘OsCr10’) in (a), given in atomic percent, of the produced thin films, and high density (b), given in weight percent.

(~ 71 nm) was well below the thin film thickness.

Even though the achieved density level of the thin films is very high, the question of where the residual oxygen came from, and if it can be minimized, should be answered. EDX measurements of Os thin films, produced at base pressures of 5×10^{-6} mbar (‘OsCr12’ and ‘OsCr13’), give practically no hint on a reduced oxygen content upon reduced background pressure, see Figure 4.19 (a).

The model for the oxygen content in a thin film is based on the O_2 arrival ratio and the sputter rate, given in Section 2.9.2, so Equation 2.63, can be rewritten to yield a relation for the base pressure that is needed to provide a certain oxygen concentration in the thin film,

$$p(R, T, C_{O_2}, \alpha_{stick}) = \frac{m_{O_2} C_{O_2} R}{\alpha_{stick}} \cdot \sqrt{\frac{2\pi k_B T}{m_{O_2}}}, \quad (4.4)$$

with R being the deposition rate in atoms/(m^2s), C_{O_2} being the oxygen content of the film, T the substrate temperature, k_B the Boltzmann constant and m_{O_2} the mass of the O_2 molecule. This can be reformulated to,

$$C_{O_2}(p, R, T, \alpha_{stick}) = 100\% \cdot \frac{p \alpha_{stick}}{m_{O_2} R} \cdot \left(\frac{2\pi k_B T}{m_{O_2}} \right)^{-1/2}, \quad (4.5)$$

yielding an expression for the oxygen concentration, depending on the base pressure, deposition rate, temperature and sticking ratio α_{stick} . The result of fitting this relation to the measured values of O-content of the thin films is shown in Figure 4.20. For lower base pressures, the measured O-contents do not follow the theoretical curve anymore, instead they are higher, hinting at the possibility that the background pressure is not the main source of O_2 . A possible explanation is be

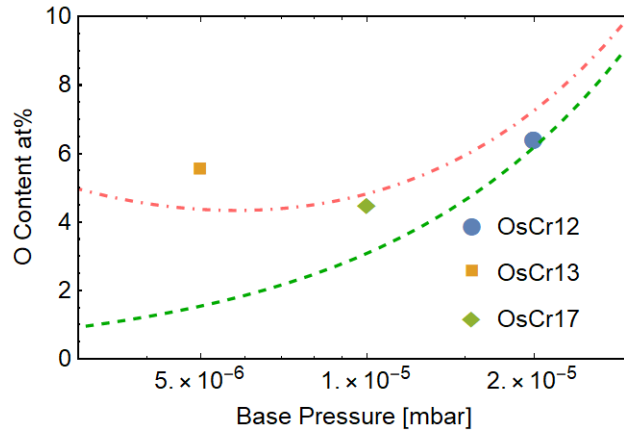


Figure 4.20: The plot exemplifies how the O-content in OsCr thin films reduces upon reduced base pressure. Only sputter runs under identical conditions have been taken in consideration. The green dashed line represent the theory according to Equation 4.5, using a sticking ratio of 0.18 and a sputtering rate of 4.17046×10^{19} Atoms/(m²s) whereas the red dashed line should only act as guide to the eye. ‘OsCr17’ shows a lower O-content than ‘OsCr13’ because a collimator was used, described in the next section.

the Ar-process gas delivery tubing, which consists of rubber tubes. In spite of it being a quite uncommon practice in scientific instrumentation, using rubber tubing for the process gas and venting gas supply lead to an interesting observation during a He-leakage measurement. It was observed that the He-signal rose after opening the Ar bleeding valve from 1×10^{-10} mbar l s⁻¹ to values between 4×10^{-9} mbar l s⁻¹ and 7×10^{-9} mbar l s⁻¹. During the Ar bleeding process it was depressed again to 1×10^{-10} mbar l s⁻¹. After the Ar flushing was finished, the leakage did not go back to the initial value, but remained at 3.6×10^{-9} mbar l s⁻¹.

This behaviour could be caused by an inflow of He into the Ar delivery hose, which is still a 2.1 m long rubber hose (Cole-Parmer) with an outer diameter of 6.2 mm, being released into the vacuum chamber upon starting the Ar flushing. Concomitantly, N₂ / O₂ / CO₂ impurities could also be present in the Ar tubing. This circumstance does not represent a problem for the deposition of noble metals, but future tests, dealing with the deposition of high purity magnetic samples, like Fe, could be affected. Besides, a lot of effort went into getting rid of oxygen in the chamber prior to sputtering, and if it now turns out that O₂ is introduced with the bleeding gas during sputtering, this issue has to be tackled.

To test this assumption, one can either try to estimate the gas leakage rate, due to permeation, according to Table 2.5, using the hose geometry and the assumption that the partial pressure of O₂ / N₂ / CO₂ inside the hose is practically zero, or try to measure the gas composition, e.g., via a rest gas analysis and a process gas analysis, using a quadrupole spectrometer.

Table 4.3: Leakage rate of the process gas line due to gas permeation for different tubing options. The permeating gas was O₂, except for Cu, where it was H₂.

Material	Q_{Perm} [mbar l s ⁻¹]
Silicone	1.97×10^{-2}
Tygon E Lab	1.98×10^{-4}
C-Flex Ultra	2.72×10^{-6}
Cu	3.3×10^{-13}

The estimated leakage rates in Table 4.3 were calculated using Equation 2.65, with the permeation rates taken from Table 2.5 in Section 2.9.2, a tube wall thickness of 1 mm, a tube length of 2.1 m, a mean tube diameter of 5 mm and a difference pressure of 1 bar. The leakage rates of the *C-Flex Ultra* tubing solution are two orders of magnitude better than the original *Tygon-E-Lab* tubing, but still orders of magnitude worse than a metal pipe solution. In addition, the leakage rates are 3 to 5 orders of magnitude worse than those of a compression or cutting ring connection (e.g., Swagelock or FITOK), which have typical leakage rates of 3×10^{-9} mbar l s⁻¹ as determined with the UL200 He-leakage detector and also found in the technical manuals.

This suggests that there could indeed be a significant inflow of impurities through the rubber tubing. Contrary to the quadrupole test mentioned above, there is another simple experiment that could, at least qualitatively, answer the question of a contamination with O₂ / N₂ / CO₂ in the bleeding gas. The optical emission spectra of N/N₂ and O/O₂ are different to the one of Ar, see Figure 4.21⁷. Thus, upon optical inspection of the plasma ignition process it should be possible to discern the presence of O/N. This was tested as follows: A CCD camera video was taken from the plasma ignition process after a pump-hold of ~1 h without the typical Ar flushing right before igniting the plasma, see Figure 4.22. It can be clearly seen that in the first few milliseconds after the plasma ignition a bluish shine is present in contrast to the pure Ar-plasma at later times, indicative of a presence of impurities. This bluish shine is not present when the chamber is flushed with Ar before the sputter run.

Therefore, it seems to be very likely that an O₂, N₂, CO₂ contamination can be introduced by the rubber tubing and with that the material choice of the process gas line is crucial. This is probably also true for the N₂ vent gas line, where O₂, as a highly reactive gas would, e.g., increase the out-gassing time of the system.

4.3.3 Optimizing the Thin Film Inner Stresses and Grain Size

Generally, the aim of the thin film deposition process should be a dense, fine-grained, highly conductive thin film. In addition to that, Figure 4.23 (a) shows another

⁷The emission spectra of N₂ / O₂ etc. are based on the Saha-LTE (local thermodynamic equilibrium) spectra from the NIST database, according to [276]

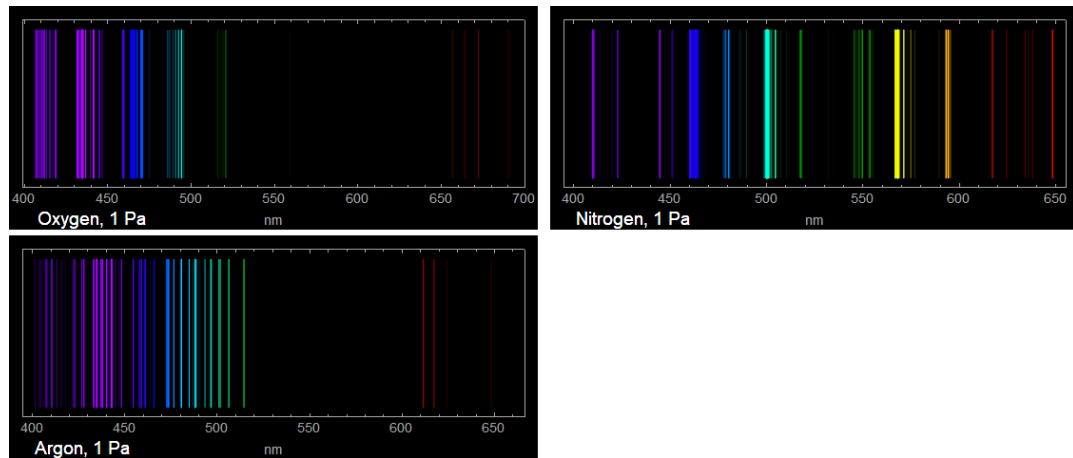


Figure 4.21: Showing the atomic emission spectra for different gas species for an electron density of $4.83 \times 10^{13} \text{ cm}^{-3}$ (a vacuum level of approximately 1 Pa) and an electron kinetic energy of 2 eV. Note the higher spectral line-density in the blue region for O/N and the differences between Ar and O/N in the wave length region 520 nm to 600 nm, making the detection of air, via optical inspection, feasible.

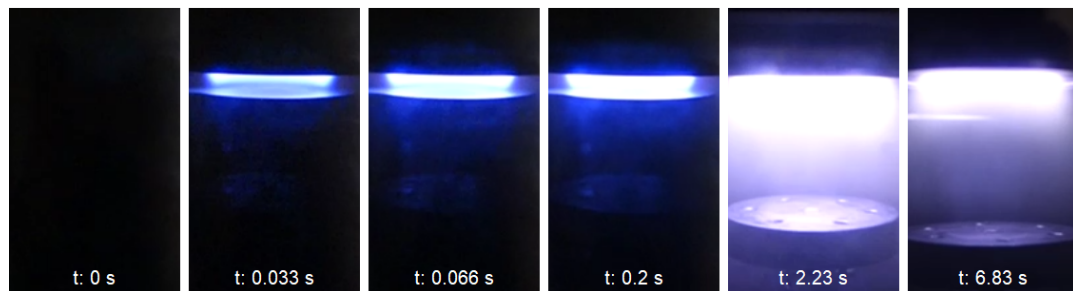


Figure 4.22: Image series extracted from a video of the ignition of the Ar plasma after ~ 1 h pump-hold and without flushing the chamber with Ar prior to sputtering. Note: the strong bluish shine in the first 200 ms is missing after 2.23 s.

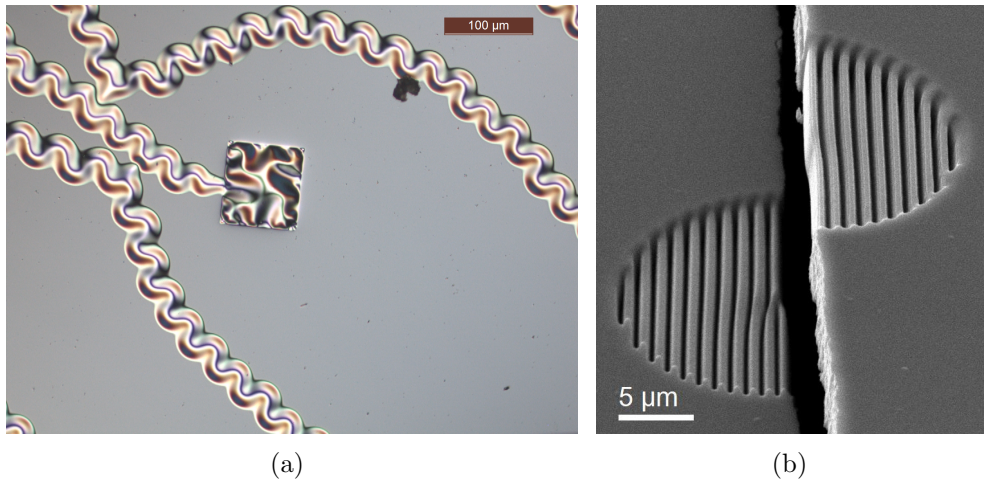


Figure 4.23: Effects of thin film inner stress. (a) A 300 nm Ir film on SiNx, using a 20 nm Ti adhesion layer, shows protruding meandering structures. This buckling is due to compressive stresses in the film. Thereby, especially the structure across the SiNx window, known as augmented tetraskelion, is indicative of this condition [277]. (b) SEM image of a HVM out of 3.8 μm Cr that was torn apart during FIB milling due to inner tensile stresses.

crucial aspect of thin film deposition for the HVM production, especially when dealing with high-modulus materials like Os/Ir. There, a light optical image of one of the first Ir thin films, deposited with the in-house Q150T sputter coater, shows periodic snake like structures, known as buckling instabilities. These are caused by strong compressive inner stresses in the thin film [277]. Contrary to that, Figure 4.23 (b) shows a HVM ruptured during the FIB milling process, due to strong tensile inner tensions in the Cr layer it was made of.

The formation of the grating collapses, i.e., agglomerate or coalescing of grating bars. The mechanism behind it was, as to the authors knowledge, not yet reported or explained, at least not in the context of holographic electron beam manipulation. In personal communications with colleagues from Dresden, adding to the experimental work presented in the preceding sections, this behaviour could be replicated. Aside from being a result of compressive inner tensions, that are released in the moment the ion-beam separates the grating bar from its surrounding support, other effects could be envisaged as being responsible, or at least contributing to the observed effect. These are, for example, plasmonic repulsion and attraction, caused by the electric fields of the passing Ga-ions, similar to the situation described in [278] for swift electrons, passing by nanoparticles or electrostatic charging of the grating bars [57] as well as, more exotic, *Casimir* forces or *Van-der-Waals* (VdW) forces due to quantum vacuum fluctuations [279, 280].

Charging effects were ruled out, since using the electron shower function of the FIB

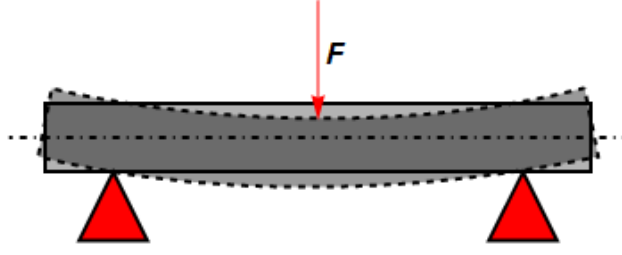


Figure 4.24: Schematic of the mechanical supporting bar model.

during milling of a holographic structure, did not prevent the formation of grating collapses. Also, the films should have a very high electrical conductivity, as shown in the preceding section.

To estimate the significance of the effects of plasmonic repulsion and/or attraction and the VdW forces, it is possible to calculate the force that is needed to bend a simple beam by using the following material mechanics relation:

$$F = \frac{45EI_z s}{l^3}, \quad (4.6)$$

where E represents the Young's or elastic modulus, describing the stiffness of the grating bar material, I_z is the geometrical moment of inertia for a rectangular grating bar cross-section, given by $I_z = (hb^3)/12$, with b , h being the bar width and height, respectively. s is the bending vector length and l is the distance between two successive supporting bars, see Figure 4.24. For the geometry and materials in use, typical bending forces are estimated to be of the order of $0.34 \mu\text{N}$ to $5.9 \mu\text{N}$ for Ir/Os grating bars and in the range from $0.05 \mu\text{N}$ to $1.8 \mu\text{N}$ for Au/Pt bars. The force per unit area, due to VdW interaction between two semi-spaces (S), can be calculated by [280],

$$F_{SS}(a) = -\frac{H}{6\pi a^3}, \quad (4.7)$$

where a represents the separation of the two plates and H is the Hamaker constant, which depends on the material properties, e.g., Au with $4.4 \times 10^{-19} \text{ J}$ [280]. Equation 4.7 is only valid for a very narrow range from 0.5 nm to 2 nm , whereas the *Casimir* force per unit area, for an ideal metal without corrections for the materials conductivity, can be given by,

$$F_{SS}^{(0)}(a) = -\frac{\pi^2 \hbar c}{240 a^4}, \quad (4.8)$$

yielding a force of 6.7 nN to $2.6 \times 10^{-2} \text{ nN}$ for a separation distance of 25 nm to 100 nm , which is roughly three orders of magnitude too low for an effective bending of the grating bar beams. Also, the plasmonic repulsion and/or attraction forces are of the order of 0.1 pN to 70 pN for swift electrons [278] and approximately three orders smaller for ions, thus, ruling out the possibility to have an influence on the

grating bar coalescences. Only if the two grating bars are in close proximity, like 4 nm to 10 nm, the VdW force increases to levels, that would be able to deform the bars, i.e.: 10.2 μN to 0.26 μN .

For thin film inner stresses ranges from -2 GPa to 1.2 GPa in Ir [275] and from -5.5 GPa to -1.5 GPa in Os [273] were measured. To estimate the impact of the effect of thin film inner tensions for the grating collapse, one can calculate the stress needed to deform a beam, like it is shown in Figure 4.24. First, the length of the deformed beam has to be determined assuming a sinusoidal deformation as: $f(x) = s \sin(2\pi/2l)$, while the length of the curve can be calculated with the relation $L = \int_a^b \sqrt{1 + f'(x)^2} dx$. Comparing the length of the bended beam L to its original length l results in a strain value $\epsilon = (L - l)/l$, for a chosen geometry. By multiplying this strain value with the elastic modulus, the compressive stress, needed to bend the beam to a length L , can be estimated as:

$$\sigma_{mech} = \epsilon E = \frac{L - l}{l} E = \left(\int_a^b \sqrt{1 + f'(x)^2} dx - l \right) \frac{E}{l}. \quad (4.9)$$

For a 10 μm long Os beam, a deformation of $s = 150$ nm could be induced by a compressive inner stress as low as 0.55 GPa, i.e.: the inner stresses should be even lower.

Routes to alleviate high intrinsic stresses are, for example, the use of a relatively thick adhesion layer, that counterbalances the stresses of the of the Ir/Os/W thin film [281]. Broadway et al. [282] argue that this procedure increases the surface roughness, due to columnar growth of the adhesion layer. Another route to balance the stress in high-modulus thin films is proposed in [282]. By depositing Cr- and Ir-layers on opposing surfaces, e.g., the Ir layer is deposited on the concave surface, while the compressive Cr (or some other compressively stressed material) layer is deposited on the opposing convex surface. This should mitigate the problem of increased surface roughness, which would otherwise result from a Cr/Ir bi-layer approach, according to the authors. An alternative approach towards using only one material is given in the publication [283]. They showed that the thin film stress can be minimized by an order of magnitude using a bilayer structure of dense and porous regions of the same material.

The most elegant way, according to [282], is sputtering at the critical pressure to get low-stress fine-grain thin films. Even though the concept of a critical pressure is well known in the literature, e.g., [235, 275, 282], with the working gas pressure where the thin film inner tension is practically reduced to zero, it was impossible to find a value for Os. However, the critical pressure scales linearly to the target material's atomic mass [235] and, thus, the critical pressure of Os could, in principle, be estimated. But owing to the sputter parameters, like the power density and specific characteristics of the used sputter coater, it is possible that the actual value differs from the theoretical one [235, 275]. Moreover, the background pressure and presence of impurities influence the thin film stresses as well [238]. Due to the high density of Ir, its critical Ar-pressure is relatively high: of the order of 3 Pa [275, 282].

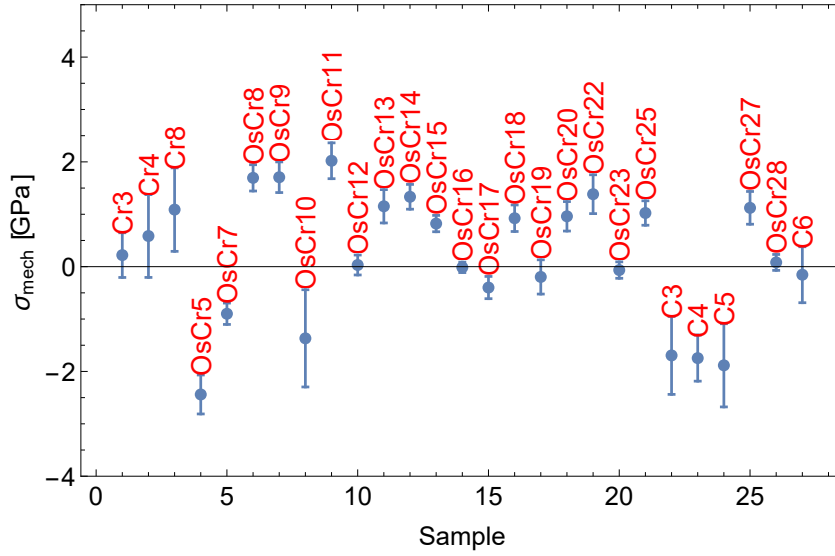


Figure 4.25: Result of the thin film tension optimization process, showing all tensiometer measurements done, testing the influence of various sputtering parameters. Measurements were done with the self-built tensiometer.

Note that a typical Ar-gas pressure for magnetron sputtering is 0.5 Pa. Additionally, in this high intrinsic stress material, which shows compressive stress on the order of a few Gigapascal, the stress variation at the critical pressure is also very high, complicating the search for an optimal sputtering pressure.

To test if the inner tensions are indeed causing this bending and sticking effects, it was necessary to quantify them in the produced thin films and to find sputter parameters where the inner tensions are strongly reduced. For the quantification a very basic tensiometer was built, as described in the Modifications chapter. The tensiometer results of this optimization process are given in Figure 4.25. The first three measurements were done using 25 nm thick Cr-layers in order to clarify the influence of the adhesion layer on the total stress. When setting the SWD to 40 mm and using the highest possible current of 150 mA, which yields a sputter rate of 2.14 nm s^{-1} at $p_B = 4 \times 10^{-5} \text{ mbar}$, the Cr layer (‘Cr3’) shows a slightly tensile inner stress of 0.2(4) GPa, but, in regard of the measurement error, it could practically be zero or slightly compressive. The same is true for the layer ‘Cr4’, where the SWD was set to 50 mm, resulting in a stress value of 0.6(8) GPa. Only ‘Cr8’, where additionally to the working distance, also the current was reduced to 100 mA, resulted in a higher 1.1(8) GPa stress level. The stage rotation in ‘Cr3’ was set to 100 % (20 RPM), while it was 30 % (6 RPM) in ‘Cr3’ and ‘Cr8’. These stress values are fairly reasonable, because the critical pressure of Cr lies at 0.27 Pa, and agree well with the literature value of the thin film tension ($\sim 0.8 \text{ GPa}$) at that working gas pressure level [235, 282]. For the following Os sputter tests the Cr adhesion layer was deposited with the ‘Cr3’ settings, such that the influence of the adhesion layer on the total stress level can be

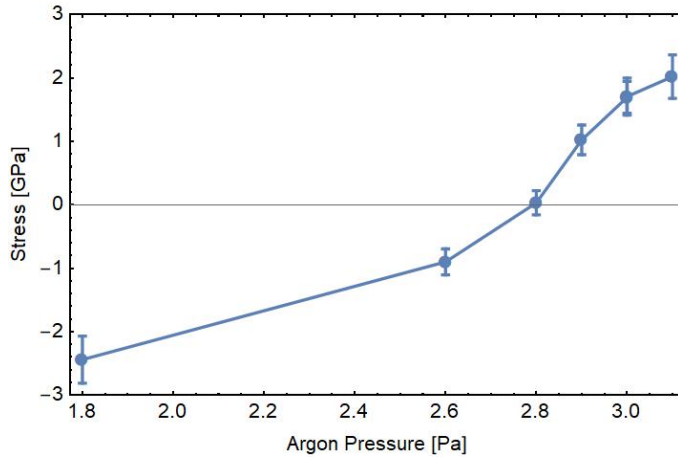


Figure 4.26: The inner stress versus Ar pressure curve reveals the critical pressure of Os to be 2.8 Pa.

minimized.

‘OsCr5’, ‘OsCr7’ to ‘OsCr9’ and ‘OsCr11’ were deposited under identical conditions except for p_{Ar} , which varied from 1.6 Pa to 3.1 Pa. For the sputter conditions used, compare to ‘Cr3’, except for the stage rotation, which was set to 6 RPM, the base pressure, which was $p_B = 1 \times 10^{-5}$ mbar and the coating thickness of ~ 200 nm. The sputter rate was 0.73 nm s^{-1} .

It is obvious that the inner stress, continuously increases with Argon pressure from $-2.4(4)$ GPa at $p_{Ar} = 1.6$ Pa, changing its sign upon going through the critical pressure, and yielding: $2.0(3)$ GPa at $p_{Ar} = 3.1$ Pa. Those sputter runs, including ‘OsCr12’ and ‘OsCr25’ (2.9 Pa), are also separately plotted in Figure 4.26 to reproduce a stress- vs. pressure-curve for Os, similar to the one for Ir, given in [275]. It was possible to determine the critical Ar-gas sputtering pressure for Os: 2.8 Pa. This was tested in the sputter run ‘OsCr12’, yielding $0.03(20)$ GPa. In literature the value for Ir ranges from 2.67 Pa to 3.04 Pa [275, 282]. Tungsten, for example, has a critical pressure of 2.67 Pa [235]. As the atomic mass of Os lies between W and Ir, the value of 2.8 Pa fits well into this picture.

It was shown that the critical pressure changes with sputter conditions [235] and the presence of rest gas impurities [238, 257]. Therefore, the influence of other sputter parameters, like the stage rotation and base pressure, was tested in further sputter tests, while keeping p_{Ar} constant. E.g., looking at ‘OsCr13’, where the base pressure was reduced to a level of 5×10^{-6} mbar, reveals that tensile stresses of $1.2(3)$ GPa are produced in the film. This can be understood by the compressive stress contribution of oxygen incorporation (shown in [284]), demonstrating the importance of constant sputter conditions for reproducible thin film stress levels.

In the sputter runs the influence of the stage rotation between ‘OsCr14’ and ‘OsCr18’ were compared: in ‘OsCr14’ the stage was stopped and in ‘OsCr18’ the rotation speed was increased to the maximum level of 20 RPM. Again, the thin film

stress value raised to the tensile regime, 1.3(2) GPa and 0.92(30) GPa, respectively, showing only a slight, non-significant, relative decrease of the inner stress between the two conditions. Please note, $p_B = 2 \times 10^{-5}$ mbar (in these two tests) was a bit worse than in the previous runs. In the ‘OsCr15’ sputter run the stage was also rotated at elevated speed, but at a base pressure comparable to the ‘OsCr13’-run ($p_B = 5 \times 10^{-6}$ mbar), and again a slight non-significant decrease was observed while the overall stress value was 0.8(2) GPa. Thus, it can be concluded that the stage rotation has, if at all, a minor effect on the thin film tension, while a decrease of the base pressure to 5×10^{-6} mbar can alter the stress level by at least one Gigapascal to the tensile regime.

The ‘OsCr16’ thin film, sputtered at 1×10^{-5} mbar, also showed vanishing inner stresses of $-0.01(10)$ GPa when the working distance was set to 60 mm, but at the cost of a massively enhanced O-content and a reduced resistivity.

Now that a set of parameters to control the thin film stresses is found, three differently stressed thin films were deposited on 200 nm SiNx membranes (SPI). Using the high-stability stage, together with the drift correction script, described in the modifications chapter, it was possible to mill HVMS into these membranes, independent of the time of the day, see Figure 4.27. Three different grating periodicities were chosen (654 nm, 545 nm, 436 nm) for the 10.9 μ m HVMS, as to see differences in the grating coalescence behaviour for the three different stress states.

The results show that compressive tensions lead to faster and more pronounced bending and deterioration of the grating bars. While for the tensile- and no-stress membranes no grating collapse (for 654 nm and 545 nm) can be observed, the compressively stressed membrane degrades at the medium grating periodicity. For the finest structures, there are more and stronger grating collapses visible for the compressively stressed membrane. Notably, no supporting bars were used, yielding a g_2/g_1 -ratio for the successfully milled medium grating periodicity of 20, which is the highest value so far observed for comparable grating periodicities. It is more than twice as high as the results given in Section 4.1 and those seen in [40]. For g_1 values of 1 μ m to 2.54 μ m, g_2/g_1 -ratios of 20 are the highest observed [139, 207]. Using UV lithography, extremely high g_2/g_1 -ratios of 40 could be reached for $g_1 = 100$ nm [285].

Even though the tensile stressed membranes show comparable good results in the FIB milling capability, both tested membranes ruptured at some point. Thus, the stress-minimized-option is indeed superior.

Note that the substrate can also have a significant influence on the stress evolution in the deposited thin film [284, 286]. But it is assumed that the SiNx leads to comparable stress values for Os thin films, as it has an amorphous surface, comparable to that of the glass slides. The low-stress SiNx membrane’s contribution to the total stress of the thin film stack is of the order of 50 MPa to 250 MPa and, thus, negligible [256].

By using a stress-reduced and density-optimized Os thin film, the possibility to mill large-scale fine-structured holograms at the in-house FIB instrument was tested. Figure 4.28 summarizes the optimization efforts done so far, as it compares two milling tests: (a) a HVM with $\varnothing 63 \mu$ m and $g = 630$ nm, was tried to mill into a non-

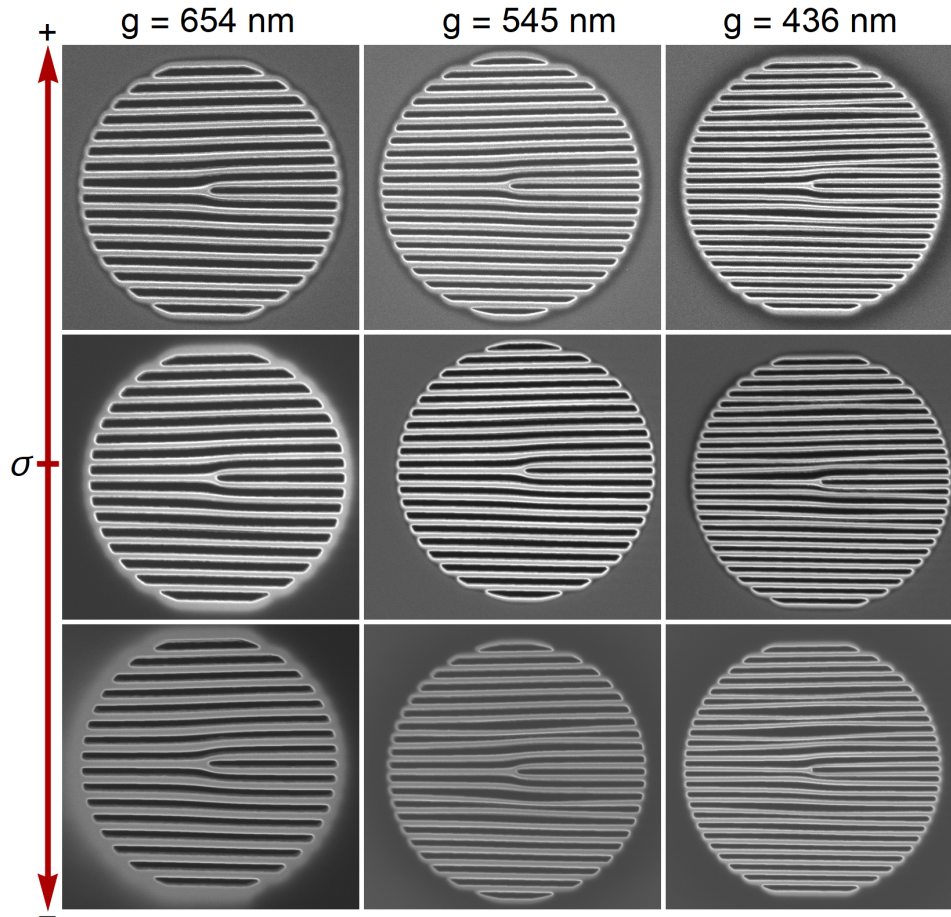


Figure 4.27: Panel showing SIM images of the FIB milling results of HVMs with decreasing grating periodicity of Os-layers, deposited at 3 Pa, uppermost series, 2.8 Pa, middle and 1.8 Pa, lowermost series. The influence of thin film inner tensions on the milling performance of fine structured HVMs can be observed. Compressive tensions lead to a faster and more pronounced bending and deterioration of the grating bars. The holograms are $10.9\ \mu\text{m}$ wide, and the grating periodicity was indicated at the top. The substrate was 200 nm low-stress SiNx (SPI).

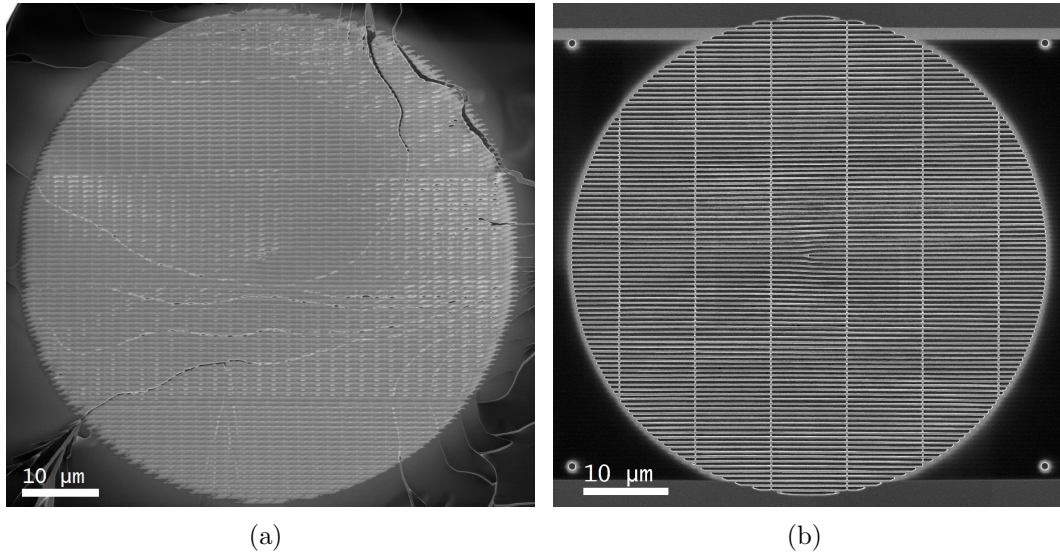


Figure 4.28: SIM images, comparing FIB milling results of large-scale HVMs with low grating periodicities. (a) HVM with $\text{Ø}63 \mu\text{m}$ and $g = 630 \text{ nm}$ tried to mill into a non-optimized $\sim 370 \text{ nm}$ Ir thin film on 200 nm SiNx without drift correction, conventional carbon tape sample mounting and a current of 100 pA . Due to strong drift and massive delamination the milling was stopped after 2 h of milling. (b) HVM with $\text{Ø}55.8 \mu\text{m}$ and $g = 558 \text{ nm}$ milled into a stress- and density-optimized 200 nm Os thin film on 200 nm SiNx, using the drift correction script and the high-stability holder, after 3 h of milling with 300 pA . The result shows that large-scale, fine-grating HVM milling is even possible on superseded FIB instruments, by using optimized conditions. The contrast reversal outside the hologram area in (b) is due to the limited drift correction window.

optimized $\sim 370 \text{ nm}$ Ir thin film on 200 nm SiNx without drift correction, conventional carbon tape sample mounting and a current of 100 pA , while in (b), a HVM with $\text{Ø}55.8 \mu\text{m}$ and $g = 558 \text{ nm}$ is shown after 3 h of milling with 300 pA , that was milled into a stress- and density-optimized 200 nm Os thin film on 200 nm SiNx, using the drift correction script and the high-stability holder.

The results show that large-scale, fine-grating HVM milling is even possible on superseded FIB instruments, using optimized conditions. Note that the grating parameters were chosen even more ambitiously than the ones for the HVMs milled at the IFW-Dresden, shown in Figure 4.6. Due to strong drift and massive delamination the milling was stopped after 2 h for the mask shown in Figure 4.28 (a). The contrast reversal outside the hologram area, seen in Figure 4.28 (b), is due to the limited drift correction window. Even though the hologram in (b) beautifully resembles the calculated pattern, milling is not completely finished. One to three passes are missing, so the achieved g_2/g_1 -ratio cannot be determined. However, it impressively shows

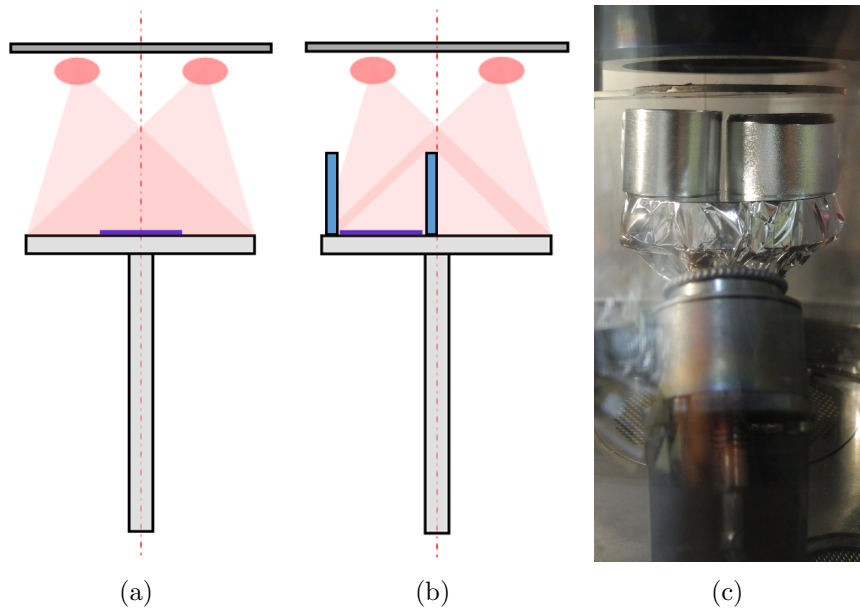


Figure 4.29: (a) Standard substrate placement geometry and (b) easy and straightforward realisation of a ‘collimated’ sputtering geometry, using a metal cylinder (blue). (c) Image of the sputter collimators (two pieces are shown).

the setup’s gain in stability and milling capabilities.

In Figure 4.27 and SEM images (not shown) show, that the grain-size of the stress-optimized films is rather large for the given purpose of the order of 50 nm.

Thus, routes are sought to reduce the grain-size, while keeping the inner stress levels low. Using a metallic ‘shield’, surrounding the sample while sputtering, see Figure 4.29, was inspired by the work of *Thornton* et al., where the oblique flux of coating atoms and reflected Ar neutrals were apertured by using a cylinder [235]. The strategy of using a metallic shield in order to block oblique incident Ar neutrals, is comparable to long-throw sputtering where the substrate is placed relatively far away from the sputter head. It kind of mimics ‘collimated’ sputtering, where, for example, an array of high aspect ratio holes is used to reduce the incident angle range of the sputtered atoms, as well as Ar neutrals, see for example [227]. Collimators are typically cell-like structures, made out of perforated-metal-sheets (e.g.: Al, Cu, Ti or Al alloys) with round, square or hexagonal opening shapes. The application of such a collimator between the sputtering target and the substrate helps to collect sputtered atoms, which are nearly aligned with the centre line of the collimator. This improves for example bottom-step coverage in narrow trenches and vias [227]. Typically, the sample/substrate (blue) is hit by target atoms stemming from the whole target region above the Ar plasma ring (red), as illustrated in Figure 4.29 (a). By using a metallic cylinder, surrounding the sample and large enough to block incoming target atoms, the acceptance angle for incoming atoms can be significantly reduced, Figure 4.29

Table 4.4: Transmission values for amplitude HVMS milled into various materials/thicknesses obtained from low-magnification TEM images.

Material	$t[nm]$	$t_{SiN_x}[nm]$	Transmission Bar [%]	Transmission Film [%]
Os	195	50	2.6	0.6
Au60/Pd40 (non-opt)	1200	250	7.0	5.9
Pt (non-opt)	450	200	26.0	6.9
Pt (non-opt)	150	200	36.7	25.2
Pt (IFW)	310	0	12.3	1.0

(b). The practical implementation of such a collimator is shown in Figure 4.29 (c).

‘OsCr17’ and ‘OsCr19’ to ‘OsCr28’ were sputtered with the collimator setup. The thin film, produced in the ‘OsCr17’, ‘OsCr19’ and ‘OsCr23’ sputter runs, which were done under the same conditions as in ‘OsCr12’, except for the collimator, show that the measured inner stress is still close to zero: $-0.4(2)$ GPa, $-0.2(3)$ GPa and $-0.07(20)$ GPa, respectively.

Electron scattering at grain boundaries increases the thin film resistivity. Thus, fine-grained films should also show an elevated resistivity compared to coarse grained films. This could indeed be determined by comparison of the ‘OsCr’ sputter results before the use of a collimator, e.g., ‘OsCr2’ to ‘OsCr18’, excluding ‘OsCr10’ and ‘OsCr16’, where other parameters were used, to the ones with a collimator in place: ‘OsCr17’ and ‘OsCr19’ to ‘OsCr28’, see Figure 4.18. The resistivity rose by a factor of approximately two. At the same time no significant change in the oxygen content of the Os-layers could be detected by EDX, see Figure 4.19, ruling out the possibility of impurities contributing to the elevated resistivity values.

Cutting the same HVM structures, as were already shown in Figure 4.27, into an Os layer comparable to ‘OsCr23’, this time deposited on 50 nm SiN_x (Norcada), lead to the results shown in Figure 4.30 (a).

The $g = 654$ nm milling test was successful: it shows a high-fidelity highly-absorbing/scattering amplitude HVM, that produces beautiful EVBs, see Figure 4.30 (b), uppermost panel. The transmission of this HVM in the area around the hologram was determined from low-magnification TEM images without the use of an OL and zero-loss filtering (as is recommended in [287]): it is 0.6 %. At the grating bars it is 2.6 %, which is strikingly low for such a thin membrane, especially compared to other non-optimized thin films, see Table 4.4. E.g., an early non-optimized Au/Pd mask with a thickness of 1200 nm still has a transmission of 5.9 % in the film area and 6.9 % at the bars. Even the transmission of a high end mask from the IFW-Dresden out of 310 nm Pt is almost five times higher than that of Os film.

Obviously, the other two gratings shown, already exhibit some grating bar collapse at a grating periodicity of 545 nm and show pronounced damage at the finest grating, comparable to the compressively stressed membranes shown in Figure 4.27. Even though, their diffraction images clearly resemble the EVB structure.

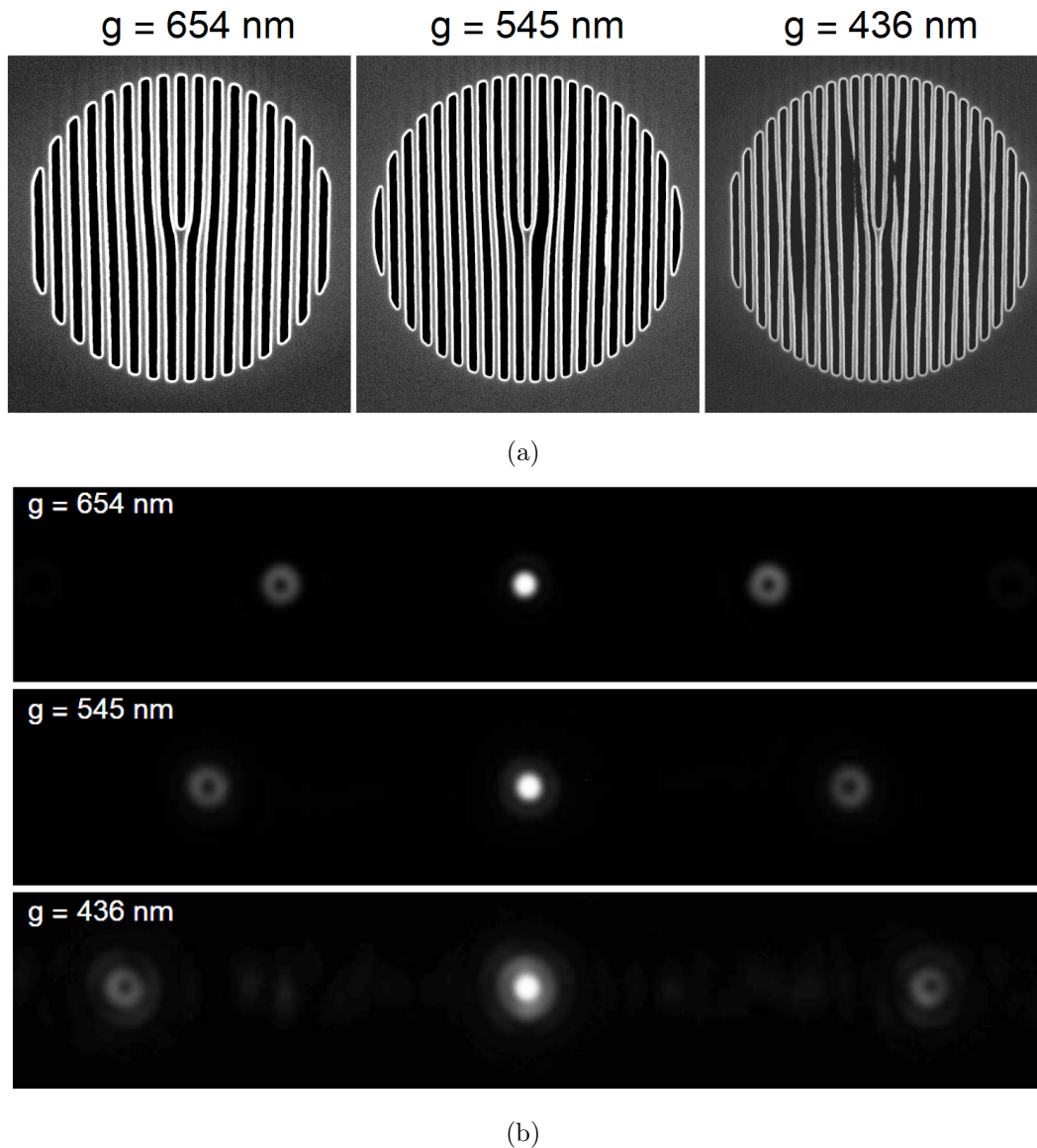


Figure 4.30: Results of the collimated sputtering approach. (a) SIM images of FIB milling results of a stress- and density-optimized 194 nm OsCr thin film on a 50 nm SiN_x membrane. The diameter of the HVM is 10.9 μm . (b) TEM diffraction images of the HVMs, placed in the sample plane, showing the perfect EVB structure gained from the 654 nm mask. The vortex order separation is 3.84 μrad , 4.61 μrad , 5.76 μrad , respectively. The images were contrast-enhanced for better visibility.

Regarding the fact that a low-stress Os membrane was used, this milling result may seem confusing at a first glance.

A possible explanation is the deposition of a thin layer of C on both sides of the OsCr-membranes, before they are transferred to the FIB instrument. This layer acts as a protection against excessive Ga-ion-beam damage during milling, due to the very low sputtering yield of C, namely 1.7. Thin film tension measurements on carbon films, ‘C3’ to ‘C5’, indicate their highly compressively stressed nature: $\sim -1.8(7)$ GPa. The deposition parameters were the same as for the Os-layers, except for the working gas pressure, 0.5 Pa to 0.7 Pa, and the base pressure, $<6 \times 10^{-6}$ mbar, with the thickness ranging from 40 nm to 85 nm.

Please note: for the non-collimator tests a 5 nm film was used, in order to avoid a strong deviation from the expected stress values.

For the milling test using collimated sputtering, a much thicker C coating (25 nm) was used, because of the much lower SiNx thickness. This could indeed shift the stress level of the thin film stack to the compressive side and explain the observed reduced milling capability of the samples shown in Figure 4.30.

Even though SEM images taken from the surface of the thin films (not shown) indicate a grain-size refinement, in TEM images (not shown) and in the SIM images, given in Figure 4.30, such a refinement cannot be observed. The given grain-size (roughly 50 nm) does not seem to alter the diffraction result of such a mask, but sputter tests were carried out, that could describe a route towards finer grained films with low-stress. Those tests included sputtering pauses after a couple of seconds, such that the thin film had some chance to relax. This intermittent sputtering, as described in [258], yielded promising results for the reduction of the compressive stress of Os-layers, see ‘OsCr28’ in Figure 4.25, which was deposited at a reduced working gas pressure of 2.7 Pa and a base pressure of 1×10^{-5} mbar, but not for tensile stressed Os films (‘OsCr27’, $p_{Ar} = 2.8$ Pa, $p_B = 9 \times 10^{-6}$ mbar). A more pronounced result is seen for a carbon layer (‘C6’), using the SCTM, described in Section 3.2: with five pauses to five minutes, including a bake out and sputter head cooling during sputtering. The stress reduction was almost two Gigapascal. The grain-size of ‘OsCr28’ was not checked, but typically lower working gas pressures lead to a grain-size refinement (see the structure zone model of *Thornton*, Figure 2.24).

The above shown results describe the influence of thin film tensions on the milling results, but they do not exclude contributions, which are due to VdW forces. To determine if indeed VdW forces are causing or contributing to the grating collapse, the following idea that comprises a three step milling process to circumvent the detrimental effect of VdW grating bar adhesion was tested. According to Equation 4.8, VdW forces can be minimized by increasing the distance between adjacent metallic plates, and/or by decreasing the plate area. So, at first, a hologram is milled using a rather dense second-order grating, acting to keep the primary grating well-separated. In a second step, the second-order grating is carefully removed. The net VdW force, due to the very localised supporting bar sites, should be negligible. The third step is indented to remove remaining leftovers of the supporting grating and kind of ‘fine polish’ the HVM structure.

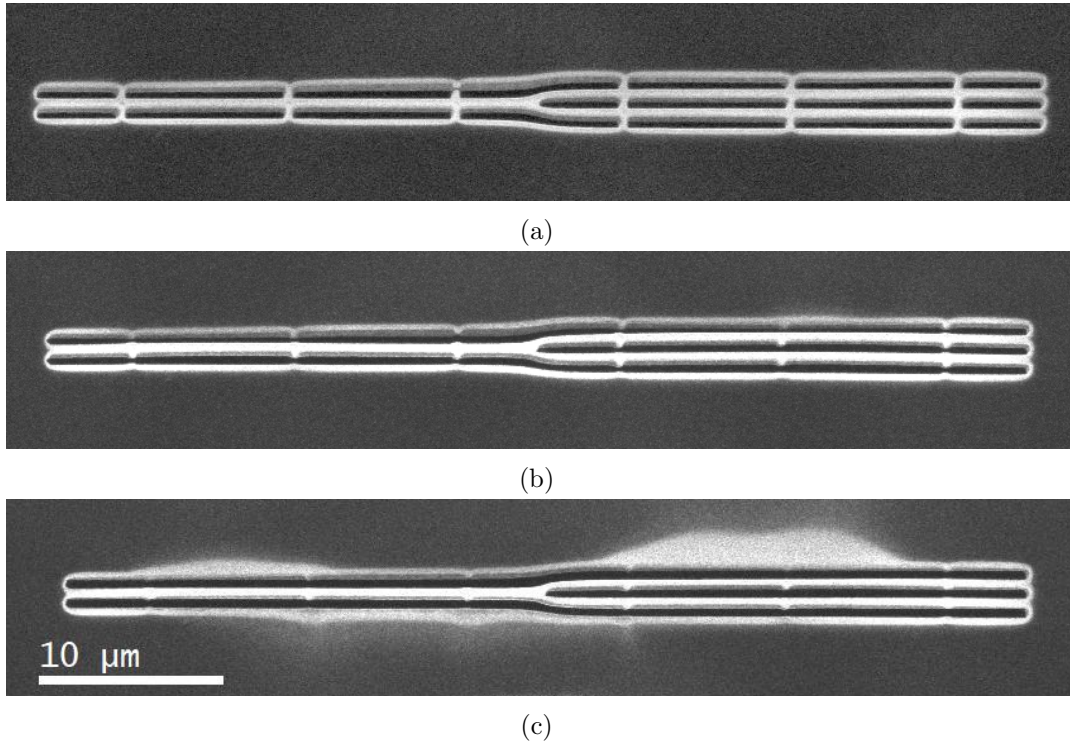


Figure 4.31: Testing the three-step milling procedure to reduce or even completely avoid the use of a supporting grating. (a) A fork dislocation test structure is milled into a 310 nm Ir membrane, deposited on 80 nm SiN_x, with the supporting bars intact. (b) In a second step only the supporting bars are removed. (c) A free standing fork-dislocation over 51 μm was produced having a g_2/g_1 -ratio of 51; some leftovers from the $g_2 = 8.5 \mu\text{m}$ supporting grating are also still visible, indicating that the duty cycle was too low in the last milling step.

Figure 4.31 shows the result of the three step milling test, carried out on a 310 nm Ir membrane, deposited on 80 nm SiN_x. There, only the dislocation region of a $D = 51 \mu\text{m}$ and $g_1 = 1 \mu\text{m}$ HVM has been milled. In the first step (Figure 4.31 (a)) the milling parameters for the Ir thin film, plus a 20 nm Ti adhesion layer were: 100 pA ion-current at 150 μs dwell time, using 25 passes. The second step included 23 passes at the same current and dwell time, Figure 4.31 (b), while the third was milled with 10 passes, Figure 4.31 (c).

After the second step, the structure was free standing, showing a very high g_2/g_1 -ratio of 51, which remained intact after the third step. Even though no stress measurement were made of films that were deposited under the exact same conditions, ‘OsCr10’ (in Figure 4.25) renders similar conditions and shows that sputtering at very low process gas pressures of 0.7 Pa, together with very low sputtering power (10 mA), results in quite low-stress films ($-1.4(9)$ GPa), probably due to the massive

inclusion of impurities. For Ir this value is most likely lower. Also, due to the high aspect ratio, the grating bars might not bend in the lateral but in the vertical direction, which may not be discernible in the SIM images. Therefore, further tests are necessary to understand the origin of this behaviour.

4.4 Binary Holographic Phase Mask Results

As will be shown in the applications chapter, the electron count rate in vortex filter EMCD experiments is very low and, thus, measures to enhance the electron collection- and diffraction-efficiency are of utmost importance.

It has been pointed out in the Fundamentals chapter and is also shown in Table 2.1, that pure binary amplitude masks are limited to $\eta_{\pm 1}^{(i)} < 10.13\%$, meaning that 10% of the electron incident on the hologram are distributed to the $m = \pm 1$ vortex orders. On the other hand, Harvey et al. [25] showed that sinusoidal phase masks can reach $\eta_{\pm 1}^{(i)}$ of 20% to 25%. Even higher DE are expected from binary phase masks, according to Table 2.1. For an ideal electron phase shift of π , which can be achieved by using approximately 42 nm of SiNx (at 200 kV AV), a DE of 40% can be expected. So far, phase masks were produced by milling grooves or trenches of 30 nm to 60 nm depth in a supporting membrane, that has to be at least 20 nm to 50 nm thicker than the groove depth. This excess material leads to pronounced high-angle scattering, drastically reducing the achieved DE.

Thus, it was tested if and how it is possible to produce a large-scale binary phase HVM, that consists of a free standing grating, practically without any excess material, except the one needed for the electron wave phase shift.

To the best of the author's knowledge there exist no reports on this kind of HVM, except in a review article on the 'Nanostructuring of electron beams' by Shiloh et al. [188], where binary phase masks were produced by milling trenches into a SiNx membrane. Their holograms supposedly showed a DE of 40% in the $m = \pm 1$ vortex orders. But the binary structure was milled into a 100 nm SiNx membrane, meaning that there is still approximately 58 nm of excess material left below the phase hologram, effectively reducing the DE by at least 50% [25].

The production of the binary phase HVM consisted of: coating a 50 nm SiNx membrane (Norcada) with a-C⁸ on the backside, mounting it in the home-built high-stability holder and moving it to the reduced working distance of 10.8 mm. Stream files including the spiral path scan-strategy and the milling direction reversal were utilized. Using nearly the full 4K DAC resolution of the FIB, it was possible to mill nearly 70 μm wide holograms with a pitch- or pixel-size of 18.4 nm. Because the stream file consisted of 3.8 MP it had to be split up in four separate files, such that the FIB control software could handle it. A dwell time of 100 μs was used and the number of passes was 2.5 and 1.5 for the holograms shown in Figure 4.32 (a) and (b), respectively. The respective Ga-ion currents were 100 pA and 300 pA, using an

⁸The carbon layer was deposited with similar parameters (like 'C6'), but with a worse vacuum and less sputtering pauses. The collimator and the SCTM were not used.

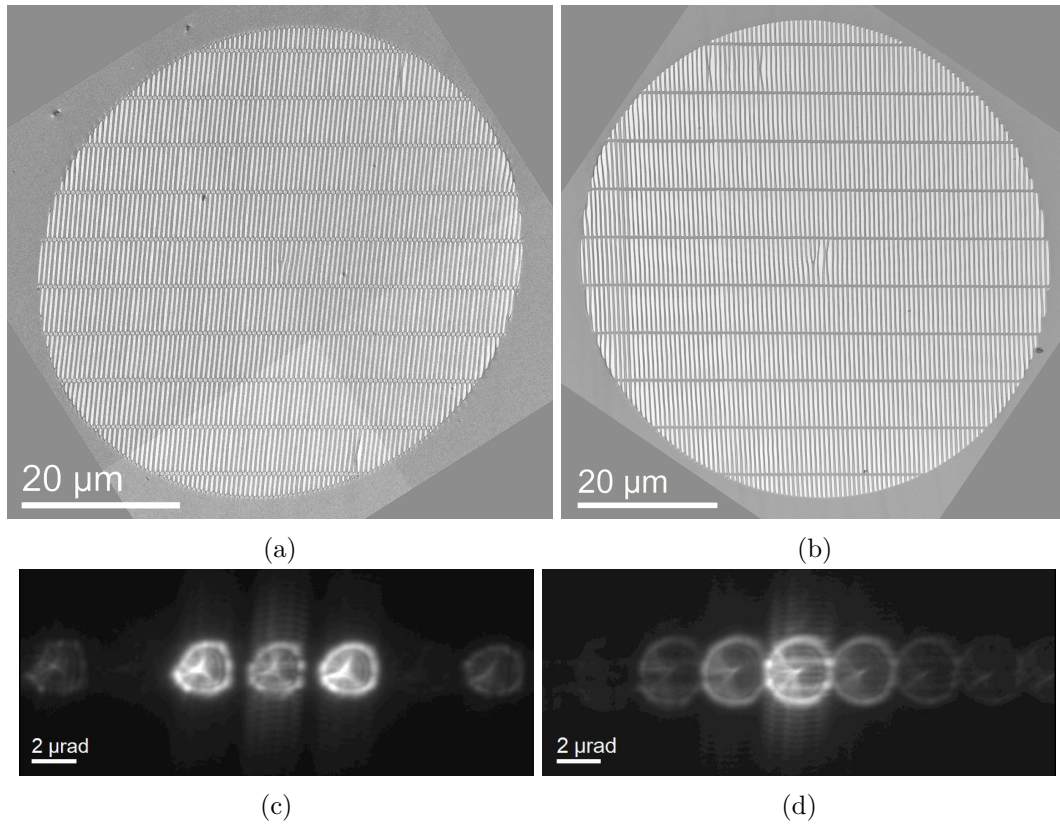


Figure 4.32: Low magnification TEM images of binary phase vortex masks with (a) a diameter of 60 μm , a grating periodicity of 600 nm and a second-order grating period of 6 μm and (b), the same as (a), but with a diameter of 68 μm , a grating period of 680 nm and a second-order grating period of 6.8 μm . The thickness for both masks was 50 nm SiNx plus 5 nm a-C. Note that the elliptic shape stems from residual astigmatism. (c) Gamma corrected far-field image of (a), and (d) far-field image of (b). The visibility of the second vortex order in (d) is due to a non-ideal duty cycle of the HVM shown in (b).

AV of 30 kV. It was tried to use the self-made drift correction script, but as the SIM contrast drastically changed and the milling times were anyway low (~ 30 min compared to 3 h to 6 h for massive Os masks), no drift correction was employed.

Figure 4.32 (c, d) depicts the low magnification TEM images of binary phase vortex masks with a diameter of $60\ \mu\text{m}$ and $68\ \mu\text{m}$, respectively. The grating periodicity was $600\ \text{nm}$ for (a) and a second-order grating period of $6\ \mu\text{m}$ was used to stabilize the main grating. In (b) the grating period was $680\ \text{nm}$ and the second-order grating had a period of $6.8\ \mu\text{m}$. The thickness for both masks was $50\ \text{nm}$ SiNx, plus $5\ \text{nm}$ a-C. Most of the structure is well defined and only a few bars tend to stick together, indicating a residue of compressive stress in the carbon film and/or in the SiNx film. Note that the elliptic shape stems from residual astigmatism. The far-field images of the produced phase holograms are shown in Figure 4.32 (c, d), strongly defocused, in order not to saturate the CCD⁹. The zeroth-order in Figure 4.32 (c) is much weaker than the orders $m = \pm 1$, indicative of a high DE and a phase shift relatively close to π . The far-field pattern of the larger hologram in Figure 4.32 (d) did not show such a damping of the zeroth-order, which is most likely due to a weaker phase shift as compared to the mask shown in (a). Notably, this structure was milled using a higher ion-dose.

Aside from the optimal phase shift, due to the material mean inner potential and thickness, the duty cycle of the grating also influences its efficiency [24].

In this approach the phase shift is (already) defined before the FIB milling step, via the membrane thickness and material. Tuning the phase shift by a dose array, like it has been done in previous works, is not feasible [25, 188]. This problem could be probably circumvented by milling the hologram into an intentionally too thin membrane and by successive depositions of thin layers of a-C, in order to increase the phase shift to the desired value.

A more in-depth study on the DE of HVM revealed that the use of phase masks is not per se superior to that of absorptions masks: it crucially depends on the amount/thickness of the supporting material below the actual phase mask structures, which are typically $\sim 50\ \text{nm}$ deep trenches cut in SiNx. For the *Jülich* phase masks a $200\ \text{nm}$ thick SiNx membrane was used, thus roughly $150\ \text{nm}$ of material act as an electron absorber or, more likely, as a high angle scatterer, which is perfectly reflected in Table 4.5. There, the absolute electron count rates of the HVM's ability to distribute incident electron counts into the $m = \pm 1$ vortex order, are estimated using measured electron count rates from vortex filter EMCD experiments and some relatively crude approximations. The values in row number one are normalized to exposure time in s , incident beam current in pA and sample thickness in nm , whereas in row number two the electron collection area, which is basically the hologram area in mm^2 , is taken into account, as well. In row number three the OAM "loss"¹⁰, due to elastic scattering in the mask material, is also included. A means to reduce

⁹The microscope was already set up for following vortex filter EMCD experiments, so the beam current was quite high for imaging zero-loss images.

¹⁰The OAM loss was estimated using multi-slice simulations through amorphous material, some of which will be shown in the applications chapter.

4.5 Prospects to Mount Holographic Vortex Masks in a Standard Objective Aperture Strip

Table 4.5: Estimated absolute DE in units of electron counts of different HVMS, based on count rate measurements. The values are normalized to incident current, exposure time and sample thickness (first row). In the second row the mask area was also taken into account and in the third row the ‘OAM’ loss is included. The binary phase HVM shows an 8.6-fold higher count rate compared to the *Jülich* phase masks. The phase shift of the binary HVM was not optimized, thus the count rate is comparable to the binary amplitude HVM, theoretically an approximately two-to-three-fold improvement of the count rate should be possible.

Unit	Binary Phase Mask 75 μm	Jülich Sine Phase Mask 1 40 μm	Jülich Sine Phase Mask 2 40 μm	Binary Amplitude Mask 30 μm
$\frac{\text{cts}}{\text{s pA nm}}$	2.074	0.142	0.143	0.254
$\frac{\text{cts}}{\text{s pA nm mm}^2}$	4.69×10^{-4}	0.89×10^{-4}	0.9×10^{-4}	4.05×10^{-4}
$\frac{\text{cts}}{\text{s pA nm mm}^2}$	4.29×10^{-4}	0.50×10^{-4}	0.50×10^{-4}	3.84×10^{-4}

electron scattering in excess material of the hologram is to use binary phase HVM. There, the thickness of the absorbing layer behind the phase shifting structures is per definition zero, and if the phase shift of the remaining diffracting grating bars is tuned to be π , a theoretical maximum of $\eta_{(i)}^{\pm 1} = 40\%$ of the incident electrons can be distributed in the first vortex order, which is the highest among the alternatives given in Table 2.1. In binary amplitude/absorption masks this value is 10.13%. Depending on the thickness of the supporting layer of sinusoidal phase masks, this value can be as low as a few percent, ranging up to 20%-25% in the optimized case, whereas the theoretical maximum is 33.85%. First tests to produce a binary phase HVM using the FIB and 50 nm thick SiNx membranes, described in Section 4.4, show promising results, as can be seen in Table 4.5: the binary phase HVM performs quite well; it shows an 8.6-fold higher absolute count rate, compared to the *Jülich* phase masks, and is slightly better than the traditional binary amplitude masks. Note that the phase shift was not optimized, which would lead to a roughly two-to-three-fold improvement in the DE.

4.5 Prospects to Mount Holographic Vortex Masks in a Standard Objective Aperture Strip

The instructive vortex filter EMCD measurements (done in *Jülich*), which will be presented in the Applications chapter, using a simplified vortex filter EMCD setup, with the filtering hologram placed in the objective aperture position of a wide-gap pole-piece, lead to the question of how to place a vortex filter mask in the objective aperture plane of a standard pole-piece TEM, with as little as possible modifications

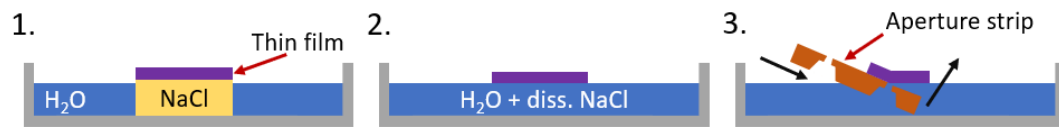


Figure 4.33: Showing schematically the floating-off process to place a thin film on an aperture strip for the production of HVM.

to the aperture strip and the TEM. Moreover, in the production of phase masks, the absorbing metal layer, which is used to aperture the electron beam, is typically deposited on a SiNx membrane with a subsequent removal of the absorbing layer in the phase mask region, using a FIB device. This process leads to some residual debris and imperfections in the surface structure of the SiNx, which can alter the holograms quality. Aside from using lithography methods, this issue could also be addressed by a lift-off approach, described in the following [190].

It is well known in EM sample preparation that thin microtome sections or a-C thin films can be floated off in a water bath, see, e.g., in [250], as exemplified in Figure 4.33. It was tested if this approach can also be used to place thin films for hologram production directly on an OL aperture strip, such that only selected apertures are covered, while the others are left as they are. For that, an a-C thin film was deposited on a freshly cleaved NaCl single crystal (Korth), using the Q150T and deposition parameters similar to ‘C6’, but with less sputtering pauses, no collimator and no SCTM-heating or -cooling. The coated crystal was then placed in a water bath using distilled H₂O, Figure 4.33 (first step). The NaCl crystal slowly dissolves in the water bath until only the thin film is left, floating on the water surface Figure 4.33 (step two). Afterwards the aperture strip was carefully moved under the floating film. Prior to the floating process the strip’s wettability was enhanced by an Air-plasma treatment (Diener Electronic, Plasma Prep 5). Under microscopical observation the aperture strip is positioned under the thin film, such that the thin film is floating directly over the apertures that need to be covered by the film. Quickly lifting the strip out of the water ensures that the film is also being placed on that position, Figure 4.33 (step three).

The result of such a floating process can be seen in Figure 4.34 (a, b) where a 40 nm a-C thin film was used. Note that only the two apertures shown in Figure 4.34 (a,b) are covered, the other six apertures can be used for normal TEM observations, as can be seen in the overview image in Figure 4.34 (c). In Figure 4.34 (a) a few ripples are visible in the a-C layer, which are probably due to the rough surface structure of the aperture strip around the aperture hole. The aperture strip used for this test was already used in the TEM and was subject to severe deformation, due to a malfunction of the TEM stage. Typically the surface of such aperture strips is very smooth. Another reason could be compressive inner stresses in the thin film, due to differences in the sputtering conditions of the film, compared to ‘C6’. Notably, this demonstration was done using thin C, as it could be used for holographic phase-plates

4.5 Prospects to Mount Holographic Vortex Masks in a Standard Objective Aperture Strip

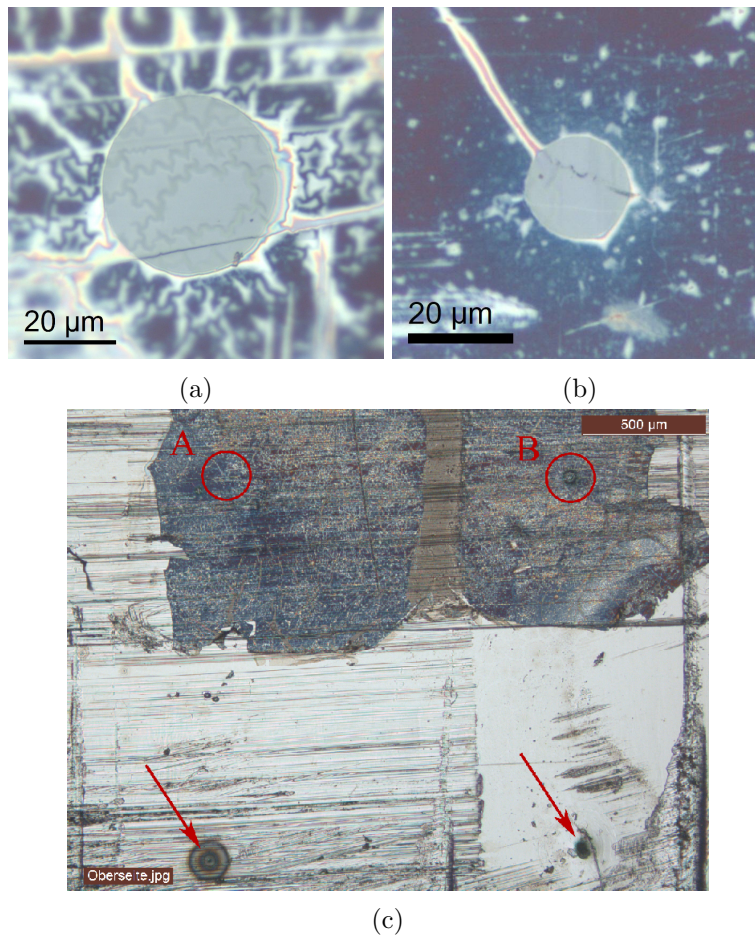


Figure 4.34: Light-optical images of a 40 nm a-C membrane, floated off a NaCl crystal and placed on the 40 μm (a) and the 20 μm (b) apertures of a TEM objective lens aperture strip. Prior to the floating process, the strip's surface tension was increased by an Air-plasma treatment. (c) Overview image, showing that the film was placed only on apertures 'A' and 'B' and does not cover other apertures on the strip, marked by red arrows.

and is semi-transparent to light, which makes the light optical observation possible. But, generally this process also works for thicker heavy metal membranes, which are typically used for holographic absorption masks.

This successful demonstration is the basis for further FIB milling steps and for the placement of a vortex filter in a standard pole-piece TEM. By that, experimentally streamlined filtering EMCD could be accessible in a much wider class of TEMs.

5 Recent Applications and Progress

In the preceding chapter certain routes to refine and optimize HVMs and their production were described. This chapter aims at giving an insight on practical applications of HVMs, and the EVBs produced thereby, with the focus set on vortex filter electron energy-loss magnetic chiral dichroism and the measurement and quantum mechanical description of fundamental rotation-dynamics of vortex beams in the magnetic field of a TEM objective lens.

5.1 Electron Vortex Beam Filter - EMCD

In general, there are two possible experimental setups, utilizing EVBs for EMCD measurements: pre- and post-specimen techniques. The pre-specimen method is described in [35, 36, 288]. Attempts to produce EVBs and to further use them for EMCD measurements did not show an effect so far [38, 40]. The possibilities and limitations of the application of a vorticity filtering HVM for EMCD measurements will be described in detail, e.g.: showing that a single atom scattering approach already delivers reasonable results, in order to estimate the EVB-EMCD effect of this technique. The principal experimental setup of a filtering vortex hologram, placed in the diffraction plane, will be discussed and this approach will be further justified via elastic- and inelastic-MS simulations. Additionally, an alternative setup will be presented, that utilizes a HVM in the SAA-holder, which is easier to access. All identified experimental challenges, as well as artefact sources, will be described, followed by a series of experimental results drawn from the attempt to minimize the identified artefacts, covering, both, diffraction plane- and SAA vorticity filtering HVM experiments.

Recently, ideas and simulations for an alternative filtering EMCD technique were presented [140], employing a rotatable and sample-symmetry-adopted aperture in the spectrometer or OL aperture holder, that collects electrons, either only from regions of positive- or negative-EMCD signal. Besides using core-loss electrons, an approach utilizing asymmetries in the elastic scattering cross-sections of electrons has been put forward to measure a magnetic signal [131, 132].

While for the pre-specimen setup, applied to crystalline materials, atomic vortices and very specific conditions for the detection of an EMCD signal are needed [35, 288], multi-slice simulations, given herein, reveal the possibility to perform vortex filter EMCD also on amorphous materials.

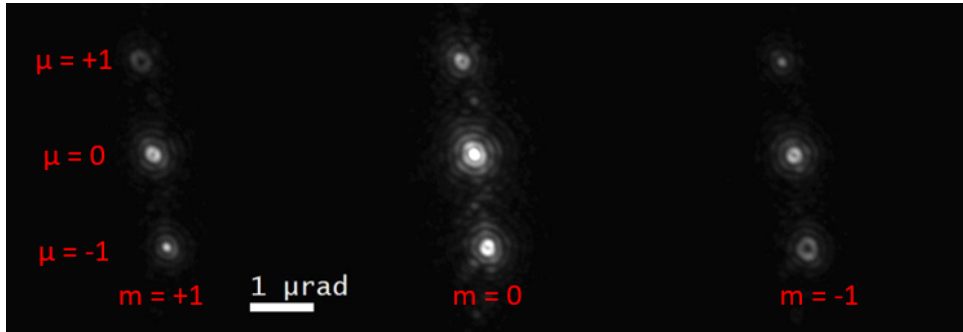


Figure 5.1: Proof of the vortex filter functionality in vacuum at the *Tecnai F20*. Vortices were produced by a HVM in the condenser system of the TEM ($\mu = \pm 1, 0$). These were incident on a second HVM, acting as a vortex filter and placed in the SAA holder ($m = \pm 1, 0$). Due to the orientation of the two HVMs, close to orthogonal, the addition and subtraction of OAM is illustrated in one single image.

5.1.1 Introduction

It has been shown that OAM can be transferred to the probing electron, when it excites electronic transitions to spin-polarized final states in the sample [133]. This manifests itself in a vortical structure of the inelastically scattered probe electron, which could be detected by a HVM after the beam-specimen interaction. As already pointed out in the Fundamentals chapter, there are various other techniques to discern the OAM content of an electron beam, with their own advantages and disadvantages. Here, the focus lies on using in-house-built binary amplitude masks and phase holograms, made by collaborators at the Ernst Ruska-Centre for Microscopy and Spectroscopy with Electrons (ER-C) in *Jülich*, for vorticity filtering.

In optics, for example, HVMs have proven to work as a chiral filter [20, 44, 289].

Likewise, vorticity filtering, as described in the Fundamentals Section 2.6, employing holographic devices, does also work for electrons, see [45, 207]. An impressive illustration of that principle can be given using two HVMs that are oriented normal to each other, see Figure 5.1. By placing the first HVM into the condenser system of a TEM, EVBs can be produced and analysed for their OAM state, when incident on the second HVM, which is placed in the SAA-holder. Due to the orientation of the two HVMs, close to orthogonal, one can clearly see the addition and subtraction of OAM, with $\mu = \pm 1, 0$ denoting the incident EVBs and $m = \pm 1, 0$ representing the vortex orders stemming from the SAA hologram.

5.1.2 Experimental Setups

In principle there are two positions accessible in the TEM that can be used to install filtering holograms: the DP and the SAD plane. From an experimental perspective, the use of the DP for vorticity filtering is the straightforward approach, as illustrated

in Figure 5.2 (a): the sample (red dot) can reside at the eucentric height and the only required modification to the illumination system is to accurately focus the beam onto the specimen. The incident electrons are, then, inelastically scattered into three scattering channels, $\mu = \pm 1, 0$. The outgoing electrons $\mu = \pm 1$ now carry OAM of one $\pm\hbar$, respectively. They are incident on a HVM in the far-field, which adds topological charges $m \in \mathbb{Z}$ to the initial OAM state. This results in a line of vortices of topological charges $\mu + m$ in the intermediate image plane. Finally, using an in-column or post-column electron energy loss filter, an EMCD signal can be measured as the difference in the radial profiles of the vortex orders $m = \pm 1$ at the respective core-loss energy.

Even though there are proposals to use spiral-phase-plates in the DP, e.g., as a probe for chiral crystal symmetries and the local OAM content of an electron wave [31, 290], up to now no successful implementation of a vortex mask in the DP of a standard pole-piece TEM was done. Typically the contrast apertures are machined into one thin metal strip, instead of having an aperture holder that can handle four individual $\text{\O}3\text{ mm}$ apertures. The strip is used because of the limited space in TEM pole-pieces (Super-Twin pole-piece gap: 5.4 mm). Only on specialised wide-gap instruments (cryo pole-piece gap: 11 mm), like the *Titan Holo* at the ER-C in *Jülich*, it is possible to use a standard aperture holder in the BFP of the OL as well. The author was granted measurement time on that machine and the results will be presented in Subsection 5.1.7.

An alternative method, which is functionally equivalent to the setup described above, employs the readily accessible SAA plane for mounting a vorticity filtering HVM, see Figure 5.2 (b). There, any custom-made apertures can be retrofitted in the SAA-holder. This setup can, thus, be carried out on any TEM. Obviously, by changing the HVM position, the electron-optical setup has to be adapted. In case of a specimen placed in the eucentric height, the intermediate image would be a magnified image of the outgoing electron wave. This couple of nanometre-sized image would be far too small to illuminate the $5\text{ }\mu\text{m}$ to $30\text{ }\mu\text{m}$ sized HVM. By lifting the sample and the cross-over above the eucentric height, the first cross-over after the sample is lifted above the SAA plane, such that the divergent ‘light cone’ now provides a proper illumination of the HVM. This ensures that the (virtual or back projected) HVM is now in the far-field of the excited atom and creates a series of images of the ionization process, as shown in Figure 5.2 (b). In principle, this setup is very similar to a standard STEM geometry, but with the specimen lifted far above the eucentric plane.

For a better understanding and to give a few more details on the setups, Figure 5.3 (a) depicts a standard diffraction TEM setup, including a HVM in the SAA-holder and compares it to the DP vortex filter setup, which is essentially a standard STEM setup, Figure 5.3 (b), as well as to the SAA-plane vortex filter setup, given in Figure 5.3 (c). Obviously, when the vortex filter mask (light blue) is placed in the SAA plane, diffracted beams emerge from the vortex mask in Figure 5.3 (a), marked by the dashed lines, and their focal position coincides with the observation or intermediate plane. In the case of inelastic scattering the intensity distribution, given in the cross-

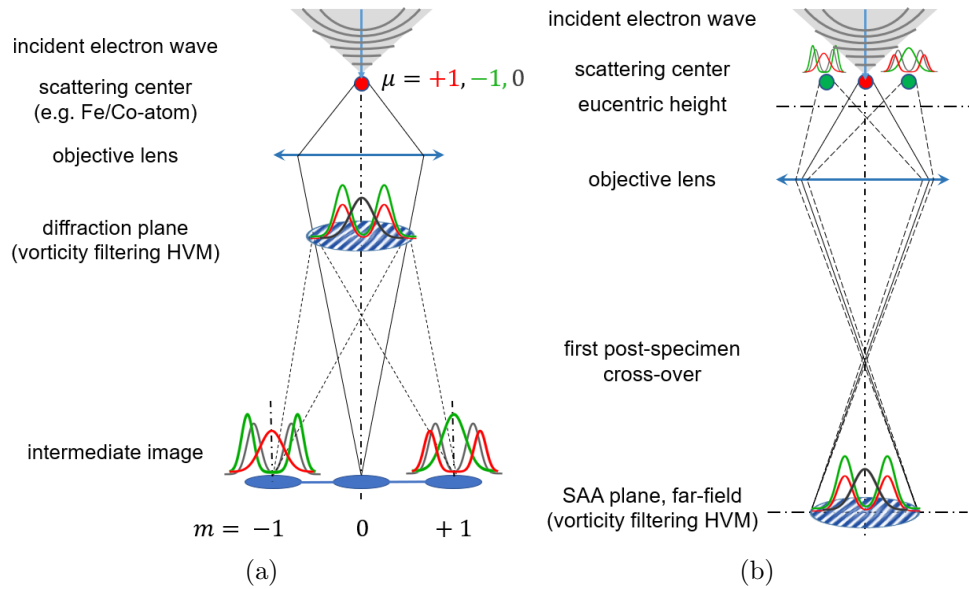


Figure 5.2: Vortex filter EMCD experimental setup using a post-specimen vortex filtering hologram, placed in the DP (a) and (b) placed in the SAA plane. The red dot represents the scattering centre, i.e., the atom/sample in the object plane. The incident electrons are inelastically scattered into three asymmetrically weighted scattering channels, $\mu = \pm 1, 0$, such that the $\mu = \pm 1$ electrons now carry OAM of one $\pm\hbar$, respectively. They are incident on a HVM in the far-field, which is either the DP or the eucentric plane, which adds topological charges $m \in \mathbb{Z}$ to the initial OAM state. This results in a line of vortices of topological charges $\mu + m$ in the intermediate image plane for setup (a) or back-projected to the sample plane in setup (b). Finally, an EMCD signal can be measured as the difference in the radial profiles of the vortex orders $m = \pm 1$.

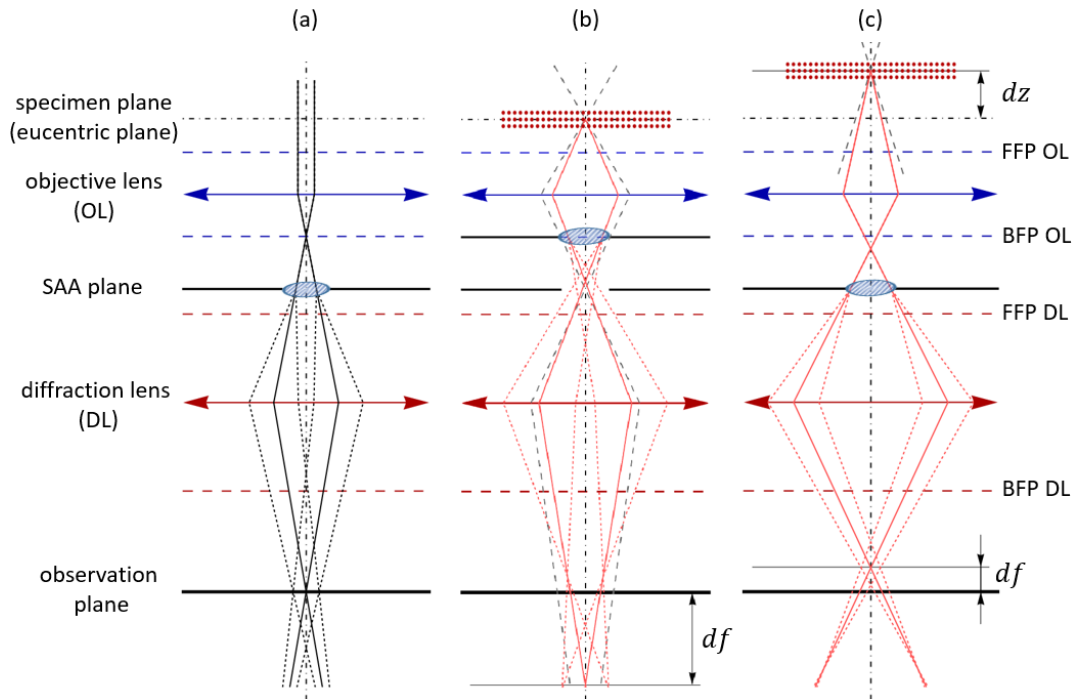


Figure 5.3: Using *Gaussian* matrix optics, a standard TEM diffraction setup, including a HVM (light blue) in the SAA-plane, is drawn (not to scale) in (a), whereas in (b) the DP vortex filter EMCD setup is shown and in (c) the SAA-plane vortex filter EMCD setup is illustrated. The specimen (red dots) is lifted by dz , in order to properly illuminate the SAA vortex filtering mask. Full and dashed black lines represent rays of elastically scattered electrons, whereas red lines depict inelastically scattered ones. Note the apparent defocus df between the observation plane and the focused row of vortices in setups (b) and (c).

over in the BFP, would resemble an incoherent sum of all illuminated atoms with the size of the illuminated area in the sample plane being typically 50 nm to 1000 nm. This would lead to a massive blurring of the intensity distribution in the observation plane, larger than the separation distance of the electron vortices and, thus, would render a successful determination of OAM asymmetries impossible. Therefore, the experimental setup, given in Figure 5.3 (b), is devised in a way to decrease the effective spot size of the inelastic scattered electron beam. This is done by focusing the incident electron beam onto the sample, which also guarantees high lateral resolution and a relatively high lateral coherence in the BFP of a tens of microns. The focusing changed the electron-optical conditions and the intermediate images of elastically- and inelastically scattered electrons are no longer focused in the observation plane. The apparent under-focus has been marked in Figure 5.3 (b) by df . A practical way to resolve that issue is to slightly lift the sample above the eucentric height until the two planes coincide. Notably, in that case any given magnification calibration is no longer correct. Additionally to df there is also a difference in the focal position of elastically- to inelastically scattered electrons, due to the higher focusing power of the lenses for slower electrons, visible in Figure 5.3 (b).

In the SAA-plane setup, shown in Figure 5.3 (c), focusing the beam onto the sample alone would not be sufficient, as mentioned above. The sample must also be lifted massively above the eucentric plane. This not only produces a proper illumination of the SAA vortex filter but also increases the transverse coherence length λ_c of the electron waves in the SAA plane. λ_c and its dependence of dz can be estimated by using $\lambda_c = (2\lambda(z_{SAA} - b))/(\pi d_{spot}M)$, with λ being the electron wavelength (2.51 pm for 200 kV), $z_{SAA} = 140.5$ mm being the z -position of the SAA plane relative to the specimen plane, b the image distance (here, position of the first cross-over beneath the sample), d_{spot} the FWHM of the incident beam and $M = b/g$ the magnification of the objective. Using the lens equation $1/f = 1/g + 1/b$, where $f = 2.7$ mm and g are the focal length and the object-distance, respectively, b can be calculated to be $b = (f^{-1} - g^{-1})^{-1}$ with $g = f + z_{euz} + dz$. $z_{euz} = 52.9$ μm is the eucentric height above the front-focal-plane (FFP). For 200 kV, a z -shift of $dz = 15$ μm and an incident spot of 3 nm, λ_c is only 0.4 μm and the magnified spot size is 120 nm, at a vortex order separation of approximately 130 nm. These settings would be very impractical for the analysis of the experimental data, due to overlapping vortex orders. Therefore, $dz > 50$ μm and incident spot sizes of ≤ 3 nm were chosen for the experiments. Notably, the effect of lifting the sample is comparable to the reduction of the effective source size in the condenser system of a TEM by adjusting the C1 lens excitation.

The apparent over-focus in that setup, marked by df in Figure 5.3 (c), can be compensated using the diffraction lens. Note that this setup is done in diffraction mode, whereas the DP setup is done in imaging mode.

Using the above given equations, the expected collection angle θ_{mask} can be given by $\theta_{mask} = (r_{mask}M)/(z_{SAA} - b)$, with r_{mask} being the radius of the vortex filter hologram. For $dz = 50$ μm and $r_{mask} = 5$ μm , this yields a collection angle of 1.9 mrad, which is quite low compared to standard EELS or EFTEM collection angles

of the order of 5 mrad to 20 mrad and also lower than the expected collection angle of 2.8 mrad of the DP setup with the same hologram size.

5.1.3 Principle and Theory of the Single Atom Scattering Approach

Now, after the description of the experimental details, an idealised single atom scattering approach will be used to get an idea of the achievable EMCD signal strength of a vortex filter setup using a HVM in the DP.

The key aspect of EMCD is the transfer of OAM between the probe beam and the target electron. For the standard case that the incident beam does not carry OAM, the inelastic scattering event transforms it into a vortex or, more generally, into a superposition of several vortex orders. Therefore, it is instructive utilizing a HVM as a vorticity filter in order to separate the different OAM components and measure their respective weights, see Figure 5.2 (a).

The reference samples used herein are transition metals that typically show a strong spin polarisation under the influence of a magnetic field, and, thus, dichroism measurements typically involve 2p-core to d-valence excitations at the $L_{2,3}$ ionization edges. The $L_{2,3}$ -edges are used due to their strong spin-orbit interaction in the initial state. Compared to using K-edges, the dichroic signal is an order of magnitude higher [291]. In the first experiments dealing with X-ray magnetic circular dichroism the dichroic effect has been seen at the iron K-edge [7]. Electric dipole-allowed transitions contribute the most to the ionization edge's signal, whereas higher multipole transitions show only low transition amplitudes, less than 10% at scattering angles of < 20 mrad [292–294].

As a starting point an atomic scale wavefunction is assumed. For an L-edge dipole-allowed transition, an OAM of $\hbar\mu$ is transferred, which changes the magnetic quantum number of an atom by μ . Therefore, an incident plane electron wave transforms into an outgoing wave [295]:

$$\psi_{\mu}(\mathbf{r}) = e^{-i\mu\varphi_r} f_{\mu}(r), \quad (5.1)$$

where φ_r is the azimuthal angle, and [296]:

$$f_{\mu}(r) = \frac{i^{\mu}}{2\pi} q_E^{1-|\mu|} \int_0^{\infty} \frac{q^{1+|\mu|} J_{|\mu|}(qr) \langle j_1(Q) \rangle_{ELSj}}{Q^3} dq, \quad (5.2)$$

with $\langle j_1(Q) \rangle_{ELSj}$ being the matrix element of the spherical *Bessel* function between the initial and the final radial atomic wavefunctions, and $Q = \sqrt{q^2 + q_E^2}$. q is the transverse scattering vector that relates to the experimental scattering angle θ , as $q = k_0\theta$. The characteristic momentum transfer is given by $\hbar q_E = \hbar k_0\theta_E$, which is the scalar difference of linear momenta of the probe electron before and after the inelastic interaction [297], whereas the characteristic scattering angle θ_E is given by $\theta_E \sim \Delta E/2E_0$, with ΔE being the threshold energy of the dipole-allowed L-edge and E_0 being the primary beam energy. For example, at an AV of 200 kV and at the Co- L_3 threshold energy of 779 eV, the characteristic scattering angle θ_E amounts to ~ 2 mrad and for the Fe- L_3 threshold energy of 708 eV, θ_E amounts to ~ 1.8 mrad.

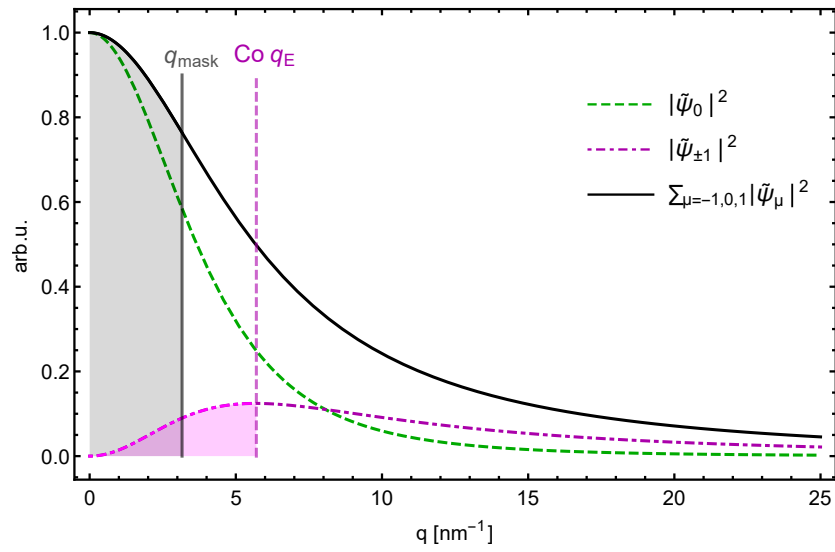


Figure 5.4: Scattering profiles for the Co L_3 -edge of $|\tilde{\psi}_0|^2$ and $|\tilde{\psi}_{\pm 1}|^2$ and their sum $\sum_{\mu=-1,0,1} |\tilde{\psi}_\mu|^2$, resulting in the *Lorentz*-profile for non-magnetic isotropic transitions in momentum space. The radius of the HVM $q_{mask} = 3.16 \text{ nm}^{-1}$ (1.26 mrad) is indicated by the grey-shaded area terminated by the full vertical line, q_E is indicated by the dashed vertical line and the magenta-shaded area. Taken from [296].

The propagation of the wavefunction, Equation 5.1, to the diffraction plane can be realized by employing *Fourier* optics, i.e., by calculating the *Fourier* transform of the incident wavefunction. This is done by using a theorem for the *Fourier-Bessel* transform for a function of azimuthal variation $e^{-i\mu\varphi}$ [298], such that the DP wavefunction now reads [296],

$$\tilde{\psi}_\mu(\mathbf{q}) = \frac{i^\mu}{2\pi} e^{-i\mu\varphi_q} \int_0^\infty f_\mu(r) J_{|\mu|}(qr) r dr. \quad (5.3)$$

Note that the outgoing electron in the DP still carries a topological charge μ , which is indicative of the topological protection of the wavefunction. In Figure 5.4 the calculated radial intensity profiles $|\tilde{\psi}_\mu(q)|^2$ for the possible transitions with $\mu \in \{-1, 0, 1\}$ and their sum $\sum_{\mu=-1,0,1} |\tilde{\psi}_\mu|^2$ are shown. They represent the *Lorentz*-profile for non-magnetic isotropic transitions of the Co L₃-edge.

Now the HVM in the DP adds topological charges $m \in \mathbb{Z}$ to the incident beam of topological charge μ . The fork-dislocation grating does not only add OAM to the incoming electrons, it also diffracts them by the m -dependent deflection angles $2\theta_{Bragg} = m\lambda/g$. Thus, a row of vortex orders with topological charge $m + \mu$ is produced in the intermediate image plane, see Figure 5.2 (a). By back-transforming Equation 5.3, with the respective vortex order m added by the mask, the radial profiles, present in the image plane, can be given by [296]:

$$\psi_{m\mu}(\mathbf{r}) = \frac{i^{m+\mu}}{2\pi} e^{-i(m+\mu)\varphi_r} \int_0^{q_{mask}} \tilde{\psi}_\mu(q) J_{|m+\mu|}(qr) e^{i(dfq^2/2k_0 + C_s q^4/4k_0^3)} q dq, \quad (5.4)$$

with $q_{mask} = k_0\theta_{mask}$ being the maximum transferred momentum, limited by the vortex mask size. Additionally, it was accounted for the spherical aberration of the imaging system and a potential defocus df by the addition of an according phase factor. Note that the respective intensities are azimuthally symmetric and show distinct radial profiles. Figure 5.2 (a) schematically shows the central three vortices overlaid by the three dipole-allowed transition channels $\mu = 0, \mp 1$. As the central vortex ($m = 0$) does not show any asymmetry, for $\mu = +1$ and $\mu = -1$, the overlays were omitted. Actually, because of this missing asymmetry, standard EELS cannot distinguish these transitions.

For the degenerate transition channels $\mu = 0, \pm 1$, the outgoing probe electron is in a mixed state. This can be described by the reduced density matrix [299, 300], but the paths of the rays cannot be visualized in such a straightforward way. The expected total intensity can be given by the trace of the matrix, which is the sum over all intensities in the respective channels. In the case of a fully spin-polarized system, i.e., the ideal EMCD condition, the radial profile intensity can be given by [296]:

$$I_m = \sum_{\mu=-1}^1 C^\mu |\psi_{m\mu}|^2, \quad (5.5)$$

where the C^μ are derived from the *Clebsch-Gordan* coefficients [16, 301] and given in Table 5.1. An intuitive schematic illustration of how this asymmetric weighting of the

Table 5.1: Coefficients C^μ for the L₃-edge taken from [16]. The weighting factors for the transitions, when the final states are completely spin-up polarized, show an asymmetry for $m + \mu = 0$, i.e., in the centre of the $m = \pm 1$ vortices.

m	-1			0			+1		
μ	-1	0	+1	-1	0	+1	-1	0	+1
$m + \mu$	-2	-1	0	-1	0	+1	0	+1	+2
C^μ	0.278	0.222	0.167	0.278	0.222	0.167	0.278	0.222	0.167

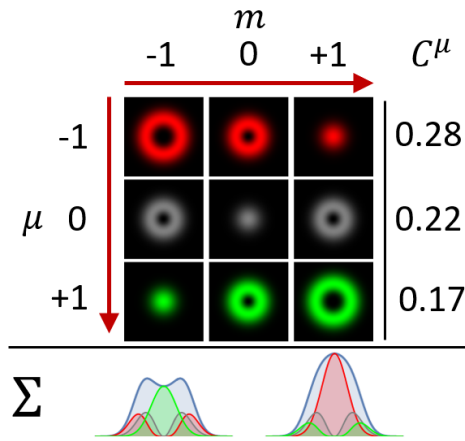


Figure 5.5: Schematic illustration of the vortex filtering principle for the three different scattering channels $\mu = 0, \pm 1$. Due to the asymmetric weighting of the transitions channels, given in Table 5.1, the radial intensity distributions in the far-field of a vortex filter I_m (blue lines) show clearly distinguishable features. Depending on the vortex filter order m , the central intensity either drops ($m = -1$) or rises ($m = +1$). Additionally, there are changes in the FWHM.

transition channels affects the radial intensity distributions of the EVBs after passing the vortex filter mask is shown in Figure 5.5. The radial intensity distributions in the far-field of a vortex filter I_m (blue lines) show clearly distinguishable features. Depending on the vortex filter order m , the central intensity either drops ($m = -1$) or rises ($m = +1$). Additionally, there are changes in the FWHM of the incoherent superposition of electron waves.

In Figure 5.6, the resulting radial intensity profiles are drawn without additional broadening. This will be discussed in more detail in Subsection 5.1.5. Note that, due to the relative small momentum transfer of the chosen HVM ($q_{mask} < 3.16 \text{ nm}^{-1}$), the radial extension of the intensity profiles in Figure 5.6 is much broader than directly at the scattering atom, where it is of the order of two Angstroms.

Similar to Equation 2.14 the EMCD signal in this geometry can be defined as the

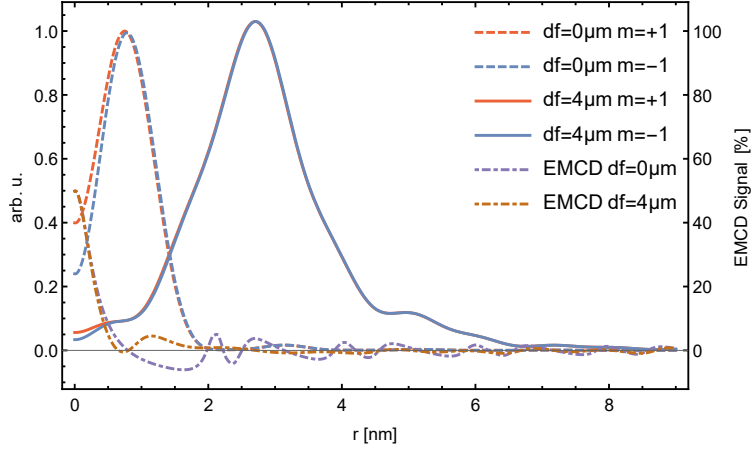


Figure 5.6: Radial intensity profiles of the $m = \pm 1$ vortex orders of a single atomic ionization, for the fully spin-polarized case, according to Equation 5.5, using two different defocus values ($df = 0 \mu\text{m}$ and $df = 4 \mu\text{m}$). The resulting r -dependent EMCD signal is given by the dot-dashed curves, according to Equation 5.6. In the centre it is as high as 50% for both defocus values. The signals are normalised to their respective total intensities. Taken from [296].

relative difference of the intensities with $m = \pm 1$ ¹,

$$I_{EMCD}(r) = 2 \cdot \frac{I_{+1}(r) - I_{-1}(r)}{I_{+1}(r) + I_{-1}(r)}. \quad (5.6)$$

Note that in this experimental setup the EMCD signal is a function of the radius r .

In Figure 5.6 the ideal case of a single atom excitation is shown for a vortex mask radius of $q_{mask} = 3.16 \text{ nm}^{-1}$. A defocus df of $0 \mu\text{m}$ and $4 \mu\text{m}$ was used, respectively. It can be seen that the r -dependent EMCD signal is strong in the centre of the vortices but rapidly decreases above $r \approx 1 \text{ nm}$. At least for this idealised approach, it reaches 50% for both defocus values in the central region of the vortices. Note that, especially for $df = 0 \mu\text{m}$, not only the central regions of the radial profiles show distinct differences, but that there is also an apparent difference of the positions of the maxima, which is a result of the asymmetrically distributed OAM content in the respective vortex orders.

¹It will be shown in Section 5.1.5, that difference signals can also be produced by artefacts, independently of the presence of a real EMCD signal, so instead of I_{EMCD} , the more general notation I_{Diff} will be used.

5.1.4 OAM Conservation in Amorphous Materials - Elastic Multi-Slice Simulations

For atom-sized EVBs propagating through a crystal lattice there are publications showing that the expectation value of the angular momentum $\langle \hat{L}_z \rangle = \langle \psi | \hat{L}_z | \psi \rangle / \langle \psi | \psi \rangle$ is strongly affected [35, 302]. This is indicating an OAM transfer between the sample and the electron beam, mediated by elastic scattering processes. The above given single atom scattering ansatz neglects elastic scattering of the EVBs produced in the ionization process in the specimen, and, thus, the question of its applicability arises. However, multi-slice simulation results, given in Subsection 5.1.6, together with reports, showing that atomic-sized EVBs do channel along atomic columns over tens of nanometres, when aligned exactly at the atomic columns [302, 303] hint at the validity of the single atom scattering approach. Because the electron vortices, which are produced in the inelastic scattering event, are intrinsically centred on the atom, it is very likely that a sufficiently thin crystalline sample, which is aligned to a zone axis (ZA), should give an EMCD signal in good accordance with the simple single atom scattering ansatz used in Section 5.1.3.

Note that the beam-splitting and -retarding action of the crystal lattice used in classical EMCD is kind of externalised in this method, in the form of the vorticity filtering HVM. Thus, one possible advantage of the filtering EMCD method could be its applicability to amorphous materials.

Amorphous or non-crystalline materials are per definition such materials, that lack any long-range order characteristic for a crystal. A prominent example of this material class, which emerged in the last few decades, are bulk metallic glasses. These metal-based alloys show no long range order in their atomic structure, as well as peculiar physical and magnetic properties, like very low magnetisation and demagnetisation losses, as well as the ability to combine strength and hardness with flexibility and toughness at high saturation magnetizations [304].

Due to the non-existent long range order in these materials, one can expect the exchange of OAM to be minimal. To further clarify if the OAM of the inelastically scattered probe electron is indeed conserved when propagating through an amorphous material, multi-slice simulations were carried out.

It can be seen in Figure 5.7 (upper two rows), that the colour-coded phase structure of the EVB, which had a convergence angle of 1.16 mrad at $U_A = 200$ kV, and its intensity distribution do not change significantly upon propagation through 60 nm of an amorphous $\text{Fe}_{80}\text{Si}_6\text{B}_{13}\text{C}_1$ alloy. In the experimental test (lowest row of Figure 5.7) the propagation of an EVB, having $m = 1$ incident on a 60 nm $\text{Fe}_{80}\text{Si}_6\text{B}_{13}\text{C}_1$ alloy, shows a relatively good conservation of the vortex structure, supporting the simulation results. Note that the simulated atomic density was rather low (2.4×10^{22} atoms/cm³), compared to a realistic density of 6.5×10^{22} atoms/cm³, explaining the observation of the measured vortex being more blurred, whereas the simulated one seems to be relatively unaltered.

Additionally, the expectation value of the angular momentum $\langle \hat{L}_z \rangle$ was analysed for two different materials, see Figure 5.8, using an atomic scale $m = 1$ EVB. Due

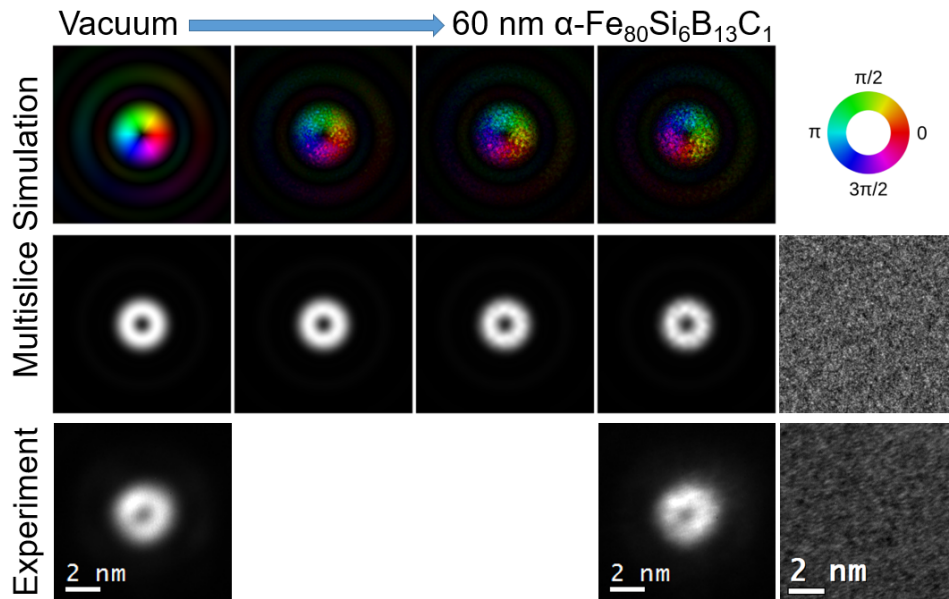


Figure 5.7: OAM conservation: Elastic multi-slice simulation (upper panel: phase, middle panel: intensity), compared to an experimental test on an amorphous Fe-based alloy (lower panel). Even though the propagation distance is 60 nm, no significant changes are visible in the vortical phase structure of the EVB, which is indicated by the relatively good conservation of its intensity distribution. This is also seen in the experimental test, although it seems to be more blurred. The used convergence angle was 1.16 mrad, $U_A = 200$ kV and the simulated atomic density was 2.4×10^{22} atoms/cm³.

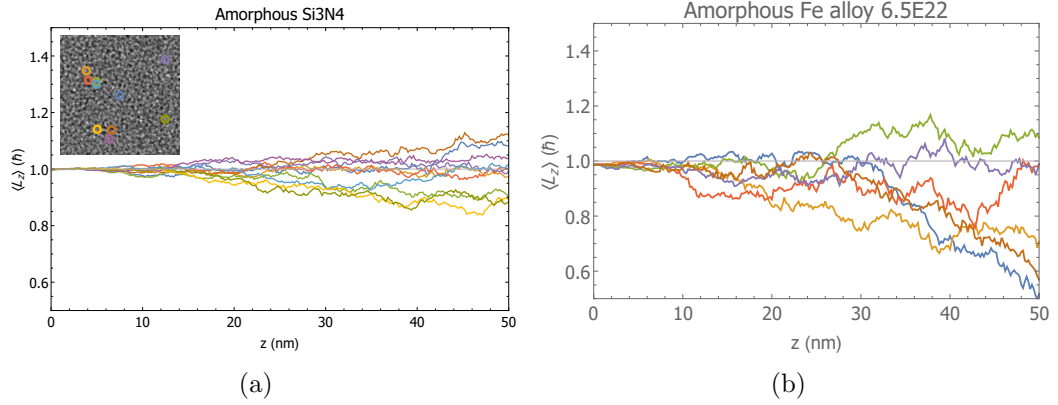


Figure 5.8: (a) Shows the expectation value of the angular momentum $\langle \hat{L}_z \rangle$ of α -Si₃N₄ with a realistic atomic density of 10.33×10^{22} atoms/cm³ and a thickness of 50 nm, whereas (b) is calculated for an Fe-based alloy (Fe₈₀Si₆B₁₃C₁, 6.5×10^{22} atoms/cm³) of 50 nm thickness. The incident beam was in both cases an atomic scale vortex with a waist radius of 1.14 Å. The simulation was run multiple times, the inset in (a) shows the positions of the incident beams, in order to clarify spatial variations of $\langle \hat{L}_z \rangle$.

to improvements in the simulation program code, realistic atomic densities² could be simulated, as compared to the results given in Figure 5.7 and in [296]. The principal message still is, that there are only moderate deviations of $\langle \hat{L}_z \rangle$ over the course of the propagation, but the effect of the OAM transfer is more pronounced. E.g., for 50 nm of the amorphous alloy, $\langle \hat{L}_z \rangle$ reduces to $\sim 50\%$ of its initial value, whereas a reduction of only $\sim 20\%$ was seen using a lower density [296]. For the low density material, which is commonly used as a substrate for phase masks [23–25], the changes in $\langle \hat{L}_z \rangle$ are less pronounced, e.g., after 50 nm the highest reduction of $\langle \hat{L}_z \rangle$ was $\sim 20\%$. Repeating the simulation for different positions on the material revealed a spatial variance of the OAM transfer for both materials, Figure 5.8 (a) and (b). This is most likely due to the highly localised probe beam, as variations of the atomic potentials do not average out over the azimuthal profile of the atomic scale EVB.

For amorphous materials with thicknesses < 20 nm the multi-slice simulation results, shown in Figure 5.8, support the assumption, that neither the expectation value of the angular momentum operator $\langle \hat{L}_z \rangle$, nor the single OAM components (not shown) show strong OAM transfer, justifying the single atom scattering approach. Nevertheless, effects like incoherent broadening must be taken into account by additional means and will be discussed in the following section.

²Due to the amorphous atoms coordinate-producing algorithm, such high densities can only be calculated using a reduction of the inter-atomic distances, e.g., up to minus 20%. This has most likely has only minor influence on the OAM transfer to the sample.

5.1.5 Artefact Sources

Single neutral atoms can be prepared either free floating in holographic optical traps [305], or suspended on graphene [81, 306]. Even core-loss EELS spectra have been taken from single atoms, suspended on graphene membranes [307] and in carbon nanotubes [112]. This clearly demonstrates that the situation described in Section 5.1.3 is not per se an over-idealisation. With state-of-the-art microscopes, measurements on single atoms have become feasible. However, for general material science applications in the TEM, the single atom scattering approach is indeed an over-simplification. To determine if and under which conditions EMCD signals can be detected in practice, the most important limitations are discussed in this subsection.

Incoherent Broadening - Illuminated Specimen Area

For extended samples and typical analytical beam sizes, more than one atom is illuminated, resulting in an incoherent superposition of signals coming from all excited atoms. This leads to a smoothing of the radial profile by a convolution with the spot shape. Evidently, the expected difference signal will be modified [35, 36].

As already pointed out in [189], it is possible to include incoherent source size broadening, which is caused by illuminating an extended area of the sample by a convolution with a *Gaussian* function, allowing to calculate the radial vortex profiles as follows [296]:

$$I_m^\sigma(r) = e^{-(1/2)(r/\sigma)^2} \int_0^\infty I_m(r') e^{-(1/2)(r'/\sigma)^2} I_0\left(\frac{rr'}{\sigma^2}\right) r' dr'. \quad (5.7)$$

with I_0 representing the zeroth order modified *Bessel* function of the first kind and σ being the amount of incoherent broadening³.

Even if the sample consists only of a single atomic monolayer, the simulation in Figure 5.9 (a) suggests that the central dip, which is well discernible in the coherent case, see also Figure 5.6, is smoothed, such that the EMCD signal drops from 50 % to 3 %. This is also true for the defocused case where the dip still is preserved. On the one hand side, this finding limits the electron current to be used in experiments and poses problems with the achievable SNR⁴, but on the other, it emphasises the need for small spot sizes that would at least theoretically produce higher EMCD effects.

Above, the question of lateral extended illumination was elucidated. In the single scattering centre model one can also regard the influence of the single atoms sitting at various z -positions. This was tested by incoherently summing up multiple intensity distributions of defocused vortices. The result given in Figure 5.9 (b) indicates, that no significant contribution can be observed from this longitudinal arrangement of scattering centres to the EMCD signal below $r < 1$ nm. This was to be expected, because the defocus values (< 100 nm) are small compared to the Rayleigh range

³The FWHM of the resulting illuminated specimen area is given by $2\sqrt{2\ln 2}\sigma \approx 2.35\sigma$.

⁴The incoherent spot size d_{Source} scales with the electron beam current I like $d_{Source} = 10^9 \frac{2}{\pi} \left(\frac{I}{\beta}\right)^{0.5} \frac{1}{\theta}$, with β being the brightness of the electron gun and θ the convergence angle [85].

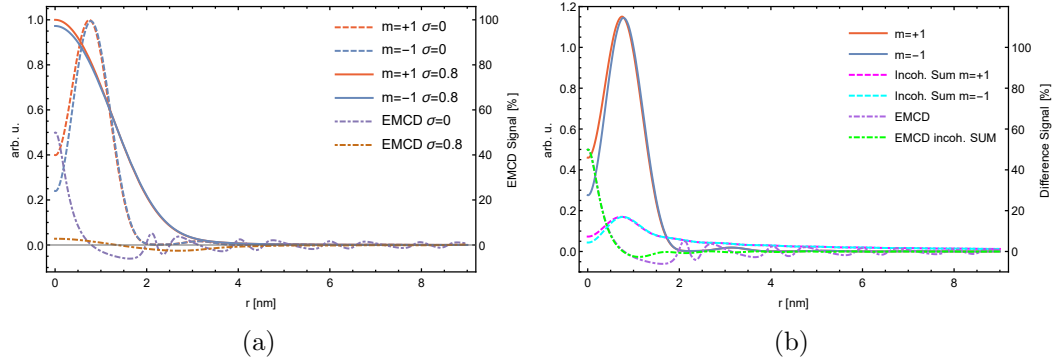


Figure 5.9: Depicting the effect of a broad beam illumination on the single atom scattering approach. (a) Incoherently broadened vortex profile using a *Gaussian* function with $\sigma = 0.8$ nm for the focused case. It shows a strong reduction of the EMCD effect, dropping to 3%. Taken from [296]. (b) Incoherent sum of 100 electrons, where each one was defocused by 1 nm with respect to the preceding one. The spreading of the radial intensity profiles, due to defocus, does not significantly alter the general statement. For $r < 1$ nm the expected EMCD signal is practically identical. Above $r = 1$ nm there are slight deviations of the order of 6%.

(~ 600 nm). The main changes, caused by this defocus, occur in the tails of the vortices, where no EMCD effect is expected.

The Influence of Vortex Size Differences, Mask Tilt and Astigmatism on the Difference Signal

Not only the aforementioned broadening effect can affect the theoretical EMCD signal, there are several ways to unintentionally introduce an artificial intensity difference, which could in principle lead to a false EMCD effect. They all have in common, that the position of the maxima, i.e., the vortex size, is different for the positive $m = +1$ and the negative $m = -1$ vortex order. These discrepancies in lateral extent induce difference signals in the vortex centre.

A straightforward method to model this, is to apply a defocus difference between the different vortex orders. Figure 5.10 (a) shows the case of a non-magnetic simulation (i.e., $m = -1$ and $m = +1$ should have the same radial profiles) but with a defocus difference of 100 nm between the two vortices. As a result, a relative difference signal reaching a maximum of 8%, dropping to 5% at the centre, can be seen. Thus, the difference signal strength is nearly twice as much as that of the EMCD signal, predicted for the fully spin-polarized case with the same simulation parameters, without defocus differences between the opposing vortex orders. Even though the central intensity differences are strong for vortex size differences, the overall course of the difference signal curve is clearly different from one induced by an EMCD effect, i.e: the difference signal does not go back to zero for $r > r_{max}$, with r_{max} being the

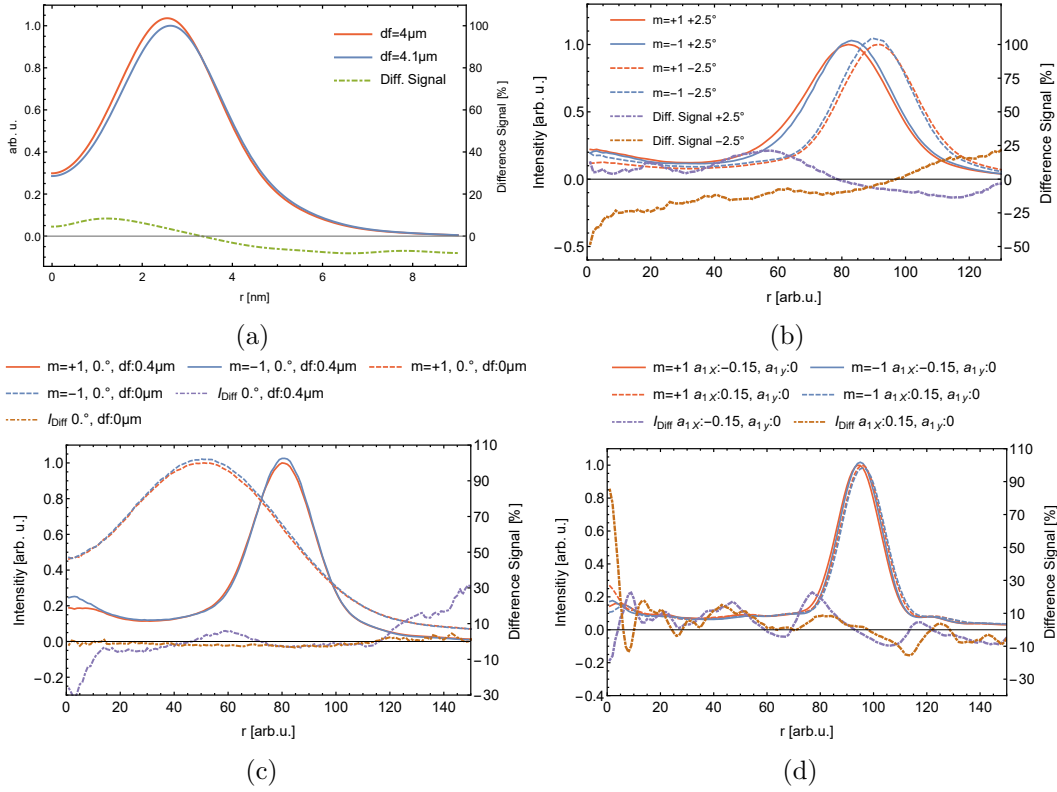


Figure 5.10: Artificial difference signals. (a) Effect of 100 nm defocus difference between left and right vortex order of a hypothetical non-dichroic signal at $4\mu\text{m}$ defocus. The difference signal in the centre is 5% and its maximum is as high as 8%. (b) An experimental test, showing that vortex size differences can be induced by tilting a HVM in the sample holder $\pm 2.5^\circ$ relative to the electron beam. A significant defocus difference between left and right diffraction order can be observed for both tilt angles. (c) the same as (b), but for zero tilt and two different defocus values, showing the strong reduction of the difference signal for $df > 0\mu\text{m}$ and the practical absence of it for $df = 0\mu\text{m}$. (d) An experimental test in vacuum, showing the influence of the (twofold) objective astigmatism (denoted by a_1) on the radial profiles (especially their centres) of $m = \pm 1$ vortex orders. The profiles are normalized to their respective total intensity.

maximal intensity radius.

Thinking about possible origins for OAM-dependent defocus differences, a plausible explanation is a geometric tilt of the optical axis combined with OAM-dependent differences in the lenses' focal lengths. However, estimating the amount of defocus differences, expected from image tilts of the order of a few mrad, via the simple geometric relation $df = 2a \tan(\alpha_{tilt})$, with a being the distance between the first vortex order and the $m = 0$ beam and α_{tilt} being the tilt angle, yields a value of ~ 0.5 nm, which can be considered negligible. Also, defocus changes due to Zeeman splitting in the magnetic field of TEM lenses have been estimated to be of the order of 1 pm to 0.5 nm [51].

In the contrary, it was found, that tilting the HVM with respect to the optical axis to angles of a few degrees, which could in principle be due to mounting misalignments and/or bending of the thin membranes, due to compressive inner stresses, see Figure 4.23 (a) in Section 4.3.3, can induce significant shifts of the maxima, equivalent to effective defocus differences of the order of a few hundred nanometres, see Figure 5.10 (b).

This was tested by inserting a HVM ($\varnothing 30 \mu\text{m}$, $g = 500$ nm) into the specimen holder, such that its primary grating was aligned parallel to the α -tilt-axis of the specimen holder. Then the microscope was switched to the low-magnification mode, where extremely high effective camera lengths of a few hundreds of metres can be used to image the far-field pattern of the hologram. Significant changes in the radial profiles (rotationally averaged) of the $0.4 \mu\text{m}$ defocused $m = -1$ and $m = +1$ EVBs can be observed for tilt angles as low as $\pm 2.5^\circ$, see Figure 5.10 (b). The central intensity differences were 10 % for 2.5° and as high as -50 % for -2.5° and with that roughly 3 to 16 times larger than the predicted EMCD effect. Again, the shape of the difference signal is clearly discernable from that of a real EMCD signal. While only slight differences in the vortex size can be observed for EVBs of the same tilt, there are pronounced differences in the vortex size between the two different tilt positions. This is most likely due to a defocus produced by stage-positioning-errors when tilting.

Note that this experiment was conducted in vacuum, without a specimen. The exact reason for this asymmetries is outstanding, but estimating the defocus difference via the above-given geometric expression, using $a = 70$ nm (camera length: 140.5 mm, diffraction angle: $5 \mu\text{rad}$) yields a value of ~ 60 nm. Compared to the used defocus value of $0.4 \mu\text{m}$, this result is fairly reasonable. Other, more exotic, origins could be electron-wall interactions, e.g., electrostatically induced image charge formation in the grating bar walls, as seen in the publications [308–311].

To avoid this effect, care must be taken in the preparation of the HVM, such that the membrane is not deformed after deposition of the metal layer, and preparing the HVM on thicker support membranes and carefully mounting it in the aperture holder may help as well. The absence of this artefact can be verified, before conducting an EMCD experiment, by using the elastically scattered electrons. E.g., in Figure 5.10 (c) rotational averaged radial profiles for zero tilt and two different defocus values

are given⁵. In both cases the difference signal is strongly reduced, compared to the tilted case. While there is still a residual difference signal for the defocused profile, especially for the innermost pixels, there is practically no difference signal ($I_{Diff} < 2\%$) for the $df = 0\ \mu\text{m}$ measurement. This is an important prerequisite for the detection of an EMCD signal.

In the work of *Guzzinati et al.* [45] it was shown that astigmatism can be used to infer the OAM state of the electron beam via an astigmatic mode-conversion [312]. This mode-conversion changes the spatial intensity distribution of the electron significantly. In an experimental test, defocused vortices, produced by a SAD HVM, were recorded for different objective lens astigmatism values, see Figure 5.10 (d). There, the values a_{1X} and a_{1Y} denote the astigmatism corrector excitation values, as shown in the *Tecnai* user interface.⁶ Again, even though these radial profiles are attained from EVBs in vacuum (without a sample), there are strong difference signals observable. For the central pixels the effect amounts to $\sim 80\%$ for the positive a_{1x} setting and -20% for the negative one, and it falls off to $< 20\%$ at higher radii. Markedly, there are oscillations of the difference signal that set the signal shape apart from a real EMCD signal. In two-dimensional image simulations (not shown), the same behaviour of introducing an EMCD-like artefact by changing the astigmatism of the objective lens could be confirmed.

This artefact can be corrected by a thorough pre-alignment of the objective lens, e.g., using the fast *Fourier* transform (FFT) of an amorphous sample region, followed by a thorough pre-alignment of the EVBs produced by the SAD HVM at zero energy loss using an appropriate high-tension offset for the core-loss of interest, e.g.: 710 eV for the Fe- L_3 -edge.

The Influence of Vortex Mask Production Artefacts on the Difference Signal

Another issue, already mentioned in [296] and revived in the experiments done at the ER-C, is the question if an asymmetrically blazed HVM could induce an artificial EMCD effect. The results shown in Section 4.2 clearly indicate that, during the FIB production process of vortex holograms, the grating bar edges are bevelled. Additional drift can induce an asymmetry in the edge bevel angles as well.

As an example see the inset in Figure 5.11 (c): a typical asymmetric line profile along the row of vortices, stemming from a $\text{\O}40\ \mu\text{m}$ HVM. The result of a numerical simulation of an amplitude HVM, including partial absorption at the edges in a wedge-like form, as well as a linear ramped phase shift, Figure 5.11 (a), are shown in Figure 5.11 (b). A strong asymmetrical redistribution of electron intensity can be observed.

In Figure 5.11 (c), the rotational averaged profiles of the $m = \pm 1$ vortices shown in (b) are given. The strong difference in total intensity does not lead to a significant

⁵Note that the $df = 0\ \mu\text{m}$ measurement was taken with a different mask.

⁶Note that, at these settings, there are only miniscule changes to the vortices' structure, they still *look* sufficiently round.

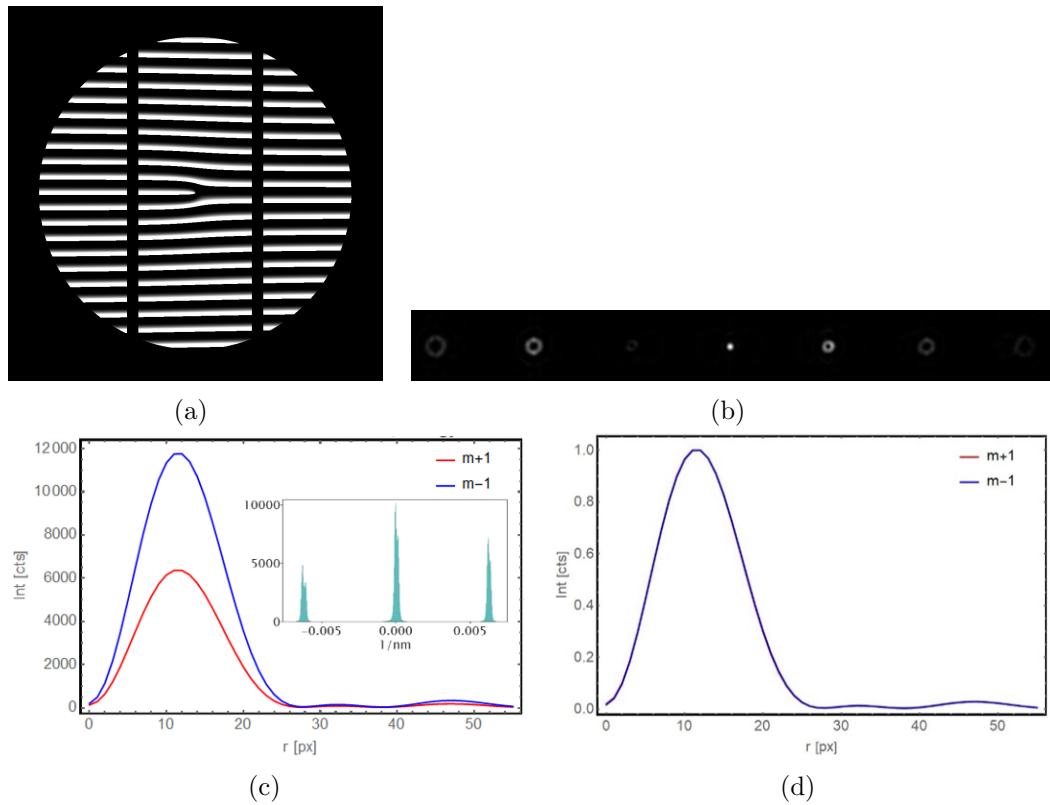


Figure 5.11: Influence of a blazed HVM on the electron intensity distribution. (a) Computer-generated blazed amplitude and phase hologram. (b) Far-field electron distribution of the blazed HVM, showing clear asymmetries in the vortex order intensities in (a). (c) shows rotational averaged beam profiles of a simulated blazed absorption HVM before and (d) after normalization to the total intensity. The inset in (c) shows a measured line profile along the diffracted vortex beams of a 40 μm phase hologram.

difference upon normalization to the same total intensity, see Figure 5.11 (d). There seems to be no influence on the beam profile shape by (partially) blazed gratings.

5.1.6 Inelastic Multi-Slice Simulations

To verify the presence and conditions necessary for the detection of an EMCD signal by the use of a vorticity filtering setup for realistic samples, IMS, as described in the Fundamentals chapter, Section 2.7, were carried out.

The in-house IMS code IXCHEL was adapted to the actual experimental setup used in vortex filter EMCD measurements. It now includes the propagation of the outgoing electron waves to the BFP by applying a FFT. In the BFP every kind of phase or amplitude aperture can now be applied to the wavefield, by simply adding the according aperture in the form of a 24 bit-‘tif’-file to the working directory. Subsequently, the electron waves are back-propagated to the sample plane via an inverse FFT operation.

It is asserted, that filtering EMCD can also be applied to amorphous materials, as opposed to classical EMCD. So far only crystalline materials could be simulated using the IXCHEL code, and therefore, a functionality to produce atom positions of amorphous materials was implemented in the code⁷. Moreover, in order to be able to calculate, e.g., extended thickness/defocus series in a reasonable amount of time (less than one week) the IXCHEL code was adapted for the utilization of computing power of high performance graphic processing units (GPUs) with NVIDIA CUDA⁸.

The results of a defocus- and thickness series of bcc-Fe and an amorphous-Fe-based alloy ($\text{Fe}_{80}\text{Si}_6\text{B}_{13}\text{C}_1$) are shown in Figure 5.12 (a) and (b), respectively. As simulation parameters, a convergence angle α of 3.8 mrad, a collection angle β of 6 mrad, an AV U_a of 200 kV, an energy-loss of 708 eV and a spherical aberration C_s of 1.2 mm were used. Each series was carried out three times, for the spin-up, -down and the non-magnetic state, i.e., asymmetric and symmetric inelastic scattering kernels, respectively. The difference signal I_{Diff} or I_{EMCD} given by Equation 5.6 was extracted from the simulated EFTEM images shown in Figure 5.12 uppermost row, by summing up the central intensities of regions $r < 0.7 \text{ \AA}$ (marked by the red square) of the $m = \pm 1$ vortices. On the one hand side, a complex thickness- and defocus-dependent difference signal for both materials can be observed, including defocus values where the difference signal reverses, and points where it vanishes. On the other hand, the simulation suggests much stronger unambiguous EMCD effects for crystalline Fe than for the amorphous material. In the amorphous material collateral difference signals are present for the non-magnetic state, which further complicates the EMCD effect detection.

Another consequence of the simulations given in Figure 5.12 is, that the optimal defocus for vortex EMCD measurements ranges from no defocus to *Scherzer* defocus. This is in accordance with the findings concerning artefact sources.

⁷This was done by Stefan Sack in the course of his Bachelor thesis.

⁸This was done by Dr. Stefan Löffler.

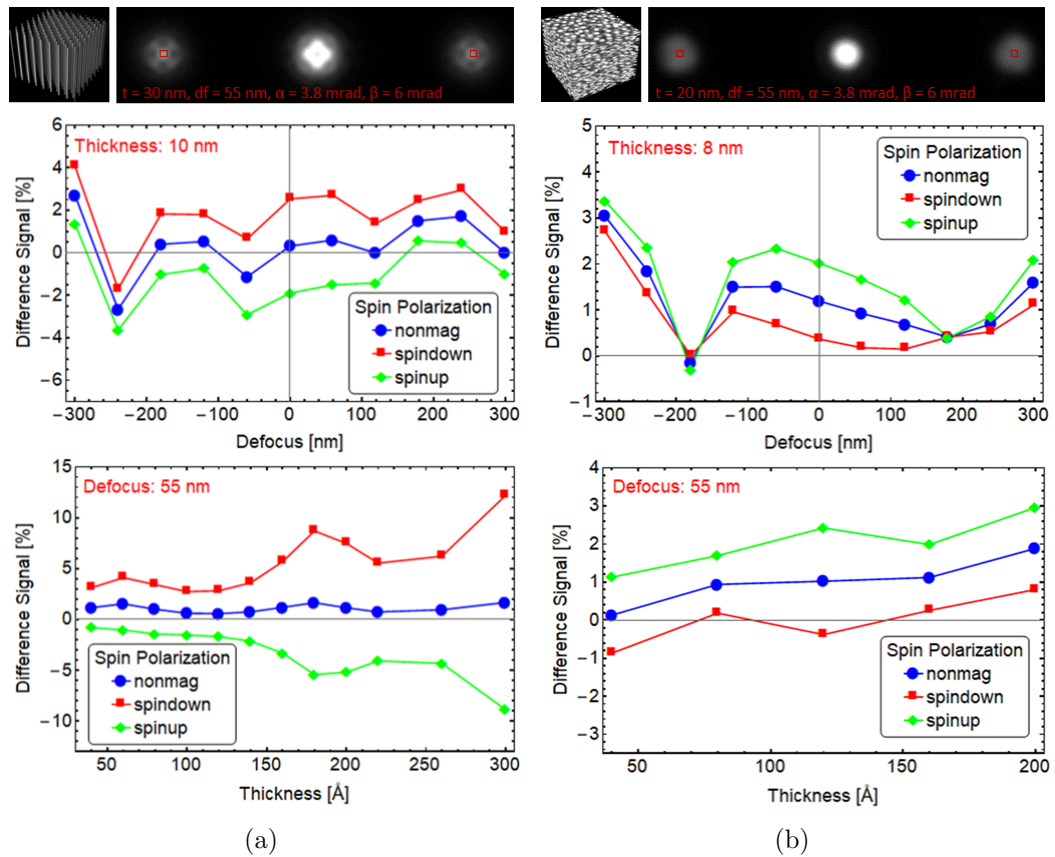


Figure 5.12: IXCHEL IMS defocus- and thickness series, calculated for an energy-loss of 708 eV for crystalline bcc-Fe (a), and an amorphous Fe-based alloy ($\text{Fe}_{80}\text{Si}_6\text{B}_{13}\text{C}_1$) (b). In (a) the beam was placed on an atomic column, the convergence angle α was set to 3.8 mrad, the collection angle β to 6 mrad, the AV U_a to 200 kV and the spherical aberration C_s to 1.2 mm. In the uppermost row the respective 3D representation of the simulated sample, together with the resulting EFTEM image is shown. A non-trivial defocus- and thickness-dependence (df/t) of the difference signal I_{Diff} can be observed in an amorphous alloy, including strong elastic contributions (blue points) in some regions, whereas in bcc-Fe a stronger and unambiguous EMCD signal is visible.

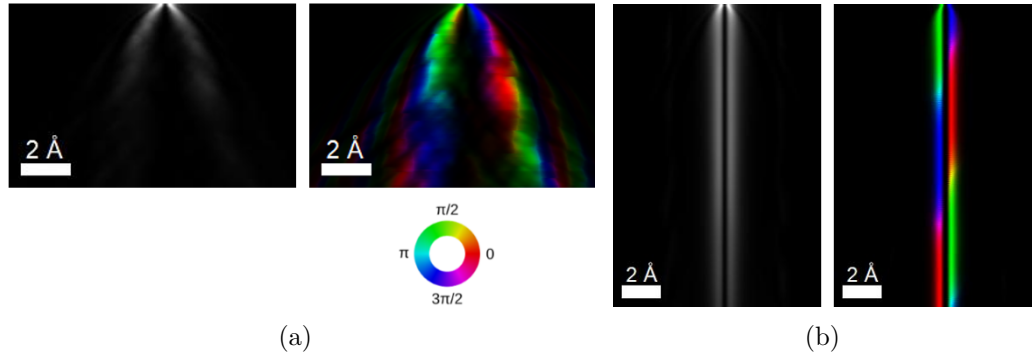


Figure 5.13: Multi-slice simulation result of elastic electron scattering of an incident atomic scale electron wavefunction, propagating through a 30 nm thick amorphous Fe alloy, (a), and through 50 nm bcc-Fe (b). Whereas in bcc-Fe strong channelling occurs, due to the inherently perfect alignment with the rest of the Fe atoms in the column, in the amorphous Fe alloy the beam spreads over one nanometre after 30 nm of propagation. The greyscale images represent electron intensity and the hue colour-coded images represent the electron phase. Note that the vertical scaling is different to the horizontal scale.

In the Subsection 5.1.4, it was argued that amorphous materials do not strongly exchange OAM with the incident electrons, which is still valid, but: in fact, pronounced beam broadening in amorphous materials is more dominant in reducing the expected EMCD effect, see Figure 5.13 (a). In bcc-Fe, oriented along the [001] zone axis, the electrons channel down the atomic columns and, kind of automatically, align themselves perfectly for the next inelastic interaction with the next atom. This can be seen in Figure 5.13, where multi-slice simulations of elastic electron scattering of an incident atomic scale EVB, propagating through a 30 nm thick amorphous Fe alloy (a) and a 50 nm thick bcc-Fe sample (b) were carried out, using the same simulation parameters as given above. An atomic scale EVB was used as incident wavefunction to simulate the situation, which is given after an inelastic scattering process.

One important question that was raised after the experiments at the ER-C is, if the expected EMCD effect is also conserved in samples thicker than 30 nm. Figure 5.13 (b), depicting impressive electron channelling along atomic columns of Fe with up to 50 nm thickness, gives a reason to believe that. And, indeed, the IMS results support this thought, as can be seen from the thickness series simulation in Figure 5.14: at a sample thickness of 30 nm, the difference signal peaks at roughly 30 %, but contrary to classical EMCD, where one would expect strong thickness-dependant oscillations of the effect, it seems to be relatively stable and high, at least up to 50 nm thickness. As the number of electron counts in (vortex) EMCD experiments is inherently low, the possibility to use thicker samples as a means to produce more inelastic scattering events is advantageous, and, in addition, thicker samples are less prone to beam-

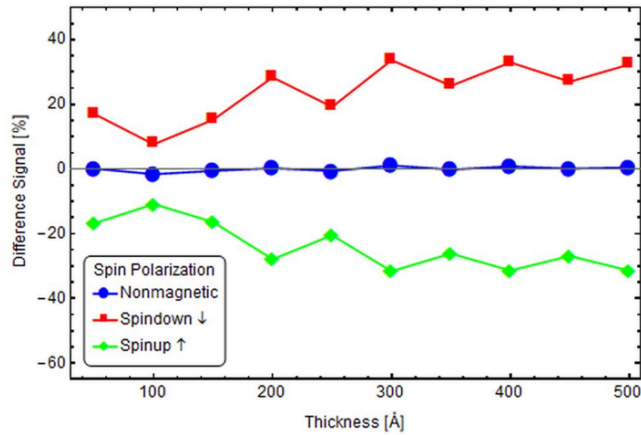


Figure 5.14: Extended IMS thickness series of bcc-Fe, showing that the difference signal I_{Diff} between two opposing vortex orders peaks at 30 nm thickness and amounts to $\sim 30\%$ and stays at this level up to 50 nm sample thickness, showing only weak oscillations. The beam was placed on an Fe column, the simulation parameters were $\alpha = 7$ mrad, $\beta = 5$ mrad, $C_s = 2.7$ mm and $U_a = 300$ kV, here, no source size broadening is included.

induced damage.

Incoherent Source Size Broadening Simulated Using IXCHEL and Mathematica

The single atom scattering model, introduced at the beginning of this chapter, already pointed out the possible effect of ISSB: massive reduction of the expected EMCD signal. The above simulation results were determined by the use of a coherent illumination, without incoherent broadening. In Subsection 5.1.5, a relatively simple, but routinely used ansatz was chosen to simulate the influence of ISSB: convoluting the coherent beam shape with a *Gaussian* function, with a FWHM corresponding to the experimental spot size.

A more realistic way to account for ISSB is now established. A control shell script for the IXCHEL program, that is repeating the simulation for multiple positions in the crystal's unit-cell was devised, comparable to simulating a raster-scanned STEM image, see Figure 5.15 (a). There, the simulated EFTEM images for each scan point in the bcc-Fe unit-cell (lattice spacing: 2.86 \AA) are shown. A *Mathematica* notebook was written, that loads these images and shifts them to crystallographic equivalent positions within a circle sized two times the desired FWHM value of the broadening, Figure 5.15 (b). This imitates the distribution of single electron arrivals within the incoherent beam. The red dots in Figure 5.15 (b) represent the atom positions. Afterwards, the images are weighted by a 2D-*Gaussian* to account for the varying number of electrons within the *Gaussian*-shaped electron beam, as indicated by the opacity variation in Figure 5.15 (b), and finally summed up incoherently. A

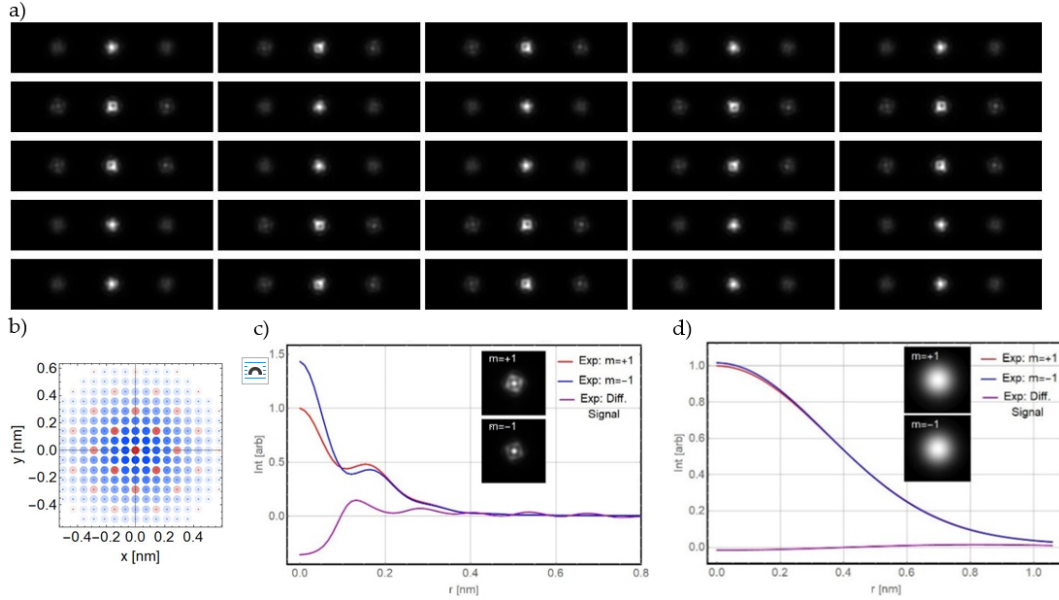


Figure 5.15: A more realistic approach to incoherent source size broadening. (a) Results of the IMS of inelastic scattering at the Fe- L_3 -edge energy for multiple points in the unit-cell of 30 nm bcc-Fe [001]. The simulation parameters were: $\alpha = 7$ mrad, $\beta = 5$ mrad, $U_a = 300$ kV, $C_s = 2.7$ mm (fitting to the *Titan Holo* configuration). (b) The single images of (a) were shifted to crystallographic equivalent positions within a circle sized two times the FWHM of the incoherent spot, here: 0.6 nm. The opacity level indicates the weighting. Atomic column positions are marked in red. (c) Rotational averaged radial profiles of the \pm first vortex orders, shown in the insets, and their difference signal for a coherent focused spot, placed directly on an atomic column. An EMCD effect of 35 % can be expected. (d) The same situation as in (c) but with an ISSB of 0.6 nm, the EMCD effect is strongly reduced: below 2 %.

Table 5.2: Shows the effect of lowering the ISSB on the beam current and the expected EMCD signal. By comparing the needed counts to overcome shot noise from the 0.6 nm value, relative to the more coherent ones, and the change of the beam current, relative to the largest spot. The beam current decreases by a factor of 85, whereas the needed counts decrease by a factor of 156. The used microscope parameters were the same as given in Figure 5.15. The energy spread of the electron source dE was 1.2 eV and a gun brightness β of 20×10^{12} A/m²/sr (X-FEG) was used.

ISSB [nm]	I [pA]	EMCD [%]	Shot noise factor	Current factor
0.6	850	1.6	1	1
0.5	600	2.5	2.4	1.4
0.4	400	4.0	6.2	2.1
0.3	200	5.0	9.8	4.2
0.2	100	8.5	28.2	8.5
0.1	10	20	156	85

comparison between the coherent case result, showing the rotational averaged radial profiles of the first positive and negative vortex order, together with their respective difference signal for 30 nm bcc-Fe. The incoherent case for an ISSB of 0.6 nm is shown in Figure 5.15 (c) and (d). The fully coherent 7 mrad beam was placed on the atomic column producing an EMCD effect as high as 30 % to 35 % in the centre of the EVBs, compared to less than 2 % in the broadened beam case.

It could be argued that with an increasing incoherent spot size, at least with the same acquisition times, the beam current rises as well, increasing the expected SNR, such that faint EMCD signals could be detected and there would be no benefit in using lower beam currents. But this is not the case: aside from the apparent gain in spatial resolution, a straightforward estimation of the needed count rate, assuming shot noise to be the predominant source of error in these measurements, shows that the needed electron counts for more coherent spots go down faster (higher shot noise factor) than the number of electrons does by lowering the spot size, see Table 5.2. Another aspect that would complicate the situation for higher beam currents, compared to lower ones, is sample damage, as it was seen in some trial experiments.

The incoherent spot size given in Table 5.2 was calculated by summing up only the incoherent contributions to the overall spot size,

$$d_{inc} = \sqrt{\left(C_c \alpha \frac{dE}{E}\right)^2 + \left(10^9 \frac{2}{\pi} \left(\frac{I_p}{\beta_{source}}\right)^{0.5} \frac{1}{\alpha}\right)^2}, \quad (5.8)$$

with C_c being the chromatic aberration of the objective, α the semi-convergence angle, dE the energy spread-, E the primary energy of the electrons, I_p the beam current and β_{source} the brightness of the electron gun. Note that, when including the coherent spot size contributions, stemming from diffraction effects at the aperture

and C_s , the calculated spot size values, using Equation 5.8, and the measured spot size/current values, using the *Tecnai F20* TEM, are in good agreement.

The SNR, due to shot noise, is given by the number of electrons N over the square root of N ($\frac{N}{\sqrt{N}}$), the relative SNR, is, thus, given by one over the square root of N and the needed electron counts for a certain EMCD strength level can be estimated by one over I_{EMCD} squared.

Now, that the simulation was carried out for multiple points in the unit-cell and was used for ISSB, it is instructive to use that data to calculate two-dimensional maps of the expected EMCD effect for ISSB spots as well, i.e.: simulating the outcome of a STEM vortex filtering EMCD experiment. In Figure 5.16 two of such 2D-EMCD maps are shown for a 30 nm bcc-Fe sample. A spatially varying EMCD signal of the order of 8 % to 20 % for an ISSB of 0.1 nm can be observed in (a). The EMCD signal is strongest around the atomic columns. If the beam in the imaging system is slightly defocused, the signal drops, but the localisation is still conserved (not shown). For higher ISSB of 0.5 nm, shown in Figure 5.16 (b), the variation throughout the unit-cell and the localization of the EMCD signal is strongly damped, as is the absolute signal, which is of the order of 2 % to 3 %.

These results are intriguing, because not only do they support the principal possibility of atomic scale vortex filtering EMCD mapping, but they also suggest that the use of higher coherence and more convergent beams is beneficial. Note that this simulations were conducted for non-corrected TEMs; but a simulation for a 20 mrad, fully coherent, corrected beam shows the same behaviour as given in Figure 5.16, upper panel, yielding an EMCD effect of up to 40 %.

5.1.7 Experimental Results

In this section the experimental results of multiple vortex filter EMCD measurements, using both introduced setups and different samples on two different TEM instruments, will be presented and compared to theory.

A Trial Experiment on Cobalt

Evidently, detecting faint EMCD signals in the vortex filtering setup, proposed in Section 5.1.2, strongly depends on the achievable SNR. Thus, a trial experiment, that shows the principal functionality of the method, and also the limitations concerning the achievable SNR, will be given in the beginning.

A thin layer of nano-crystalline Co, that was produced by Co incorporation into a continuous beam of He droplets, that were incident on a NaCl crystal, was used for the experiment in order to assess the typically achievable SNR. The film, provided by the IFW-Dresden, with a thickness between ~ 50 nm and ~ 70 nm was floated off the salt crystal, similar to the method described in Section 4.5, and placed on a standard TEM Cu-grid. The instrument used for this experiment was a *Tecnai F20* FEG TEM (FEI/ThermoFisher) equipped with a *Gatan Imaging Filter* (GIF) *Trididem* spectrometer (Gatan), which was already described in Section 2.1. The sample was

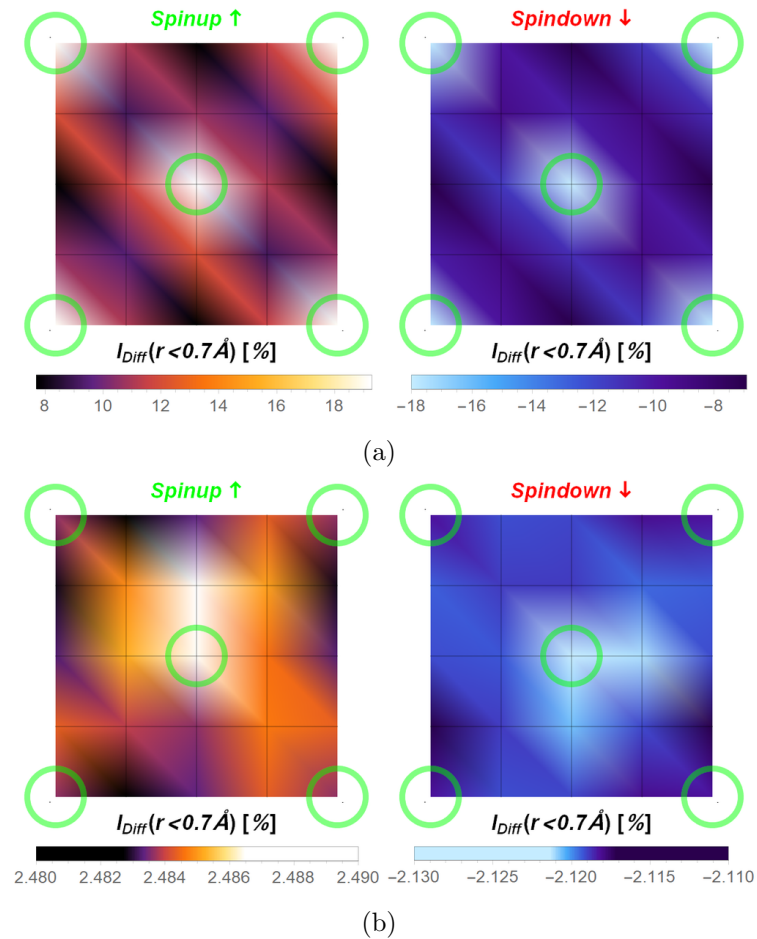


Figure 5.16: IXCHEL simulation including ISSB of 0.1 nm showing 2D EMCD maps in (a), using the parameters $\alpha = 7 \text{ mrad}$, $\beta = 5 \text{ mrad}$, $C_s = 2.7 \text{ mm}$, $U_a = 300 \text{ kV}$, $df = 73 \text{ nm}$ (Scherzer defocus) and a simulated thickness of the Fe sample of 30 nm. (b) 2D EMCD maps simulation using a ISSB of 0.5 nm. For the 0.1 nm spot a variation of the EMCD effect, well localized at the atomic columns, can be observed, which is strongly damped for the 0.5 nm spot.

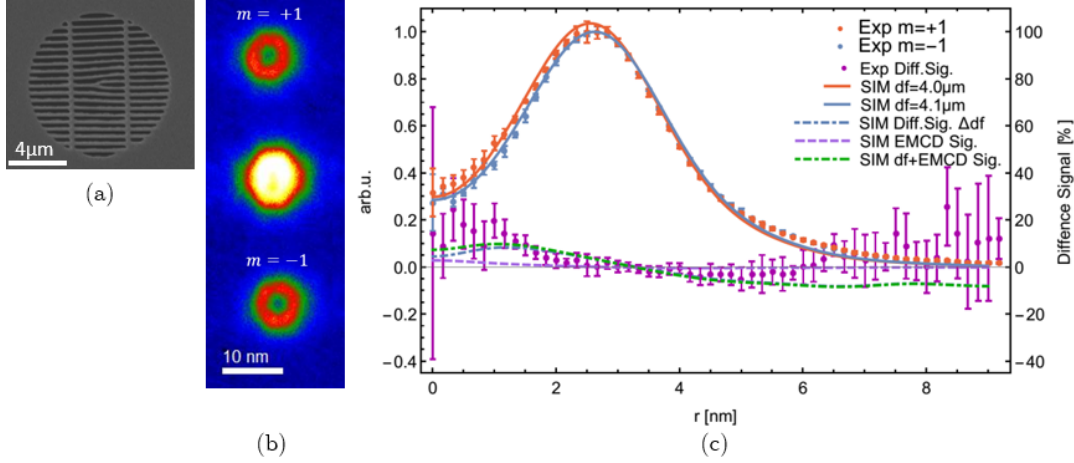


Figure 5.17: Early trial vortex filtering EMCD experiment taken at reversed OL field. (a) A $\text{\O}10\ \mu\text{m}$ and $g = 500\ \text{nm}$ binary amplitude HVM was used as a OAM filtering element. (b) EFTEM images showing the well-separated vortex orders $m = +1$ (upper) and $m = -1$ (lower) between the intense central $m = 0$ beam (middle), produced by (a) lifted to $dz = 75\ \mu\text{m}$ at the Co L_3 -edge defocused by $4\ \mu\text{m}$. (c) Azimuthally averaged radial intensity profiles of $m = \pm 1$ EVB in (b) compared to the single scattering centre simulation. A defocus variation of $0.1\ \mu\text{m}$ improves the agreement between the simulation and the experiment but the achievable SNR is very low. Note that the profiles are normalized to their respective total intensity, in order to account for asymmetries in the vortex order distribution; this is also true for the following measurements.

lifted above the eucentric height at $dz = 75\ \mu\text{m}$ and the AV was set to $200\ \text{kV}$, whereas the setup of the condenser system was aimed at achieving a high beam current at a sufficiently small spot size on the sample, i.e., providing a beam current of $\sim 500\ \text{pA}$, incident on the sample in a FWHM $\sim 1.9\ \text{nm}$ probe ($\sigma = 0.8$), having a convergence semi-angle α of $3.8\ \text{mrad}$.

The vortex filtering SAA HVM was a $m = 1$ binary amplitude vortex hologram with a diameter of $10\ \mu\text{m}$, a primary grating periodicity of $500\ \text{nm}$ and an orthogonal secondary stabilisation grating with a periodicity of $4\ \mu\text{m}$, see Figure 5.17 (a). It was prepared by FIB milling with a non-optimized $150\ \text{nm}$ Pt thin film on $200\ \text{nm}$ SiNx. The HVM's collection angle was $\beta = \sim 1.3\ \text{mrad}$ ($q_{\text{mask}} = \sim 3.2\ \text{nm}^{-1}$).

Figure 5.17 (b) shows the experimental EFTEM using the SAA HVM at an energy threshold of $780\ \text{eV}$ and an energy selecting slit of $15\ \text{eV}$. The vortex orders $m = \pm 1$ are well-separated from the central peak for a defocus value of $df = 4\ \mu\text{m}$. The B-field of the OL was in the reversed state. This image was acquired by taking four frames with an acquisition time of $100\ \text{s}$ per frame using four-fold binning of the GIF CCD. Subsequently, the frames were combined to an image stack and aligned using Image J [313].

To extract the rotationally averaged radial profiles, shown in Figure 5.17 (c), a DM script was devised. The script prompts the user to pre-define a region of interest (ROI) that contains the vortex centre. It then iterates through each and every pixel (also sub-pixel) within that ROI and calculates the rotationally averaged radial profile for every point using a coordinate transformation to polar coordinates. The vortex order's centre is found by searching the point with the highest peak intensity in the radial profiles. Then the script crops and extracts the rotational (azimuthal) average for each selected vortex order in the image. The rotational averaged radial profiles of the two opposing vortex orders were then normalized under use of the total intensity of the respective vortex order $\int_0^\infty I_m(r)rdr$.

For the estimation of the error in each radial pixel two different methods were employed. For the results of the trial experiment, given in Figure 5.17, the stacked images were used to calculate the STD-value pixel by pixel. This has the advantage that systematic errors, e.g., stemming from the azimuthal intensity variations of the vortices, are minimized. Whereas for the other experiments shown, the error-estimate was determined including shot noise $\sigma_{SN}(r) = \sqrt{I_m(r)}$, thermal- or dark current noise $\sigma_{DC} = \sqrt{N_e^{DC}}$, where N_e^{DC} is the number of dark current electrons estimated by taking the mean STD value of the outermost pixels of a radial profile, and CCD electronics read-out noise σ_{RO} , which was calculated by taking two 'zero'-seconds-exposure-time dark-frames of the GIF CCD, subtracting them from each other, calculating the STD of the difference image and finally multiplying it by $1/\sqrt{2}$ [314]. As these error sources are uncorrelated, they can be combined in quadratures as $\sigma_{I_{\pm 1}} = \sqrt{\sigma_{SN}^2(r) + \sigma_{DC}^2 + \sigma_{RO}^2}$ [315, 316]. An additional factor of two was added as a safety-factor to account for uncertainties in the used error determination process. To account for the improvement of the error, due to averaging over many measured values with increasing radius, a weighting factor of $1/\sqrt{N_{mea}}$, with N_{mea} being the number of measured pixels at a certain radius, was introduced.

Then the intensity-values of each vortex order's rotational average ($I_{\pm 1}$) and absolute STD values ($\sigma_{I_{\pm 1}}$) of that analysis have been used to estimate the relative STD-value of an EMCD, or difference signal σ_{EMCD} , via error propagation [317] resulting in the relation:

$$\sigma_{EMCD} \approx \sqrt{2} \left| \frac{I_{+1} - I_{-1}}{I_{+1} + I_{-1}} \right| \sqrt{\frac{(I_{+1}^2 + I_{-1}^2)(\sigma_{I_{+1}}^2 + \sigma_{I_{-1}}^2)}{(I_{+1}^2 - I_{-1}^2)^2}}. \quad (5.9)$$

Note that the radial dependency was omitted for clarity in Equation 5.9.

To estimate the error for the central region of the vortex orders, shown in Figure 5.17 (c), Equation 5.9 was simplified to $\sigma_{EMCD} \approx \sqrt{2} \frac{\sigma_{I_{+1}}}{I_{+1}} = \frac{\sqrt{2}}{SNR}$, under the following approximation: the differences between I_{+1} and I_{-1} are small, thus, $I_{+1} \approx I_{-1}$ and that their STD values are approximately the same, $\sigma_{I_{+1}} \approx \sigma_{I_{-1}}$. For the central region of the vortices ($r < 0.7$ nm) the averaged counts of both vortex orders and their STD-value amount to 108(9) ($SNR = 12, 8.3\%$). Using Equation 5.9 this results in $\sigma_{EMCD} = 11.8\%$. Therefore, the SNR has to be raised by an order of magnitude in order to be able to discern the theoretically predicted EMCD signal of

3%, at least when using the experimental parameters (vortex mask size, spot size, dz) given above.

In Figure 5.17 (c) the azimuthally averaged radial intensity distributions of the $m = \pm 1$ vortices are shown together with the single scattering simulation result. The simulation agrees well with the measured profiles, but the measured I_{Diff} is much stronger than expected from simulations, and as already pointed out above, its SNR is too low. Introducing a defocus difference of 100 nm in the simulation could partially explain the higher difference signal. But looking at the course of the simulated difference curve at higher radii, it significantly departs from the measured one. Interestingly, the measured curve shape hints at a real EMCD signal rather than at an artificial one.

Note that the origin of the azimuthal intensity variations in Figure 5.17 (b), visible as a six-fold symmetry, was clarified by two-dimensional image simulations, indicating that the variations are systematic effects, due to the presence of the stabilisation- or supporting-bars used in the HVM design.

Sample Damage

In the experiment given above, a relatively high beam current, bundled in a focused probe, is incident on the sample for a very long recording time. Hence, this issue is treated in the following.

For conducting materials like Fe/Co, high dose rates and a high AV of 200 kV knock-on electron sputtering is the primary damage mechanism [318]. For metals and carbon, typical characteristic doses, i.e., the dose where diffraction spots or spectral features disappear or fall by a factor of two or e , are within the range $2 \times 10^3 \text{ C cm}^{-2}$ to $8 \times 10^5 \text{ C cm}^{-2}$ for accelerating voltages of 100 kV to 300 kV [318].

To estimate the electron-dose given in the vortex filter EMCD experiments, the spot sizes were determined by using a non-linear least squares (NLLS) fitting routine, which is part of a *Gatan* EELS plugin for DM 3, to fit a *Gaussian* to the centred and cropped rotational averaged profile of an image of the focused spot, projected at the GIF camera. The GIF camera was used because of the post magnification of 20.78 in the GIF optics. A slit of 0.2 eV was used to reduce the beam current on the CCD's scintillator. For measurement of the beam current in the respective spot, the GIF was employed as a Faraday cup by directing the electron beam towards the drift tube walls using a shift voltage of 10 000 V and connecting a Pico-amperemeter to the drift tube voltage-connector. Note that the current, measured on the viewing screen and indicated in the microscope's control software, is roughly 20% to 30% too high for medium currents between 200 pA to 1200 pA and strongly overestimates the electron current by 75% at small current values of the order of 14 pA.

The electron density n_e can be calculated by $n_e = (IN_e\delta)/(d_{spot}^2\pi/4)$, with I being the measured electron current, N_e the number of electrons per second for one Ampere ($6.24151 \times 10^{18} \text{ e/s}$), and d_{spot} being the measured FWTM spot size containing 71.8% of the measured current. This is taken into account by using the beam current correction factor $\delta = 0.718$. Thus, the dose can be readily calculated

using $D_c = n_e t_{exp}$, where t_{exp} is the exposure time.

Electron densities, used in trial experiments (Spot 3, Gun lens 3, *Schottky* gun) were of the order of $2.5 \times 10^6 \text{ e}/\text{\AA}^2/\text{s}$. This electron density induced damage to the relatively thick (50 nm to 70 nm) Co- and Fe-samples after 400 s of irradiation. With a dose of $1.6 \times 10^6 \text{ C cm}^{-2}$ and in regard to the values given by Egerton, this is not surprising. However, densities of $1.4 \times 10^5 \text{ e}/\text{\AA}^2/\text{s}$ (Spot 6, Gun lens 3, *Schottky* gun) did not induce visible damage to an Fe sample after 400 s (dose: $8.8 \times 10^5 \text{ C cm}^{-2}$). Using a high brightness X-FEG⁹, the spot size, the current or the recording time, or a combination of them, has to be decreased in order to stay beneath the damage threshold. For example, the measurements done at the *Titan Holo* at the ER-C where conducted at an electron density of $1.6 \times 10^7 \text{ e}/\text{\AA}^2/\text{s}$, which is an order of magnitude higher than that of ordinary *Schottky* guns, but due to the much shorter recording times of 50 s, the overall dose was limited to $1.3 \times 10^6 \text{ C cm}^{-2}$.

The Second Generation of Vortex Filter EMCD Experiments

From the findings gained in the trial experiment (in fact there were many more), it is clear that the SNR has to be improved. This can either be done by increasing the incident beam current and using the same or higher acquisition times, or by increasing the collection angle β of the setup. But higher beam currents lead to a larger incoherent spot size, which inevitably drops the expected EMCD signal even further, to values at or below 2%. Also, elevated beam damage can be expected for higher beam currents, which would complicate the situation. This is even more pronounced using the high-brightness X-FEG. The latter possibility to increase the collection angle can be implemented by two ways: either the sample-lifting dz is reduced, which would also lead to a strongly reduced lateral coherence in the SAA plane, or by increasing the diameter of the vortex filtering HVM.

Another approach pointed out by the single scattering and IMS above, is the EMCD signal enhancement upon reducing the incident spot size. Furthermore, the IMS showed that measurements done at approximately $df = 0$, yield the highest and most consistent EMCD signal.

Experiments as an attempt to implement these measures, will be shown in the following.

A cross-sectional FIB lamella of epitaxially grown FeRh on MgO was provided by the CEITEC collaboration partners, see Figure 5.18 (a). After Ar-ion-milling (Technoorg Linda, Gentle Mill), the sample thickness could be reduced to $\sim 50 \text{ nm}$. FeRh is a material that shows an antiferromagnetic-to-ferromagnetic phase-transition at 400 K, thus the experiment was conducted in a double-tilt heating holder (Gatan) at 450 K. The instrument used for this experiment, was the same as in the trial experiment: working at 200 kV, providing a beam current of $\sim 270 \text{ pA}$, incident on the sample in a FWHM $\sim 1 \text{ nm}$ probe, having a convergence semi-angle α of 3.8 mrad.

⁹In the course of the PhD-thesis the *Schottky* electron source of the *Tecnai F20* TEM was replaced by an X-FEG. Also, the *Titan Holo* at the ER-C is equipped with an X-FEG.

The sample was lifted above the eucentric height by $dz = 100 \mu\text{m}$.

The vortex filtering SAA HVM was a $m = 1$ binary amplitude vortex hologram with a much higher outer diameter of $30 \mu\text{m}$ compared to the trial experiment with an inner diameter of $10 \mu\text{m}$. The primary grating periodicity was 500 nm and an orthogonal secondary stabilisation grating with a periodicity of $5 \mu\text{m}$ was used, see Figure 5.18 (b). It was prepared by stream file FIB milling using a non-optimized 450 nm Pt thin film on 200 nm SiNx. The HVM's collection angle range was $\beta = 1 \text{ mrad}$ to 3 mrad . The relatively large central-beam-stop was introduced to block electrons of the $\mu = 0$ transition, which do not contribute to the EMCD signal strength, see Table 5.1 and Figure 5.4. The EFTEM data was recorded by taking 10 frames, a 10 s, at six-fold binning.

Note that the *Gatan* DM script 'Acquire Multiple Diffraction Patterns' was used for these experiments, as it records a series of images without a significant delay between the single frames and allows to do the image-alignment right within in the *Gatan* microscopy suite.

In Figure 5.18 (c), the azimuthally averaged radial intensity distributions of the $m = \pm 1$ vortices, imaged at the Fe L_3 -edge energy-threshold, are shown together with the IMS result, using a slit of 10 eV and a defocus of $df = \sim 0 \text{ nm}$. There, a strong central negative difference signal, with significantly improved SNR, is measured. The difference signal is higher than the simulated one, possibly hinting at the effect of residual astigmatism, as can be seen from the insets in 5.18 (c), and from the astigmatism indicator value in 5.18 (d) of 0.08 , which was the same for both measurements¹⁰. But the general agreement between measured- and simulated difference signal is good. Also, a difference signal reversal can be observed for the reversal of the OL field, see Figure 5.18 (d).

By analysing the *Gouy* rotation under the use of a knife-edge (KE), as described in Section 5.2, It was asserted that the vorticity of the $m = \pm 1$ EVBs does not change upon field-reversal of the OL.

The need for heating and the relatively low Fe-signal (only 50 % of the alloy are Fe) complicated the experiment. The next series was done on a free standing nanocrystalline Fe thin film of 70 nm thickness, provided by IFW-Dresden, see Figure 5.19 (a). This film was produced using the same He-droplet-deposition-method described above. The thin film was thinned down to 50 nm using the Ar-ion mill. The microscope settings were the same as mentioned in the FeRh-experiment, except for the convergence angle $\alpha = 5.5 \text{ mrad}$ and the beam current, which was $\sim 500 \text{ pA}$. As an OAM filtering element, the same vortex filter mask was used, Figure 5.19 (b). And the image acquisition was done by taking 4 frames, a 25 s, at four-fold binning. It was tried to position the beam intentionally on crystallites, oriented in $[001]$ zone axis.

Again, in Figure 5.19 (c), the simulated radial profiles agree well with the measure-

¹⁰The astigmatism indicator is calculated by taking the arithmetic mean of STD values along the azimuthal direction $\varphi = 0^\circ$ to 360° from $r = 0$ to $r \leq r_{max}/3$, with r_{max} being the maximal radius of the radial profile. The best value seen in other measurements is 0.02 .

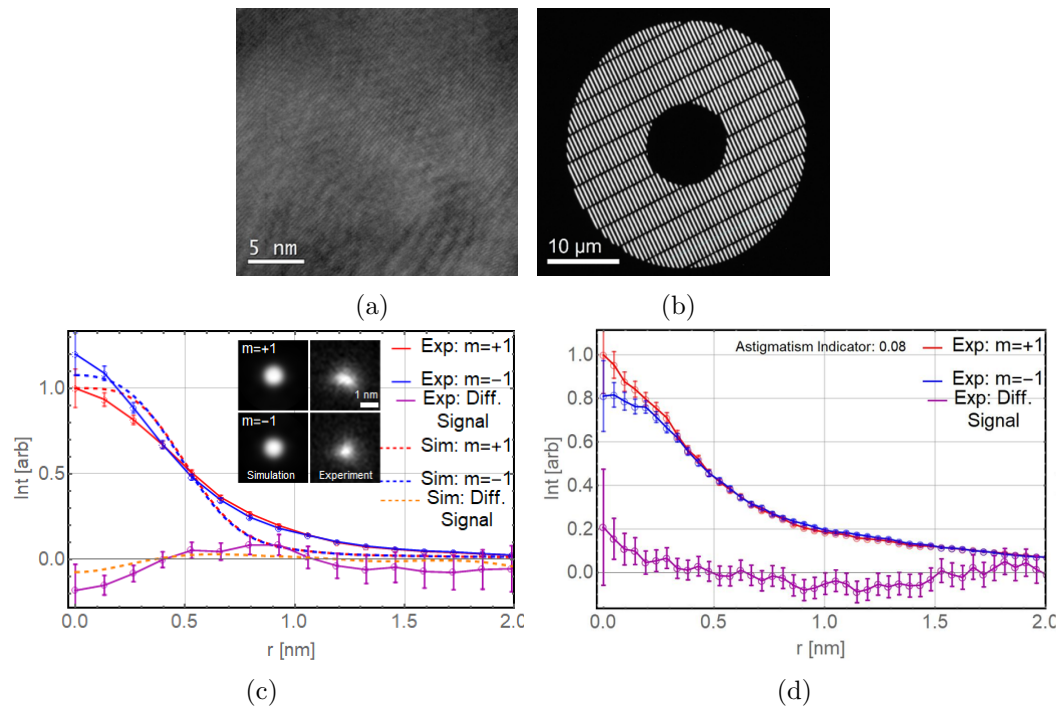


Figure 5.18: SAA vortex filter EMCD experiment on FeRh. (a) HRTEM image of the ~ 50 nm FeRh sample. (b) Low-magnification TEM image of the $\text{\O}30$ nm $g = 500$ nm HVM ($\beta = 1$ mrad to 3 mrad) (c) Azimuthally averaged radial intensity profiles of $m = \pm 1$ EVB at the Fe L_3 -edge using a slit of 10 eV, $df = \sim 0$ nm and $dz = 100$ μm , compared to an IMS of 50 nm FeRh using a ISSB of 0.3 nm. The insets show measured vortices on the right side and the simulated ones on the left. (d) same as (c), but with the OL field reversed. The measured difference signal is higher than the simulated one in the centre, but the general agreement between measured and simulated difference signal is good. A difference signal reversal can be observed for the reversed OL field measurement.

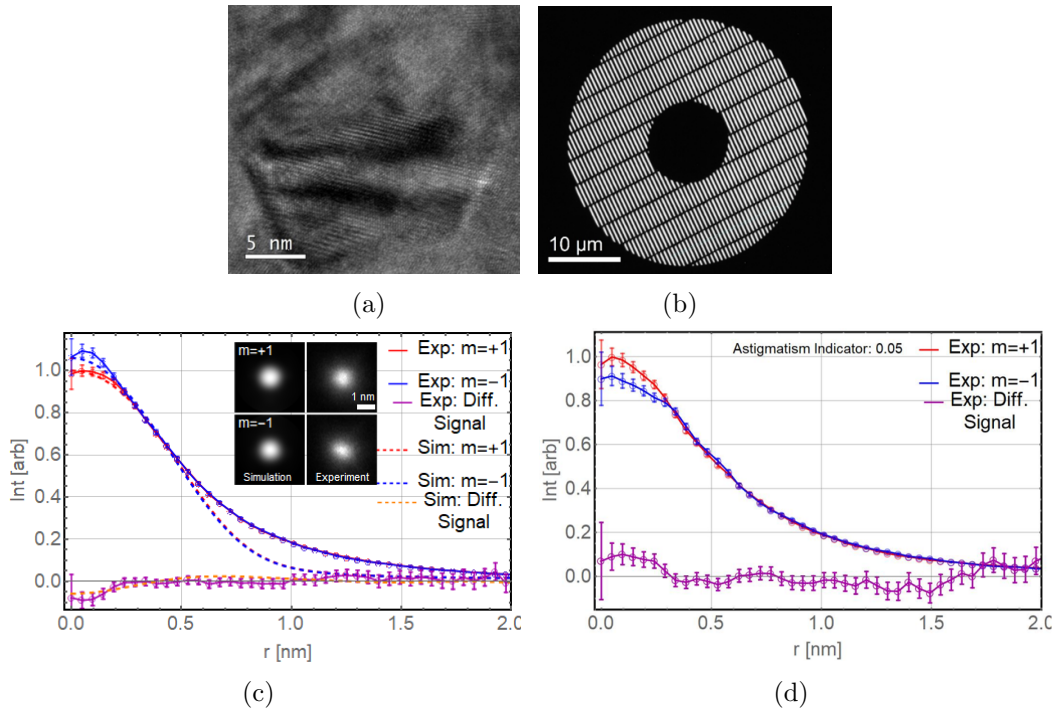


Figure 5.19: SAA vortex filter EMCD experiment on pure Fe. (a) HRTEM image of the 50 nm nano-crystalline Fe film. (b) Low-magnification TEM image of the $\text{\O}30$ nm $g = 500$ nm HVM ($\beta = 1$ mrad to 3 mrad) (c) Azimuthally averaged radial intensity profiles of $m = \pm 1$ EVB at the Fe L_3 -edge using a slit of 10 eV, $df = \sim 0$ nm and $dz = 100$ μm , compared to an IMS of 30 nm Fe using an ISSB of 0.4 nm. The insets show the measured vortices on the right side and the simulated ones on the left. (d) same as (c) but at the L_2 -edge. Both measurements were done with the OL field in normal direction. The same trend of the difference signal can be seen in comparison to the FeRh sample, but the SNR is much better and the measured difference signal shows a good accordance to the simulation. A difference signal reversal can also be observed for the L_2 -edge.

ment, the difference signal is weaker than the one from the previous measurement and fits very good to the simulated one with even better SNR. This could be due to the improved astigmatism value, which is 0.04 for the L_3 -edge. The difference signal at the L_2 -edge, shown in Figure 5.18 (d), reverses its sign.

At the ER-C in *Jülich* it was possible to test the functionality of the DP vortex filter setup on a wide-gap *Titan Holo* (FEI/ThermoFisher) working at 300 kV and equipped with a GIF *Tridien* (Gatan) using a $\varnothing 40 \mu\text{m}$, $g = 160 \text{ nm}$ phase HVM produced by the ER-C, see Figure 5.20 (b). A 30 nm magnetron-sputtered Fe thin film, deposited on a 5 nm SiNx membrane (Norcada), was used as a sample, see Figure 5.20 (a). The sample was produced in-house by the thin film group of the Institute of Solid State Physics, TU Wien, (IFP) with the aim of producing larger crystallites by post-deposition annealing steps.

Testing a phase hologram, instead of the binary amplitude holograms, was motivated by their presumably higher DE, which should further enhance the count rate in the first vortex orders. But, as was already shown in Table 4.5 in Section 4.4, it turned out, that strong high-angle scattering in the relatively thick SiNx-support of the phase hologram structure massively reduces the achievable DE to values, way below the ones achieved with binary amplitude holograms. Nevertheless, the higher collection angle of 5 mrad somewhat compensated the ‘electron-loss’ in the phase mask support material.

The instrument’s condenser system was set up to deliver a beam current of $\sim 600 \text{ pA}$, incident on the sample in a FWHM $\sim 0.8 \text{ nm}$ probe, having a convergence semi-angle α of 7 mrad. The 50 s-acquisition was done using a binning of four. Due to the defocus-issue, explained in Subsection 5.1.2, the sample had to be lifted slightly above the eucentric height.

The results, given in Figure 5.20 (c) and (d), show that using a vortex filter HVM in the DP is feasible and relatively straightforward. A faint 3.5%, but significant difference signal that follows the simulated vortex filter EMCD signal very well can be seen in Figure 5.20 (c). Also, the simulated profiles closely resemble the measured profiles. Interestingly, the astigmatism-indicator-value could be further reduced to 0.02 and 0.03 in the $L_{3,2}$ -edge measurements, respectively. This is most likely a result of the higher stability of the system in comparison to the *Tecnai* instrument, as well as the higher count rates, which allowed for a better alignment of the EFTEM image in the viewing-mode. The SNR is comparable to or even slightly better than that of the measurements done on Fe at the *Tecnai* instrument, even though the mask’s DE was sub-optimal. The difference signal reversal at the L_2 -edge, Figure 5.20 (d), further hints at the presence of a real EMCD signal. Note that the L_2 -edge difference signal is higher than the L_3 -edge signal, whereas in classical EMCD measurements it is the other way round, due to, e.g., multiple scattering, see [6, 14, 319]. This may indicate the presence of residual artefacts in the L_2 measurement. With the incident beam size being smaller than one nanometre, a very high lateral resolution could be achieved in this proof-of-principle experiment.

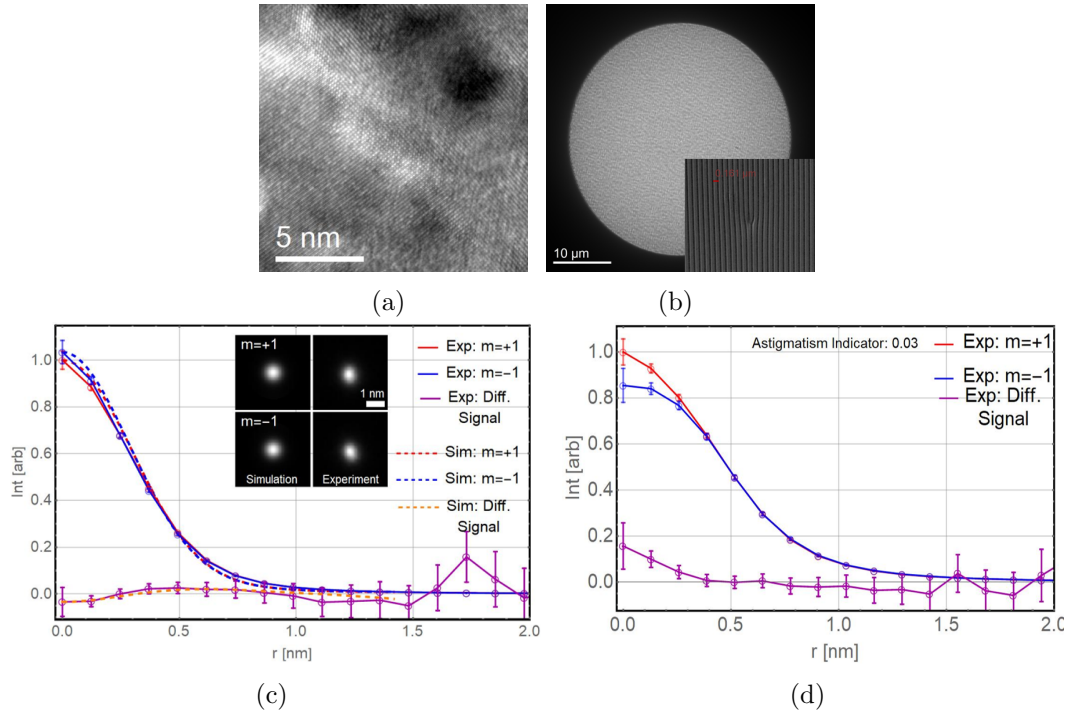


Figure 5.20: DP vortex filter EMCD experiment on Fe. (a) HRTEM image of the 30 nm fine crystalline Fe film. (b) Low-magnification TEM image of the $\text{Ø}40$ nm $g = 160$ nm phase HVM ($\beta = 5$ mrad). The inset shows a zoom-in to the central region of the phase mask. (c) Azimuthally averaged radial intensity profiles of $m = \pm 1$ EVB at the Fe L_3 -edge using a slit of 10 eV and $df = \sim 0$ nm, compared to an IMS of 30 nm Fe using an ISSB of 0.4 nm. The insets show the measured vortices on the right side and the simulated ones on the left. (d) same as (c) but at the L_2 -edge. The measured central difference signal is of the order of 4%, shows a high SNR and is in good agreement with the IMS for the DP vortex filter setup. A difference signal reversal can also be observed for the L_2 -edge.

5.1.8 Discussion

The measurements done on two different machines and different samples, clearly point out that optimized experimental conditions lead to the detection of a difference signal, which very much indicates the presence of a real EMCD signal, also being in good agreement with IMSs. Both experimental setups can in principle be used, but the streamlined DP setup allows, e.g., for the implementation of well-established STEM techniques like line profiles and 2D- mapping.

The trial experiment on Co, together with the according theoretical estimate of the expected EMCD signal, called for higher count rates, a reduction of the incident spot size and the use of small or no image-defocus-values. These issues were tackled in the second generation of experiments, which significantly improved the outcome. Though the second generation of experiments pointed out, that without a proper astigmatism control, the difference signals are stronger than expected, i.e.: with decreasing astigmatism indicator values the measured signal came closer to the simulated one. In [320] the influence of drift and non-isochromaticity on EFTEM EMCD measurements are pointed out. Concerning non-isochromaticity, the spectrometer was tuned before the measurements, but it was not yet estimated how residual non-isochromaticity would effect the expected difference signal. For the long recording times needed in this very low count rate application, drift is inherently problematic, smearing out the achievable EMCD signal. Thus, the measurements done in *Vienna* were carried out at night under otherwise stable conditions. Additionally, clearly drift-affected images were excluded. Anyway, measurements done on the *Tecnai* microscope showed higher intensities than predicted by the simulation in the profile tails, whereas, the measurement done at the high-stability *Titan* system was missing this feature/artefact. Thus, it may be a residual drift artefact (or a slight defocus). Both of which could be corrected more easily with a higher count rate, which was also seen in the ER-C measurements. Further improvements in the count rates are definitely possible, either by enhancing the collection angle, which is only limited by chromatic aberrations of the OL, and/or by the improvement of the DE of the vortex filter HVM. For example, at the *Tecnai* instrument working at 200 kV, the maximal aperture size will be approximately 6 mrad, yielding a spatial resolution of ~ 0.5 nm (C_c -limited). Using a C_c corrected machine this limitation could be lifted, such that in future measurements atomic resolution could be achieved. Concerning the DE, the tests employing a binary phase mask are promising (see Section 4.4).

What was not mentioned so far, is the question on the influence of the background signal. Core-loss-edges typically sit on a background, stemming from the tails of the bulk-plasmon, the amount of which is directly related to the sample thickness. Thus, it was tried to reduce the influence of the non-dichroic background by choosing thin samples (< 50 nm), which yielded jump ratios of, e.g., 3 to 4 in the Fe-measurements carried out in *Jülich* and *Vienna*. Additionally, it was tried to take pre-edge-images, but they were often artefact-dominated, due to the (even) lower count rate and defocus changes, as a result of the lower electron energy. An effective background subtraction, as it is done in conventional EFTEM imaging, was definitely not possible.

Probably this gets feasible with further improvement of the count rate, such that focus-variations are clearly discernible and the operator can refocus after changing the slit-energy. Notably, in the measurements done on Fe and the normal-B-field measurement on FeRh the difference signals taken at pre-edge energies, showed a relatively flat curve at $\sim 0\%$, or were flat and shifted by $\pm 5\%$.

In the simulations a fully spin-polarized sample was inherently assumed. This was not explicitly checked, but the saturation magnetic flux density of crystalline Fe is 2.14 T [321], and it was shown by magnetometry on powders, made of Fe nanoparticles, that, whatever nanoparticle size was used, they exhibited the bulk saturation-level of Fe [128]. Another experimental aspect of using nano-crystalline samples is, that, due to instrument-instabilities during recording, the beam/stage could drift away from the chosen crystallite, which could change the expected difference signal. Thus, in the Fe sample, that was used in the *Jülich* experiments, larger crystallites (~ 25 nm) were produced by post-annealing. Ideally, a single-crystalline sample should be used for such proof-of-principle experiments.

The IMSs did also show that a faint dichroic signal, being clearly smaller than that for a crystalline material, can also be expected for amorphous materials, but in the light of the experimental challenges in detecting a viable signal for crystalline materials, this can be considered a future task.

5.2 Production of Peculiar Rotational States in Magnetic Fields Using Electron Vortex Beams

This chapter will give an insight on how EVBs in a TEM can be utilized to produce a peculiar set of rotational states, including no-, slow-*Larmor*- and double-*Larmor*-rotation as well as fast *Gouy*-rotations. The equivalence of EVBs – at a certain defocus – to solutions of the paraxial Schrödinger equation in a homogeneous magnetic field, renders them a tool to produce free-electron *Landau*-states in the TEM.

This chapter is based on and will follow the author's publication *Peculiar rotation of electron vortex beams*, published as a follow-up of his diploma thesis in the Journal *Ultramicroscopy* [32] (in 2015). Recently, *Han et al.* [322] also elucidated a classical description of EVB rotational dynamics in magnetic fields, using a model that consists of constructing electron vortices by the synchronized motion of classical electrons in their cyclotron orbits. Interestingly, an intuitive understanding for the three rotation-regimes, described in the following, could be given on that basis.

Standard electron optics predicts *Larmor*-image-rotation in the magnetic lens field of a TEM. With the introduction of the possibility to produce EVBs with quantized OAM, the question of their rotational dynamics in the presence of a magnetic field came up. In a preceding publication, co-authored by the author, *Schattschneider et al.* [34] showed that EVBs can be prepared as free-electron LS, exhibiting peculiar rotational dynamics, including no- and cyclotron- (double-*Larmor*) rotation. Additionally, very fast *Gouy*-rotation of EVBs has also been observed by *Guzzinati* in 2013 [323]. In this chapter, a model will be developed, based on diffracting LG modes, revealing that the rotational dynamics of electron vortices are a combination of slow-*Larmor* and fast *Gouy*-rotations and that the *Landau*-states naturally occur in the transition region in between the two regimes. This general picture is confirmed by experimental data, which shows an extended set of peculiar rotations, including no-, cyclotron-, *Larmor*- and rapid *Gouy*-rotations, all present in one single convergent electron vortex beam.

5.2.1 Introduction

Many theoretical papers deal with the propagation of EVBs: see [3, 144, 174, 302, 324, 325]. The most intriguing prediction is the peculiar rotation mechanism of vortex beams in a magnetic field. It was shown, that exact solutions of the paraxial Schrödinger equation in a homogeneous magnetic field acquire a phase upon propagation along the z -axis [324]. This phase shift causes a quantized rotation of a coherent superposition of LG modes, which is falling in one of three possible groups: showing either cyclotron-, *Larmor*-, or zero-frequency, depending on the topological charges involved.

This momentarily surprising prediction was confirmed experimentally by the use of beams, closely resembling non-diffracting solutions of the Schrödinger equation in a homogeneous magnetic field [34]. Contrary to this quantized rotation, rapid *Gouy*-rotation could be observed when investigating EVBs close to the focus [323]. These

experiments seem to contradict each other, as well as the standard theory of electron movement in a TEM, that predicts *Larmor*-rotation of paraxial ray pencils between object and image in a round magnetic lens [33]. It was this puzzling combination of rotation-regimes that called for a re-evaluation of the rotation-dynamics of convergent and divergent electron beams in the TEM, including beams with non-vanishing topological charge.

As already pointed out, a quantum mechanical description of *diffracting* electron vortices based upon radius r and an angular momentum $m\hbar$, their time-evolution will be given in the following. It was found that the rotation-dynamics are a function of the OAM and the expectation value $\langle \hat{r}^{-2} \rangle$ (the second moment of the inverse beam radius) or, rather, its rescaled variant $\langle \hat{\xi}^{-2} \rangle = \langle (\hat{r}^{-2}/w(z)^{-2}) \rangle$. This finding will be supported by experiments tracking the rotation of convergent electron waves with topological charge in the lens field of the TEM objective. It will be proven that the whole range of rotation-dynamics, namely 'classical' Larmor-rotation (LR), rapid *Gouy*-rotation, cyclotron- (double-*Larmor*) and zero-rotation occurs in one beam, and can be described within a uniform picture.

5.2.2 Theory of the Rotation Dynamics

Diffracting Laguerre-Gaussian Modes

EVBs in magnetic fields and their rotation-dynamics were associated with the concept of *Bohmian* trajectories [324], which can be thought of as streamlines of the quantum mechanical particle current density in the form:

$$\mathbf{j}(\mathbf{r}) = \frac{1}{m_e} \Re[\psi^*(\mathbf{r}) \mathbf{p}(\mathbf{r}) \psi(\mathbf{r})] = \frac{1}{m_e} \Re[\psi^*(\mathbf{r}) (-i\hbar \nabla - e\mathbf{A}(\mathbf{r})) \psi(\mathbf{r})]. \quad (5.10)$$

Here, a constant homogeneous magnetic field \mathbf{B} is assumed, pointing in z -direction, giving rise to a vector-potential in the form of $\hat{\mathbf{A}} = -\frac{\hat{\mathbf{r}} \times \mathbf{B}}{2}$, using the *Coulomb* gauge, while $\hat{\mathbf{p}} = \hat{\mathbf{p}} - e\hat{\mathbf{A}}$ which is the observable *kinetic* or *covariant* momentum operator, whereas $\hat{\mathbf{p}}$ is the canonical momentum operator, which is gauge-dependent and not an observable.

This approach at hand, it is possible to calculate the angular velocity of a quantum fluid by following these streamlines, yielding a relation for the expectation value of the angular frequency. In Section 2.4 the properties of DLG modes were described in detail. Taking these DLG modes, it turns out, that by using a scaling method in the form of $\hat{\xi} = \hat{r}/w(z)$, the expectation value of the angular frequency of a DLG mode can be written as [32]:

$$\langle \omega(z) \rangle = \frac{\hbar}{m_e w(z)^2} \sum_m m \langle \hat{\xi}^{-2} \rangle_m + \sigma \Omega = \Omega \left(\frac{w_B^2}{w(z)^2} \sum_m \text{sgn } m + \sigma \right), \quad (5.11)$$

where the *Larmor*-frequency $\Omega = |eB_z/2m_e|$ and the magnetic beam-waist or -length $w_B = \sqrt{(2\hbar)/|eB|} = \sqrt{\hbar/(m_e\Omega)}$ were used. The magnetic beam-waist is the radius

5 Recent Applications and Progress

that encloses one magnetic flux-quantum, i.e., the magnetic flux through a circle of radius w_B is $w_B^2 \pi B = h/e$. $\sigma = \text{sgn } B_z = \pm 1$ designates the direction of the axial magnetic field. As derived in the appendix of [32], for a single radial mode the relation $\langle \hat{\xi}^{-2} \rangle_m = \frac{1}{|m|}$, which is independent of n , was used. Taking an eigenstate m of \hat{L}_z , and with Equation 2.23 (given in the Fundamentals chapter) this is:

$$\langle \omega(z) \rangle = \Omega \left(\frac{w_B^2}{w_0^2} \frac{\text{sgn } m}{1 + (z/z_R)^2} + \sigma \right). \quad (5.12)$$

Equation 5.12 shows some peculiar features of converging electron beams described by DLG modes. Depending on the relative weight of the two terms, the EVBs will rotate differently. E.g., far off the focal plane, when $z/z_R \gg 1$ and $w(z) \gg w_B$, the rotation frequency resembles the *Larmor*-frequency and, depending on the magnetic field orientation σ , this rotation will be clockwise or counter-clockwise. In this regime, which is called ‘LR-region’ in the following, the OAM of the electron does not influence the rotation frequency.

In case of the electron-beam-waist being of the same size as the magnetic length $w(z) \simeq w_B$, the EVBs approximate LS, see Section 5.2.2, showing no rotation for anti-parallel orientation of the OAM with respect to the magnetic field B_z and cyclotron-rotation (double-LR) for parallel orientation. This region is denominated as ‘LS-region’.

Obviously, for the condition $w(z) \ll w_B$ the rotation frequency increases drastically. In this so-called ‘Gouy-regime’ or ‘Gouy-region’, simulations show that focused vortices with $m = 1$ can rotate with a rotation frequency of $\sim 10^3 \Omega$, corresponding to the cyclotron-frequency in enormously strong fields of the order of 1000 T.

Note that with setting the defocus to $z = z_B$, the beam-waist equals the magnetic length, $w(z) = w_B$, and thus Equation 5.12 reduces to:

$$\langle \omega(z_B) \rangle = \Omega(\text{sgn}(m) + \sigma), \quad (5.13)$$

implying a quantized angular frequency with only three possible absolute values: 0, Ω , or 2Ω for $\sigma m < 0$, $\sigma m = 0$, $\sigma m > 0$. This surprising result was derived in [324] and experimentally verified in [34]. At this defocus, Equation 2.22 reads,

$$\psi_{m,n}(r, \varphi, z_B) = LS_{m,n}(r, \varphi, z_B) e^{i \frac{k r^2}{2R(z)}} e^{-i(2n+|m|+1)\zeta(z_B)}, \quad (5.14)$$

where

$$LS_{m,n} = \sqrt{\frac{n!}{\pi w_B^2 (n + |m|)!}} \left(\frac{r}{w_B} \right)^{|m|} \times L_n^{|m|} \left(\frac{r^2}{w_B^2} \right) e^{-r^2/2w_B^2} e^{i(m\varphi + k_z z_B)}, \quad (5.15)$$

represents the wavefunction of a LS.

To check the applicability of this approach for converging EVBs in the TEM, a first step is to compare the transverse EVB profiles of a $\psi_{3,0}$ DLG mode, Equation 2.22, given in the Fundamentals chapter, to numerically simulated transverse profiles for

5.2 Production of Peculiar Rotational States in Magnetic Fields Using Electron Vortex Beams

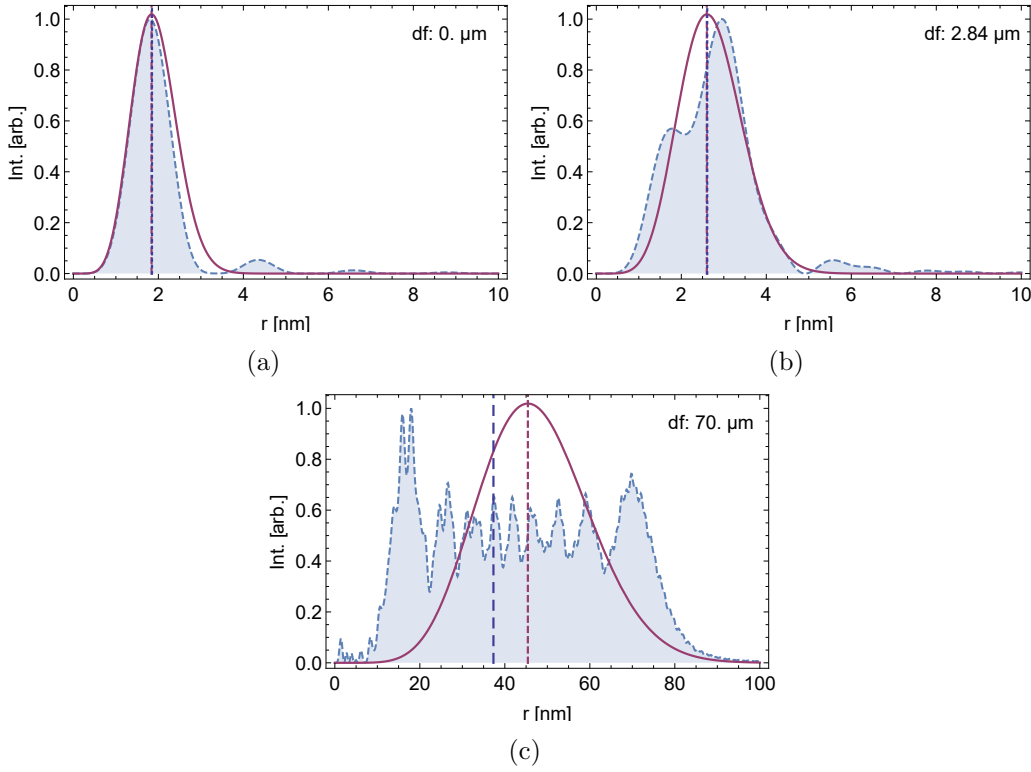


Figure 5.21: Comparison between an numerical simulated EVB (blue dashed line) and the analytical LG mode $\psi_{3,0}$ (purple solid line) in focus with $w_0 = 1.5$ nm (a), at z_R (b) and a defocus of $70 \mu\text{m}$ in (c) for an OAM $\hbar m = 3\hbar$ EVB with $z_R = 2.84 \mu\text{m}$. The blue dotted vertical lines represent the $w_B \langle \hat{\xi}^{-2} \rangle^{-1/2}$ -values of the numerical simulated EVB, whereas the purple dashed ones belong to the analytical LG modes.

different z -values, see Figure 5.21. More details are discussed in Section 5.2.3. It is evident that DLG modes approximate the intensity distributions very well between the focal plane and the *Rayleigh*-range z_R . For higher z -values, the EVB profiles deviate considerably from the DLG modes, but in regard to their rotation-dynamics, there is no significant difference between these two approaches because of their similar $\langle \hat{\xi}^{-2} \rangle$ -values, see the vertical lines in the Figure 5.21. A multitude of parameters, like the *Larmor*-frequency, the OAM, the magnetic length w_B and the z -dependent vortex radius, influence the rotation frequency of EVBs in magnetic field. This renders a comparison between different experiments to each other, as well as to theory and simulation impractical. Fortunately, this can be solved by defining a *Rayleigh*-frequency $\omega_R = \Omega w_B^2 / w_0^2 = \hbar k / m_e z_R = v_z / z_R$, which is the reciprocal time the electron takes to traverse the *Rayleigh*-range of a DLG mode. For the

propagation along the z -axis a dimensionless variable is introduced, which relates the z -value to the *Rayleigh*-range, as $\zeta = z/z_R$. For DLG modes the rotation frequency Equation 5.12, expressed as a dimensionless rotation frequency, follows a universal *Lorentz*-function [32]:

$$\frac{\langle \omega(z) \rangle - \sigma \Omega}{\text{sgn}(m) \omega_R} = \frac{1}{1 + \zeta^2}. \quad (5.16)$$

With the relation given in Equation 5.16 one can now compare experiments that were done with different parameters, or numerical simulations with the analytical result for DLG modes, given in Equation 5.12.

5.2.3 Simulation

Knife Edge Cutting

Rotational dynamics contained in the expectation value $\langle \omega(z) \rangle$ of a azimuthally symmetric electron distribution are not accessible. In order to resolve that issue the EVB symmetry has to be broken. This can be accomplished by a well established technique in optics [326, 327], which was also recently used in electron physics [323]. There, a sharp knife-edge (KE) is used to break the circular symmetry of the annular shaped EVB by blocking half of the electron-intensity's distribution. As a result, the azimuthal rotation angle $\varphi(z)$ of the cut intensity-pattern can be determined. Since $\omega = d\varphi/dt = d\varphi/dz v_z$, where $dz/dt = v_z$ is the velocity of the electron in the z -direction, rotational frequencies are accessible by shifting the KE along the z -axis. For general wavefunctions the azimuthal rotation angle can be calculated by [32],

$$\varphi(z) = \frac{\Omega}{v_z} \left(\sum_m m \int_{z_{df}}^z \langle \hat{\xi}^{-2} \rangle_m dz + \int_{z_{df}}^z \sigma dz \right), \quad (5.17)$$

with z_{df} being the defocus of the observation plane. Equation 5.17 can be used to translate measured the azimuthal angle into rotational dynamics. For diffracting LG modes, Equation 2.22, an analytic expression for this mapping procedure can be found by integration of Equation 5.12 over z [32]:

$$\varphi(z) = \frac{m}{|m|} \left(\arctan \left(\frac{z}{z_R} \right) - \arctan \left(\frac{z_{df}}{z_R} \right) \right) + \frac{\Omega}{v_z} \sigma (z - z_{df}). \quad (5.18)$$

The question if cutting the EVB by a KE introduces an unwanted effect to the rotation-dynamics, was clarified by expressing the truncated beam's wavefunction ψ_c via a *Fourier*-series in the azimuthal angle,

$$\psi_c(r, \varphi) = f(r) \sum_{\mu} c_{\mu} e^{i(m+\mu)\varphi}. \quad (5.19)$$

It was found out in [32] that the expectation value of the angular frequency is not changed after cutting the vortex, which is in accordance with recent observations of electron vortices, see [323], as well as optical vortices [326, 327].

Numerical Simulation and Error Sources

The angular frequency can be determined, if the OAM of the incident EVB and the moment $\langle \xi^{-2} \rangle$ as a function of z are known. In the plane of the cutting-edge this moment depends only on the radial density of the (cut) vortex, so a standard FFT-based procedure using the *Fresnel* propagator can be used. Even though, it is well-studied that the FFT results are reliable, the LR is not included. Therefore, it has to be added by using a so-called co-rotating coordinate system [328]. Lens aberrations can also be included, but for the low convergence angles, of the order of 1 mrad, used in the experiments, they are of no significance, which was also checked in the simulations. Thus, $\langle \xi^{-2} \rangle$ was calculated as a function of the position z of the obstructive edge, from which the rotation angle of the vortical structure can be quantified via Equation 5.17.

As already pointed out in Section 2.4.4 in the Fundamentals chapter, it is a well established method to use HVMs for the production of EVBs. Even though binary amplitude HVMs are among those methods, that produce EVBs with the highest purity, they still carry a certain amount of OAM-impurities [47]. One probable reason are irregularities in the mask geometry, but the excitation of vortical plasmon modes [329] could be responsible, as well. This means that a certain vortex order does not carry a quantized OAM anymore, it consists of weighted admixtures of different OAM modes. Although it was argued above that there are no changes in the rotation-dynamics of a vortex if a sector is cut out, irregularities in the obstructing edge, as well as diffuse scattering at its rim may well cause OAM-impurities in a vortex. For a vortex of the order m_0 , one can make the approach [32]:

$$\langle \omega(z) \rangle = \Omega \left(m_0 \langle \hat{\xi}^{-2} \rangle_{m_0} + \sigma \right) + \Omega \sum_{m \neq m_0} m \langle \hat{\xi}^{-2} \rangle_m, \quad (5.20)$$

to estimate the influence of impurities to the angular frequency. The last term in Equation 5.20 causes a deviation from the rotation-dynamics of the quantized vortex m_0 . It is small, because the coefficients measure the small admixtures of other OAMs, so: $\langle \hat{\xi}^{-2} \rangle_{m \neq m_0} \ll \langle \hat{\xi}^{-2} \rangle_{m_0}$.

Another potential source of errors is the diffraction at the obstructing edge. Instead of a rotated shadow image of the cut vortex, one observes a blurred half-ring-structure with *Fresnel* fringes. These fringes add to the challenge of measuring a rotation angle of the edge. Nevertheless, since these angles are measured in a series of z -positions of the edge, the difference of two consecutive measurements is less sensitive to the smoothly changing fringe contrast. Mind that the insertion of a KE into the electron beam path is a means to do inline holography and was used to determine the OAM content of EVBs in one of the first publications on EVBs in a TEM [5].

5.2.4 Experimental

In order to experimentally access the rotation-dynamics of EVBs in a magnetic field, the setup shown in Figure 5.22 (a) was employed: it can be seen that EVBs are

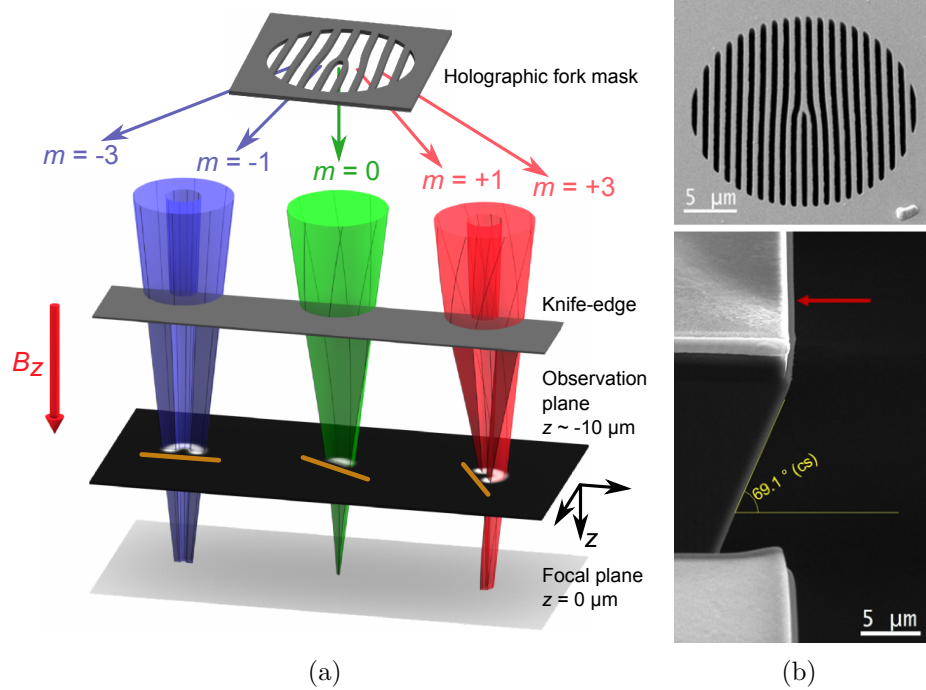


Figure 5.22: The principal experimental setup is shown in (a), adapted from [34]. A holographic fork mask splits the incident electron beam into EVBs, such that the diffraction orders on either side of the zero-beam carry negative and positive OAM ($m = \dots, -3, -1, 0, 1, 3, \dots$), respectively. The convergent EVBs enter the longitudinal magnetic field B_z of the objective lens and are incident on a KE. The cut EVBs propagate down the column reaching the observation plane at $z \approx -10 \mu\text{m}$, a few *Rayleigh*-ranges above the focal plane. By varying the position of the KE the EVBs' rotational dynamics can be measured as azimuthal angle variation of the half-moon-like intensity-patterns in the observation plane. (b) SEM images of the HVM that was used to produce the EVB and the Si-KE employed in the experiments. The red arrow marks the cutting-edge. It was produced by breaking a Si-wafer along a low-indexed zone axis.

produced by using a HVM ($\text{Ø}21 \mu\text{m}$, $g = 1050 \text{ nm}$, milled into $1200 \text{ nm Au}_{60}\text{Pd}_{40}$, shown in Figure 5.22 (b) (upper image)). This mask is then placed in the C2 aperture holder of the instrument shown in Figure 2.1 (b) in Section 2.1. The convergent EVBs are incident on an Si-KE, placed in the sample plane, see Figure 5.22 (b) (lower image). Please note that the axial magnetic field within a TEM OL lens is $B_z = 1.9 \text{ T}$ and that there are no significant deviations to that value within the accessible range, and moreover the radial field component was calculated to be less than $10^{-6} B_z$. The KE is shifted in the z -direction, in order to make the azimuthal dynamics visible as angular deviations of the cut-in-half EVBs, as described in Section 5.2.3. This

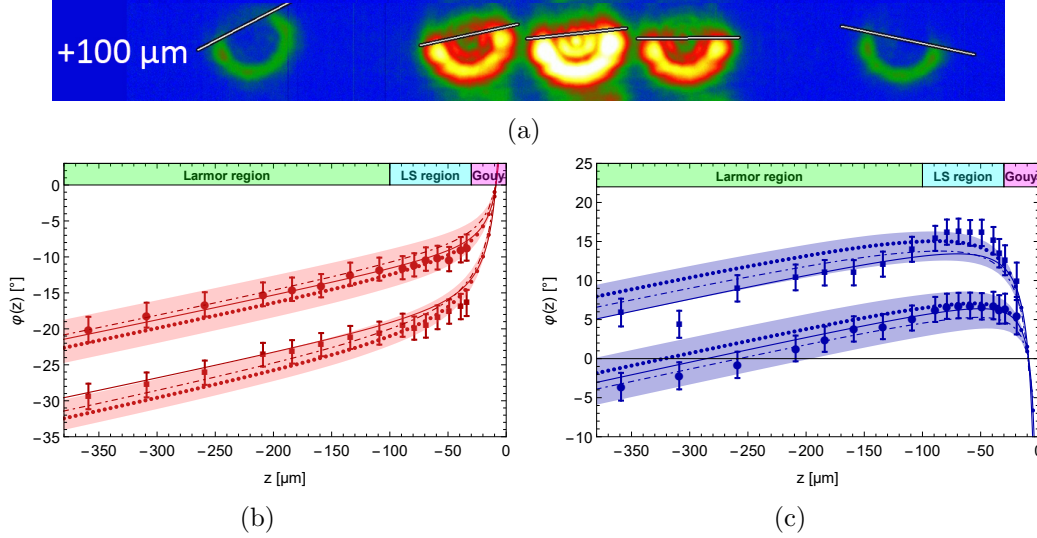


Figure 5.23: (a) Experimental image of cut EVBs with a diameter of 20 nm of a single z -shift value. The non-overlapping vortex orders $|m| = 0, 1, 3$ are visible. The measured azimuthal rotation angle is indicated as a faint solid line. (b+c) Experimental data (large dots with error bars, $|m| = 1$, squares $|m| = 3$, (b) red, $m > 0$, and (c) blue, $m < 0$), showing the azimuthal rotation angle $\varphi(z)$ of cut EVBs over the z -shift value for an experiment scanning the LR- and LS-region. Equation 5.17 was used to calculate the small dots, using moments from the numerical simulation. For the solid lines, moments from the DLG modes (Equation 2.22) were taken, using $z_R = 1.46 \mu\text{m}$ for $|m| = 1$ and $z_R = 2.84 \mu\text{m}$ for $|m| = 3$. The dot-dashed lines show the influence of symmetric OAM-impurities being applied to the pure numerical simulated vortices, using Equation 5.20, whereas the shaded areas indicate solely asymmetric OAM-impurity-contributions. The error bars include the estimated reading error, knife-edge roughness and stage-positioning-error.

leads to a miniscule, but still detectable vortex rotation of 3.3° per $100 \mu\text{m}$ z -shift of the KE. The defocus of the EVBs is used to increase the angular resolution and to reduce the beam dose on the CCD. Further details on the experimental setup are given in [32]. Figure 5.23 (a) shows an experimental image of the cut EVBs for one z -shift value out of a whole measurement series, including $|m| = 0, 1, 3$ EVB orders. The angles between, e.g., a horizontal line and the faint solid lines represent the measured azimuthal angles $\varphi(z)$ for a z -shift value of the KE of $100 \mu\text{m}$. Note that, for better angular determination the image contrast was enhanced by colour-coding and gamma-correction. For a detailed description of the angle determination see [119].

Figure 5.23 shows the measured azimuthal angles for positive vortex orders (b)

Table 5.3: Rotational frequencies in units of Ω for the numerical calculation, the diffracting LG approximation (Equation 5.12) and the experimental data. The errors indicated for the theory values represent standard deviations over the selected z -range, whereas the error for the experimental data gives the standard error of the mean weighted with the estimated experimental errors.

Mode	Origin	LR-region	LS-region	Mode	LR-region	LS-region
m = -3	DLG	0.85(12)	-0.38(87)	m = +3	1.15(12)	2.38(87)
	Numerical	0.73(20)	-1.05(116)		1.27(20)	3.05(116)
	Experimental	0.64(16)	0.18(21)		1.30(17)	2.02(21)
m = -1	DLG	0.89(8)	0.03(61)	m = +1	1.11(8)	1.97(61)
	Numerical	0.89(9)	0.04(60)		1.11(9)	1.96(60)
	Experimental	0.99(14)	0.15(29)		1.25(14)	1.85(27)

and negative vortex orders (c) for the LR- and LS-regions, and compares them to the numerical simulated values, as well as to the analytical model: Equation 5.18. To be able to resolve the salient LS-features, a finer z -scanning was used where the vortex size approaches the LS-size. The measured azimuthal angles agree with the theoretical predictions. They indeed show LR, independent of the EVB's OAM, for beam-radii significantly larger than w_B . Moreover, when the beam size approaches the LS-size, LR smoothly turns into quantized LS-rotational behaviour with no-rotation for negative OAM and cyclotron-rotation for positive OAM. By further decreasing the EVB's size, well below w_B , the angular frequency is strongly enhanced, indicating that *Gouy*-rotation is observed. In Figure 5.23 (b) and (c), OAM-admixtures were added, according to findings in [47], indicated by the shaded areas. For detailed values see [32].

Table 5.3 compares rotational frequencies in units of Ω , averaged over the LR-region and the LS-region, stemming from multiple experiments for the vortex orders $|m| = 1, 3$ with the numerical simulation and the diffracting LG model, Equation 5.12. It shows the remarkable agreement between the experimentally gained rotational frequencies and the theoretically expected ones, and renders, thus, further evidence, that EVBs in magnetic fields exhibit peculiar rotations. Note that, due to the averaging over extended z -shift regions and the smooth transition between different rotational regimes, the rotational frequency of EVBs slightly increases or decreases compared to the LR in the LR-region and to the zero- and cyclotron-rotation in the LS-region, respectively.

In principle, the error-estimates are calculated as a combination of three effects: the stage-positioning-error, the surface-roughness of the used KE, to block half of the incoming EVBs, which is very crucial and should lie below $R_z < 1$ nm, and the reading error, stemming from the azimuthal cutting-angle-determination. Altogether, the estimated error of the azimuthal angle-determination-techniques used, is of the

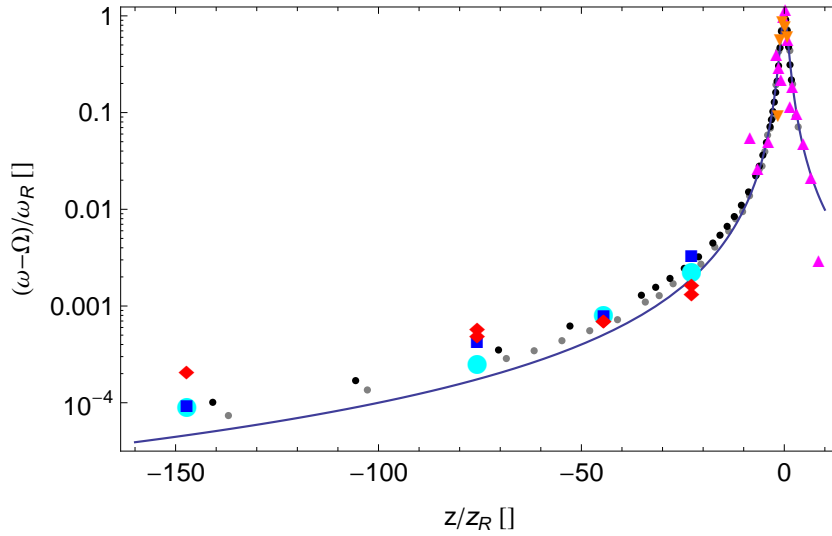


Figure 5.24: Comparison of various experimental results with theory and numerical simulations by using the universal function Equation 5.16, covering four orders of magnitude. The curve represents DLG modes, Equation 5.12, with the large cyan dots representing their averages in the LR- and LS-regions. The small gray and black dots mark the numerical simulation for $m = 1, 3$, respectively, with the blue squares indicating their averages in the respective regions. Red diamonds stand for the experimental values for $|m| = 1, 3$, averaged over the same ranges, whereas the triangles show experimental values for the *Gouy*-region. Magenta-up triangle values were measured by the author, and the orange down-triangles were taken from [323].

order of $\pm 2^\circ$. For more detail on the error-estimation, given in Figure 5.23 and Tab. 5.3, see [32, 119].

The rotation-dynamics included in Equation 5.11 represent the main finding. With the universal-form-Equation 5.16 it is possible to summarize experimental data, including the *Gouy*-region-data, the numerical simulation and the diffracting LG model, Equation 5.12, see Figure 5.24. The logarithmic scale of Figure 5.24 covers four orders of magnitude of the dimensionless rotation-dynamics. Evidently, the numerical simulations, based on the moments of the defocused vortices, follow the universal curve (valid for LG modes) up to $\zeta \sim 10$ quite well. For higher z -values, the $m = 1$ simulation shows somewhat higher values than the *Lorentz*-curve, while the simulation for the $m = 3$ lies above the $m = 2$ mode values. For the *Gouy*-region, Figure 5.24 includes experimental values acquired by the author, as well as values taken from [323], in order to demonstrate the capability of Equation 5.16 to summarize experiments, which were taken under different experimental conditions, e.g., voltage and convergence angle. The experimental results in the entire range, covering *Larmor*-, *Landau*-

5 *Recent Applications and Progress*

and *Gouy*-behaviour, can be well reproduced by both: the numerical simulations and the analytical approach using DLG modes. Considering the experimental difficulties in the determination of faint variations in the azimuthal rotation angles and the fact, that these rotation frequencies cover four orders of magnitude, this is a remarkable result.

6 Conclusions and Outlook

In the course of this thesis it was tried to gain knowledge about- and control over the full chain of measures needed to produce and apply electron vortex beams in electron microscopy. This included the deposition of thin metal films and their structuring in the focused-ion-beam (FIB) instrument, as well as the utilization of holographic devices for the detection of the complex rotational behaviour of electron vortices in magnetic fields and their application in vortex filter energy-loss magnetic chiral dichroism (EMCD) experiments.

It was shown that the material choice and thin film deposition parameters can significantly influence the FIB milling result of holographic devices, especially when large-scale structures with fine grating periodicities are desired. E.g.: under use of the highest density, high-modulus materials Iridium and Osmium showed less grating deteriorations/collapses than the traditionally used material Platinum. By optimizing the sputter deposition parameters – including the improvement of the sputter system’s vacuum system – it was possible to massively reduce the electron transmission of the thin films needed for the production of binary amplitude holographic vortex masks. However, this optimized thin film density came at the expense of high compressive inner tensions. A practicable route to reduce these inner tensions was laid out by finding the critical working gas pressure of Osmium for the system at hand. Additionally, a correlation between the degree of grating bar collapse and compressive inner tensions was found and hints at *Van-der-Waals* forces being involved. These findings enabled the production of holographic structures with a minimal need for supporting bars.

The realization of a sputter coater bake-out- and cooling-system helped to produce high quality low-stress carbon thin films, that were used as prospective layers for the heavy metal membranes. Future applications of that system, that also comprises a newly constructed heating- and cooling-stage, will include the production of new epitaxially grown magnetic test samples.

When it comes to FIB milling of the holographic structures, it was shown that advanced milling strategies, like spiral vector-scanning and spatial dwell time modifications have no significant influence on the vortex mask’s structure-fidelity. In fact, more basal parameters, like the ion-beam-current and the plain pixel density, determine the quality of the milled structure. Introducing modifications to the FIB instrument, like a custom drift correction script and a newly designed high-stability sample holder combined with the optimized heavy metal membranes, impressively improved the FIB machine’s milling capabilities, such that now large-scale high-fidelity vortex holograms can be produced.

As an outlook, these holographic devices will be used to further boost the signal-

6 Conclusions and Outlook

to-noise ratio of vortex filter EMCD measurements and to extend their application to multi-point-measurements. Also, it may be possible to use the drift correction routine as an online monitoring system, already detecting the onset of grating collapses during milling and instantaneously adapting the milling strategy in order to avoid further grating damage. This could enable the production of nearly support-less large-scale binary vortex masks.

Recently, an international research group successfully used binary amplitude masks – that were fabricated using optimization routines presented herein – for the production of electron vortex beams in the scanning electron microscope. This may open up the field of electron beam shaping and singular electron wavefronts to a much broader community.

An important question, that naturally arises with the inception of new phenomena, like electron vortex beams, is: ‘What can they be used for?’.

In this work two examples of novel applications are given.

The first application deals with detecting an EMCD signal when incorporating a holographic vortex mask as a vortex filter in a post-specimen geometry. Two essentially very similar experimental setups, where the vortex filter is either placed in the diffraction plane or in the selected area aperture holder of a field-emission transmission electron microscope (TEM), were presented. In the selected area aperture plane vortex filter setup the sample is lifted far above the eucentric height, such that the vortex filter mask in the selected area aperture plane can be properly illuminated and produces well-separated vortex orders, which carry the dichroic information in the asymmetry of their respective central intensities. In the diffraction plane vortex filter setup only minor adaptations are necessary, relative to a typical scanning-transmission electron microscopy geometry. But placing a vortex filter hologram in the diffraction plane is a non-trivial task, whereas replacing apertures in the selected area aperture holder is a standard procedure. First preparational steps were taken, to place vortex filters to TEMs with a standard gap pole-piece under minimal modifications. Also, artefact sources like vortex mask tilt and astigmatism were identified and routes towards their reduction were suggested and implemented. Notably, by using an external orbital angular momentum filter in the form of a holographic vortex mask, crystalline samples can be measured in zone axis, while a tedious alignment of the sample – as needed in classical EMCD – is unnecessary.

Experiments on two different machines and different samples show difference signals that fit well to inelastic multi-slice simulations with a high signal-to-noise ratio, when astigmatism and defocus are well-controlled. The observed difference signals in the wide-gap pole-piece TEM using the diffraction plane vortex filter are of the order of 3.5% and, thus, comparable to the signal-strength in classical EMCD measurements on the same material and with comparable resolution. For the measurements on a standard pole-piece TEM, with the vortex filtering mask placed in the selected area aperture holder, a signal strength of $\sim 7\%$ was observed. Experiments with a reversed objective lens magnetic field (antiparallel magnetisation), with two dif-

ferent vortex filter masks showed a consistent positive central difference signal for the L₃-edge, whereas measurements under a normal oriented magnetic field (parallel magnetisation) showed a negative difference signal. Also, signal reversals between the L₃- and L₂-edges could be observed, backing the evidence for the measurement of a real EMCD signal.

Nevertheless, the recording times are still of the order of tens of seconds and instrument- and sample-stability play a major role, such that further improvements of the collection-efficiency (via high diffraction efficiency large-scale vortex masks), as well as measures for the reduction of drift and electron-detection-noise are crucial. With the advent of direct detection cameras, an improvement of the signal-to-noise ratio by a factor of two to three can be expected.

More particularly, as the spot size in the (single-spot) experiments in *Vienna* was roughly 1 nm and even 0.8 nm in the measurements in *Jülich*, sub-nanometre resolution was already achieved in this proof-of-principle experiments. For the classical EMCD method it took two years to reach 1.7 nm resolution from the first proof-of-principle measurements on and further eight years to reach a spatial resolution of 1 nm. Atomic plane resolution in classical EMCD measurements could recently be reached.

Interestingly, inelastic multi-slice simulations, carried out in the course of this work, suggest, that atomic resolution should be feasible with the vortex filter approach, when chromatic-aberration-corrected instruments are employed.

The vortex filtering technique is also a promising method for studying magnetic properties of amorphous materials, without the need for the crystal acting as a beam splitter, as it is in the classical EMCD setup. But so far the aforementioned limitations have to be tackled first. Excessive beam broadening in amorphous materials, that leads to a strong reduction of the EMCD signal, could possibly be reduced by employing non-diffracting *Bessel* beams instead of *Gaussian* ones.

Despite its current limitations, post-specimen vorticity filtering offers considerable possibilities for new, technologically important EMCD applications, and thus encourages future work in this exciting field. This new approach may be used for the exploration of interface magnetism or the study of peculiarities of the giant magneto-resistance in thin film stacks. Atomic resolution magnetic characterisation may pave the way for the development of magnetic memory technologies with bit-densities, orders of magnitude higher than traditional hard-disk-drives.

The second example deals with the application of electron vortices to study their fundamental properties. Peculiar rotation-dynamics were observed and could be interpreted as a combination of slow-*Larmor* and fast *Gouy*-rotations. Standard *Larmor*-rotation is found for large vortex radii, far from the focus, whereas rapid *Gouy*-rotation appears close to the focus of electron vortex beams. It was experimentally demonstrated that freely floating *Landau*-states appear in the intermediate regime. A quantum approach reconciles the three different regimes of rotational behaviour of electron vortices in a magnetic field. Using a universal *Lorentz*-function the rotational dynamics of electron vortex beams, acquired under different experimental conditions

6 Conclusions and Outlook

and covering four orders of magnitude, could be summarized and explained.

This could possibly be used to study Faraday-rotation of electron vortex beams in magnetic materials and by that access their longitudinal magnetic fields, complementary to *Lorentz*-microscopy. A well-established application, using the *Larmor*-rotations of electrons in the objective lens field, is the measurement of its magnetic field strength without a Hall sensor. Due to resonance effects, mapping of *Landau*-states in the solid could become possible by using a probe beam, which is shaped to resemble a free-electron *Landau*-state.

Abbreviations

- Si₃N₄** stoichiometric silicon nitride. 102
- SiN_x** non-stoichiometric silicon nitride. 18, 21, 37, 53, 54, 57, 61, 74, 109, 110, 120, 134–139, 147, 152–154, 156–164, 195, 199, 202
- AC** alternating current. 84, 99
- ADC** analog-to-digital converter. 88, 100, 103
- AV** acceleration voltage. 29, 35, 135, 138, 142, 160, 162, 173, 187, 188, 195, 197
- BFP** back-focal-plane. 31, 169, 172, 187
- BMP** bitmap. 117, 119–124, 138
- CBED** convergent beam electron diffraction. 29, 31
- CCD** charge-coupled-device. 26, 32, 33, 36, 68, 81, 105, 145, 162, 195–197, 213
- CEITEC** Central European Institute of Technology, Brno,. 118, 125, 138, 198
- CMOS** complementary metal-oxide-semiconductor. 32, 33
- DAC** digital-to-analog converter. 101, 103, 118, 160
- DC** direct current. 68, 84, 99, 132, 137
- DCR** drift correction routine. 112–115
- DE** diffraction efficiency. 15, 55, 56, 132, 133, 160, 162, 163, 202, 204
- DFF** dynamic form factor. 42
- DLG** diffracting *Laguerre-Gaussian*. 11, 47–51, 207–210, 213, 215, 216
- DM** Gatan Digital Micrograph. 119, 196, 197, 199
- DOS** density of states. 40, 41
- DP** diffraction plane. 14, 168–173, 175, 202–204
- DPC** differential phase contrast. 26, 32, 39

Abbreviations

- EBID** electron beam-induced deposition. 125, 126, 129, 131
- EDP** energy dispersive plane. 36
- EDT** edge-dwell-time. 13, 15, 126, 128–131
- EDX** energy dispersive x-ray spectrometry. 35, 78, 140–143, 156
- EELS** electron energy loss spectrometry. 11, 22, 33, 35, 37, 38, 43, 55, 56, 172, 175, 181, 197
- EFTEM** energy-filtered transmission electron microscopy. 33, 36, 38, 172, 187, 188, 190, 195, 199, 202, 204
- ELNES** energy-loss near edge structure. 38, 39
- EM** electron microscopy. 24, 26, 45, 52, 61, 70, 164
- EMCD** electron energy-loss magnetic chiral dichroism. 11, 13–15, 17, 19, 21, 22, 31, 39–41, 43, 55, 59, 87, 117, 121, 160, 162, 163, 166, 167, 169–171, 173, 175–178, 181, 182, 184, 185, 187–204, 218, 219
- ER-C** Ernst Ruska-Centre for Microscopy and Spectroscopy with Electrons. 168, 169, 185, 189, 198, 202, 204
- EVB** electron vortex beam. 11, 13, 14, 17–22, 45, 46, 51, 52, 54, 56–58, 117, 125, 156, 157, 167, 168, 176, 178–180, 184, 185, 189, 192, 195, 199–201, 203, 206–214
- FEG** field-assisted thermionic emitters. 11, 26, 27, 29, 30, 54, 143, 193, 198
- FFP** front-focal-plane. 172
- FFT** fast *Fourier* transform. 185, 187, 211
- FIB** focused-ion-beam machine. 12, 13, 21, 53–55, 57, 58, 65–68, 70, 74, 78, 102, 107–113, 117–121, 125, 126, 129, 132, 134–139, 147, 152–154, 157, 158, 160, 162–164, 166, 185, 195, 198, 199, 217
- FPM** fluoro-elastomer materials. 76, 92, 94, 96, 102
- FT** Fourier transform. 59, 63, 64
- FTM** film thickness monitor. 70, 78–80, 135
- FWHM** full-width at half maximum. 27, 35, 37, 67, 172, 176, 181, 190, 191, 195, 198, 202
- FWTM** full-width at tenth maximum. 37, 197
- GIF** *Gatan Imaging Filter*. 193, 195–197, 202

- GUI** graphical user interface. 100, 101, 103
- HAADF** high-angular annular dark field. 32
- HM** holographic mask. 17, 18, 22
- HRSTEM** high-resolution scanning transmission electron microscopy. 58
- HRTEM** high-resolution transmission electron microscopy. 32, 44, 57, 64, 200, 201, 203
- HVM** holographic vortex mask. 11–15, 18, 19, 21, 22, 27, 52, 53, 55, 56, 59, 60, 67, 68, 78, 82, 87, 98, 102, 109, 110, 117, 119–123, 125, 127, 131–133, 135–139, 147, 152–154, 156–164, 167–171, 173–176, 178, 183–186, 195, 197–204, 211, 212
- IFP** Institute of Solid State Physics, TU Wien,. 202
- IFW-Dresden** Leibnitz Institute for Solid State and Materials Research Dresden. 111, 117, 118, 120, 122, 126, 154, 156, 193, 199
- IMS** inelastic scattering multi-slice simulation. 14, 187–191, 198–201, 203–205
- ISI-CAS** Institute of Scientific Instrumentation at the Czech Academy of Science. 109, 136, 137
- ISSB** incoherent source size broadening. 14, 15, 190–194, 200, 201, 203
- KE** knife-edge. 199, 210–214
- LG** *Laguerre-Gaussian*. 14, 15, 206, 209, 210, 214, 215
- LMIS** liquid metal ion source. 67
- LR** Larmor-rotation. 207, 208, 211, 213–215
- LS** *Landau-states*. 19, 44, 206, 208, 213–215
- MC** *Monte-Carlo*. 89, 111, 140
- MDFF** mixed dynamic form factor. 42, 64
- MFP** mean free path. 38
- MS** multi-slice. 11, 14, 61, 64, 167
- NLLS** non-linear least squares. 197

Abbreviations

- OAM** orbital angular momentum. 14, 18–21, 39, 41, 46, 47, 50, 51, 56–61, 117, 125, 162, 163, 168–170, 172, 173, 175, 177–180, 184, 185, 189, 195, 199, 206–209, 211–214
- OL** objective lens. 29–31, 156, 164, 167, 169, 195, 199–201, 204, 212
- OVB** optical vortex beam. 45, 46, 51
- PVD** physical vapour deposition. 68, 140
- ROI** region of interest. 196
- RPI** *Raspberry Pi*. 100, 101, 103
- SAA** selected area aperture. 14, 167–172, 195, 198–201
- SAD** selected area diffraction. 31, 168, 185
- SAM** spin angular momentum. 46
- SC** sputter coater. 88
- SCTM** sputter coater thermal management. 98, 103, 104, 158, 160, 164
- SDD** silicon drift detector. 143
- SE** secondary electrons. 67, 68
- SEA** spectrometer entrance aperture. 35, 36, 42, 43
- SEM** scanning electron microscope. 15, 20, 21, 32, 65, 68, 78, 107–110, 122, 126, 131, 135, 138, 143, 147, 155, 158, 212
- SIM** scanning ion microscope. 13, 68, 108, 109, 112, 153, 154, 157, 158, 160, 162
- SNR** signal-to-noise ratio. 21, 22, 29, 117, 181, 192, 193, 195–199, 201–203
- SQUID** superconducting quantum interference device. 39
- STD** standard deviation of the mean. 86, 128, 196, 199
- STEM** scanning-transmission electron microscope. 19, 27, 29, 30, 32, 33, 39, 44, 55, 56, 61, 65, 66, 169, 190, 193, 204
- SWD** sputter working distance. 69, 135, 141, 142, 150
- TEM** transmission electron microscope. 11–14, 17–22, 24–35, 37, 39, 41, 43–45, 51–54, 56, 58, 59, 61, 62, 65, 78, 109, 110, 117, 156–158, 161–169, 171, 172, 181, 184, 193, 198, 200, 201, 203, 206–208, 211, 212, 218

TMP turbo molecular pump. 12, 69, 75, 76, 89–92, 94, 95, 97, 98, 100

USTEM University Service Centre for Transmission Electron Microscopy. 65, 68, 73, 107, 111

VdW *Van-der-Waals*. 147–149, 158

WD working distance. 12, 70, 107–110, 112

XMCD X-ray magnetic chiral dichroism. 17, 39, 41

ZA zone axis. 178

Bibliography

- [1] S. Beckwith and The Hubble Heritage Team. By NASA, ESA, s. beckwith (STScI), and the hubble heritage team (STScI/AURA) [CC BY 3.0 (<http://creativecommons.org/licenses/by/3.0>)], via wikimedia commons. online, 2005. URL <https://commons.wikimedia.org/wiki/File%3AMessier51.jpg>.
- [2] NASA. Wake vortex study at wallops island. Online, 1990. URL <http://lisar.larc.nasa.gov/UTILS/info.cgi?id=EL-1996-00130>.
- [3] Konstantin Yu. Bliokh, Yury P. Bliokh, Sergey Savel'ev, and Franco Nori. Semi-classical dynamics of electron wave packet states with phase vortices. *Physical Review Letters*, 99:190404, Nov 2007. DOI: 10.1103/PhysRevLett.99.190404. URL <http://link.aps.org/doi/10.1103/PhysRevLett.99.190404>.
- [4] M. Uchida and A. Tonomura. Generation of electron beams carrying orbital angular momentum. *Nature*, 464:737–739, 2010. DOI: 10.1038/nature08904.
- [5] J. Verbeeck, H. Tian, and P. Schattschneider. Production and application of electron vortex beams. *Nature*, 467(7313):301–304, 2010. DOI: 10.1038/nature09366.
- [6] P. Schattschneider, S. Rubino, C. Hébert, J. Ruzs, J. Kuneš, P. Novák, E. Carlino, M. Fabrizio, G. Panaccione, and G. Rossi. Detection of magnetic circular dichroism using a transmission electron microscope. *Nature*, 441:486–488, 2006. DOI: 10.1038/nature04778.
- [7] G. Schütz, W. Wagner, W. Wilhelm, P. Kienle, R. Zeller, R. Frahm, and G. Materlik. Absorption of circularly polarized X-rays in iron. *Physical Review Letters*, 58(7):737–740, 1987. DOI: 10.1103/PhysRevLett.58.737.
- [8] M.R. Fitzsimmons, S.D. Bader, J.A. Borchers, G.P. Felcher, J.K. Furdyna, A. Hoffmann, J.B. Kortright, Ivan K. Schuller, T.C. Schulthess, S.K. Sinha, M.F. Toney, D. Weller, and S. Wolf. Neutron scattering studies of nanomagnetism and artificially structured materials. *Journal of Magnetism and Magnetic Materials*, 271(1):103 – 146, 2004. ISSN 0304-8853. DOI: <https://doi.org/10.1016/j.jmmm.2003.09.046>. URL <http://www.sciencedirect.com/science/article/pii/S030488530300742X>.
- [9] Z. Q. Qiu and S. D. Bader. Surface magneto-optic Kerr effect. *Review of Scientific Instruments*, 71(3):1243–1255, 2000. DOI: 10.1063/1.1150496. URL <http://dx.doi.org/10.1063/1.1150496>.

Bibliography

- [10] J. Verbeeck, C. Hébert, S. Rubino, P. Novák, J. Rusz, F. Houdellier, C. Gatel, and P. Schattschneider. Optimal aperture sizes and positions for EMCD experiments. *Ultramicroscopy*, 108(9):865–872, 2008. DOI: 10.1016/j.ultramic.2008.02.007.
- [11] Warot-Fonrose B., Gatel C., Calmels L., Serin V., Snoeck E., and Cherifi S. Magnetic properties of FeCo alloys measured by energy-loss magnetic chiral dichroism. *Journal of Applied Physics*, 107(9):09D301, 2010. DOI: 10.1063/1.3358217.
- [12] Z.Q. Wang, X.Y. Zhong, R. Yu, Z.Y. Cheng, and Zhu J. Quantitative experimental determination of site-specific magnetic structures by transmitted electrons. *Nature Communications*, 4:1395, 2013. DOI: 10.1038/ncomms2323.
- [13] Shunsuke Muto, Ján Rusz, Kazuyoshi Tatsumi, Roman Adam, Shigeo Arai, Vancho Kocevski, Peter M. Oppeneer, Daniel E. Bürgler, and Claus M. Schneider. Quantitative characterization of nanoscale polycrystalline magnets with electron magnetic circular dichroism. *Nature Communications*, 5:3138, 2014. DOI: 10.1038/ncomms4138.
- [14] P. Schattschneider, M. Stöger-Pollach, S. Rubino, M. Sperl, C. Hurm, J. Zweck, and J. Rusz. Detection of magnetic circular dichroism on the two-nanometer scale. *Physical Review B - Condensed Matter and Materials Physics*, 78(10):104413, 2008. DOI: 10.1103/PhysRevB.78.104413.
- [15] Juan Salafranca, Jaume Gazquez, Nicols Pérez, Amilcar Labarta, Sokrates T. Pantelides, Stephen J. Pennycook, Xavier Batlle, and Maria Varela. Surfactant organic molecules restore magnetism in metal-oxide nanoparticle surfaces. *Nano Letters*, 12(5):2499–2503, 2012. DOI: 10.1021/nl300665z. URL <http://dx.doi.org/10.1021/nl300665z>. PMID: 22497711.
- [16] P. Schattschneider, B. Schaffer, I. Ennen, and J. Verbeeck. Mapping spin-polarized transitions with atomic resolution. *Physical Review B*, 85:134422, 2012. DOI: 10.1103/PhysRevB.85.134422.
- [17] I. Ennen, S. Löffler, C. Kübel, D. Wang, A. Auge, A. Hütten, and P. Schattschneider. Site-specific chirality in magnetic transitions. *Journal of Magnetism and Magnetic Materials*, 324(18):2723 – 2726, 2012. ISSN 0304-8853. DOI: 10.1016/j.jmmm.2012.03.050. URL <http://www.sciencedirect.com/science/article/pii/S0304885312003058>.
- [18] L. Allen, Stephen M. Barnett, and Miles J. Padgett. *Optical Angular Momentum*. Number ISBN 9780750309011. Institute of Physics Publishing, 2003.
- [19] J. F. Nye and M. V. Berry. Dislocations in wave trains. *Proceedings of the Royal Society of London A: Mathematical, Physical and Engineering Sciences*, 336(1605):165–190, 1974. ISSN 0080-4630. DOI: 10.1098/rspa.1974.0012. URL <http://rspa.royalsocietypublishing.org/content/336/1605/165>.

- [20] V.Y. Bazhenov, M.V. Vasnetsov, and M.S. Soskin. Laser beams with screw dislocations in their wavefronts. *JETP Letters*, 52(8):429–431, 1990. URL http://www.jetpletters.ac.ru/ps/1159/article_17529.pdf.
- [21] L. Allen, M. W. Beijersbergen, R. J. C. Spreeuw, and J. P. Woerdman. Orbital angular momentum of light and the transformation of Laguerre-Gaussian laser modes. *Phys. Rev. A*, 45:8185–8189, Jun 1992. DOI: 10.1103/PhysRevA.45.8185. URL <http://link.aps.org/doi/10.1103/PhysRevA.45.8185>.
- [22] Charles W. Clark, Roman Barankov, Michael G. Huber, Muhammad Arif, David G. Cory, and Dmitry A. Pushin. Controlling neutron orbital angular momentum. *Nature*, 525:504–506, 2015. DOI: 10.1038/nature15265.
- [23] Roy Shiloh, Yossi Lereah, Yigal Lilach, and Ady Arie. Sculpturing the electron wave function using nanoscale phase masks. *Ultramicroscopy*, 144:26 – 31, 2014. ISSN 0304-3991. DOI: 10.1016/j.ultramic.2014.04.007. URL <http://www.sciencedirect.com/science/article/pii/S0304399114000801>.
- [24] Vincenzo Grillo, Gian Carlo Gazzadi, Ebrahim Karimi, Erfan Mafakheri, Robert W. Boyd, and Stefano Frabboni. Highly efficient electron vortex beams generated by nanofabricated phase holograms. *Applied Physics Letters*, 104:043109, 2014. DOI: 10.1063/1.4863564. URL <http://dx.doi.org/10.1063/1.4863564>.
- [25] Tyler R. Harvey, Jordan S. Pierce, Amit K. Agrawal, Peter Ercius, Martin Linck, and Benjamin J. McMorran. Efficient diffractive phase optics for electrons. *New Journal of Physics*, 16:093039, 2014. DOI: 10.1088/1367-2630/16/9/093039.
- [26] Giulio Guzzinati, Armand Béch e, Hugo Lourenço-Martins, J er ome Martin, Mathieu Kociak, and Jo Verbeeck. Probing the symmetry of the potential of localized surface plasmon resonances with phase-shaped electron beams. *Nature Communications*, 8(14999), 2017. DOI: 10.1038/ncomms14999.
- [27] L. Clark, G. Guzzinati, A. B ech e, A. Lubk, and J. Verbeeck. Symmetry-constrained electron vortex propagation. *Phys. Rev. A*, 93:063840, Jun 2016. DOI: 10.1103/PhysRevA.93.063840. URL <http://link.aps.org/doi/10.1103/PhysRevA.93.063840>.
- [28] Roy Shiloh, Roei Remez, and Ady Arie. Prospects for electron beam aberration correction using sculpted phase masks. *Ultramicroscopy*, 163:69 – 74, 2016. ISSN 0304-3991. DOI: <http://dx.doi.org/10.1016/j.ultramic.2016.02.002>. URL <http://www.sciencedirect.com/science/article/pii/S0304399116300092>.

Bibliography

- [29] A. Ashkin, J. M. Dziedzic, J. E. Bjorkholm, and Steven Chu. Observation of a single-beam gradient force optical trap for dielectric particles. *Opt. Lett.*, 11(5):288–290, May 1986. DOI: 10.1364/OL.11.000288. URL <http://ol.osa.org/abstract.cfm?URI=ol-11-5-288>.
- [30] Jo Verbeeck, He Tian, and Gustaaf Van Tendeloo. How to manipulate nanoparticles with an electron beam? *Advanced Materials*, 25(8):1114–1117, 2013. ISSN 1521-4095. DOI: 10.1002/adma.201204206. URL <http://dx.doi.org/10.1002/adma.201204206>.
- [31] Roeland Juchtmans and Jo Verbeeck. Orbital angular momentum in electron diffraction and its use to determine chiral crystal symmetries. *Physical Review B*, 92:134108, Oct 2015. DOI: 10.1103/PhysRevB.92.134108. URL <http://link.aps.org/doi/10.1103/PhysRevB.92.134108>.
- [32] T. Schachinger, S. Löffler, M. Stöger-Pollach, and P. Schattschneider. Peculiar rotation of electron vortex beams. *Ultramicroscopy*, 158:17 – 25, 2015. ISSN 0304-3991. DOI: 10.1016/j.ultramic.2015.06.004.
- [33] W. Glaser. *Grundlagen der Elektronenoptik*. Springer-Verlag Wien, 1952.
- [34] P. Schattschneider, T. Schachinger, M. Stöger-Pollach, S. Löffler, A. Steiger-Thirsfeld, K.Y. Bliokh, and F. Nori. Imaging the dynamics of free-electron landau states. *Nature Communications*, 5:4586, 2014. DOI: 10.1038/ncomms5586.
- [35] Ján Rusz and Somnath Bhowmick. Boundaries for efficient use of electron vortex beams to measure magnetic properties. *Physical Review Letters*, 111:105504, Sep 2013. DOI: 10.1103/PhysRevLett.111.105504. URL <http://link.aps.org/doi/10.1103/PhysRevLett.111.105504>.
- [36] P. Schattschneider, S. Löffler, M. Stöger-Pollach, and Verbeeck. Is magnetic chiral dichroism feasible with electron vortices? *Ultramicroscopy*, 136:81 – 85, 2014. ISSN 0304-3991. DOI: <http://dx.doi.org/10.1016/j.ultramic.2013.07.012>. URL <http://www.sciencedirect.com/science/article/pii/S0304399113001988>.
- [37] P. Schattschneider, M. Stöger-Pollach, and J. Verbeeck. Novel vortex generator and mode converter for electron beams. *Phys. Rev. Lett.*, 109:084801, Aug 2012. DOI: 10.1103/PhysRevLett.109.084801. URL <http://link.aps.org/doi/10.1103/PhysRevLett.109.084801>.
- [38] D. Pohl, S. Schneider, J. Rusz, and B. Rellinghaus. Electron vortex beams prepared by a spiral aperture with the goal to measure EMCD on ferromagnetic films via STEM. *Ultramicroscopy*, 150:16–22, 2015. DOI: 10.1016/j.ultramic.2014.11.025.

- [39] A. Béch e, R. Juchtmans, and J. Verbeeck. Efficient creation of electron vortex beams for high resolution STEM imaging. *Ultramicroscopy*, pages 12–19, 2016. ISSN 0304-3991. DOI: 10.1016/j.ultramic.2016.05.006. URL <http://www.sciencedirect.com/science/article/pii/S0304399116300584>.
- [40] Darius Pohl, Sebastian Schneider, Paul Zeiger, J an Ruzs, Peter Tiemeijer, Sorin Lazar, Kornelius Nielsch, and Bernd Rellinghaus. Atom size electron vortex beams with selectable orbital angular momentum. *Scientific Reports*, 7(934), 2017. DOI: 10.1038/s41598-017-01077-9.
- [41] J. Ruzs, J. C. Idrobo, and S. Bhowmick. Achieving atomic resolution magnetic dichroism by controlling the phase symmetry of an electron probe. *Physical Review Letters*, 113(14), 2014. DOI: 10.1103/PhysRevLett.113.145501.
- [42] Juan Carlos Idrobo, J an Ruzs, Jakob Spiegelberg, Michael A. McGuire, Christopher T. Symons, Ranga Raju Vatsavai, Claudia Cantoni, and Andrew R. Lupini. Detecting magnetic ordering with atomic size electron probes. *Advanced Structural and Chemical Imaging*, 2(1):5, 2016. ISSN 2198-0926. DOI: 10.1186/s40679-016-0019-9. URL <http://dx.doi.org/10.1186/s40679-016-0019-9>.
- [43] J an Ruzs and Juan Carlos Idrobo. Aberrated electron probes for magnetic spectroscopy with atomic resolution: Theory and practical aspects. *Phys. Rev. B*, 93:104420, Mar 2016. DOI: 10.1103/PhysRevB.93.104420. URL <http://link.aps.org/doi/10.1103/PhysRevB.93.104420>.
- [44] Robert Fickler, Radek Lapkiewicz, William N. Plick, Mario Krenn, Christoph Schaeff, Sven Ramelow, and Anton Zeilinger. Quantum entanglement of high angular momenta. *Science*, 338(6107):640–643, 2012. ISSN 0036-8075. DOI: 10.1126/science.1227193.
- [45] Giulio Guzzinati, Laura Clark, Armand B ech e, and Jo Verbeeck. Measuring the orbital angular momentum of electron beams. *Physical Review A*, 89:025803, Feb 2014. DOI: 10.1103/PhysRevA.89.025803. URL <http://link.aps.org/doi/10.1103/PhysRevA.89.025803>.
- [46] Brijesh Kumar Singh, Roei Remez, Yuval Tsur, and Ady Arie. Measurement of acceleration and orbital angular momentum of Airy beam and Airy-vortex beam by astigmatic transformation. *Opt. Lett.*, 40(22):5411–5414, Nov 2015. DOI: 10.1364/OL.40.005411. URL <http://ol.osa.org/abstract.cfm?URI=ol-40-22-5411>.
- [47] L. Clark, A. B ech e, G. Guzzinati, and J. Verbeeck. Quantitative measurement of orbital angular momentum in electron microscopy. *Physical Review A*, 89:053818, May 2014. DOI: 10.1103/PhysRevA.89.053818. URL <http://link.aps.org/doi/10.1103/PhysRevA.89.053818>.

Bibliography

- [48] Mohammad Mirhosseini, Mehul Malik, Zhimin Shi, and Robert W. Boyd. Efficient separation of the orbital angular momentum eigenstates of light. *Nature Communications*, 4(2781), 2013. DOI: 10.1038/ncomms3781.
- [49] Vincenzo Grillo, Amir H. Tavabi, Federico Venturi, Hugo Larocque, Roberto Balboni, Gian Carlo Gazzadi, Stefano Frabboni, Peng-Han Lu, Erfan Mafakheri, Frédéric Bouchard, Rafal E. Dunin-Borkowski, Robert W. Boyd, Martin P. J. Lavery, Miles J. Padgett, and Ebrahim Karimi. Measuring the orbital angular momentum spectrum of an electron beam. *Nature Communications*, 8:15536, May 2017. URL <http://dx.doi.org/10.1038/ncomms15536>.
- [50] Benjamin J McMorran, Tyler R Harvey, and Martin P J Lavery. Efficient sorting of free electron orbital angular momentum. *New Journal of Physics*, 19(2):023053, 2017. URL <http://stacks.iop.org/1367-2630/19/i=2/a=023053>.
- [51] Tyler R. Harvey, Vincenzo Grillo, and Benjamin J. McMorran. Stern-Gerlach-like approach to electron orbital angular momentum measurement. *Physical Review A*, 95:021801, Feb 2017. DOI: 10.1103/PhysRevA.95.021801. URL <http://link.aps.org/doi/10.1103/PhysRevA.95.021801>.
- [52] Hugo Larocque, Frédéric Bouchard, Vincenzo Grillo, Alicia Sit, Stefano Frabboni, Rafal E. Dunin-Borkowski, Miles J. Padgett, Robert W. Boyd, and Ebrahim Karimi. Nondestructive measurement of orbital angular momentum for an electron beam. *Phys. Rev. Lett.*, 117:154801, Oct 2016. DOI: 10.1103/PhysRevLett.117.154801. URL <http://link.aps.org/doi/10.1103/PhysRevLett.117.154801>.
- [53] Vincenzo Grillo, Ebrahim Karimi, Roberto Balboni, Gian Carlo Gazzadi, Federico Venturi, Stefano Frabboni, Jordan S Pierce, Benjamin J McMorran, and Robert W Boyd. Electron holograms encoding amplitude and phase for the generation of arbitrary wavefunctions. *Proceedings of Microscopy & Microanalysis*, 21(S3):503–504, 2015. DOI: 10.1017/S1431927615003311.
- [54] E. Mafakheri, A. H. Tavabi, P.-H. Lu, R. Balboni, F. Venturi, C. Menozzi, G. C. Gazzadi, S. Frabboni, A. Sit, R. E. Dunin-Borkowski, E. Karimi, and V. Grillo. Realization of electron vortices with large orbital angular momentum using miniature holograms fabricated by electron beam lithography. *Applied Physics Letters*, 110(9):093113, 2017. DOI: 10.1063/1.4977879. URL <http://dx.doi.org/10.1063/1.4977879>.
- [55] Shigeyuki Morishita, Masaki Mukai, Kazu Suenaga, and Hidetaka Sawada. Atomic resolution imaging at an ultralow accelerating voltage by a monochromatic transmission electron microscope. *Phys. Rev. Lett.*, 117:153004, Oct 2016. DOI: 10.1103/PhysRevLett.117.153004. URL <http://link.aps.org/doi/10.1103/PhysRevLett.117.153004>.

- [56] R.H. van Aken, D.J. Maas, C.W. Hagen, J.E. Barth, and P. Kruit. Design of an aberration corrected low-voltage SEM. *Ultramicroscopy*, 110(11):1411 – 1419, 2010. ISSN 0304-3991. DOI: <http://dx.doi.org/10.1016/j.ultramicro.2010.07.012>. URL <http://www.sciencedirect.com/science/article/pii/S0304399110002123>.
- [57] R.F. Egerton, P. Li, and M. Malac. Radiation damage in the TEM and SEM. *Micron*, 35:399–409, 2004. DOI: 10.1016/j.micron.2004.02.003.
- [58] M. Stöger-Pollach, H. Franco, P. Schattschneider, S. Lazar, B. Schaffer, W. Grogger, and H.W. Zandbergen. Čerenkov losses: A limit for bandgap determination and Kramers–Kronig analysis. *Micron*, 37(5):396 – 402, 2006. ISSN 0968-4328. DOI: <https://doi.org/10.1016/j.micron.2006.01.001>. URL <http://www.sciencedirect.com/science/article/pii/S0968432806000047>. Proceedings of the International Workshop on Enhanced Data Generated with Electrons (EDGE).
- [59] Robert Winkler, Aleksandra Szkudlarek, Jason D Fowlkes, Philip D Rack, Ivo Utke, and Harald Plank. Toward ultraflat surface morphologies during focused electron beam induced nanosynthesis: disruption origins and compensation. *ACS applied materials & interfaces*, 7(5):3289–3297, February 2015. ISSN 1944-8244. DOI: 10.1021/am508052k. URL <http://dx.doi.org/10.1021/am508052k>.
- [60] Steven I. Hajdu. The discovery of blood cells. *Annals of Clinical & Laboratory Science*, 33(2):237–238, 2003. URL <http://www.annclinlabsci.org/content/33/2/237.short>.
- [61] Robert Hooke. *Micrographia: or, Some physiological descriptions of minute bodies made by magnifying glasses*. Royal Society of London, 1665.
- [62] E. Abbe. Beiträge zur Theorie des Mikroskops und der mikroskopischen Wahrnehmung. *Archiv für mikroskopische Anatomie*, 9(1):413–418, 1873. ISSN 0176-7364. DOI: 10.1007/BF02956173. URL <http://dx.doi.org/10.1007/BF02956173>.
- [63] Stefan W. Hell and Jan Wichmann. Breaking the diffraction resolution limit by stimulated emission: stimulated-emission-depletion fluorescence microscopy. *Opt. Lett.*, 19(11):780–782, Jun 1994. DOI: 10.1364/OL.19.000780. URL <http://ol.osa.org/abstract.cfm?URI=ol-19-11-780>.
- [64] Nobelprize.org. The nobel prize in chemistry 2014. Nobelprize.org. Nobel Media AB 2014. Web. 9 Apr 2017., 2017. URL http://www.nobelprize.org/nobel_prizes/chemistry/laureates/2014/.
- [65] W. Lukosz and M. Marchand. Optischen Abbildung unter Überschreitung der Beugungsbedingten Auflösungsgrenze. *Optica Acta: International Journal of*

Bibliography

- Optics*, 10(3):241–255, 1963. DOI: 10.1080/713817795. URL <http://dx.doi.org/10.1080/713817795>.
- [66] Mats G.L. Gustafsson, Lin Shao, Peter M. Carlton, C. J. Rachel Wang, Inna N. Golubovskaya, W. Zacheus Cande, David A. Agard, and John W. Sedat. Three-dimensional resolution doubling in wide-field fluorescence microscopy by structured illumination. *Biophysical Journal*, 94(12):4957–4970, 2008. DOI: 10.1529/biophysj.107.120345. URL <http://dx.doi.org/10.1529/biophysj.107.120345>.
- [67] U. Dürig, D. W. Pohl, and F. Rohner. Near-field optical-scanning microscopy. *Journal of Applied Physics*, 59(10):3318–3327, 1986. DOI: 10.1063/1.336848. URL <http://dx.doi.org/10.1063/1.336848>.
- [68] Ernst Ruska. The development of the electron microscope and of electron microscopy (nobel lecture). *Angewandte Chemie International Edition in English*, 26(7):595–605, 1987. ISSN 1521-3773. DOI: 10.1002/anie.198705953. URL <http://dx.doi.org/10.1002/anie.198705953>.
- [69] E. Brüche and H. Johannson. Elektronenoptik und Elektronenmikroskop. *Naturwissenschaften*, 20(21):353–358, 1932. ISSN 1432-1904. DOI: 10.1007/BF01504926. URL <http://dx.doi.org/10.1007/BF01504926>.
- [70] Reinhold Rüdénberg. The early history of the electron microscope. *Journal of Applied Physics*, 14(8):434–436, 1943. DOI: 10.1063/1.1715011. URL <http://dx.doi.org/10.1063/1.1715011>.
- [71] C. J. Calbick. Historical background of electron optics. *Journal of Applied Physics*, 15(10):685–690, 1944. DOI: 10.1063/1.1707371. URL <http://dx.doi.org/10.1063/1.1707371>.
- [72] S. Nomura. *Design of apochromatic TEM composed of usual round lenses*, pages 41–42. Springer Berlin Heidelberg, Berlin, Heidelberg, 2008. ISBN 978-3-540-85156-1. URL http://dx.doi.org/10.1007/978-3-540-85156-1_21.
- [73] P.W. Hawkes. Can the Nomura lens be free of spherical aberration? *Journal of Microscopy*, 234(3):325–325, 2009. ISSN 1365-2818. DOI: 10.1111/j.1365-2818.2009.03166.x. URL <http://dx.doi.org/10.1111/j.1365-2818.2009.03166.x>.
- [74] O. Scherzer. Über einige Fehler von Elektronenlinsen. *Zeitschrift für Physik*, 101(9):593–603, 1936. ISSN 0044-3328. DOI: 10.1007/BF01349606. URL <http://dx.doi.org/10.1007/BF01349606>.
- [75] P. W. Hawkes. Aberration correction past and present. *Philosophical Transactions of the Royal Society of London A: Mathematical, Physical and Engineering Sciences*, 367(1903):3637–3664, 2009. ISSN 1364-503X.

- DOI: 10.1098/rsta.2009.0004. URL <http://rsta.royalsocietypublishing.org/content/367/1903/3637>.
- [76] Rolf Erni, Marta D. Rossell, Christian Kisielowski, and Ulrich Dahmen. Atomic-resolution imaging with a sub-50-pm electron probe. *Phys. Rev. Lett.*, 102:096101, Mar 2009. DOI: 10.1103/PhysRevLett.102.096101. URL <http://link.aps.org/doi/10.1103/PhysRevLett.102.096101>.
- [77] Sara Bals, Sandra Van Aert, and Gustaaf Van Tendeloo. High resolution electron tomography. *Current Opinion in Solid State and Materials Science*, 17(3):107 – 114, 2013. ISSN 1359-0286. DOI: <http://doi.org/10.1016/j.cossms.2013.03.001>. URL <http://www.sciencedirect.com/science/article/pii/S1359028613000120>. Electron Tomography.
- [78] Andreas Rosenauer, Florian F. Krause, Knut Müller, Marco Schowalter, and Thorsten Mehrtens. Conventional transmission electron microscopy imaging beyond the diffraction and information limits. *Phys. Rev. Lett.*, 113:096101, Aug 2014. DOI: 10.1103/PhysRevLett.113.096101. URL <https://link.aps.org/doi/10.1103/PhysRevLett.113.096101>.
- [79] H. Yang, R. N. Rutte, L. Jones, M. Simson, R. Sagawa, H. Ryll, M. Huth, T. J. Pennycook, M.L.H. Green, H. Soltau, Y. Kondo, B. G. Davis, and P. D. Nellist. Simultaneous atomic-resolution electron ptychography and Z-contrast imaging of light and heavy elements in complex nanostructures. *Nature Communications*, 7(12532), 2016. DOI: 10.1038/ncomms12532.
- [80] Knut Müller, Florian F. Krause, Armand Béché, Marco Schowalter, Vincent Galioit, Stefan Löffler, Johan Verbeeck, Josef Zweck, Peter Schattschneider, and Andreas Rosenauer. Atomic electric fields revealed by a quantum mechanical approach to electron picodiffraction. *Nature Communications*, 5(5653), 2014. DOI: 10.1038/ncomms6653.
- [81] Jannik C. Meyer, C. O. Girit, M. F. Crommie, and A. Zettl. Imaging and dynamics of light atoms and molecules on graphene. *Nature*, 454:319–322, 2008. DOI: 10.1038/nature07094.
- [82] Ahmed H. Zewail. Four-dimensional electron microscopy. *Science*, 328(5975): 187–193, 2010. ISSN 0036-8075. DOI: 10.1126/science.1166135. URL <http://science.sciencemag.org/content/328/5975/187>.
- [83] Armin Feist, Katharina E. Echternkamp, Jakob Schauss, Sergey V. Yalunin, Sascha Schäfer, and Claus Ropers. Quantum coherent optical phase modulation in an ultrafast transmission electron microscope. *Nature*, 521:200–203, 2014. DOI: 10.1038/nature14463.

Bibliography

- [84] A. Ryabov and P. Baum. Electron microscopy of electromagnetic waveforms. *Science*, 353(6297):374–377, 2016. ISSN 0036-8075. DOI: 10.1126/science.aaf8589. URL <http://science.sciencemag.org/content/353/6297/374>.
- [85] David B. Williams and C. Barry Carter. *Transmission Electron Microscopy - A Textbook for Materials Science*. Springer US, 2 edition, 2009. DOI: 10.1007/978-0-387-76501-3.
- [86] Helmut Kohl and Ludwig Reimer. *Transmission Electron Microscopy - Physics of Image Formation*, volume 36 of *0342-4111*. Springer New York, 5 edition, 2008. DOI: 10.1007/978-0-387-40093-8.
- [87] Peter Schattschneider, Michael Stöger-Pollach, and Wolfgang Werner. Electron Beam Techniques for Nanoanalysis, lecture notes, TU Wien, 2011.
- [88] Michael Stöger-Pollach. Techniken der analytischen Elektronenmikroskopie, lecture notes: LVA 138.103, TU Wien, 2016.
- [89] Niels de Jonge and Jean-Marc Bonard. Carbon nanotube electron sources and applications. *Philosophical Transactions of the Royal Society of London A: Mathematical, Physical and Engineering Sciences*, 362(1823):2239–2266, 2004. ISSN 1364-503X. DOI: 10.1098/rsta.2004.1438. URL <http://rsta.royalsocietypublishing.org/content/362/1823/2239>.
- [90] Andrew J McCulloch, Ben M Sparkes, and Robert E Scholten. Cold electron sources using laser-cooled atoms. *Journal of Physics B: Atomic, Molecular and Optical Physics*, 49:164004, 2016. DOI: 10.1088/0953-4075/49/16/164004.
- [91] Han Zhang, Jie Tang, Jinshi Yuan, Yasushi Yamauchi, Taku T. Suzuki, Norio Shinya, Kiyomi Nakajima, and Lu-Chang Qin. An ultrabright and monochromatic electron point source made of a LaB6 nanowire. *Nat Nano*, 11(3):273–279, March 2016. ISSN 1748-3387. URL <http://dx.doi.org/10.1038/nnano.2015.276>.
- [92] B. Cho, T. Ichimura, R. Shimizu, and C. Oshima. Quantitative evaluation of spatial coherence of the electron beam from low temperature field emitters. *Phys. Rev. Lett.*, 92:246103, Jun 2004. DOI: 10.1103/PhysRevLett.92.246103. URL <https://link.aps.org/doi/10.1103/PhysRevLett.92.246103>.
- [93] Tatiana Latychevskaia. Spatial coherence of electron beams from field emitters and its effect on the resolution of imaged objects. *Ultramicroscopy*, 175:121 – 129, 2017. ISSN 0304-3991. DOI: <https://doi.org/10.1016/j.ultramic.2016.11.008>. URL <http://www.sciencedirect.com/science/article/pii/S0304399116301826>.

- [94] N. Dellby, N.J. Bacon, P. Hrnčirik, M.F. Murfitt, G.S. Skone, Z.S. Szilagy, and O.L. Krivanek. Dedicated STEM for 200 to 40 keV operation*. *Eur. Phys. J. Appl. Phys.*, 54(3):33505, 2011. DOI: 10.1051/epjap/2011100429. URL <https://doi.org/10.1051/epjap/2011100429>.
- [95] Ernst Ruska-Centre for Microscopy and Spectroscopy with Electrons (ER-C). FEI Titan G3 50-300 PICO. *Journal of large-scale research facilities*, 1(A34), 2015. DOI: 10.17815/jlsrf-1-57.
- [96] Sunao Sadamatsu, Masaki Tanaka, Kenji Higashida, and Syo Matsumura. Transmission electron microscopy of bulk specimens over 10 μ m in thickness. *Ultramicroscopy*, 162:10 – 16, 2016. ISSN 0304-3991. DOI: <https://doi.org/10.1016/j.ultramic.2015.09.001>. URL <http://www.sciencedirect.com/science/article/pii/S0304399115300243>.
- [97] Radostin Danev and Kuniaki Nagayama. Transmission electron microscopy with Zernike phase plate. *Ultramicroscopy*, 88(4):243 – 252, 2001. ISSN 0304-3991. DOI: [https://doi.org/10.1016/S0304-3991\(01\)00088-2](https://doi.org/10.1016/S0304-3991(01)00088-2). URL <http://www.sciencedirect.com/science/article/pii/S0304399101000882>.
- [98] Kuniaki Nagayama and Radostin Danev. Phase-plate electron microscopy: a novel imaging tool to reveal close-to-life nano-structures. *Biophysical Reviews*, 1(1):37–42, 2009. ISSN 1867-2469. DOI: 10.1007/s12551-008-0006-z. URL <http://dx.doi.org/10.1007/s12551-008-0006-z>.
- [99] Radostin Danev, Bart Buijsse, Maryam Khoshouei, Jürgen M. Plitzko, and Wolfgang Baumeister. Volta potential phase plate for in-focus phase contrast transmission electron microscopy. *Proceedings of the National Academy of Sciences*, 111(44):15635–15640, 2014. DOI: 10.1073/pnas.1418377111. URL <http://www.pnas.org/content/111/44/15635.abstract>.
- [100] G. McMullan, S. Chen, R. Henderson, and A.R. Faruqi. Detective quantum efficiency of electron area detectors in electron microscopy. *Ultramicroscopy*, 109(9):1126 – 1143, 2009. ISSN 0304-3991. DOI: <https://doi.org/10.1016/j.ultramic.2009.04.002>. URL <http://www.sciencedirect.com/science/article/pii/S0304399109001120>.
- [101] Ján Rusz, Shunsuke Muto, Jakob Spiegelberg, Roman Adam, Kazuyoshi Tsumi, Daniel E. B \ddot{u} rgler, Peter M. Oppeneer, and Claus M. Schneider. Erratum: Magnetic measurements with atomic-plane resolution. *Nature Communications*, 7:13159–, October 2016. URL <http://dx.doi.org/10.1038/ncomms13159>.
- [102] H. Ryll, M. Simson, R. Hartmann, P. Holl, M. Huth, S. Ihle, Y. Kondo, P. Kotula, A. Liebel, K. Müller-Caspary, A. Rosenauer, R. Sagawa, J. Schmidt, H. Soltau, and L. Strüder. A pnCCD-based, fast direct single electron imaging

Bibliography

- camera for TEM and STEM. *Journal of Instrumentation*, 11(04):P04006, 2016. URL <http://stacks.iop.org/1748-0221/11/i=04/a=P04006>.
- [103] Yihan Zhu, Jim Ciston, Bin Zheng, Xiaohe Miao, Cory Czarnik, Yichang Pan, Rachid Sougrat, Zhiping Lai, Chia-En Hsiung, Kexin Yao, Ingo Pinnau, Ming Pan, and Yu Han. Unravelling surface and interfacial structures of a metal-organic framework by transmission electron microscopy. *Nature Materials*, 16:532–536, 2017. DOI: 10.1038/nmat4852.
- [104] Sriram Subramaniam, Werner Kühlbrandt, and Richard Henderson. CryoEM at IUCrJ: a new era. *IUCrJ*, 3(1):3–7, Jan 2016. DOI: 10.1107/S2052252515023738. URL <https://doi.org/10.1107/S2052252515023738>.
- [105] Kazuhisa Sato and Hidehiro Yasuda. Fluctuation of long-range order in Co-Pt alloy nanoparticles revealed by time-resolved electron microscopy. *Applied Physics Letters*, 110(15):153101, 2017. DOI: 10.1063/1.4980077. URL <http://dx.doi.org/10.1063/1.4980077>.
- [106] R F Egerton. Electron energy-loss spectroscopy in the TEM. *Reports on Progress in Physics*, 72(1):016502, dec 2008. DOI: 10.1088/0034-4885/72/1/016502. URL <https://doi.org/10.1088/0034-4885/72/1/016502>.
- [107] R.F. Egerton. *Electron Energy-Loss Spectroscopy in the Electron Microscope*. Springer US, 3 edition, 2011. ISBN 978-1-4419-9582-7. DOI: 10.1007/978-1-4419-9583-4.
- [108] John C H Spence. Absorption spectroscopy with sub-angstrom beams: ELS in STEM. *Reports on Progress in Physics*, 69(3):725–758, feb 2006. DOI: 10.1088/0034-4885/69/3/r04. URL <https://doi.org/10.1088/0034-4885/69/3/r04>.
- [109] O.L. Krivanek, N. Dellby, J.A. Hachtel, J.-C. Idrobo, M.T. Hotz, B. Plotkin-Swing, N.J. Bacon, A.L. Bleloch, G.J. Corbin, M.V. Hoffman, C.E. Meyer, and T.C. Lovejoy. Progress in ultrahigh energy resolution EELS. *Ultramicroscopy*, 2018. ISSN 0304-3991. DOI: <https://doi.org/10.1016/j.ultramic.2018.12.006>. URL <http://www.sciencedirect.com/science/article/pii/S0304399118303668>.
- [110] G. Kothleitner, M. J. Neish, N. R. Lugg, S. D. Findlay, W. Grogger, F. Hofer, and L. J. Allen. Quantitative elemental mapping at atomic resolution using X-ray spectroscopy. *Phys. Rev. Lett.*, 112:085501, Feb 2014. DOI: 10.1103/PhysRevLett.112.085501. URL <https://link.aps.org/doi/10.1103/PhysRevLett.112.085501>.

- [111] M. Varela, A.R. Lupini, K. van Benthem, A.Y. Borisevich, M.F. Chisholm, N. Shibata, E. Abe, and S.J. Pennycook. Materials characterization in the aberration-corrected scanning transmission electron microscope. *Annual Review of Materials Research*, 35(1):539–569, 2005. DOI: 10.1146/annurev.matsci.35.102103.090513. URL <https://doi.org/10.1146/annurev.matsci.35.102103.090513>.
- [112] Ryosuke Senga and Kazu Suenaga. Single-atom detection of light elements: Imaging or spectroscopy? *Ultramicroscopy*, 180:150 – 155, 2017. ISSN 0304-3991. DOI: <https://doi.org/10.1016/j.ultramic.2016.12.007>. URL <http://www.sciencedirect.com/science/article/pii/S0304399116303771>. Ondrej Krivanek: A research life in EELS and aberration corrected STEM.
- [113] Lorenzo Pardini, Stefan Löffler, Giulio Biddau, Ralf Hambach, Ute Kaiser, Claudia Draxl, and Peter Schattschneider. Mapping atomic orbitals with the transmission electron microscope: Images of defective graphene predicted from first-principles theory. *Phys. Rev. Lett.*, 117:036801, Jul 2016. DOI: 10.1103/PhysRevLett.117.036801. URL <https://link.aps.org/doi/10.1103/PhysRevLett.117.036801>.
- [114] Stefan Löffler, Matthieu Bugnet, Nicolas Gauquelin, Sorin Lazar, Elias Assmann, Karsten Held, Gianluigi A. Botton, and Peter Schattschneider. Real-space mapping of electronic orbitals. *Ultramicroscopy*, 177:26 – 29, 2017. ISSN 0304-3991. DOI: <http://doi.org/10.1016/j.ultramic.2017.01.018>. URL <http://www.sciencedirect.com/science/article/pii/S0304399117300517>.
- [115] G. Möllenstedt and F. Heise. Die elektrostatische Linse als hochauflösender Geschwindigkeits-Analysator. *Physikalische Blätter*, 5(2):80–93, 1949. URL <https://onlinelibrary.wiley.com/toc/15213722/1949/5/2>.
- [116] Eugene Wilkins. Lecture 4 - spectroscopy. Online - slideplayer.com, 2016. URL <https://slideplayer.com/slide/5668584/>.
- [117] Gatan. *Datasheet GIF Continuum and Continuum S*. Gatan Inc., 2018. URL <http://www.gatan.com/products/tem-imaging-spectroscopy/gif-continuum-and-continuum-s>.
- [118] Sergei Lopatin, Bin Cheng, Wei-Ting Liu, Meng-Lin Tsai, Jr-Hau He, and Andrey Chuvilin. Optimization of monochromated TEM for ultimate resolution imaging and ultrahigh resolution electron energy loss spectroscopy. *Ultramicroscopy*, 184(Part A):109 – 115, 2018. ISSN 0304-3991. DOI: <https://doi.org/10.1016/j.ultramic.2017.08.016>. URL <http://www.sciencedirect.com/science/article/pii/S0304399117302073>.
- [119] Thomas Schachinger. Electron vortex beams in magnetic fields. Diploma Thesis, TU Wien, Vienna, 2014. URL <http://katalog.ub.tuwien.ac.at/AC11312766>.

Bibliography

- [120] Jerome J. Cuomo, James P. Doyle, John Bruley, and Joyce C. Liu. Sputter deposition of dense diamond-like carbon films at low temperature. *Applied Physics Letters*, 58(5):466–468, feb 1991. DOI: 10.1063/1.104609. URL <https://doi.org/10.1063/1.104609>.
- [121] L Piazza, T.T.A. Lummen, E Quinonez, Y Murooka, B.W. Reed, B Barwick, and F Carbone. Simultaneous observation of the quantization and the interference pattern of a plasmonic near-field. *Nature Communications*, 6:6407–, March 2015. URL <https://doi.org/10.1038/ncomms7407>.
- [122] J. M. D. Coey. *Magnetism and magnetic materials*. Cambridge [u.a.] : Cambridge Univ. Press, 2010.
- [123] Roland Wiesendanger. Spin mapping at the nanoscale and atomic scale. *Rev. Mod. Phys.*, 81:1495–1550, Nov 2009. DOI: 10.1103/RevModPhys.81.1495. URL <https://link.aps.org/doi/10.1103/RevModPhys.81.1495>.
- [124] Sergey Zayko, Ofer Kfir, Christina Nolte, Murat Sivis, Marcel Möller, Fabian Ganss, Birgit Hebler, Daniel Steil, Sascha Schäfer, Manfred Albrecht, Oren Cohen, Stefan Mathias, and Claus Ropers. Nanoscale imaging of magnetic domains using a high-harmonic source. In *Conference on Lasers and Electro-Optics*, page FW1H.8. Optical Society of America, 2017. DOI: 10.1364/CLEO_QELS.2017.FW1H.8. URL http://www.osapublishing.org/abstract.cfm?URI=CLEO_QELS-2017-FW1H.8.
- [125] Sebastian Loth, Markus Etzkorn, Christopher P. Lutz, D. M. Eigler, and Andreas J. Heinrich. Measurement of fast electron spin relaxation times with atomic resolution. *Science*, 329(5999):1628–1630, 2010. ISSN 0036-8075. DOI: 10.1126/science.1191688. URL <http://science.sciencemag.org/content/329/5999/1628>.
- [126] Taeyoung Choi, William Paul, Steffen Rolf-Pissarczyk, Andrew J. Macdonald, Fabian D. Natterer, Kai Yang, Philip Willke, Christopher P. Lutz, and Andreas J. Heinrich. Atomic-scale sensing of the magnetic dipolar field from single atoms. *Nature Nanotechnology*, 12:420–424, 2017. DOI: 10.1038/nnano.2017.18.
- [127] Falk Röder, Gregor Hlawacek, Sebastian Wintz, René Hübner, Lothar Bischoff, Hannes Lichte, Kay Potzger, Jürgen Lindner, Jürgen Fassbender, and Rantej Bali. Direct depth- and lateral- imaging of nanoscale magnets generated by ion impact. *Scientific Reports*, 5(16786), 2015. DOI: 10.1038/srep16786.
- [128] Christophe Gatel, Francisco Javier Bonilla, Anca Meffre, Etienne Snoeck, Bénédicte Warot-Fonrose, Bruno Chaudret, Lise-Marie Lacroix, and Thomas Blon. Size-specific spin configurations in single iron nanomagnet: From flower to exotic vortices. *Nano Letters*, 15(10):6952–6957, 2015. DOI: 10.1021/acs.nanolett.5b02892. URL <http://dx.doi.org/10.1021/acs.nanolett.5b02892>. PMID: 26407034.

- [129] Kayla X. Nguyen, Prafull Purohit, Robert Hovden, Emrah Turgut, Mark W. Tate, Lena F. Kourkoutis, Gregory D. Fuchs, Sol M. Gruner, and David A. Muller. 4D-STEM for quantitative imaging of magnetic materials with enhanced contrast and resolution. *Microscopy and Microanalysis*, 22(S3): 1718–1719, 2016. DOI: 10.1017/S1431927616009430.
- [130] Naoya Shibata, Takehito Seki, Gabriel Sánchez-Santolino, Scott D. Findlay, Yuji Kohno, Takao Matsumoto, Ryo Ishikawa, and Yuichi Ikuhara. Electric field imaging of single atoms. *Nature Communications*, 8:15631, May 2017. URL <https://doi.org/10.1038/ncomms15631>.
- [131] Alexander Edström, Axel Lubk, and Ján Ruzs. Elastic scattering of electron vortex beams in magnetic matter. *Phys. Rev. Lett.*, 116:127203, Mar 2016. DOI: 10.1103/PhysRevLett.116.127203. URL <http://link.aps.org/doi/10.1103/PhysRevLett.116.127203>.
- [132] Alexander Edström, Axel Lubk, and Ján Ruzs. Magnetic effects in the paraxial regime of elastic electron scattering. *Phys. Rev. B*, 94:174414, Nov 2016. DOI: 10.1103/PhysRevB.94.174414. URL <http://link.aps.org/doi/10.1103/PhysRevB.94.174414>.
- [133] P. Schattschneider. Exchange of angular momentum in EMCD experiments. *Ultramicroscopy*, 109(1):91 – 95, 2008. ISSN 0304-3991. DOI: <https://doi.org/10.1016/j.ultramic.2008.08.004>. URL <http://www.sciencedirect.com/science/article/pii/S030439910800226X>.
- [134] J. Ruzs, O. Eriksson, P. Novák, and P.M. Oppeneer. Spin and orbital moment sum-rules for the electron energy loss chiral magnetic dichroism. *Physica B: Condensed Matter*, 403(5-9):1614–1615, apr 2008. DOI: 10.1016/j.physb.2007.10.322. URL <http://dx.doi.org/10.1016/j.physb.2007.10.322>.
- [135] Thomas Thersleff, Jan Ruzs, Stefano Rubino, Björgvin Hjörvarsson, Yasuo Ito, Nestor J. Zaluzec, and Klaus Leifer. Quantitative analysis of magnetic spin and orbital moments from an oxidized iron (1 1 0) surface using electron magnetic circular dichroism. *Scientific Reports*, 5:13012, 2015. DOI: 10.1038/srep13012.
- [136] Sebastian Schneider, Darius Pohl, Stefan Löffler, Jan Ruzs, Deepa Kasinathan, Peter Schattschneider, Ludwig Schultz, and Bernd Rellinghaus. Magnetic properties of single nanomagnets: Electron energy-loss magnetic chiral dichroism on FePt nanoparticles. *Ultramicroscopy*, 171:186 – 194, 2016. ISSN 0304-3991. DOI: 10.1016/j.ultramic.2016.09.009.
- [137] Zechao Wang, Amir H. Tavabi, Lei Jin, Ján Ruzs, Dmitry Tyutyunnikov, Hanbo Jiang, Yutaka Moritomo, Joachim Mayer, Rafal E. Dunin-Borkowski,

Bibliography

- Rong Yu, Jing Zhu, and Xiaoyan Zhong. Atomic scale imaging of magnetic circular dichroism by achromatic electron microscopy. *Nature Materials*, 17(3):221–225, 2018. ISSN 1476-4660. URL <https://doi.org/10.1038/s41563-017-0010-4>.
- [138] Dongsheng Song, Amir H. Tavabi, Zi-An Li, András Kovács, Ján Ruzs, Wenting Huang, Gunther Richter, Rafal E. Dunin-Borkowski, and Jing Zhu. An in-plane magnetic chiral dichroism approach for measurement of intrinsic magnetic signals using transmitted electrons. *Nature Communications*, 8:15348–, May 2017. URL <http://dx.doi.org/10.1038/ncomms15348>.
- [139] Stefan Löffler. *Study of real space wave functions with electron energy loss spectrometry*. PhD thesis, TU Wien, 2013. URL <http://repositum.tuwien.ac.at/urn:nbn:at:at-ubtuw:1-75497>.
- [140] Devendra Negi, Jakob Spiegelberg, Shunsuke Muto, Thomas Thersleff, Masahiro Ohtsuka, Linus Schönström, Kazuyoshi Tatsumi, and Ján Ruzs. Proposal for measuring magnetism with patterned apertures in a transmission electron microscope. *Phys. Rev. Lett.*, 122:037201, Jan 2019. DOI: 10.1103/PhysRevLett.122.037201. URL <https://link.aps.org/doi/10.1103/PhysRevLett.122.037201>.
- [141] C Hébert and P Schattschneider. A proposal for dichroic experiments in the electron microscope. *Ultramicroscopy*, 96(3-4):463—468, September 2003. ISSN 0304-3991. DOI: 10.1016/S0304-3991(03)00108-6. URL [https://doi.org/10.1016/S0304-3991\(03\)00108-6](https://doi.org/10.1016/S0304-3991(03)00108-6).
- [142] Peter Schattschneider. *Fundamentals of Inelastic Electron Scattering*. Springer, 1986. ISBN ISBN 978-3-7091-8866-8.
- [143] M. Nelhiebel, P. Schattschneider, and B. Jouffrey. Observation of ionization in a crystal interferometer. *Phys. Rev. Lett.*, 85:1847–1850, Aug 2000. DOI: 10.1103/PhysRevLett.85.1847. URL <https://link.aps.org/doi/10.1103/PhysRevLett.85.1847>.
- [144] P. Schattschneider and J. Verbeeck. Theory of free electron vortices. *Ultramicroscopy*, 111(9–10):1461 – 1468, 2011. ISSN 0304-3991. DOI: 10.1016/j.ultramic.2011.07.004. URL <http://www.sciencedirect.com/science/article/pii/S0304399111001811>.
- [145] K.Y. Bliokh, I.P. Ivanov, G. Guzzinati, L. Clark, R. Van Boxem, A. Béch e, R. Juchtmans, M.A. Alonso, P. Schattschneider, F. Nori, and J. Verbeeck. Theory and applications of free-electron vortex states. *Physics Reports*, pages –, 2017. ISSN 0370-1573. DOI: <https://doi.org/10.1016/j.physrep.2017.05.006>. URL <http://www.sciencedirect.com/science/article/pii/S0370157317301515>.

- [146] S. M. Lloyd, M. Babiker, G. Thirunavukkarasu, and J. Yuan. Electron vortices: Beams with orbital angular momentum. *Rev. Mod. Phys.*, 89:035004, Aug 2017. DOI: 10.1103/RevModPhys.89.035004. URL <https://link.aps.org/doi/10.1103/RevModPhys.89.035004>.
- [147] Peter Schattschneider, Thomas Schachinger, and Johan Verbeeck. Ein Whirlpool aus Elektronen. *Physik in unserer Zeit*, 49(1):22–28, 2018. ISSN 1521-3943. DOI: 10.1002/piuz.201801495. URL <http://dx.doi.org/10.1002/piuz.201801495>.
- [148] Hugo Larocque, Ido Kaminer, Vincenzo Grillo, Gerd Leuchs, Miles J. Padgett, Robert W. Boyd, Mordechai Segev, and Ebrahim Karimi. ‘Twisted’ electrons. *Contemporary Physics*, 59(2):126–144, 2018. DOI: 10.1080/00107514.2017.1418046. URL <https://doi.org/10.1080/00107514.2017.1418046>.
- [149] Roy Shiloh and Ady Arie. 3D shaping of electron beams using amplitude masks. *Ultramicroscopy*, 177:30 – 35, 2017. ISSN 0304-3991. DOI: <https://doi.org/10.1016/j.ultramic.2017.02.001>. URL <http://www.sciencedirect.com/science/article/pii/S0304399116301796>.
- [150] Noa Voloch-Bloch, Yossi Lereah, Yigal Lilach, Avraham Gover, and Ady Arie. Generation of electron Airy beams. *Nature*, 494:331, February 2013. URL <https://doi.org/10.1038/nature11840>.
- [151] Vincenzo Grillo, Amir H. Tavabi, Emrah Yucelen, Peng-Han Lu, Federico Venturi, Hugo Larocque, Lei Jin, Aleksei Savenko, Gian Carlo Gazzadi, Roberto Balboni, Stefano Frabboni, Peter Tiemeijer, Rafal E. Dunin-Borkowski, and Ebrahim Karimi. Towards a holographic approach to spherical aberration correction in scanning transmission electron microscopy. *Opt. Express*, 25(18):21851–21860, Sep 2017. DOI: 10.1364/OE.25.021851. URL <http://www.opticsexpress.org/abstract.cfm?URI=oe-25-18-21851>.
- [152] Colin Ophus, Jim Ciston, Jordan Pierce, Tyler R. Harvey, Jordan Chess, Benjamin J. McMorran, Cory Czarnik, Harald H. Rose, and Peter Ercius. Efficient linear phase contrast in scanning transmission electron microscopy with matched illumination and detector interferometry. *Nature Communications*, 7:10719, February 2016. URL <https://doi.org/10.1038/ncomms10719>.
- [153] Roei Remez, Yuval Tsur, Peng-Han Lu, Amir H. Tavabi, Rafal E. Dunin-Borkowski, and Ady Arie. Superoscillating electron wave functions with sub-diffraction spots. *Phys. Rev. A*, 95:031802, Mar 2017. DOI: 10.1103/PhysRevA.95.031802. URL <https://link.aps.org/doi/10.1103/PhysRevA.95.031802>.

Bibliography

- [154] Hans Wolter. Zur Frage des Lichtweges bei Totalreflexion. *Zeitschrift für Naturforschung A*, 5(5):276–283, 1950. DOI: <https://doi.org/10.1515/zna-1950-0505>. URL <https://www.degruyter.com/downloadpdf/j/zna.1950.5.issue-5/zna-1950-0505/zna-1950-0505.pdf>.
- [155] W. Braunbeck and G. Laukien. Einzelheiten zur Halbebenenbeugung. *Optik*, 9:174–179, 1952.
- [156] J.W. Findlay. The phase and group paths of radio waves returned from region e of the ionosphere. *Journal of Atmospheric and Terrestrial Physics*, 1(5):353 – 366, 1951. ISSN 0021-9169. DOI: [https://doi.org/10.1016/0021-9169\(51\)90010-4](https://doi.org/10.1016/0021-9169(51)90010-4). URL <http://www.sciencedirect.com/science/article/pii/0021916951900104>.
- [157] Joseph O. Hirschfelder, Albert C. Christoph, and William E. Palke. Quantum mechanical streamlines. i. square potential barrier. *The Journal of Chemical Physics*, 61(12):5435–5455, 1974. DOI: 10.1063/1.1681899. URL <https://doi.org/10.1063/1.1681899>.
- [158] H. He, M. E. J. Friese, N. R. Heckenberg, and H. Rubinsztein-Dunlop. Direct observation of transfer of angular momentum to absorptive particles from a laser beam with a phase singularity. *Phys. Rev. Lett.*, 75(5):826–829, Jul 1995. DOI: 10.1103/PhysRevLett.75.826.
- [159] Z. P. Luo, Y. L. Sun, and K. N. An. An optical spin micromotor. *Applied Physics Letters*, 76(13):1779–1781, 2000.
- [160] S. Kuppens, M. Rauner, M. Schiffer, K. Sengstock, W. Ertmer, F. E. Van Dorselaer, and G. Nienhuis. Polarization-gradient cooling in a strong doughnut-mode dipole potential. *Physical Review A - Atomic, Molecular, and Optical Physics*, 58(4):3068–3079, 1998.
- [161] T. Tsurumi and M. Wadati. Ground state properties of a toroidally trapped Bose-Einstein condensate. *Journal of the Physical Society of Japan*, 70(6):1512–1518, 2001.
- [162] M. Krenn, R. Fickler, M. Fink, J. Handsteiner, M. Malik, T. Scheidl, R. Ursin, and A. Zeilinger. Communication with spatially modulated light through turbulent air across vienna. *New Journal of Physics*, 16:113028, 2014.
- [163] E. Serabyn, D. Mawet, and R. Burruss. An image of an exoplanet separated by two diffraction beamwidths from a star. *Nature*, 464(7291):1018–1020, 2010.
- [164] S. Franke-Arnold, L. Allen, and M. Padgett. Advances in optical angular momentum. *Laser & Photonics Reviews*, 2(4):299–313, 2008. DOI: 10.1002/lpor.200810007. URL <https://onlinelibrary.wiley.com/doi/abs/10.1002/lpor.200810007>.

- [165] Miles Padgett and Richard Bowman. Tweezers with a twist. *Nature Photonics*, 5:343, May 2011. URL <https://doi.org/10.1038/nphoton.2011.81>.
- [166] Arthur Ashkin. Facts – 2018. nobelprize.org. nobel media ab 2019. wed. 6 feb 2019., 2019. URL <https://www.nobelprize.org/prizes/physics/2018/ashkin/facts/>.
- [167] A. H. W. Beck and W. P. C. Mills. Millimetre-wave generator working at half the cyclotron resonance frequency. *Electronics Letters*, 7(18):533–534, 1971. URL <https://ieeexplore.ieee.org/stamp/stamp.jsp?arnumber=4235261>.
- [168] E. Munro. *Computer-aided-design methods in electron optics*. PhD thesis, University of Cambridge, 1971.
- [169] A. H. W. Beck and W. P. C. Mills. Millimetre-wave generator that uses a spiralling electron beam. *Proceedings of the Institution of Electrical Engineers*, 120(2):197 – 205, 1973. DOI: 10.1049/piee.1973.0042. URL <http://dx.doi.org/10.1049/piee.1973.0042>.
- [170] Edward A. McCullough and Robert E. Wyatt. Dynamics of the collinear H+H₂ reaction. i. probability density and flux. *The Journal of Chemical Physics*, 54(8):3578–3591, 1971. DOI: 10.1063/1.1675384. URL <https://doi.org/10.1063/1.1675384>.
- [171] Yu Chekh, Alexey Goncharov, and I M. Protsenko. Large-scale electron vortex structure formation in a plasma lens. *Technical Physics Letters*, 32:51–54, 01 2006. DOI: 10.1134/S1063785006010172.
- [172] Vincenzo Grillo, Ebrahim Karimi, Gian Carlo Gazzadi, Stefano Frabboni, Mark R. Dennis, and Robert W. Boyd. Generation of nondiffracting electron Bessel beams. *Physical Review X*, 4:011013, Jan 2014. DOI: 10.1103/PhysRevX.4.011013. URL <http://link.aps.org/doi/10.1103/PhysRevX.4.011013>.
- [173] Andrea Aiello, Girish S. Agarwal, Martin Paúr, Bohumil Stoklasa, Zdeněk Hradil, Jaroslav Řeháček, Pablo de la Hoz, Gerd Leuchs, and Luis L. Sánchez-Soto. Unraveling beam self-healing. *Opt. Express*, 25(16):19147–19157, Aug 2017. DOI: 10.1364/OE.25.019147. URL <http://www.opticsexpress.org/abstract.cfm?URI=oe-25-16-19147>.
- [174] Konstantin Y. Bliokh, Mark R. Dennis, and Franco Nori. Relativistic electron vortex beams: Angular momentum and spin-orbit interaction. *Phys. Rev. Lett.*, 107:174802, Oct 2011. DOI: 10.1103/PhysRevLett.107.174802. URL <http://link.aps.org/doi/10.1103/PhysRevLett.107.174802>.
- [175] Stephen M. Barnett. Relativistic electron vortices. *Physical Review Letters*, 118:114802, Mar 2017. DOI: 10.1103/PhysRevLett.118.114802. URL <http://link.aps.org/doi/10.1103/PhysRevLett.118.114802>.

Bibliography

- [176] Iwo Bialynicki-Birula and Zofia Bialynicka-Birula. Relativistic electron wave packets carrying angular momentum. *Phys. Rev. Lett.*, 118:114801, Mar 2017. DOI: 10.1103/PhysRevLett.118.114801. URL <http://link.aps.org/doi/10.1103/PhysRevLett.118.114801>.
- [177] Konstantin Y. Bliokh, Mark R. Dennis, and Franco Nori. Position, spin, and orbital angular momentum of a relativistic electron. *Phys. Rev. A*, 96:023622, Aug 2017. DOI: 10.1103/PhysRevA.96.023622. URL <https://link.aps.org/doi/10.1103/PhysRevA.96.023622>.
- [178] Mario Krenn and Anton Zeilinger. On small beams with large topological charge: II. photons, electrons and gravitational waves. *New Journal of Physics*, 20(6):063006, jun 2018. DOI: 10.1088/1367-2630/aac7eb. URL <https://doi.org/10.1088%2F1367-2630%2Faac7eb>.
- [179] Yeong Deok Han, Taeseung Choi, and Sam Young Cho. Singularity of relativistic vortex beam and proper relativistic observables. *Arxiv*, 2019. URL <https://arxiv.org/abs/1902.09805>.
- [180] Ruben Van Boxem, Jo Verbeeck, and Bart Partoens. Spin effects in electron vortex states. *EPL (Europhysics Letters)*, 102(4):40010, may 2013. DOI: 10.1209/0295-5075/102/40010. URL <https://doi.org/10.1209%2F0295-5075%2F102%2F40010>.
- [181] P. Schattschneider, V. Grillo, and D. Aubry. Spin polarisation with electron bessel beams. *Ultramicroscopy*, 176:188 – 193, 2017. ISSN 0304-3991. DOI: <https://doi.org/10.1016/j.ultramic.2016.11.029>. URL <http://www.sciencedirect.com/science/article/pii/S0304399117301122>. 70th Birthday of Robert Sinclair and 65th Birthday of Nestor J. Zaluzec PICO 2017 – Fourth Conference on Frontiers of Aberration Corrected Electron Microscopy.
- [182] Dennis Gabor. A new microscopic principle. *Nature*, 161:777–778, 1948. URL <https://www.nature.com/nature/journal/v161/n4098/pdf/161777a0.pdf>.
- [183] M. E. Haine and T. Mulvey. The formation of the diffraction image with electrons in the Gabor diffraction microscope. *Journal of the Optical Society of America*, 42(10):763–773, 1952.
- [184] G. Möllenstedt and H. Düker. Beobachtungen und Messungen an Biprisma-Interferenzen mit Elektronenwellen. *Zeitschrift für Physik*, 145(3):377–397, 1956. ISSN 0044-3328. DOI: 10.1007/BF01326780. URL <http://dx.doi.org/10.1007/BF01326780>.
- [185] J.M. Cowley. Twenty forms of electron holography. *Ultramicroscopy*, 41(4):335 – 348, 1992. ISSN 0304-3991. DOI: [https://doi.org/10.1016/0304-3991\(92\)90213-4](https://doi.org/10.1016/0304-3991(92)90213-4). URL <http://www.sciencedirect.com/science/article/pii/0304399192902134>.

- [186] B. J. McMorran, A. Agrawal, I.M. Anderson, A. A. Herzing, H.J. Lezec, J. J. McClelland, and J. Unguris. Electron vortex beams with high quanta of orbital angular momentum. *Science*, 331(6014):192–195, 2011. DOI: 10.1126/science.1198804.
- [187] J. Verbeeck, H. Tian, and A. Béch e. A new way of producing electron vortex probes for STEM. *Ultramicroscopy*, 113:83 – 87, 2012. ISSN 0304-3991. DOI: <https://doi.org/10.1016/j.ultramic.2011.10.008>. URL <http://www.sciencedirect.com/science/article/pii/S0304399111002531>.
- [188] Roy Shiloh, Peng-Han Lu, Roei Remez, Amir H Tavabi, Giulio Pozzi, Rafal E Dunin-Borkowski, and Ady Arie. Nanostructuring of electron beams. *Physica Scripta*, 94(3):034004, jan 2019. DOI: 10.1088/1402-4896/aaf258. URL <https://doi.org/10.1088/1402-4896/aaf258>.
- [189] P. Schattschneider, M. St oger-Pollach, S. L offler, A. Steiger-Thirsfeld, J. Hell, and J. Verbeeck. Sub-nanometer free electrons with topological charge. *Ultramicroscopy*, 115:21–25, 2012. DOI: 10.1016/j.ultramic.2012.01.010.
- [190] Simon Hettler, Lukas Gr unewald, and Marek Malac. Quasi non-diffractive electron Bessel beams using direct phase masks with applications in electron microscopy. *New Journal of Physics*, 21(3):033007, mar 2019. DOI: 10.1088/1367-2630/ab03da. URL <https://doi.org/10.1088/1367-2630/ab03da>.
- [191] H. Shinotsuka, S. Tanuma, C. J. Powell, and D. R. Penn. Calculations of electron inelastic mean free paths. x. data for 41 elemental solids over the 50 eV to 200 keV range with the relativistic full penn algorithm. *Surface and Interface Analysis*, 47(9):871–888, jul 2015. DOI: doi:10.1002/sia.5789.
- [192] Konstantin Iakoubovskii and Kazutaka Mitsuishi. Elastic scattering of 200 keV electrons in elemental solids: experimental observation of atomic-number-dependent oscillatory behavior. *Journal of Physics: Condensed Matter*, 21(15):155402, mar 2009. DOI: 10.1088/0953-8984/21/15/155402. URL <https://doi.org/10.1088/0953-8984/21/15/155402>.
- [193] Gerald Kothleitner, Werner Grogger, Martina Dienstleder, and Ferdinand Hofer. Linking TEM analytical spectroscopies for an assumptionless compositional analysis. *Microscopy and Microanalysis*, 20(3):678–686, 2014. DOI: 10.1017/S1431927614000130.
- [194] T. Malis, S. C. Cheng, and R. F. Egerton. EELS log-ratio technique for specimen-thickness measurement in the TEM. *Journal of Electron Microscopy Technique*, 8(2):193–200, 1988. DOI: 10.1002/jemt.1060080206. URL <https://onlinelibrary.wiley.com/doi/abs/10.1002/jemt.1060080206>.
- [195] A. B ech e, R. Winkler, H. Plank, F. Hofer, and J. Verbeeck. Focused electron beam induced deposition as a tool to create electron vortices. *Micron*, 80:34 –

Bibliography

- 38, 2016. ISSN 0968-4328. DOI: <http://doi.org/10.1016/j.micron.2015.07.011>.
URL <http://www.sciencedirect.com/science/article/pii/S0968432815300275>.
- [196] L. Clark, A. Béché, G. Guzzinati, A. Lubk, M. Mazilu, R. Van Boxem, and J. Verbeeck. Exploiting lens aberrations to create electron-vortex beams. *Phys. Rev. Lett.*, 111:064801, Aug 2013. DOI: 10.1103/PhysRevLett.111.064801. URL <https://link.aps.org/doi/10.1103/PhysRevLett.111.064801>.
- [197] A.M. Blackburn and J.C. Loudon. Vortex beam production and contrast enhancement from a magnetic spiral phase plate. *Ultramicroscopy*, 136:127 – 143, 2014. ISSN 0304-3991. DOI: <https://doi.org/10.1016/j.ultramic.2013.08.009>.
URL <http://www.sciencedirect.com/science/article/pii/S0304399113002544>.
- [198] Arthur M. Blackburn. Observation of an electron vortex beam created from a self-charging rod. *Microscopy and Microanalysis*, 22(S3):1710–1711, 2016. DOI: 10.1017/S1431927616009399.
- [199] Giulio Pozzi, Peng-Han Lu, Amir H. Tavabi, Martial Duchamp, and Rafal E. Dunin-Borkowski. Generation of electron vortex beams using line charges via the electrostatic Aharonov-Bohm effect. *Ultramicroscopy*, 181:191 – 196, 2017. ISSN 0304-3991. DOI: <https://doi.org/10.1016/j.ultramic.2017.06.001>. URL <http://www.sciencedirect.com/science/article/pii/S0304399116303175>.
- [200] Amir H. Tavabi, Hugo Larocque, Peng-Han Lu, Martial Duchamp, Vincenzo Grillo, Ebrahim Karimi, Rafal E. Dunin-Borkowski, and Giulio Pozzi. Generation of electron vortices using non-exact electric fields. *arXiv*:, pages 1809.07613v1 [quant-ph] 20 Sep 2018, 2018. URL <https://arxiv.org/pdf/1809.07613.pdf>.
- [201] Christina J. Naify, Charles A. Rohde, Theodore P. Martin, Michael Nicholas, Matthew D. Guild, and Gregory J. Orris. Generation of topologically diverse acoustic vortex beams using a compact metamaterial aperture. *Applied Physics Letters*, 108(22):223503, 2016. DOI: 10.1063/1.4953075. URL <http://dx.doi.org/10.1063/1.4953075>.
- [202] Ryo Imai, Natsuki Kanda, Takuya Higuchi, Kuniaki Konishi, and Makoto Kuwata-Gonokami. Generation of broadband terahertz vortex beams. *Opt. Lett.*, 39(13):3714–3717, Jul 2014. DOI: 10.1364/OL.39.003714. URL <http://ol.osa.org/abstract.cfm?URI=ol-39-13-3714>.
- [203] K. Miyamoto, K. Suizu, T. Akiba, and T. Omatsu. Direct observation of the topological charge of a terahertz vortex beam generated by a Tsurupica spiral phase plate. *Applied Physics Letters*, 104(26):261104, 2014. DOI: 10.1063/1.4886407. URL <http://dx.doi.org/10.1063/1.4886407>.

- [204] Wei Cai, Ori Reinhardt, Ido Kaminer, and F. Javier García de Abajo. Efficient orbital angular momentum transfer between plasmons and free electrons. *Phys. Rev. B*, 98:045424, Jul 2018. DOI: 10.1103/PhysRevB.98.045424. URL <https://link.aps.org/doi/10.1103/PhysRevB.98.045424>.
- [205] F. J. García de Abajo, B. Barwick, and F. Carbone. Electron diffraction by plasmon waves. *Phys. Rev. B*, 94:041404, Jul 2016. DOI: 10.1103/PhysRevB.94.041404. URL <https://link.aps.org/doi/10.1103/PhysRevB.94.041404>.
- [206] Jo Verbeeck, Armand Béché, Knut Müller-Caspary, Giulio Guzzinati, Minh Anh Luong, and Martien Den Hertog. Demonstration of a 2 by 2 programmable phase plate for electrons. *Ultramicroscopy*, 190:58 – 65, 2018. ISSN 0304-3991. DOI: <https://doi.org/10.1016/j.ultramic.2018.03.017>. URL <http://www.sciencedirect.com/science/article/pii/S0304399117305041>.
- [207] Koh Saitoh, Yuya Hasegawa, Kazuma Hirakawa, Nobuo Tanaka, and Masaya Uchida. Measuring the orbital angular momentum of electron vortex beams using a forked grating. *Phys. Rev. Lett.*, 111:074801, Aug 2013. DOI: 10.1103/PhysRevLett.111.074801. URL <https://link.aps.org/doi/10.1103/PhysRevLett.111.074801>.
- [208] Earl J. Kirkland. *Advanced Computing in Electron Microscopy*. Springer US, 2010. DOI: 10.1007/978-1-4419-6533-2.
- [209] Martin Zauner. Multislice approach for high resolution energy filtered inelastic image simulation, 2010. Wien, Techn. Univ., Dipl.-Arb., 2010.
- [210] P. Goodman and A. F. Moodie. Numerical evaluations of n -beam wave functions in electron scattering by the multi-slice method. *Acta Crystallographica Section A*, 30(2):280–290, Mar 1974. DOI: 10.1107/S056773947400057X. URL <https://doi.org/10.1107/S056773947400057X>.
- [211] P. Schattschneider and B. Jouffrey. Density matrix of inelastically scattered fast electrons. *Physical Review B - Condensed Matter and Materials Physics*, 59(16):10959–10969, 1999. DOI: 10.1103/PhysRevB.59.10959. URL <https://www.scopus.com/inward/record.uri?eid=2-s2.0-0012209954&doi=10.1103%2fPhysRevB.59.10959&partnerID=40&md5=7828495faea317697a80eeaa0fdc0b6c>. cited By 66.
- [212] P. Schattschneider, M. Nelhiebel, H. Souchay, and B. Jouffrey. The physical significance of the mixed dynamic form factor. *Micron*, 31(4):333 – 345, 2000. ISSN 0968-4328. DOI: [https://doi.org/10.1016/S0968-4328\(99\)00112-2](https://doi.org/10.1016/S0968-4328(99)00112-2). URL <http://www.sciencedirect.com/science/article/pii/S0968432899001122>.
- [213] Jo Verbeeck, Peter Schattschneider, and Andreas Rosenauer. Image simulation of high resolution energy filtered TEM images. *Ultramicroscopy*, 109(4):350 – 360, 2009. ISSN 0304-3991.

Bibliography

- DOI: <https://doi.org/10.1016/j.ultramic.2009.01.003>. URL <http://www.sciencedirect.com/science/article/pii/S0304399109000047>.
- [214] Ampere A Tseng. Recent developments in micromilling using focused ion beam technology. *Journal of Micromechanics and Microengineering*, 14(4):R15, 2004. URL <http://stacks.iop.org/0960-1317/14/i=4/a=R01>.
- [215] Nan Yao. *Focused Ion Beam System—a Multifunctional Tool for Nanotechnology*, pages 247–286. 01 2005. DOI: 10.1007/1-4020-8006-9_9.
- [216] L. Bruchhaus, P. Mazarov, L. Bischoff, J. Gierak, A. D. Wieck, and H. Hövel. Comparison of technologies for nano device prototyping with a special focus on ion beams: A review. *Applied Physics Reviews*, 4(1):011302, 2017. DOI: 10.1063/1.4972262. URL <https://doi.org/10.1063/1.4972262>.
- [217] A. Nadzeyka, L. Peto, S. Bauerdick, M. Mayer, K. Keskinbora, C. Grévent, M. Weigand, M. Hirscher, and G. Schütz. Ion beam lithography for direct patterning of high accuracy large area x-ray elements in gold on membranes. *Microelectronic Engineering*, 98:198 – 201, 2012. ISSN 0167-9317. DOI: <https://doi.org/10.1016/j.mee.2012.07.036>. URL <http://www.sciencedirect.com/science/article/pii/S0167931712003188>. Special issue MNE 2011 - Part II.
- [218] Jason D. Fowlkes, Robert Winkler, Brett B. Lewis, Michael G. Stanford, Harald Plank, and Philip D. Rack. Simulation-guided 3D nanomanufacturing via focused electron beam induced deposition. *ACS Nano*, 10(6):6163–6172, 2016. DOI: 10.1021/acs.nano.6b02108. URL <http://dx.doi.org/10.1021/acs.nano.6b02108>. PMID: 27284689.
- [219] Mukesh Tripathi, Andreas Mittelberger, Nicholas A. Pike, Clemens Mangler, Jannik C. Meyer, Matthieu J. Verstraete, Jani Kotakoski, and Toma Susi. Electron-beam manipulation of silicon dopants in graphene. *Nano Letters*, 18(8):5319–5323, 2018. DOI: 10.1021/acs.nanolett.8b02406. URL <https://doi.org/10.1021/acs.nanolett.8b02406>. PMID: 29945442.
- [220] Michael Schmid. A simple sputter yield calculator. Online, 2006. URL <https://www.iap.tuwien.ac.at/www/surface/sputteryield>.
- [221] Noriaki Matsunami, Yasunori Yamamura, Yukikazu Itikawa, Noriaki Itoh, Yukio Kazumata, Soji Miyagawa, Kenji Morita, Ryuichi Shimizu, and Hiroyuki Tawara. Energy dependence of the ion-induced sputtering yields of monatomic solids. *Atomic Data and Nuclear Data Tables*, 31(1):1 – 80, 1984. ISSN 0092-640X. DOI: [https://doi.org/10.1016/0092-640X\(84\)90016-0](https://doi.org/10.1016/0092-640X(84)90016-0). URL <http://www.sciencedirect.com/science/article/pii/0092640X84900160>.
- [222] Y. Yamamura and Shigeru Shindo. An empirical formula for angular dependence of sputtering yields. *Radiation Effects*, 80(1-2):57–72,

1984. DOI: 10.1080/00337578408222489. URL <https://doi.org/10.1080/00337578408222489>.
- [223] Zheng Cui. *Nanofabrication; principles, capabilities and limits*. Springer, New York, NY, 2008. ISBN 978-0-387-75576-2; 0-387-75576-4. DOI: 10.1007/978-0-387-75577-9.
- [224] Anton Bergauer and Christoph Eisenmenger-Sittner. Physik und Technologie dünner Schichten. Lecture Notes, 2006. LVA: 138.030,138.032.
- [225] Paul Heinz Mayrhofer. Oberflächentechnik/surface technology lecture script (308.875 ss 2017). Lecture Script, 2017.
- [226] Gerhard Franz. Sputterprozesse - TU München - Lecture Notes. Online Lecture Notes, 2015. URL https://www.fb06.fh-muenchen.de/fb/index.php/de/download.html?f_id=18123.
- [227] Jaydeep Sarkar. Chapter 2 - sputtering and thin film deposition. In Jaydeep Sarkar, editor, *Sputtering Materials for VLSI and Thin Film Devices*, pages 93 – 170. William Andrew Publishing, Boston, 2014. ISBN 978-0-8155-1593-7. DOI: <https://doi.org/10.1016/B978-0-8155-1593-7.00002-3>. URL <https://www.sciencedirect.com/science/article/pii/B9780815515937000023>.
- [228] Eric E. Fullerton, M. J. Conover, J. E. Mattson, C. H. Sowers, and S. D. Bader. 150% magnetoresistance in sputtered Fe/Cr(100) superlattices. *Applied Physics Letters*, 63(12):1699–1701, 1993. DOI: 10.1063/1.110689. URL <https://doi.org/10.1063/1.110689>.
- [229] Y. Kudriavtsev, A. Villegas, A. Godines, and R. Asomoza. Calculation of the surface binding energy for ion sputtered particles. *Applied Surface Science*, 239(3):273 – 278, 2005. ISSN 0169-4332. DOI: <https://doi.org/10.1016/j.apsusc.2004.06.014>. URL <http://www.sciencedirect.com/science/article/pii/S0169433204009560>.
- [230] Hiroki Matsui, Hirotaka Toyoda, and Hideo Sugai. High-energy ions and atoms sputtered and reflected from a magnetron source for deposition of magnetic thin films. *Journal of Vacuum Science & Technology A*, 23(4):671–675, 2005. DOI: 10.1116/1.1943452. URL <https://doi.org/10.1116/1.1943452>.
- [231] D. W. Hoffman. Perspective on stresses in magnetron-sputtered thin films. *Journal of Vacuum Science & Technology A: Vacuum, Surfaces, and Films*, 12(4):953–961, 1994. DOI: 10.1116/1.579073. URL <http://dx.doi.org/10.1116/1.579073>.
- [232] Kitty W. Lee, Yu-Hsia Chen, Yip-Wah Chung, and Leon M. Keer. Hardness, internal stress and thermal stability of TiB₂/TiC multilayer coatings synthesized by magnetron sputtering with and without substrate rotation. *Surface*

Bibliography

- and Coatings Technology*, 177(Supplement C):591 – 596, 2004. ISSN 0257-8972. DOI: [https://doi.org/10.1016/S0257-8972\(03\)00931-9](https://doi.org/10.1016/S0257-8972(03)00931-9). URL <http://www.sciencedirect.com/science/article/pii/S0257897203009319>. Proceedings of the 30th International Conference on Metallurgical Coatings and Thin Films.
- [233] N. Panich and Y. Sun. Effect of substrate rotation on structure, hardness and adhesion of magnetron sputtered TiB₂ coating on high speed steel. *Thin Solid Films*, 500(1):190 – 196, 2006. ISSN 0040-6090. DOI: <https://doi.org/10.1016/j.tsf.2005.11.055>. URL <http://www.sciencedirect.com/science/article/pii/S0040609005022650>.
- [234] Ivan A. Starkov, Ilya A. Nyapshaev, Alexander S. Starkov, Sergey N. Abolmasov, Alexey S. Abramov, Vladimir S. Levitskii, and Evgeny I. Terukov. Influence of substrate movement on the ITO film thickness distribution during magnetron sputtering. *Journal of Vacuum Science & Technology A: Vacuum, Surfaces, and Films*, 35(6):061301, 2017. DOI: 10.1116/1.4991527. URL <http://dx.doi.org/10.1116/1.4991527>.
- [235] John A. Thornton and D.W. Hoffman. Stress-related effects in thin films. *Thin Solid Films*, 171(1):5 – 31, 1989. ISSN 0040-6090. DOI: [https://doi.org/10.1016/0040-6090\(89\)90030-8](https://doi.org/10.1016/0040-6090(89)90030-8). URL <http://www.sciencedirect.com/science/article/pii/0040609089900308>.
- [236] A.M. Engwall, Z. Rao, and E. Chason. Origins of residual stress in thin films: Interaction between microstructure and growth kinetics. *Materials & Design*, 110:616 – 623, 2016. ISSN 0264-1275. DOI: <https://doi.org/10.1016/j.matdes.2016.07.089>. URL <http://www.sciencedirect.com/science/article/pii/S026412751630987X>.
- [237] A. Walkiewicz. The influence of coating quality on SEM imaging of PVdF electrospinning fibres. Technical report, Quorum Technologies, 2018. URL <https://www.quorumtech.com/case-study/the-influence-of-coating-quality-on-sem-imaging-of-pvdf-electrospinning-fibres>
- [238] H.P. Martinz and R. Abermann. Interaction of O₂, CO, H₂O, H₂ and N₂ with thin chromium films studied by internal stress measurements. *Thin Solid Films*, 89(2):133 – 138, 1982. ISSN 0040-6090. DOI: [https://doi.org/10.1016/0040-6090\(82\)90440-0](https://doi.org/10.1016/0040-6090(82)90440-0). URL <http://www.sciencedirect.com/science/article/pii/0040609082904400>.
- [239] A. Misra and M. Nastasi. The role of oxygen in the intrinsic tensile residual stress evolution in sputter-deposited thin metal films. *Journal of Vacuum Science & Technology A: Vacuum, Surfaces, and Films*, 18(5):2517–2521, 2000. DOI: 10.1116/1.1286393. URL <http://avs.scitation.org/doi/abs/10.1116/1.1286393>.

- [240] Rebecca Grinham and Andrew Chew. A review of outgassing and methods for its reduction. *Applied Science and Convergence Technology*, 26(5):95 – 109, 09 2017. DOI: 10.5757/asct.2017.26.5.95. URL <https://doi.org/10.5757/ASCT.2017.26.5.95>.
- [241] TeamOfAuthors. Leak detection compendium. Technical report, Pfeiffer Vacuum GmbH, 2013. URL <https://leak-detection.pfeiffer-vacuum.com/filepool/File/Literature/PL0006PEN-Leak-detection-Compendium.pdf>.
- [242] Max Wutz, Herman Adam, and Wilhelm Walcher. *Theorie und Praxis der Vakuumtechnik*. Vieweg, 3.auflage edition, 1986.
- [243] J D Fast. Experiments on the permeation of gases through metal walls. *Phillips Technical Review*, 7(3):74 – 82, 1942.
- [244] Etienne Cuche, Yves Emery, and Frédéric Montfort. One-shot analysis. *Nature Photonics*, 3:633, 2009. URL <https://doi.org/10.1038/nphoton.2009.207>.
- [245] Mikhail N. Polyanskiy. Refractive index database. <https://refractiveindex.info>. Accessed on 2019-02-20.
- [246] N. Savvides and B. Window. Diamondlike amorphous carbon films prepared by magnetron sputtering of graphite. *Journal of Vacuum Science & Technology A: Vacuum, Surfaces, and Films*, 3(6):2386–2390, 1985. DOI: 10.1116/1.572887. URL <https://doi.org/10.1116/1.572887>.
- [247] Li Yan and John A. Woollam. Optical constants and roughness study of dc magnetron sputtered iridium films. *Journal of Applied Physics*, 92(8):4386–4392, 2002. DOI: 10.1063/1.1509091. URL <https://doi.org/10.1063/1.1509091>.
- [248] Rene A. Haefler. *Oberflächen- und Dünnschicht-Technologie*. Springer-Verlag Berlin Heidelberg, 1987. ISBN 978-3-540-16723-5. DOI: 10.1007/978-3-642-82835-5.
- [249] C Salvador, T Freire, C G Bezerra, C Chesman, E A Soares, R Paniago, E Silva-Pinto, and B R A Neves. Properties of Fe/MgO (1 0 0) nanometric films grown by dc sputtering. *Journal of Physics D: Applied Physics*, 41(20):205005, sep 2008. DOI: 10.1088/0022-3727/41/20/205005. URL <https://doi.org/10.1088/0022-3727/41/20/205005>.
- [250] Anna Walkiewicz. Carbon thin film preparation for ambient and cryo-TEM grids using the Q150V plus. Technical report, Quorum Technologies, 2018. URL https://www.quorumtech.com/__assets__/WebPages/00162/Carbon-application-Rev-0.pdf.

Bibliography

- [251] I. Stokroos, D. Kalicharan, J. J. L. Van Der Want, and W. L. Jongebloed. A comparative study of thin coatings of Au/Pd, Pt and Cr produced by magnetron sputtering for FE-SEM. *Journal of Microscopy*, 189(1):79–89, 1998. DOI: 10.1046/j.1365-2818.1998.00282.x. URL <https://doi.org/10.1046/j.1365-2818.1998.00282.x>.
- [252] Pfeiffer Vacuum Operating Instructions. *Pfeiffer Compact FullRangeTM Gauge, FPM sealed, PKR 251*. Pfeiffer Vacuum, 2019. URL https://www.idealvac.com/files/brochures/Pfeiffer_PKR_251_Pirani_ColdCathode.pdf.
- [253] TeamOfAuthors. *The Vacuum Technology Book Volume II*. PfeifferVacuumGmbH, 2013. URL https://www.pfeiffer-vacuum.com/filepool/file/vacuum-technology-book/vacuum-technology-book-ii-band-2.pdf?referer=1456&request_locale=de_DE.
- [254] S. D. Bernstein, T. Y. Wong, and R. W. Tustison. Magnetron sputtering of Fe onto GaAs substrates: Energetic bombardment effects. *Journal of Applied Physics*, 72(9):4358–4365, 1992. DOI: 10.1063/1.352200. URL <https://doi.org/10.1063/1.352200>.
- [255] Yasuo Gondō. Domain structure in single-crystal thin films of iron. *Journal of the Physical Society of Japan*, 17(7):1129–1136, 1962. DOI: 10.1143/JPSJ.17.1129. URL <https://doi.org/10.1143/JPSJ.17.1129>.
- [256] Niklas Luhmann, Artur Jachimowicz, Johannes Schalko, Pedram Sadeghi, Markus Sauer, Annette Foelske-Schmitz, and Silvan Schmid. Effect of oxygen plasma on nanomechanical silicon nitride resonators. *Applied Physics Letters*, 111(6):063103, 2017. DOI: 10.1063/1.4989775. URL <https://doi.org/10.1063/1.4989775>.
- [257] R. Abermann and R. Koch. Internal stress of thin silver and gold films and its dependence on gas adsorption. *Thin Solid Films*, 62(2):195 – 208, 1979. ISSN 0040-6090. DOI: [https://doi.org/10.1016/0040-6090\(79\)90306-7](https://doi.org/10.1016/0040-6090(79)90306-7). URL <http://www.sciencedirect.com/science/article/pii/0040609079903067>.
- [258] Junyoung Yu and Youngman Kim. Stress shift to tensile side by the interruption of deposition during Al and Cr film processing. *MATERIALS TRANSACTIONS*, 55(11):1777–1780, 2014. DOI: 10.2320/matertrans.M2014207.
- [259] Liang Liu, Wei guo Liu, Na Cao, and Chang long Cai. Study on the performance of PECVD silicon nitride thin films. *Defence Technology*, 9(2):121 – 126, 2013. ISSN 2214-9147. DOI: <https://doi.org/10.1016/j.dt.2013.10.004>. URL <http://www.sciencedirect.com/science/article/pii/S2214914713000366>.
- [260] SCHOTT. *Datasheet: BOROFLOAT® 33 – Mechanical Properties*. SCHOTT Technical Glass Solutions GmbH, 2018. URL https://www.schott.com/d/borofloat/4fa3f803-e7bf-4f88-8754-511971ecfa65/1.4/borofloat33_mech_de_web_08_2018.pdf.

- [261] Ivan Shorubalko, Kyoungjun Choi, Michael Stiefel, and Hyung Gyu Park. Ion beam profiling from the interaction with a freestanding 2D layer. *Beilstein Journal of Nanotechnology*, 8:682–687, 2017. ISSN 2190-4286. DOI: 10.3762/bjnano.8.73.
- [262] S A Rishton, S P Beaumont, and C D W Wilkinson. Measurement of the profile of finely focused electron beams in a scanning electron microscope. *Journal of Physics E: Scientific Instruments*, 17(4):296–303, apr 1984. DOI: 10.1088/0022-3735/17/4/011. URL <https://doi.org/10.1088/0022-3735/17/4/011>.
- [263] Yasuyuki Ishii, Akira Isoya, Takuji Kojima, and Kazuo Arakawa. Estimation of keV submicron ion beam width using a knife-edge method. *Nuclear Instruments and Methods in Physics Research Section B: Beam Interactions with Materials and Atoms*, 211(3):415 – 424, 2003. ISSN 0168-583X. DOI: [https://doi.org/10.1016/S0168-583X\(03\)01370-3](https://doi.org/10.1016/S0168-583X(03)01370-3). URL <http://www.sciencedirect.com/science/article/pii/S0168583X03013703>.
- [264] Leonhardt. ZAMG daily geomagnetic variation. Online, 2019. URL <http://www.conrad-observatory.at/zamg/index.php/de/data-de/daily-magnetogram-de>.
- [265] R. Leonhardt, J. Matzka, and M. Wack. MagPy - a python based software for analyzing geomagnetic observatory measurements. In *XVth IAGA Workshop on Geomagnetic Observatory Instruments, Acquisition and Processing*, pages 169–172, 2013.
- [266] Anto Yasaka, Fumio Aramaki, Masashi Muramatsu, Tomokazu Kozakai, Osamu Matsuda, Yasuhiko Sugiyama, Toshio Doi, Osamu Takaoka, Ryoji Hagiwara, and Koji Nakamae. Application of vector scanning in focused ion beam photomask repair system. *Journal of Vacuum Science & Technology B: Microelectronics and Nanometer Structures Processing, Measurement, and Phenomena*, 26(6):2127–2130, 2008. DOI: 10.1116/1.2976574. URL <https://avs.scitation.org/doi/abs/10.1116/1.2976574>.
- [267] Lothar Bischoff and Jochen Teichert. Focused ion beam sputtering of silicon and related materials. *Research Center Rossendorf Inc., FZR-217*, 1998. URL <https://www.hzdr.de/publications/PublDoc-1805pdf>.
- [268] Hong-Shi Kuo, Ing-Shouh Hwang, Tsu-Yi Fu, Ying-Siang Hwang, Yi-Hsien Lu, Chun-Yueh Lin, Jin-Long Hou, and Tien T Tsong. A single-atom sharp iridium tip as an emitter of gas field ion sources. *Nanotechnology*, 20(33):335701, 2009. URL <http://stacks.iop.org/0957-4484/20/i=33/a=335701>.
- [269] W. M. Haynes, editor. *CRC Handbook of Chemistry and Physics*. Taylor & Francis Ltd., 97th edition edition, 2016. ISBN 9781498754286.

Bibliography

- URL http://www.ebook.de/de/product/25831956/crc_handbook_of_chemistry_and_physics_96th_edition.html.
- [270] Michael Marko, Xing Meng, Chyongere Hsieh, James Roussie, and Christopher Striemer. Methods for testing zernike phase plates and a report on silicon-based phase plates with reduced charging and improved ageing characteristics. *Journal of Structural Biology*, 184(2):237 – 244, 2013. ISSN 1047-8477. DOI: <https://doi.org/10.1016/j.jsb.2013.08.008>. URL <http://www.sciencedirect.com/science/article/pii/S1047847713002141>.
- [271] Jani Hämäläinen, Timo Sajavaara, Esa Puukilainen, Mikko Ritala, and Markku Leskelä. Atomic layer deposition of Osmium. *Chemistry of Materials*, 24(1): 55–60, 2012. DOI: [10.1021/cm201795s](https://doi.org/10.1021/cm201795s). URL <http://dx.doi.org/10.1021/cm201795s>.
- [272] L. Dubrovinsky, N. Dubrovinskaia, E. Bykova, M. Bykov, V. Prakapenka, C. Prescher, K. Glazyrin, H.-P. Liermann, M. Hanfland, M. Ekholm, Q. Feng, L. V. Pourovskii, M. I. Katsnelson, J. M. Wills, and I. A. Abrikosov. The most incompressible metal osmium at static pressures above 750 gigapascals. *Nature*, 525:226–, August 2015. URL <https://doi.org/10.1038/nature14681>.
- [273] S.L. Li, C.Y. Ma, Q.Y. Zhang, X.P. Liu, C. Zhang, and Z. Yi. Preparation and characterization of osmium films on quartz substrate by magnetron sputtering method. *Surface and Coatings Technology*, 282:1 – 5, 2015. ISSN 0257-8972. DOI: <https://doi.org/10.1016/j.surfcoat.2015.10.010>. URL <http://www.sciencedirect.com/science/article/pii/S0257897215303066>.
- [274] D. Josell, C. Witt, and T. P. Moffat. Osmium barriers for direct copper electrodeposition in damascene processing. *Electrochemical and Solid-State Letters*, 9(2):C41–C43, 2006. DOI: [10.1149/1.2149214](https://doi.org/10.1149/1.2149214). URL <http://esl.ecsd1.org/content/9/2/C41.abstract>.
- [275] M. A. El Khakani, M. Chaker, and B. Le Drogoff. Iridium thin films deposited by radio-frequency magnetron sputtering. *Journal of Vacuum Science & Technology A: Vacuum, Surfaces, and Films*, 16(2):885–888, 1998. DOI: [10.1116/1.581029](https://doi.org/10.1116/1.581029). URL <http://dx.doi.org/10.1116/1.581029>.
- [276] Alexander Kramida and Yuri Ralchenko. NIST atomic spectra database, NIST standard reference database 78, 1999. URL <https://doi.org/10.18434/T4W30F>.
- [277] V. Ziebart, O. Paul, and H. Baltes. Strongly buckled square micromachined membranes. *Journal of Microelectromechanical Systems*, 8(4):423–432, Dec 1999. ISSN 1057-7157. DOI: [10.1109/84.809057](https://doi.org/10.1109/84.809057).
- [278] P.E. Batson, A. Reyes-Coronado, R.G. Barrera, A. Rivacoba, P.M. Echenique, and J. Aizpurua. Nanoparticle movement: Plasmonic forces and phys-

- ical constraints. *Ultramicroscopy*, 123:50 – 58, 2012. ISSN 0304-3991. DOI: <http://dx.doi.org/10.1016/j.ultramic.2012.05.004>. URL <http://www.sciencedirect.com/science/article/pii/S0304399112001064>. Albert Victor Crewe Memorial Issue.
- [279] S. K. Lamoreaux. Demonstration of the Casimir force in the 0.6 to 6 μm range. *Phys. Rev. Lett.*, 78:5–8, Jan 1997. DOI: 10.1103/PhysRevLett.78.5. URL <http://link.aps.org/doi/10.1103/PhysRevLett.78.5>.
- [280] G. L. Klimchitskaya, U. Mohideen, and V. M. Mostepanenko. Casimir and van der waals forces between two plates or a sphere (lens) above a plate made of real metals. *Phys. Rev. A*, 61:062107, May 2000. DOI: 10.1103/PhysRevA.61.062107. URL <https://link.aps.org/doi/10.1103/PhysRevA.61.062107>.
- [281] David L. Windt. Low-stress W/Cr films for SCALPEL® mask scattering layers. *Journal of Vacuum Science & Technology B: Microelectronics and Nanometer Structures Processing, Measurement, and Phenomena*, 17(4):1385–1389, 1999. DOI: 10.1116/1.590841. URL <http://avs.scitation.org/doi/abs/10.1116/1.590841>.
- [282] David M Broadway, Jeffrey Weimer, Danielle Gurgew, Tomasz Lis, Brian D Ramsey, Stephen L O’Dell, Mikhail Gubarev, A Ames, and R Bruni. Achieving zero stress in iridium, chromium, and nickel thin films. In *SPIE Optics+ Optoelectronics*, pages 95100E–95100E. International Society for Optics and Photonics, 2015.
- [283] Arif Sinan Alagoz, Jan-Dirk Kamminga, Sergey Grachev, Toh-Ming Lu, and Tansel Karabacak. Residual stress reduction in sputter deposited thin films by density modulation. *MRS Proceedings*, 1224, 01 2009. DOI: 10.1557/PROC-1224-FF05-22.
- [284] D. Winau, R. Koch, and K. H. Rieder. The influence of oxygen on intrinsic stress and growth of iron and nickel films. *Applied Physics Letters*, 59(9): 1072–1074, 1991. DOI: 10.1063/1.106348. URL <https://doi.org/10.1063/1.106348>.
- [285] T. A. Savas, M. L. Schattenburg, J. M. Carter, and Henry I. Smith. Large-area achromatic interferometric lithography for 100 nm period gratings and grids. *Journal of Vacuum Science & Technology B, Nanotechnology and Microelectronics: Materials, Processing, Measurement, and Phenomena*, 14:4167, 1996. DOI: 10.1116/1.588613.
- [286] Hang Z. Yu and Carl V. Thompson. Stress engineering using low oxygen background pressures during Volmer–Weber growth of polycrystalline nickel films. *Journal of Vacuum Science & Technology A*, 33(2):021504, 2015. DOI: 10.1116/1.4902957. URL <https://doi.org/10.1116/1.4902957>.

Bibliography

- [287] Radostin Danev, Robert M. Glaeser, and Kuniaki Nagayama. Practical factors affecting the performance of a thin-film phase plate for transmission electron microscopy. *Ultramicroscopy*, 109(4):312 – 325, 2009. ISSN 0304-3991. DOI: <https://doi.org/10.1016/j.ultramic.2008.12.006>. URL <http://www.sciencedirect.com/science/article/pii/S0304399108003367>.
- [288] Ján Rusz, Somnath Bhowmick, Mattias Eriksson, and Nikolaj Karlsson. Scattering of electron vortex beams on a magnetic crystal: Towards atomic-resolution magnetic measurements. *Physical Review B*, 89:134428, Apr 2014. DOI: 10.1103/PhysRevB.89.134428. URL <http://link.aps.org/doi/10.1103/PhysRevB.89.134428>.
- [289] R. Steiger, S. Bernet, and M. Ritsch-Marte. Mapping of phase singularities with spiral phase contrast microscopy. *Optics Express*, 21(14):16282–16289, 2013. DOI: 10.1364/OE.21.016282.
- [290] Roeland Juchtmans and Jo Verbeeck. Local orbital angular momentum revealed by spiral-phase-plate imaging in transmission-electron microscopy. *Physical Review A*, 93:023811, Feb 2016. DOI: 10.1103/PhysRevA.93.023811. URL <http://link.aps.org/doi/10.1103/PhysRevA.93.023811>.
- [291] Y. Wu, J. Stöhr, B. D. Hermsmeijer, M. G. Samant, and D. Keller. Enhanced orbital magnetic moment on Co atoms in Co/Pd multilayers: A magnetic circular X-ray dichroism study. *Physical Review Letters*, 69(15):2307–2310, 1992. DOI: 10.1103/PhysRevLett.69.2307.
- [292] S. T. Manson. Inelastic collisions of fast charged particles with atoms: Ionization of the aluminum L- shell. *Physical Review A*, 6:1013–1024, 1972. DOI: 10.1103/PhysRevA.6.1013.
- [293] S. Löffler, I. Ennen, F. Tian, P. Schattschneider, and N. Jaouen. Breakdown of the dipole approximation in core losses. *Ultramicroscopy*, 111(8):1163 – 1167, 2011. DOI: 10.1016/j.ultramic.2011.03.006.
- [294] Jutta M. Auerhammer and Peter Rez. Dipole-forbidden excitations in electron-energy-loss spectroscopy. *Physical Review B*, 40:2024–2030, Aug 1989. DOI: 10.1103/PhysRevB.40.2024. URL <http://link.aps.org/doi/10.1103/PhysRevB.40.2024>.
- [295] P. Schattschneider, J. Verbeeck, V. Mauchamp, M. Jaouen, and A. Hamon. Real-space simulations of spin-polarized electronic transitions in iron. *Physical Review B - Condensed Matter and Materials Physics*, 82(14), 2010. DOI: 10.1103/Physrevb.82.144418.
- [296] T. Schachinger, S. Löffler, A. Steiger-Thirsfeld, M. Stöger-Pollach, S. Schneider, D. Pohl, B. Rellinghaus, and P. Schattschneider. EMCD with an electron vortex filter: Limitations and possibilities. *Ultramicroscopy*, 179:15 – 23, 2017. ISSN

- 0304-3991. DOI: <http://dx.doi.org/10.1016/j.ultramic.2017.03.019>. URL <http://www.sciencedirect.com/science/article/pii/S0304399117301195>.
- [297] R F Egerton. Electron energy-loss spectroscopy in the TEM. *Reports on Progress in Physics*, 72(1):016502 (25pp), 2009. DOI: 10.1088/0034-4885/72/1/016502. URL <http://stacks.iop.org/0034-4885/72/016502>.
- [298] M. Abramowitz and I. Stegun. *Handbook of Mathematical Functions*. Dover Publications, 1965.
- [299] P. Schattschneider, M. Nelhiebel, and B. Jouffrey. Density matrix of inelastically scattered fast electrons. *Physical Review B*, 59:10959–10969, Apr 1999. DOI: 10.1103/PhysRevB.59.10959. URL <http://link.aps.org/doi/10.1103/PhysRevB.59.10959>.
- [300] Stefan Löffler and Peter Schattschneider. Transition probability functions for applications of inelastic electron scattering. *Micron (Oxford, England : 1993)*, 43(9):971–977, September 2012. ISSN 0968-4328. DOI: 10.1016/j.micron.2012.03.020. URL <http://europepmc.org/articles/PMC3425432>.
- [301] P. Schattschneider, I. Ennen, S. Löffler, M. Stöger-Pollach, and J. Verbeeck. Circular dichroism in the electron microscope: Progress and applications (invited). *Journal of Applied Physics*, 107(9):09D311, 2010. DOI: 10.1063/1.3365517.
- [302] S. Löffler and P. Schattschneider. Elastic propagation of fast electron vortices through crystals. *Acta Crystallographica Section A*, A68:443–447, 2012. DOI: 10.1107/S0108767312013189.
- [303] Huolin L. Xin and Haimei Zheng. On-column 2p bound state with topological charge ± 1 excited by an atomic-size vortex beam in an aberration-corrected scanning transmission electron microscope. *Microscience and Microanalytics*, 18:711, 2012. DOI: 10.1017/S1431927612000499.
- [304] Giseller Herzer. Modern soft magnets: Amorphous and nanocrystalline materials. *Acta Materialia*, 61(3):718 – 734, 2013. ISSN 1359-6454. DOI: <https://doi.org/10.1016/j.actamat.2012.10.040>. URL <http://www.sciencedirect.com/science/article/pii/S1359645412007872>. The Diamond Jubilee Issue.
- [305] Hikaru Tamura, Tomoyuki Unakami, Jun He, Yoko Miyamoto, and Ken’ichi Nakagawa. Highly uniform holographic microtrap arrays for single atom trapping using a feedback optimization of in-trap fluorescence measurements. *Opt. Express*, 24(8):8132–8141, Apr 2016. DOI: 10.1364/OE.24.008132. URL <http://www.opticsexpress.org/abstract.cfm?URI=oe-24-8-8132>.

Bibliography

- [306] Daobin Liu, Chuanqiang Wu, Shuangming Chen, Shiqing Ding, Yaofeng Xie, Changda Wang, Tao Wang, Yasir A. Haleem, Zia ur Rehman, Yuan Sang, Qin Liu, Xusheng Zheng, Yu Wang, Binghui Ge, Hangxun Xu, and Li Song. In situ trapped high-density single metal atoms within graphene: Iron-containing hybrids as representatives for efficient oxygen reduction. *Nano Research*, 11(4): 2217–2228, Apr 2018. ISSN 1998-0000. DOI: 10.1007/s12274-017-1840-8. URL <https://doi.org/10.1007/s12274-017-1840-8>.
- [307] Yung-Chang Lin, Po-Yuan Teng, Po-Wen Chiu, and Kazu Suenaga. Exploring the single atom spin state by electron spectroscopy. *Phys. Rev. Lett.*, 115: 206803, Nov 2015. DOI: 10.1103/PhysRevLett.115.206803. URL <http://link.aps.org/doi/10.1103/PhysRevLett.115.206803>.
- [308] R. E. Grisenti, W. Schöllkopf, J. P. Toennies, G. C. Hegerfeldt, and T. Köhler. Determination of atom-surface van der Waals potentials from transmission-grating diffraction intensities. *Phys. Rev. Lett.*, 83:1755–1758, Aug 1999. DOI: 10.1103/PhysRevLett.83.1755. URL <http://link.aps.org/doi/10.1103/PhysRevLett.83.1755>.
- [309] R. E. Grisenti, W. Schöllkopf, J. P. Toennies, J. R. Manson, T. A. Savas, and Henry I. Smith. He-atom diffraction from nanostructure transmission gratings: The role of imperfections. *Physical Review A*, 61:033608, Feb 2000. DOI: 10.1103/PhysRevA.61.033608. URL <http://link.aps.org/doi/10.1103/PhysRevA.61.033608>.
- [310] Brett Barwick, Glen Gronniger, Lu Yuan, Sy-Hwang Liou, and Herman Batelaan. A measurement of electron-wall interactions using transmission diffraction from nanofabricated gratings. *Journal of Applied Physics*, 2006. DOI: 10.1063/1.2357000.
- [311] Ben McMorran, John D. Perreault, T.A. Savas, and Alex Cronin. Diffraction of 0.5 keV electrons from free-standing transmission gratings. *Ultramicroscopy*, 106(4-5):356 – 364, 2006. ISSN 0304-3991. DOI: <http://dx.doi.org/10.1016/j.ultramic.2005.11.003>. URL <http://www.sciencedirect.com/science/article/pii/S0304399105002329>.
- [312] C. Kramberger, S. Löffler, T. Schachinger, P. Hartel, J. Zach, and P. Schattschneider. $\pi/2$ mode converters and vortex generators for electrons. *Ultramicroscopy*, 204:27–33, 2019. ISSN 0304-3991. DOI: <https://doi.org/10.1016/j.ultramic.2019.05.003>. URL <http://www.sciencedirect.com/science/article/pii/S0304399118304029>.
- [313] C.A. Schneider, W.S. Rasband, and K.W. Eliceiri. Nih image to imagej: 25 years of image analysis. *Nature Methods*, 9:671–675, 2012. DOI: 10.1038/nmeth.2089.

- [314] Michael Richmond. Physics 373: Observational astronomy, readout noise, and total noise. Online Lecture Notes, 2014. URL <http://spiff.rit.edu/classes/phys373/lectures/readout/readout.html>.
- [315] Photometrics. Keep the noise down! low noise: An integral part of high-performance CCD (HCCD) camera systems. Technical note, Photometrics, 2010. URL <https://www.photometrics.com/resources/technotes/pdfs/snr.pdf>.
- [316] Steve B. Howell. Two-dimensional aperture photometry - signal-to-noise ratio of point-source observations and optimal data-extraction techniques. *Publications of the Astronomical Society of the Pacific*, 101:616, jun 1989. DOI: 10.1086/132477. URL <https://doi.org/10.1086%2F132477>.
- [317] John R. Taylor. *An Introduction to Error Analysis: The Study of Uncertainties in Physical Measurements*. University Science Books, 2nd edition, 1997.
- [318] R.F. Egerton. Mechanisms of radiation damage in beam-sensitive specimens, for TEM accelerating voltages between 10 and 300 kV. *Microscopy Research and Technique*, 75(11):1550–1556, 2012. DOI: 10.1002/jemt.22099.
- [319] Thomas Thersleff, Ján Ruzs, Björgvin Hjörvarsson, and Klaus Leifer. Detection of magnetic circular dichroism with subnanometer convergent electron beams. *Phys. Rev. B*, 94:134430, Oct 2016. DOI: 10.1103/PhysRevB.94.134430. URL <https://link.aps.org/doi/10.1103/PhysRevB.94.134430>.
- [320] C. Gatel, B. Warot Fonrose, and P. Schattschneider. Distortion corrections of ESI data cubes for magnetic studies. *Ultramicroscopy*, 109(12):1465–1471, 2009. ISSN 0304-3991. DOI: <https://doi.org/10.1016/j.ultramic.2009.08.001>. URL <http://www.sciencedirect.com/science/article/pii/S0304399109001843>.
- [321] Matahiro Komuro, Yuzoo Kozono, Masanobu Hanazono, and Yutaka Sugita. Epitaxial growth and magnetic properties of Fe₁₆N₂ films with high saturation magnetic flux density (invited). *Journal of Applied Physics*, 67(9):5126–5130, 1990. DOI: 10.1063/1.344689. URL <https://doi.org/10.1063/1.344689>.
- [322] Yeong Deok Han and Taeseung Choi. Classical understanding of electron vortex beams in a uniform magnetic field. *Physics Letters A*, 381(16):1335 – 1339, 2017. ISSN 0375-9601. DOI: <https://doi.org/10.1016/j.physleta.2017.02.031>. URL <http://www.sciencedirect.com/science/article/pii/S0375960116311859>.
- [323] Giulio Guzzinati, Peter Schattschneider, Konstantin Y. Bliokh, Franco Nori, and Jo Verbeeck. Observation of the larmor and gouy rotations with electron vortex beams. *Physical Review Letters*, 110:093601, Feb 2013. DOI: 10.1103/PhysRevLett.110.093601. URL <http://link.aps.org/doi/10.1103/PhysRevLett.110.093601>.

Bibliography

- [324] Konstantin Y. Bliokh, Peter Schattschneider, Jo Verbeeck, and Franco Nori. Electron vortex beams in a magnetic field: A new twist on Landau levels and Aharonov-Bohm states. *Physical Review X*, 2:041011, Nov 2012. DOI: 10.1103/PhysRevX.2.041011. URL <http://link.aps.org/doi/10.1103/PhysRevX.2.041011>.
- [325] Axel Lubk, Laura Clark, Giulio Guzzinati, and Jo Verbeeck. Topological analysis of paraxially scattered electron vortex beams. *Physical Review A*, 87:033834, Mar 2013. DOI: 10.1103/PhysRevA.87.033834. URL <http://link.aps.org/doi/10.1103/PhysRevA.87.033834>.
- [326] J. Arlt. Handedness and azimuthal energy flow of optical vortex beams. *Journal of Modern Optics*, 50:1573–1580, 2003. DOI: 10.1080/09500340308235231.
- [327] H. X. Cui, X. L. Wang, B. Gu, Y. N. Li, J. Chen, and H. T. Wang. Angular diffraction of an optical vortex induced by the Gouy phase. *Journal of Optics*, 14:055707, 2012. DOI: 10.1088/2040-8978/14/5/055707.
- [328] L. Reimer. *Transmission Electron Microscopy - Physics of Image Formation and Microanalysis*, volume 36 of *Springer Series in Optical Sciences*. Springer, 1984. ISBN 3-540-11794-6.
- [329] Matteo Zanfagnini, Enzo Rotunno, Stefano Frabboni, Alicia Sit, Ebrahim Karimi, Ulrich Hohenester, and Vincenzo Grillo. Orbital angular momentum and energy loss characterization of plasmonic excitations in metallic nanostructures in TEM. *ACS Photonics*, 6(3):620–627, 2019. DOI: 10.1021/acsp Photonics.9b00131. URL <https://doi.org/10.1021/acsp Photonics.9b00131>.

.:Curriculum Vitae – DI Thomas Schachinger - 2019:.

Title/Name: Dipl. Ing. Thomas Schachinger
Date/Place of Birth 26.08.1983 in Wels in Upper Austria
Nationality: Austria
Address: USTEM, Wiedner Hauptstraße 8-10/E057B, A-1040 Vienna
E-Mail: thomas.schachinger@tuwien.ac.at
Family status: Married, 4 children



Work/Project Experience:

- 2014-ongoing:** Electron microscopist at USTEM, working in the field of analytical transmission electron microscopy (TEM, STEM, EDX, EELS, EFTEM, Cathodoluminescence) on various material classes like nanostructured clathrates, oxide materials for solid oxide fuel cells and organic solar cells, TU Wien, Austria.
- 2005:** Service and product development engineer at Lasercon GmbH, producing laser projectors for measurement applications, Arnoldstein, Austria.
- 2004:** Development and installation of a new turnstile-less entrance system, which was using horizontal water jets as a barrier element. This “Watergate” was set up in the entrance area of the Austrian pavilion on the world exposition 2004 in Aichi, Japan.
- 2003-2004:** Military service in the “Jägerbattalion 26”, Spittal an der Drau, Carinthia.

Academic Progress:

- 2014-ongoing:** PhD studies at the TU Wien supervised by Prof. Peter Schattschneider.
- 2012-2014:** Diploma thesis on “Electron Vortex Beam Propagation in Magnetic Fields”, supervised by Prof. Peter Schattschneider at the Institute of Solid-State Physics, TU Wien, Austria.
- 2008-2009** Studies abroad at the Technical University of Dresden, Germany, dealing with high-resolution transmission electron microscopy and holography at the Triebenberg lab of Prof. H. Lichte.
- 2005-2014** Studies of technical physics at the TU Wien, Austria.

Compulsory- and College Education:

- 1998-2003** Technical College (Höhere Technische Bundeslehranstalt Mössingerstraße) for electrical engineering; Final thesis: „Bike-Air-System“, a novel system which engages mountain bikers to dynamically adopt the pressure of their tires to the terrain characteristics, on the fly, when riding the bike, Klagenfurt, Carinthia.
- 1994-1998** Grammar School St. Martin, Villach, Carinthia, Austria.
- 1990-1994** Elementary School Latschach, Carinthia, Austria.

Awards:

"Best Image Award" awarded at the Microscopy Conference 2017 (MC2017) in Lausanne, Switzerland, for an outstanding micrograph of "Iridium Thin Film Buckling - A Picturesque Sign of Compressive Internal Stress", 25.8.2017.

Theodor-Körner-Preis 2017 awarded by the Theodor Körner Fonds for the project, “Magnetic chiral dichroism measurements with nanometre resolution using a vortex filter”, 14.06.2017.

Fritz-Grasenick-Preis 2015 awarded by the Austrian Society of Electron Microscopy (ASEM) for the Ultramicroscopy publication “*Peculiar Rotation of Electron Vortex Beams*”, 22.1.2016.

Funding:

Hochschuljubiläumsstiftung der Stadt Wien, 18.10.2016-30.06.2019, 11 k€, "Production of holographic electron vortex mask", H-294689/2016, PI.

DOC Austrian Academy of Science (ÖAW) Scholarship, 01.07.2017-30.06.2019, 79.8 k€, "Vorticity Filtering for Magnetic Dichroism Measurements with Nanometre Spatial Resolution", PI.

Journal Articles:

C. Kramberger, S. Löffler, T. Schachinger, P. Hartel, J. Zach, P. Schattschneider: „*Pi/2 Mode Converters and Vortex Generators for Electrons*“, Ultramicroscopy 204 (2019), 27-33, DOI: 10.1016/j.ultramic.2019.05.003.

T. Götsch, E.-M. Wernig, B. Klötzer, T. Schachinger, J. Kunze-Liebhäuser, S. Penner: „*An ultra-flexible modular high vacuum setup for thin film deposition*“, Review of Scientific Instruments, 90 (2019), 023902.

E. Aschauer, S. Sackl, T. Schachinger, T. Wojcik, M. Arndt, P. Polcik, H. Riedl, P.H. Mayrhofer: "*Nano-structural investigation of Ti-Al-N/Mo-Si-B multilayer coatings: A comparative study by APT and HR-TEM*", Vacuum 157 (2018), 173-179.

L. Schlicker, M. Bekheet, A. Gili, A. Doran, A. Gurlo, K. Ploner, T. Schachinger, S. Penner: "*Hydrogen reduction and metal-support interaction in a metastable metaloxide system: Pd on rhombohedral In₂O₃*", Journal of Solid State Chemistry 266 (2018), 93 - 99.

T. Schachinger: "*Dem Magnetfeld auf der Spur*"; Forschen und Entdecken 1 (2018), 1.

E. Aschauer, S. Sackl, T. Schachinger, H. Bolvardi, M. Arndt, P. Polcik, H. Riedl, P.H. Mayrhofer: "*Atomic scale investigations of thermally treated nano-structured Ti-Al-N/Mo-Si-B multilayers*", Surface & Coatings Technology 349 (2018), 480 - 487.

P. Schattschneider, T. Schachinger, J. Verbeeck: "*Transmissions-Elektronenmikroskopie mit Elektronenwirbeln Ein Whirlpool aus Elektronen*", Physik Unserer Zeit 1 (2018), 49, 22 - 28.

T. Schachinger, S. Löffler, A. Steiger-Thirsfeld, M. Stöger-Pollach, S. Schneider, D. Pohl, B. Rellinghaus, P. Schattschneider: "*EMCD with an electron vortex filter: Limitations and possibilities*", Ultramicroscopy 179 (2017), 15 - 23.

T. Götsch, T. Schachinger, R. Kaindl, S. Penner: "*PVD-Deposited Micro-SOFC Model Systems*", ECS Transactions 78 (2017), 1, 1771 - 1780.

T. Götsch, T. Schachinger, M. Stöger-Pollach, R. Kaindl, S. Penner: "*Carbon tolerance of Ni-Cu and Ni-Cu/YSZ sub-m sized SOFC thinfilm model systems*", Applied Surface Science 402 (2017), 1 - 11.

S. Pollitt, E. Pittenauer, C. Rameshan, T. Schachinger, O. V. Safonova, V. Truttmann, A. Bera, G. Allmaier, N. Barrabes, G. Rupprechter: "*Synthesis and properties of monolayer protected Cox(SC₂H₄Ph)_m clusters*", The Journal of Physical Chemistry 121 (2017), 10948 - 10956.

M. Stöger-Pollach, T. Schachinger, K. Biedermann, V. Beyer: "*Valence EELS below the limit of inelastic delocalization using conical dark field EFTEM or Bessel beams*", Ultramicroscopy 173 (2017), 24 - 30.

M. Kogler, E.-M. Köck, B. Klötzer, T. Schachinger, W. Wallisch, R. Henn, C. W. Huck, C. Hejny, S. Penner: "*High-Temperature Carbon Deposition on Oxide Surfaces by CO Disproportionation*", Journal of Physical Chemistry C 120 (2016), 1795-1807.

M. Kogler, E.-M. Köck, M. Stöger-Pollach, S. Schwarz, T. Schachinger, B. Klötzer, S. Penner: "*Distinct carbon growth mechanisms on the components of Ni/YSZ materials*", Materials Chemistry and Physics 173 (2016), 508-515.

R. Christian, M. Ikeda, G. Lientschnig, L. Prochaska, A. Prokofiev, P. Tomes, X. Yan, A. Zolriasatein, J. Bernardi, T. Schachinger, S. Schwarz, A. Steiger-Thirsfeld, P. Rogl, S. Populoh, A. Weidenkaff, S. Paschen: "Nanostructured clathrates and clathrate-based nanocomposites"; *Physica Status Solidi A* 213 (2016), 784-801.

Löffler, S., Schachinger, T., Stöger-Pollach, M. and Schattschneider, P.: "The Surprising Dynamics of Electron Vortex Beams"; *Microscopy and Microanalysis* 21 (Supplement S3) (2015), 19-20.

T. Schachinger, S. Löffler, M. Stöger-Pollach, P. Schattschneider: "*Peculiar Rotation of Electron Vortex Beams*"; *Ultramicroscopy* 185 (2015), 17-25.

P. Schattschneider, T. Schachinger, M. Stöger-Pollach, S. Löffler, A. Steiger-Thirsfeld, K. Bliokh, F. Nori: "*Imaging the dynamics of free-electron Landau states*"; *Nature Communications* 5 (2014), 1 – 6.

Books:

T. Schachinger: "*Electron Vortex Beams in Magnetic Fields: Imaging Landau States of Free Electrons*"; AV Akademikerverlag, Saarbrücken, BRD (2014), ISBN: 978-3-639-62537-0; 176 S.

Patents:

M. Stöger-Pollach, S. Löffler, T. Schachinger: "*Kathodolumineszenzdetektor für TEM*"; patent: Austria, Nr. PCT/AT2014/050203; submitted: 12.09.2014.

Diploma Thesis:

"*Electron Vortex Beams in Magnetic Fields*"; supervisor: P. Schattschneider; E052/USTEM, 2014; final examination: 21.01.2014.

Selected Talks:

Invited: T. Schachinger: " *Electron Vortex Beams in a TEM: From peculiar Landau state rotations towards magnetic measurements on the nanoscale* "; International Seminar, Group of Microscopy and Spectroscopy of Surfaces, Institute of Scientific Instruments of the Czech Academy of Science, Brno, Czech Republic; 04.12.2017 - 05.12.2017.

Invited: T. Schachinger: "*Peculiar rotations of electron vortex beams*"; Fritz-Grasenick-Preisverleihung, ASEM General Assembly, Vienna; 22.01.2016.

T. Schachinger, A. Steiger-Thirsfeld, M. Stöger-Pollach, P. Schattschneider: "*Bessel beams with high OAM: Prospects for unconventional electrodynamics*"; Microscopy Conference 2015 (MC2015), Göttingen, Germany; 06.09.2015 - 11.09.2015.

T. Schachinger, A. Steiger-Thirsfeld, M. Stöger-Pollach, P. Schattschneider: "*Generation of Massively Twisted Electron Vortex Beams in a TEM*"; Joint Annual Meeting of ÖPG, SPS, ÖGAA, SGAA, TU Wien; 03.09.2015.

T. Schachinger, A. Steiger-Thirsfeld, M. Stöger-Pollach, P. Schattschneider: "*Electrons with a magnetic moment of 10^3 Bohr magnetons*"; 12th Multinational Congress on Microscopy (MCM), Eger, Hungary; 23.08.2015 - 28.08.2015.

Invited: T. Schachinger: "*Electron Vortex Beams in Magnetic Fields: Revealing Peculiar Rotations and Landau State Dynamics*"; Semintalk, IFW Dresden, Germany; 01.12.2014.

T. Schachinger, P. Schattschneider, S. Löffler: "*Resolving Landau State Dynamics with Electron Vortex Beams*"; 18th International Microscopy Congress, Prague; 07.09.2014 - 12.09.2014, ISBN: 978-80-260-6720-7; Paper-Nr. IT-8-O-2020.

T. Schachinger, S. Löffler, M. Stöger-Pollach, A. Steiger-Thirsfeld, P. Schattschneider: "*Electron vortex propagation in the magnetic lens field*"; Microscopy Conference 2013, University of Regensburg, Germany; 25.08.2013 - 30.08.2013, in: "*MC2013 Proceedings Part 1*", (2013), P. 228 - 229.

T. Schachinger, S. Löffler, M. Stöger-Pollach, A. Steiger-Thirsfeld, P. Schattschneider: "*Influences of the objective lens on electron vortices*", 3rd ASEM-Workshop on Advanced Electron Microscopy, Medical University of Vienna, 25.04.2013 - 26.04.2013.

T. Schachinger, S. Löffler, P. Schattschneider: "*Numerical simulations of classical 200keV electrons passing atomic magnetostatic dipoles*"; 2nd ASEM - Workshop, Salzburg, Austria; 26.04.2012 - 27.04.2012.

Selected Posters:

T. Schachinger, A. Steiger-Thirsfeld, S. Löffler, M. Stöger-Pollach, S. Schneider, D. Pohl, B. Rellinghaus, P. Schattschneider: "*Towards EMCD with an Electron Vortex Filter*"; EMC 2016 – The 16th European Microscopy Conference, Lyon, France; 28.08.2016-02.09.2016.

T. Schachinger, A. Steiger-Thirsfeld, S. Löffler, M. Stöger-Pollach, P. Schattschneider, S. Schneider, D. Pohl, B. Rellinghaus: "*Preparation of holographic vortex masks for EMCD vortex filter experiments using advanced FIB milling strategies*"; EMC 2016 – The 16th European Microscopy Conference, Lyon, France; 28.08.2016-02.09.2016.

P. Schattschneider, V. Grillo, T. Schachinger, S. Löffler: "*Spin polarisation with electron Bessel beams?*"; EMC2016 - The 16th European Microscopy Congress, Lyon, France; 28.08.2016-02.09.2016.

T. Schachinger, A. Steiger-Thirsfeld, S. Löffler, M. Stöger-Pollach, P. Schattschneider, S. Schneider, D. Pohl, B. Rellinghaus: "*Preparation of holographic vortex masks for EMCD vortex filter experiments using advanced FIB milling strategies*"; IFEXS - Workshop on Imaging with Femtosecond Electron and X-ray pulses, Trieste, Italy; 01.02.2016-03.02.2016.

T. Schachinger, P. Schattschneider, S. Löffler, M. Stöger-Pollach, A. Steiger-Thirsfeld, K. Bliokh, F. Nori: "*Electron Vortex Beams in Magnetic Fields: Imaging Peculiar Rotations and Landau States*"; CCEM Summer School, McMaster University, Hamilton, Canada; 02.06.2014 - 06.06.2014.

Selected Co-Authored Talks:

Invited: S. Löffler, T. Schachinger, M. Stöger-Pollach, P. Schattschneider: "*The Surprising Dynamics of Electron Vortex Beams*"; Microscopy and Microanalysis 2015 Meeting, Portland, Oregon, USA; 02.08.2015 - 06.08.2015.

Invited: M. Stöger-Pollach, T. Schachinger, W. Hetaba, D. Abou-Ras, R. Rodemeier: "*Low Voltage EELS and Bessel Beams in Semiconductor Science*"; SALVE - Symposium 2015, University of Ulm, BRD; 17.02.2015 - 18.02.2015.

Invited: P. Schattschneider, T. Schachinger, M. Stöger-Pollach, S. Löffler, A. Steiger-Thirsfeld, K. Bliokh: "*Mode conversion, peculiar rotations, and the Landau-Zeeman-Berry phase in electron vortex beams*"; Microscopy Conference 2013, Universität Regensburg, BRD; 25.08.2013 - 30.08.2013.

Invited: P. Schattschneider, M. Stöger-Pollach, S. Löffler, T. Schachinger, K. Bliokh: "*Peculiar rotation of electron vortices in magnetic fields*"; ICOAM 2013, The Burrell Collection, Glasgow, UK; 03.06.2013 - 05.06.2013.